An enquiry into dark matter physics

by

Mudit Rai

B.Tech in Engineering Physics, Indian Institute of Technology, Bombay, 2017

Submitted to the Graduate Faculty of

the Dietrich School of Arts and Sciences in partial fulfillment

of the requirements for the degree of

Doctor of Philosophy

University of Pittsburgh

2023

UNIVERSITY OF PITTSBURGH

DIETRICH SCHOOL OF ARTS AND SCIENCES

This dissertation was presented

by

Mudit Rai

It was defended on

April 5th 2023

and approved by

Brian Batell, Associate Professor, University of Pittsburgh

Daniel Boyanovsky, Professor, University of Pittsburgh

Andrew Zentner, Professor, University of Pittsburgh

Colin Morningstar, Professor, Carnegie Mellon University

Joseph Boudreau, Professor, University of Pittsburgh

An enquiry into dark matter physics

Mudit Rai, PhD

University of Pittsburgh, 2023

This thesis aims to address some of the issues plaguing the Standard Model of particle physics and cosmology, with a particular focus on new theoretical and phenomenological approaches to the dark matter puzzle.

First we perform an in-depth phenomenological analysis of the potential observable consequences of the Higgs and neutrino portal dark sector models at the Fermilab DarkQuest proton beam fixed-target experiment. Our findings show that DarkQuest will have excellent sensitivity to new weakly coupled scalars and fermions in the GeV-scale mass range. Next, we construct and investigate renormalizable models of Flavor-Specific Scalar mediators, which dominantly couple with a certain specific fermion mass eigenstate. This work opens a pathway for new dark sector theories with novel flavor structures and distinctive phenomenology. We also investigate the cosmological production of ultra-light scalar dark matter with a feeble coupling to the Higgs field where we analyzed the effects of the SM thermal bath and the electroweak phase transition on the late time relic abundance. Our results include new relic density targets which can be compared with experimental and observational tests.

In a complementary direction,we also study several foundational questions in early universe cosmology, which, in addition to their instrinsic theoretical interest, can also provide an altogether different framework for understanding dark matter. Firstly, we study the emergence of entropy in the gravitational production of ultralight dark matter particles. Thereafter, we investigate the transition rates and cross sections for two-to-two scattering processes in a spatially flat radiation dominated cosmology. We then focus on the infrared dressing of bosonic or fermionic heavy particles by a cloud of (nearly) massless particles, which can lead to a unique production mechanism of ultralight dark matter or dark radiation in a radiation-dominated cosmology. We find that the initial amplitude of the single particle decays in time with a power law behaviour, instead of the usual exponential decay of the asymptotic Minkowski spacetime.

Table of Contents

List of Tables

List of Figures

Preface

I am very grateful to my Ph.D. advisor, Brian Batell for his incredible guidance and for providing unwavering support during my graduate studies. I really enjoyed working with him, and could not have asked for a better supervisor in terms of personality and providing the necessary room and freedom to excel. I would also like to express my deep gratitude towards Daniel Boyanovsky, who has been a reference point in terms of how a physicist should be, with an amazing intellect and great mathematical acumen. In addition to our wonderful collaborations, I learnt a great deal from his courses as well as from the stimulating discussions we had in his office.

I would like to thank my collaborators from whom I have learned a lot. I am also thankful to all of my committee members for their constructive feedback. I would like to thank all of my course instructors at PITT and CMU, who taught me the nuances of physics, as well as having patience for my questions. It was definitely one of the best times in my graduate school life.

No amount of words can express my gratitude towards my parents, who have always provided me with immense love and support. I would also thank my brothers and my close friends, who have always been there for me, despite living in different time zones, yet always a call away.

1.0 Introduction

We will begin our journey by taking a historical tour to get a glimpse of where we stand, how far have we come, and what the future might hold for us. Since the times of antiquity, humans have been curious to understand the natural phenomena happening around them. A detailed study of this historical survey merits its own thesis, but we will restrict ourselves to picking out some of the key milestones which motivated this research work.

As early as around 200 BCE [262], Maharishi Kanada, Diganga and other philosophers in Ancient India came up with the theory of atom-ism, which basically hypothesise what constitutes the macroscopic objects around us, with "parmanu" (Atom) being the smallest particle of matter which cannot be further subdivided. In the coming centuries in ancient India, debates raged about this theory, giving it a philosophical as well as metaphysical fervour. Similarly, in the western hemisphere, the early Greek philosophers, embarked on the journey of understanding about nature in a more systematic form, leading up to "Aristotelian physics", where Aristotle makes a herculean effort in understanding the natural phenomena around us in terms of four basic elements - "earth, water, air, and fire." Such was the impact, that it remained a cornerstone of science in Europe for the next millineum to come, until being replaced by the advent of modern science. There was a period of lull during the Dark Ages in the West, while some important developments were made in other parts of the world, notably in the Middle East, India and Far East. The beginning of the 16th century marks a turnaround, with the Scientific Revolution gripping Europe, with the advent of the Industrial revolution and kick-starting the modern era. Again, even describing the glories of humankind in this work would be akin to confining an ocean in a small vessel, and instead we would pick out some of the fundamental ideas which will help set up the tone. In the late 17th century, Sir Isaac Newton formulated the famous "three laws of motion", which together with the law of gravitation could describe the motion of macroscopic particles at large enough distances (compared to atomic size) and slow enough (compared to speed of light) speed quite correctly. It explained not only the motion of small objects like the apple falling on earth, but could also explain the revolution of Earth around the Sun and so on [291]. The

other fundamental force governing the physics of charged objects and light, which we now understand as Electromagnetism, was coherently put together by James Clerk Maxwell, in the form of "Maxwell Equations" in 1870s. By the late 19th century, it was widely believed that humans had made enough progress in understanding about our nature in a consistent manner.[1]. Yet, by the start of 20th century, a host of recently discovered phenomena such as photoelectric effect, the blackbody radiation as well as thought experiments challenged the fundamentals of classical physics. Other major developments such as the discovery of electron and the X-Rays led to questions regarding whether the atom was indeed the smallest, indestructible constituent of matter.

In the same epoch, a new era begun with Albert Einstein as its leading light. Einstein revolutionized our understanding of space and time, beginning with the Special Theory of Relativity published in 1905, and the General Theory of Relativity, published in 1915, capping of one of the crowing achievement of human intellect. Amongst a host of key concepts entailed in these theories, the curvature of space-time took the center stage, describing the gravitational effect at each point in space, thereby replacing the Newtonian's gravity. [2] More than a century later, it stands firm and is in agreement with the experimental tests.

Contemporary to relativity, a new paradigm was shaping up. Quantum Mechanics, the theory describing physics of subatomic particles, or more generally phenomena at the smallest of scales, was gradually established by a number of brilliant scientists, namely Max Planck, Niels Bohr, Erwin Schrodinger, Werner Heisenberg, Max Born, Paul Dirac, Pauli, Louis De Broglie, Wolfgang Pauli and Einstein. Dirac went on to unite Special Relativity and Quantum Mechanics (for spin half particles) into the Relativistic Quantum Mechanics. It was further developed to consistently understand the interaction of photons (light) with electrons, under the banner of Quantum Electrodynamics, pioneered independently by Richard Feynmann, Shin'ichirō Tomonaga and Julian Schwinger towards the mid-20th century. The subsequent discovery of new particles and their description in terms of field quanta led to new insights. For example, Hideki Yukawa came up with the idea of "short range" force that could be mediated by a massive particle inside the nuclei (done prior to the renormalization

[1] Claims such as "An eminent physicist remarked that the future truths of physical science are to be looked for in the sixth place of decimals [232]" were made.

[2] It can be derived from Einstein's equations in the classical limit.

of QED was firmly established).

During the later half of the twentieth century, the zeal for having an umbrella theory which could encapsulate all of the four fundamental forces, viz., the weak, the strong, gravity and electromagnetic, led to the birth of Standard Model, which successfully explains three of the four forces (except gravity) on the basis of symmetries structure and will be described in length in this chapter.

Thus, the inherent desire to understand about our nature, inspired by the phenomena around us, spelled out in the elegant language of mathematics, is a fundamental aspect of human intellect, and is ubiquitous in the human history. Physics codifies this zeal of enhancing our understanding of the universe in a well structured and mathematically coherent way.

1.1 The Standard Model of Particle Physics

The Standard Model of particle physics incorporates the fundamentals of physics at the smallest distances (or highest of energies) in a coherent and elegent way, and encapsulates within its framework, three of the four fundamental interactions/forces in our universe : the Electromagnetic, the Strong and the weak interactions. The electroweak theory in the standard model is due to the great work of Abdus Salam[311], Steven Weinberg [345] and Sheldon Glashow[202]. Key contributions to the strong interactions come from Gell-Mann and Gross, Wliczek, and Politzer. The basic structure of Standard Model (SM) consists of the gauge group $SU(3)_C \times SU(2)_L \times U(1)_Y$, where $SU(n)$ denotes the special unitary group of $n \times n$ unitary matrices with unit determinant, and $U(1)$ corresponds to the group of complex numbers with unit modulus. The subscripts C, L and Y denote color, weak isospin and hypercharge, respectively.

1.1.1 Particle content of Standard Model

The fundamental fields in SM and their quantum numbers are as follows:

$$Q_L = \begin{pmatrix} u_L \\ d_L \end{pmatrix} \equiv (3,2)_{1/6},\ u_R \equiv (3,1)_{2/3},\ d_R \equiv (3,1)_{-1/3} \tag{1.1.1}$$

$$L_L = \begin{pmatrix} \nu_L \\ e_L \end{pmatrix} \equiv (1,2)_{-1/2},\ e_R \equiv (1,1)_{-1} \tag{1.1.2}$$

$$W^a_\mu \equiv (1,3)_0\,,\ a = \{1,2,3\}\,,\ B_\mu \equiv (1,1)_0 \tag{1.1.3}$$

$$G^a_\mu \equiv (8,1)_0\,,\ a = \{1,2,3...8\} \tag{1.1.4}$$

$$H = \begin{pmatrix} h^+ \\ h_0 \end{pmatrix} \equiv (1,2)_{1/2}. \tag{1.1.5}$$

The electromagnetic charge, which emerges after the electroweak symmetry breaking is given by,

$$Q = T_3 + Y. \tag{1.1.6}$$

The convention followed for SM charges is $(c,d)_Y$, where c corresponds to the representation under $SU(3), d$, being the representation under $SU(2)$ and Y is the hypercharge.

We will try to keep the discussion concise, and to this end, let us write out the Standard Model Lagrangian, which can be partitioned into four parts, as :

$$\mathcal{L}_{SM} = \mathcal{L}_{gauge} + \mathcal{L}_{fermions} + \mathcal{L}_{Yuk} + \mathcal{L}_{Higgs}, \tag{1.1.7}$$

where, implies the kinetic terms corresponding to the Gauge sector, $fermions$ corresponds to the fermionic sector (comprising of leptons and quarks), Yuk corresponds to the terms which generate masses for the fermions after symmetry breaking, and $Higgs$ refers to the Higgs sector which would be responsible for the electroweak symmetry breaking. This is the Lagrangian at the tree level, and for the sake of keeping the discussion brief, we will not go in other technicalities which are beyond the scope of this work.

1.1.2 Gauge Sector

The gauge sector corresponds to the spin-1 fields, which gives rise to the vector particles known as gauge bosons, acting as the force mediators for the corresponding gauge groups. In general, for a spin-1 field A_μ, we can define its field strength tensor as:

$$X^a_{\mu\nu} = \partial_\mu A^a_\nu - \partial_\nu A^a_\mu + g_X f^{abc} A^b_\mu A^c_\nu, \tag{1.1.8}$$

where, μ, ν are the Lorentz group indices, a, b, c corresponds to the indices associated with the generators of the gauge group, g_X corresponds to the gauge coupling constant. f^{abc} is the structure constant of the gauge group, which satisfies the commutation relations of its generators t_i as,

$$[t_a, t_b] = i f^{abc} t_c. \tag{1.1.9}$$

Now, for the SM, we have three different gauge groups, viz. $SU(3)_c$ which in its fundamental representation has 8 generators, which are given via the Gell-Mann matrices, $t_a = \frac{1}{2}\lambda_a$. The gluon field tensor will be denoted via $G^a_{\mu\nu}$, where $a = 1, 2, \ldots 8$ labels to the 8 generators of $SU(3)$ and g_s denotes the strong coupling constant. Explicitly, the Gell Mann matrices are :

$$\lambda_1 = \begin{pmatrix} 0 & 1 & 0 \\ 1 & 0 & 0 \\ 0 & 0 & 0 \end{pmatrix}; \lambda_2 = \begin{pmatrix} 0 & -i & 0 \\ i & 0 & 0 \\ 0 & 0 & 0 \end{pmatrix}; \lambda_3 = \begin{pmatrix} 1 & 0 & 0 \\ 0 & -1 & 0 \\ 0 & 0 & 0 \end{pmatrix};$$

$$\lambda_4 = \begin{pmatrix} 0 & 0 & 1 \\ 0 & 0 & 0 \\ 1 & 0 & 0 \end{pmatrix}; \lambda_5 = \begin{pmatrix} 0 & 0 & -i \\ 0 & 0 & 0 \\ i & 0 & 0 \end{pmatrix}; \lambda_6 = \begin{pmatrix} 0 & 0 & 0 \\ 0 & 0 & 1 \\ 0 & 1 & 0 \end{pmatrix};$$

$$\lambda_7 = \begin{pmatrix} 0 & 0 & 0 \\ 0 & 0 & -i \\ 0 & i & 0 \end{pmatrix}; \lambda_8 = \frac{1}{\sqrt{3}} \begin{pmatrix} 1 & 0 & 0 \\ 0 & 1 & 0 \\ 0 & 0 & -2 \end{pmatrix}.$$

For $SU(2)_L$, we have the Pauli matrices σ^a in its fundamental representation as its generators ($T^a = \sigma^a/2$), satisfying, $[T^a, T^b] = i\epsilon^{abc} T^c$. We will use $W^a_{\mu\nu}$ as the notation for

its field strength tensor, the gauge coupling constant is given as g, and the field being written as W^a_μ, $a = 1, 2, 3$. The Pauli matrices are given as :

$$\sigma_1 = \begin{pmatrix} 0 & 1 \\ 1 & 0 \end{pmatrix} ; \sigma_2 \begin{pmatrix} 0 & -i \\ i & 0 \end{pmatrix} ; \sigma_3 = \begin{pmatrix} 1 & 0 \\ 0 & -1 \end{pmatrix}. \tag{1.1.10}$$

For the gauge tensor for $U(1)_Y$ group, we use the notation $B_{\mu\nu}$, with the gauge coupling being g' and the field being denoted as B_μ. Thus, writing it out explicitly, we have :

$$\mathcal{L}_{gauge} = -\frac{1}{4} B_{\mu\nu} B^{\mu\nu} - \frac{1}{2} \mathrm{Tr} W_{\mu\nu} W^{\mu\nu} - \frac{1}{2} \mathrm{Tr} G_{\mu\nu} G^{\mu\nu}. \tag{1.1.11}$$

where the trace is over the corresponding group generators, i.e $\mathrm{Tr}\, X_{\mu\nu} X^{\mu\nu} = \frac{1}{2} X^a_{\mu\nu} X_{a,\mu\nu}$.

1.1.3 Fermionic Sector

The fermionic sector includes the gauge interactions and the kinetic terms for the fermions in the Standard Model. Depending on the SM charges, the gauge fields of different groups will interact with these fermions. One can schematically write it out in terms of covariant derivatives (where the generators and their corresponding representations are self implied and thus suppressed here),

$$\mathcal{L}_{fermion} = i \bar{\psi} \not{D} \psi, \tag{1.1.12}$$

where,

$$D_\mu \psi = (\partial_\mu + i g_s \, t^a G^a_\mu + i g \, T^a W^a_\mu + i g' \, Y \, B_\mu) \psi. \tag{1.1.13}$$

where $\not{X} = \gamma^\mu X_\mu$ is the standard Feynmann slashed notation.

1.1.4 Higgs and Yukawa Sector

The Higgs mechanism was proposed in the 1960s [228, 219, 171], in order to explain the generation of mass for gauge bosons and fermions without spoiling the symmetry structure in the Standard Model.

In the most minimal scenario, and within the Standard Model, this tantamount to introducing a complex scalar doublet, charged under $SU(2)_L \times U(1)_Y$, which through its potential, leads to a spontaneous symmetry breaking of symmetries $SU(2)_L \times U(1)_Y \to U(1)_{EM}$. This leads to the generation of masses for SM fields in the new broken vacuum. In the SM, all the fields acquire their masses through their coupling to Higgs, and the values of the couplings have been fixed experimentally from the observed particle content. [3]

We can explicitly write down the higgs doublet as:

$$H = \frac{1}{\sqrt{2}} \begin{pmatrix} h^+ \\ h^0 \end{pmatrix}. \tag{1.1.14}$$

The hypercharge of both components is $\frac{1}{2}$, and the $SU(2)_L$ charges (T_3) would be $\pm\frac{1}{2}$ for h^+, h^0 respectively.

The Lagrangian containing the potential and interaction with gauge bosons is given as :

$$\mathcal{L}_{\text{Higgs}} = |D_\mu H|^2 + \mu^2 H^\dagger H - \lambda (H^\dagger H)^2, \tag{1.1.15}$$

where $\mu^2, \lambda > 0$, giving rise to the "wine-bottle" potential, and upon choosing the Unitary gauge, one can set $h^+ = 0$, $\langle h^0 \rangle = v = \frac{\mu}{\sqrt{\lambda}}$. This corresponds to the non-zero vacuum expectation value (vev) of the Higgs, and one can check that upon expanding the field around this non-zero minima, we have the spontaneous breaking of the symmetry of the gauge group from $SU(2)_L \times U(1)_Y \to U(1)_{EM}$. For the gauge bosons, after rotating to the mass basis, the W and Z boson masses are given as

$$m_W^2 = \frac{g^2 v^2}{4}, \; m_Z^2 = \frac{(g^2 + g'^2) v^2}{4}. \tag{1.1.16}$$

[3] Neutrinos are massless in the SM paradigm, but experimentally it has been found that they have non-zero mass(at least two generations are massive).

The Higgs vev is given by $v = 246$ GeV, obtained from the Fermi's constant, $G_F = 1.16639 \times 10^{-5}\,\text{GeV}^{-2}$ from the decay $\mu \to \nu_\mu\, e\, \bar{\nu}_e$ [263], which can be used to calculate the Higgs mass, $m_h = 125$GeV, using the correct quartic coupling value.

The Yukawa sector encodes the Higgs interaction with the fermions, which leads to the mass generation of quarks and leptons (apart from neutrinos) in the SM. Schematically, it is given as,

$$\mathcal{L}_{Yuk} = -y_{u\,ij}\,\overline{Q}_i\,\tilde{H} u_{Rj} - y_{d\,ij}\,\overline{Q}_i H\,d_{Rj} - y_{e\,ij}\,\overline{L}_i\,H\,e_{Rj} + h.c. \tag{1.1.17}$$

where $\tilde{H} = i\sigma_2\,H^*$ [315]. Once we diagonalize the Yukawa matrices y_e, y_d, y_u and go to the mass basis, then the fermionic masses are schematically given via, $m_f = \frac{y_f v}{\sqrt{2}}$.

We will briefly take a look at the flavour structure, focusing on the quark sector within the SM, which will also prove useful in understanding the symmetry structures involved in the chapter three on flavor specific scalars.

In QCD sector, flavor is a global symmetry, which is explicitly broken by the presence of Yukawa terms in the lagrangian,

$$U(3)_q \times U(3)_u \times U(3)_d \longrightarrow U(1)_B, \tag{1.1.18}$$

resulting in 26 broken generators, giving rise to $36 - 26 = 10$ physical parameters, which can be thought of as the 6 quark masses, 3 mixing angles, and one overall CP phase. The Yukawa couplings of fermions are responsible for generation of their mass, after diagonalizing to its mass basis. To be more specific, we have, in the flavor basis,

$$\mathcal{L}_{Yuk} \supseteq -\bar{u}_{Li}(m_u)_{ij}u_{Rj} - \bar{d}_{Li}(m_d)_{ij}d_{Rj},\ m_{x,ij} = \frac{y_{x,ij}v}{\sqrt{2}}. \tag{1.1.19}$$

The diagonalization is carried out by bi-unitary transformations,

$$m_{u,diag} = V_{uL} m_u V_{uR}^\dagger,\ m_{d,diag} = V_{dL} m_d V_{dR}^\dagger \tag{1.1.20}$$

This leads to the generation of mixing in the charged current sector (fermion interactions mediated by $W^\pm$ boson), which implies mixing between different families of quarks, with the mixing parameters given by the CKM matrix.

$$\frac{g}{\sqrt{2}}\bar{u_L}\gamma^\mu W_\mu^+ V_{CKM} d_L + h.c \tag{1.1.21}$$

where $a \in \{1, 2\}$, and $W_\mu^\pm = (W_\mu^1 \mp iW_\mu^2)/\sqrt{2}$, and the V_{CKM} is the famous Cabibbo-Kobayashi-Maskawa(CKM) matrix, given by

$$V_{CKM} = V_{uL} V_{dl}^\dagger. \tag{1.1.22}$$

The experimentally measured values for the magnitudes of the CKM elements are, [357]

$$V_{CKM} = \begin{bmatrix} |V_{ud}| & |V_{us}| & |V_{ub}| \\ |V_{cd}| & |V_{cs}| & |V_{cb}| \\ |V_{td}| & |V_{ts}| & |V_{tb}| \end{bmatrix} \tag{1.1.23}$$

$$= \begin{bmatrix} 0.97370 \pm 0.00014 & 0.2245 \pm 0.0008 & 0.00382 \pm 0.00024 \\ 0.221 \pm 0.004 & 0.987 \pm 0.011 & 0.0410 \pm 0.0014 \\ 0.0080 \pm 0.0003 & 0.0388 \pm 0.0011 & 1.013 \pm 0.030 \end{bmatrix}. \tag{1.1.24}$$

The CKM phase is given by $\delta_{13} = 1.20 \pm 0.08$ radians.

1.2 Standard Model of Cosmology

In the previous sections, we have primarily focused on the building blocks of the matter around us, but we haven't addressed one of the foremost questions pondered over by humanity - where did it all began? Trying to answer this question within the purview of science, we will focus on the standard model of cosmology, which provides the best-fitting picture for describing the statistical properties of the Universe on large scales [316]. In this framework, the basic assumptions [4] are [308]

- The universe was created in the Big Bang.
- The energy content of the universe is approximately given by 5% ordinary matter, 27% dark matter, and 68% dark energy.
- The gravitational interactions between the aforementioned components of universe are well described by the General Theory of Relativity at the cosmological scales
- The universe is homogeneous and isotropic on sufficiently large (cosmic) scales.

[4] For a more holistic survey of the assumptions, please refer to Table II [316]

This model, also known as ΛCDM model, is one of the simplest model which has proven to agree quite reasonably with a number of observations, such as explaining the structure of cosmic microwave background, the large scale structure of galaxy distribution, the abundance of elements in the universe as well as the important experimental observation which led to the idea that our universe isn't a static entity but is a dynamic, expanding with an acceleration, as observed in the recession speed of galaxies.

1.2.1 Brief Review of General Relativity

General Relativity forms the backbone over which we can build our ideas in a coherent and mathematically elegant way, and try to understand how our universe works, within the framework of the aforementioned ΛCDM model. General relativity(GR) was the magnum opus of Einstein, his crowning achievement, in which he showed that the force of gravitation can be thought in terms of the curvature and geometry of spacetime, generalizing special relativity and Newton's law of gravitation in one powerful framework. A systematic exposition of this wonderful theory is beyond the scope of this work, but we will shed light on the basic machinery used in cosmological setting.

The metric tensor (which in a naive sense can be thought of a quantity which helps measure distance), is a symmetric, rank-2 tensor on the space time manifold, which describes the local geometry of spacetime and captures all the important geometric and causal information of the spacetime. On a set of local coordinate system, let's say x^μ, where $\mu = 0, 1, 2, 3$ in a $(3+1)$ space-time, we can define the line element with the help of metric tensor $g_{\mu\nu}$ as,

$$ds^2 = g_{\mu\nu} dx^\mu dx^\nu. \tag{1.2.1}$$

For completeness, we will write out the Einstein's field equation, which explicitly relates the geometry of spacetime to the energy momentum tensor (the matter content), via

$$G_{\mu\nu} \equiv R_{\mu\nu} - \frac{1}{2} R\, g_{\mu\nu} = 8\pi G_N T_{\mu\nu}, \tag{1.2.2}$$

where $R_{\mu\nu}$ is the Ricci tensor, $R = g_{\mu\nu} R^{\mu\nu}$ is the Ricci scalar and $T_{\mu\nu}$ is the energy-momentum tensor.

Using observations from CMB experiments such as Planck [17], it is inferred that the early universe is almost homogeneous and isotropic over large scales. Thus, we can use a special metric, known as the Friedmann–Lemaître–Robertson–Walker (FLRW) metric, which describes a homogeneous, isotropic and expanding universe. More precisely, the line element, in terms of radial polar coordinates, in $(+,-,-,-)$ convention, is given as

$$ds^2 = dt^2 - a^2(t)(\frac{dr^2}{1-kr^2} + r^2 d\Omega^2),\ d\Omega^2 = d\theta^2 + \sin^2\theta\, d\phi^2, \tag{1.2.3}$$

where $a(t)$ is the scale factor, which contains all the time dependence of the spatial part, and can be thought of encoding the expansion of universe. k is a constant which represents the curvature of space, and can take up discrete values amongst $\{-1, 0, 1\}$ which correspond to open, flat[5] or closed universe respectively.

1.2.2 Expansion of universe

In the FLRW metric, the scale factor $a(t)$ contains the information of the expansion, and hence we need to calculate its evolution to understand how the energy content of the universe drives its expansion. By solving the Einstein's field equations, via assuming a isotropic and homogeneous energy-momentum tensor (to a good approximation, it is assumed to be a perfect fluid, which relates its pressure and the energy density via $\nabla_\mu T^{\mu\nu} = 0$), we get the Friedmann equation, which yields the time evolution of the scale factor in terms of the total energy density of the universe.

$$H^2 \equiv (\frac{\dot{a}}{a})^2 = \frac{8\pi G_N}{3}\rho_{tot}. \tag{1.2.4}$$

where the quantity H is the Hubble parameter.

Now, the total energy density $\rho_{tot} = \rho_m + \rho_{rad} + \rho_\Lambda$, consists of three different parts, each of which have a different equation of state, i.e $\rho = p(\rho)$, which can be solved to get $\rho = f(a)$. On doing this calculation, one finds,

$$\rho = \rho_0 \begin{cases} 1\,, & \text{Vacuum Energy} \\ (\frac{a(t)}{a_0})^{-4}, & \text{Radiation} \\ (\frac{a(t)}{a_0})^{-3}, & \text{Matter} \end{cases} \tag{1.2.5}$$

[5]For our purposes, we will set $k = 0$.

where, ρ_0, a_0 is some reference value for energy density at some reference time t_0. During different epochs, different components dominate the energy content of the universe, so that the one dominating will lead to setting the scaling of the scale factor as a function of time. During the early universe, the epoch was dominated by vacuum energy (VD)(inflation), which slowly gave way to Radiation dominated (RD) era, where basically the particles were highly relativistic, thus behaving as nearly massless. As the universe expanded and slowly cooled down, the particle content became non-relativistic, leading to the matter dominated (MD) era. Presently, we are in the cosmological constant (vacuum energy) dominated era. Hence, upon solving for the scale factor, we get

$$a = a_0 \begin{cases} e^{Ht}, & \text{VD era} \\ t^{1/2}, & \text{RD era} \\ t^{2/3}, & \text{MD era} \end{cases} \tag{1.2.6}$$

1.2.3 A glimpse into the cosmic history of our universe

The observation that our universe expands implies that it was hot and dense in the past. Over the course of time, it underwent various transitions and certain important landmarks can be identified, as shown in the Figure 1. We will briefly review our understanding of the cosmic history in a chronological order:

- **Inflation** : It is widely believed that before the start of cosmological hot era, there was a period of rapid, exponential expansion of the universe, dominated by "inflaton" field. The scale factor scaled as $a \propto e^{Ht}$, with Hubble being nearly constant. This went on till the inflation gave away to a period of "reheating", where the potential energy of inflaton was reinjected into the SM (and non-SM) degrees of freedom, and resulted in a formation of high temperature thermal bath. The key reason of introducing this paradigm was to solve some major problems with the hot big bang, viz., explaining the the origin of the large-scale structure of the universe by seeding primordial in-homogeneity, explaining why the universe is flat, isotropic and nearly homogeneous (e.g.,cosmic microwave background radiation exhibiting nearly uniform temperature).

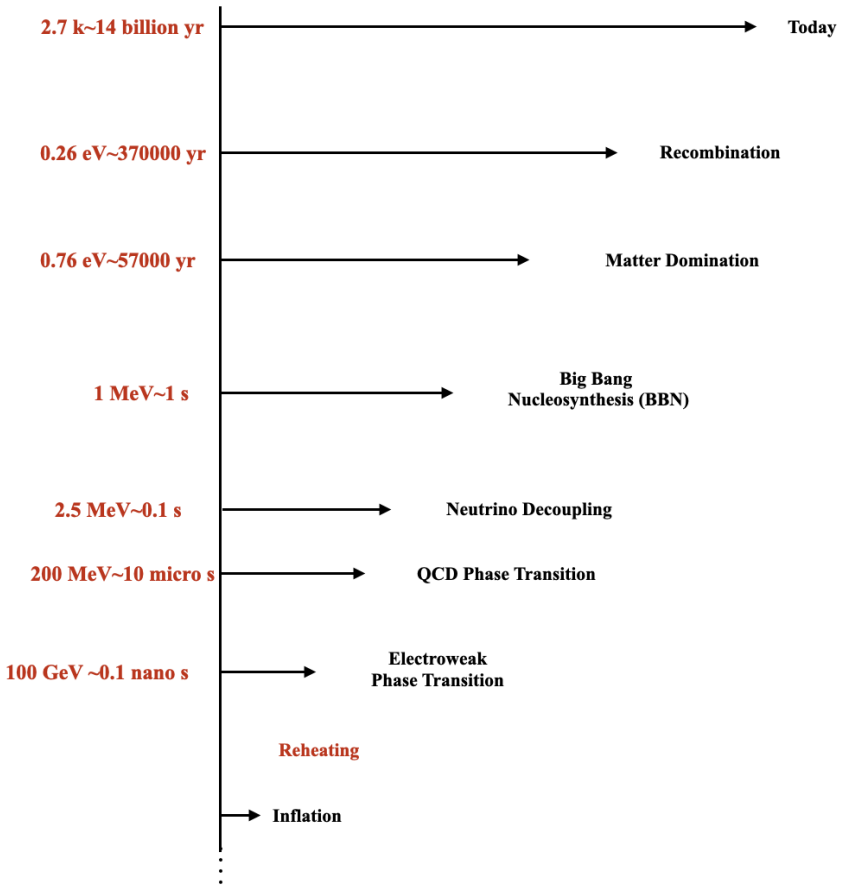

Figure 1: Cosmic history of universe.

- **Reheating** - The ending of inflation of is constrained to happen above $T_{RH} > 3$ MeV to have succesful Big Bang nucleosynthesis. But it can occur at much higher temperatures, depending on the model of the inflationary sector. The case where the reheating happens above a few hundered GeV will have phases where the electroweak symmetry was unbroken till the electroweak phase transition, and at lower temperature of about $T \sim \Lambda_{QCD} \sim 200$ MeV, the QCD phase transition, where the free quarks hadronise to form hadrons.
- **Big Bang Nucleosynthesis(BBN,** $T \sim 1$ MeV)- For temperatures of the scale of binding energies of nuclei, $O(1-10)$ MeV, the universe cooled down enough for the

capture of neutrons in nuclei, leading to formation of light elements (in the form of ions). The BBN era marks the time from which we can be confident about our understanding of the cosmic history.

- **Matter-Radiation equality ($T \sim 1$eV)** - As the universe cools down and the temperature drops below the mass of particles, they become non-relativistic. Thus, by equating the $\rho_m = \rho_{rad}$, we get $T \sim 0.8$eV which gives the approximate value when matter-radiation equality is attained. Everything apart from photons and neutrinos is in the non-relativistic regime, and thus the universe starts to be dominated by matter, which implies that the scale factor scales like $a \sim t^{2/3}$ instead of $a \sim t^{1/2}$.
- **Recombination ($T \sim$0.3 eV)** - Around the temperatures of around, $0.3 - 0.2$ eV there is a transition to states where the free electrons can be captured by the ions, which leads to the formation of neutral atoms, mostly hydrogen and helium. This also leads to photons being free streamed since the photon-matter interaction becomes negligible. These photons can still be detected as the cosmic microwave background (CMB), giving the oldest direct observation of universe. The temperature of the CMB has been redshifted to about 2.7 K on average today, but it also encodes the CMB anisotropies (variations) across the sky, which provides valuable information like the energy density of baryons with respect to the dark matter content.
- **Vacuum Domination**(today)- In recent (at redshift $z \sim 0.5$ [309]) times, observations have shown that the energy density of the universe is being dominated by vacuum energy, which gives to a regime of an accelerated expansionary epoch.

1.3 Limitations of Standard Model

The Standard Model is a remarkably successful framework, explaining how this universe works in the best possible manner, and has successfully passed hosts of experimental tests with unprecedented accuracy. However, despite its tremendous success, there remain some fundamental open problems: What makes up the energy content of our universe and what are the mysterious dark Matter and dark Energy? Why do particle masses and coupling

constants have the values that we measure? Why are there three generations of fermions? How do neutrinos obtain mass? Why is there a matter-antimatter asymmetry? How can we systematically pair up gravity with the Standard Model? Here we will briefly go over some of these important questions, and will try to motivate our research topics which follow in the subsequent chapters.

1.3.1 Dark Matter

A host of astrophysical and cosmological signatures have revealed the presence of dark matter (DM) and dark energy, making up the bulk of the energy content in our universe. Thus it is imperative to understand and study it in depth. DM candidates can range all the way from fundamental particles as light as $10^{-22}eV$ to heavy composite objects (e.g., primordial black holes) as heavy as 10 solar masses.

We will start historically, collecting up the evidences for DM, which is currently one of major topics for research and provides a shining light for new physics directions. Towards the turn of the twentieth century, starting with Lord Kelvin and Poincare, the first indications for presence of non-luminous matter in the universe started showing up. In the following, we will discuss some of the pivotal moments in the history of research.

- Galaxy clusters : In 1933 Fritz Zwicky applied the virial theorem to the Coma Cluster and obtained evidence of unseen mass. Measuring the galactic orbital velocities, he found that the values were way too high in order for the clusters to be held together only by luminous mass. Using obsolete values of Hubble, he determined that the mass-to-light ratio was around 500. Even after correcting the Hubble value, the mass-to-light ratio would be around 8, implying that there is a lot more matter than what is visible [356].
- Galactic velocity curves : The velocity curve of a galaxy is a plot of the orbital velocities of stars around the galactic centre vs distance from the centre. For spiral galaxies, this would mean that the velocity curve will drop off with the increasing distance. In the 1970s, Vera Rubin and other scientists made measurements of luminous galaxies, and found that all of them showed a flat profile instead of the anticipated tail-off [310]. This showed the possibility of non-luminous matter in the form of halos around the galaxies.

- Gravitational lensing : Gravitational mass results in the change in curvature around it, which results in bending of light passing nearby. Mass can be predicted studying the amount of deviation measured on earth, and is called gravitational lensing. It has been found that the observed lensing effect from galaxies cannot be explained if it was only composed of ordinary, luminous matter. This indicates the existence of DM around the galaxies, which will explain the lensing [59].
- Bullet Cluster: Bullet cluster consists of the collision of two galaxy clusters. It was found that the center of mass is far displaced from the baryonic center of mass, which strongly point towards the existence of DM.[134].
- Structure formation : This corresponds to the formation of all the large scale structures that we observe, be it galaxies, galaxy clusters etc., starting from small early density fluctuations. For ordinary matter to explain this, we would need around two orders of magnitude more density perturbations at the time of recombination than that measured from the CMB [252].

Observations of the matter power spectrum and CMB imply that the DM has only gravitational interactions and they also have to be non-relativistic (corresponding to $z < 10^7$). In many models, the physics that sets the DM relic abundance occurs at early times in order to preserve the physics after BBN, which is observationally well studied. DM candidates are also constrained to be long lived and should have decay time larger than the age of universe[269]. If DM decays to certain kinds of SM particles, such as photons, the lifetime constraint is even more stringent.

While there are a wide variety of proposed DM candidates, in this introduction, we will focus the discussion on one particular class of models spanning masses below $\sim$ keVscale, and are referred as ultralight bosonic dark matter. The relic abundance for such light particles may be set by the so-called misalignment mechanism, whereby the DM field is offset from its minimum in the early universe, and begins to oscillate about its minimum as the universe cools down. For example, consider a scalar field ϕ, with Lagrangian

$$\mathcal{L} = \frac{1}{2}\, g^{\mu\nu}\partial_\mu\phi\partial_\nu\phi - \frac{1}{2}m^2\phi^2. \tag{1.3.1}$$

The equation of motion, for it's homogeneous part is given by, considering FRW geometry,

$$\ddot{\phi} + 3H\dot{\phi} + V'(\phi) = 0 \ , \ V'(\phi) = m^2\phi. \tag{1.3.2}$$

In the radiation era, $H = \frac{1}{2t}$, and even without solving the equation exactly [6], one can easily deduce the behaviour of the field at early times and at the late times, with solution given as

$$\phi(t) \sim \begin{cases} \phi_i & H \gg m \\ \frac{2\Gamma(\frac{5}{4})\,\phi_i}{\sqrt{\pi}\,(mt)^{3/4}} \sin(m\,t + c_0) & H \ll m \end{cases} \tag{1.3.3}$$

This is because at early times, the Hubble friction term dominates over the mass term. Hence we have $\ddot{\phi} + 3H\dot{\phi} \sim 0$, which keeps the field fixed at it's initial value. As the universe expands and cools down, Hubble parameter becomes smaller than the mass, and the field slowly starts oscillating around it's minima. The time at which it starts oscillating is given by

$$3H(t) = m \Longrightarrow t_{osc} = \frac{3}{2m}. \tag{1.3.4}$$

The energy density is given as

$$\rho_\phi = \frac{\dot{\phi}^2}{2} + \frac{m^2\phi^2}{2}. \tag{1.3.5}$$

We can use the exact solution to calculate this quantity, and one can show that it scales as $\rho_\phi(t) \propto \frac{\sqrt{m}\phi_i^2}{t^{3/2}}$, i.e. it is dependent on the inital condition (which can be the value of the field at the end of inflation) [333].

The late time energy density can also be related to the time at which the oscillation starts in the following manner: The comoving number density (so called yield) is a conserved quantity, i.e.,

$$Y \equiv \frac{n_\phi}{s} = \frac{\rho_\phi}{m\,s} = constant, \tag{1.3.6}$$

where s, is the entropy density, given via $s = \frac{2\pi^2}{45} g_*(T) T^3$, where the temperature T and time is related as $T = \left(\frac{M_{pl}}{2\gamma\,t}\right)^{1/2}$ and g_* is the effective number of relativistic degrees of freedom and $\gamma = \sqrt{\frac{\pi^2 g_*}{90}}$. Now it is straightforward to derive the late time energy density in terms of time where oscillation starts,

$$\rho(T_0) = \rho(T_{osc})\frac{s(T_0)}{s(T_{osc})} = \rho(T_{osc})\frac{g_*^0}{g_*^{osc}}\left(\frac{T_0}{T_{osc}}\right)^3. \tag{1.3.7}$$

[6] The exact solution is given in terms of Bessel functions, $\phi(t) = 2^{1/4}\Gamma(\frac{5}{4})\phi_i(mt)^{-1/4}J_{1/4}(mt)$.

The late time relic abundance is given by,

$$\Omega_{\phi}^{0} = \frac{\rho_{\phi,0}}{\rho_c} \sim 0.3 \times \sqrt{\frac{m}{10^{-12}eV}} \left(\frac{\phi_i/M_{pl}}{2\times 10^{-4}}\right)^2 \times \left(\frac{g_*^{osc}}{10}\right)^{-1/4}, \tag{1.3.8}$$

where, $\rho_c = 3.7 \times 10^{-47} GeV$ is the critical density of universe at $T = 2.7K$.

Although the above discussion show a remarkably simple model for DM, without any interactions with the Standard Model it is extremely difficult to detect and test. An interesting alternative scenario for DM physics with a rich variety of experimental and observational signatures is given by the "dark sector" framework. The mediator and the DM can be part of another family of particles outside the SM particle content, and the dark sector particles can act as mediators between our SM and the DM. The portals which are relevant for dark sector-SM interactions can be classified based on the spin of the mediator and are greatly constrained by the SM gauge group and Lorentz symmetry. At the renormalizable level, there are just three such portal interactions:

- $(\mu S + \lambda S^2)\, H^\dagger H$: Scalar portal, where the mediator generally goes by the name of dark Higgs and has feeble couplings to the SM Higgs.
- $-\frac{\kappa}{2} B_{\mu\nu} V^{\mu\nu}$: Vector Portal, where the mediator is also called as dark photon, which can kinetically mix with the SM photon (or SM hypercharge boson).
- $y\, LHN$: Neutrino portal, with the sterile neutrinos acting as potential candidates with their feeble coupling to active neutrinos, while also explaining the neutrino mass issue.

In the recent times, this has led to a dedicated effort to search for these particles, extending to looking at complementary signatures at high energy colliders (Energy Frontier), or at fixed target experiments (Intensity Frontier) . One can also search for such particles using astrophysical signatures (Cosmic Frontier). This represents an orthogonal way of thinking to the usual top-down approach motivated by fundamental physics problems where we explore the new phenomenological directions using experimental signatures, relying more on expanding the experimental searches and data [269].

1.3.2 Neutrino Mass

In the SM, neutrinos are charge and color neutral fermions which come in as part of the leptonic doublet with the corresponding lepton. We have three active neutrinos, each with electon, muon and tau flavor. Due to the gauge structure of SM, we do not have a mass term like that for charged leptons which can generate masses for neutrinos and hence neutrinos are massless within the SM. Thus, any mass generating mechanism for neutrinos needs the existence of physics beyond the Standard Model.

Neutrino oscillation experiments,including those studying solar and atmospheric neutrinos, oscillation data have shown that at least two of the three active neutrinos have to be massive. Experimentally, neutrinos are labelled under different categories depending on how they are produced. One of the prominent sources of neutrinos comes from the sun, named as "Solar Neutrinos". They are generically produced either via a *pp* chain, in the fusion reaction of $4p \rightarrow He + 2e^{+}2\nu_e$, and in electron capture by isotopes of carbon, and oxygen, termed as CNOs. In both cases, the dominant flavor predicted by SM would be that of electron neutrinos. But as the observations were made at the Homestake, Kamiokande, GALLEX, SAGE, Super-Kamiokande, and SNO experiments, only about a third of the predicted ν_e flux was observed. This posed the so called "solar neutrino problem", the resolution of which was the concept of neutrino flavor oscillations including the Mikheyev–Smirnov–Wolfenstein (MSW) matter effect in the sun. This requires neutrinos to be massive. Atmospheric neutrinos are produced in earth's atmosphere due to cosmic ray interactions, generally via the decay of pions and muons via charged current interactions. Atmospheric neutrinos are produced in the atmosphere, about order 10 km above surface of the earth. However, the atmospheric neutrinos can travel through and even across the earth to the detector. Also the detector is typically underground. Super Kamiokande detected the oscillation in atmospheric neutrinos, which was again explained using the idea of neutrino oscillation. The observed fluxes helps put constraints on the mass squared difference, which in turn may provide information about the new physics which generates the active neutrino masses. Finally, the accelerator and reactor based neutrinos are the ones produced in the laboratory environment. Experimental facilities are generally grouped as long baseline or short baseline, depending on the

size of the experimental facilities. The long baseline experiments generally have two detectors, one placed close to the detector (generally less than a km away from source) termed as near detector, and another placed as far as a thousand km away, termed as far detector. In general, the experimental setup is chosen so that $\frac{L}{E} \sim \frac{1}{\Delta m^2_{ij}}$, where Δm^2_{ij} corresponds to the mass squared difference between different mass eigenstates of active neutrinos, L corresponds to the distance between the source and detector, and E is the typical energy of neutrino. Lab based neutrino facilities are quite useful since due to the large achievable neutrino fluxes, controllable energy and baseline and detailed knowledge of the neutrino flavor at the source. As an example, we may consider the upcoming Fermilab neutrino facility called DUNE (Deep Underground Neutrino Experiment), which has a $120GeV$ proton beam impinged on graphite target, a near detector at a distance of $O(500\,m)$ from the target , and a far detector $1,300\,km$ at the Sanford Underground Research Facility in South Dakota.

For the case of 3 active neutrinos scenario, there are 6 parameters which describe the probability for a neutrino to oscillate between flavors, namely the two mass squared differences, $\Delta m^2_{21}, \Delta m^2_{31}$, the three mixing angles, $\theta_{12}, \theta_{23}, \theta_{13}$ and the phase, δ. If neutrinos are Majorana particles there are two additional phases in general. In addition, there are two possible mass ordering, which refers to the sign of Δm^2_{31}, with positive being the normal ordering (NO)and negative being inverse ordering (IO). Different experiments give best fits for different parameters, and we will summarize the global fit values [154]. Δm^2_{21} has a best fit value of $7.5 \times 10^{-5} eV^2$, with KamLAND, a long baseline reactor based facility contributing the most. Δm^2_{31} has a best fit value of $2.55 \times 10^{-3} eV^2$ for NO and $2.45 \times 10^{-3} eV^2$ for IO, from a combination of long baseline accelerator based (LBL), atmospheric and reactor based facilities. For the mixing angles, θ_{12} has a best fit of 34.4° measured at solar detectors, while θ_{23} has a best fit value of 49.26° for NO and 49.46° for IO from a combination of LBL and atmospheric detectors. θ_{13} has a best fit value of 8.53° for NO and 8.58° for IO measured at short baseline reactor based detectors. Finally, the phase has the best fit values of 1.08π for NO and 1.58π for IO, dominated by observations at LBL facilities.

There are a number of ways to generate neutrino masses beyond the SM physics, but we will restrict ourselves to the "Type-1" See-saw model. In this mechanism, one introduces

two or more singlet fermions, termed as sterile neutrinos, with the Lagrangian given as[357],

$$\mathcal{L} \supseteq -M_D \bar{N} \nu_L - \frac{M_N}{2} \bar{N}\, N^c + h.c. \tag{1.3.9}$$

where we introduced n sterile neutrinos, M_d is a $n \times 3$ complex matrix, M_N is a $n \times n$ symmetric matrix. One can consider a larger $(3+n)$ active + sterile vector space in which the mass matrices for the different sterile and active neutrinos form blocks, and we can diagonalize it to get the mass eigenstates. As a simple example, consider a $(1+1)$ scenario, then the mass matrix looks like

$$\mathcal{M} = \begin{pmatrix} 0 & M_D \\ M_D & M_N \end{pmatrix} \tag{1.3.10}$$

The eigenvalues become,

$$\lambda_\pm = M_N \pm \sqrt{M_N^2 + 4M_D^2}, \tag{1.3.11}$$

and in the case where the sterile neutrino is several orders of magnitude heavier, the approximate mass of the light active neutrino is,

$$m_\nu \sim \lambda_- \sim -\frac{M_D^2}{M_N}. \tag{1.3.12}$$

This mechanism not only gives the mass to the active state, but also explains why the neutrino is so light, which can come from its mixing with massive sterile neutrino state. We also get a host of signatures for the sterile neutrinos, since a diagonalization to mass basis lead to the coupling of the sterile neutrinos to the SM in the same way as that of the active neutrino, suppressed by the mixing angle [97]

$$\mathcal{L}_{int} = \frac{g}{\sqrt{2}} W_\mu^+ \bar{N} \sum_\alpha U_\alpha^* \gamma^\mu P_L L_\alpha + \frac{g}{2\cos\theta_W} Z_\mu \bar{N} \sum_\alpha U_\alpha^* \gamma^\mu P_L \nu_\alpha + h.c. \tag{1.3.13}$$

where the (small) mixing angle is given by,

$$U_\alpha = \frac{M_\alpha}{M_N};\ \alpha = e, \mu, \tau. \tag{1.3.14}$$

1.3.3 Issues related to flavor physics and CP violation

Flavor physics is arguably beset by a number of puzzles. One of the foremost issues arises from the hierarchy in the masses/Yukawa couplings of the quarks and leptons in the SM, with $m_e : m_\mu : m_\tau \sim 10^{-3} : 10^{-1} : 1$ for the lepton sector. In principle, one might have thought that the Yukawa couplings of all three leptons should have been of the same order, yet Nature gives us values which begets an explanation. The same is true in the case of quarks, where it is even more pronounced. In the up-type family, we have $m_u : m_c : m_t \sim 10^{-5} : 10^{-2} : 1$, and in the down-type family, we have, $m_d : m_s : m_b \sim 10^{-3} : 10^{-2} : 1$.

There are various proposals to explain the hierarchy, which generally involve new fields added to the SM at some high scale. This can induce modifications to flavor physics observables, and may therefore face tight constraints from experiments. Even in BSM models that do not address the flavor puzzle, flavor physics often imposes relevant constraints. Among the most stringent bounds arise from processes involving flavor-changing neutral currents (FCNCs). .Within the SM there are no flavor-changing neutral current(FCNC) at the tree level, and even at loop level they are suppressed due to the GIM mechanism[201]. It is based on the unitarity of the CKM matrix, and helps in explaining the small rate of certain rare flavor changing processes, such as $K_L \to \mu^+\mu^-$. In SM, due to loop suppression as well as small CKM elements, the decay rate is suppressed, hence any new physics will lead to deviations. Thus, in general, adding new physics in the flavor sector is highly constrained, e.g., if there's an addition of a vector-like-quark (VLQ) charged under SM gauge group, then it will mix with the SM quarks, which modifies the CKM as well as enters loop calculations like the one in box diagram in Kaon mixing.

Within the SM gauge sector, there exists a gauge invariant term, also known as the θ term in the gluon sector, given by,

$$\mathcal{L}_\theta = \theta \frac{g^2}{32\pi^2} \tilde{G}_{\mu\nu} G^{\mu\nu}, \ \tilde{G}_{\alpha\beta} = \epsilon_{\alpha\beta\gamma\delta} G^{\gamma\delta}. \tag{1.3.15}$$

This is a total derivative term, i.e. it can be shown that it is equal to $\partial_\mu K^\mu$, K^μ being a function of gluon field. Thus, upon its addition to the action, one would naively expect that

it will have no effect on the physics. But, for a non-Abelian group like $SU(3)$, but there exist a non-trivial vacuum configurations which have integral winding numbers, i.e.

$$\frac{g^2}{32\pi^2}\int d^4x\,\tilde{G}G = \int d\Sigma^\mu K_\mu = n;\; n \in \mathrm{Re}\,. \tag{1.3.16}$$

The QCD θ term contributes to the neutron electric dipole moment, which has been measured quite accurately,

$$d_n = \theta\frac{e}{\Lambda^2_{QCD}}\left(\frac{m_u m_d}{m_u + m_d}\right) < 3\times 10^{-26} e\,cm\,[53] \tag{1.3.17}$$

This yields a bound on the theta parameter, with $|\theta| < 10^{-10}$. The question of why θ is so small is what constitutes the Strong CP problem. In the last 50 years, there have been numerous attempts to counter this issue, with the QCD axion being the most famous one. The axion is a pseudo-goldstone boson[7] of a spontaneously broken $U(1)_{PQ}$ symmetry. The PQ symmetry was introduced by Peccei and Quinn, but it was quickly pointed out by Weinberg and Wilczek that there should be an associated Goldstone Boson. The characteristic feature of the QCD axion is its coupling to gluons, $\frac{a}{f_a}\frac{g^2}{32\pi^2}G\tilde{G}$, which dynamically relaxes the theta term to zero, thus giving a dynamical solution to the Strong CP problem. In addition to this, it can also serve as an ultralight DM candidate, making up a part or whole of the cold DM abundance.

1.4 Basics of QFT in curved space-time

We would like to do a brief survey of the effect of gravitational backgrounds on quantum fields. In order to keep the calculations minimal, we choose to study here a non-interacting real scalar field in an FLRW background, motivated by the ΛCDM model and aligning with the subsequent chapters presenting in this thesis. The case of fermions is discussed in the chapter 5, as well as a scenario of interacting fields in curved backgrounds are discussed in chapter 6 [289, 226, 305, 306, 297].

[7] A goldstone boson is a massless boson resulting from the spontaneous breaking of a continuous symmetry. In the presence of soft explicit symmetry breaking terms, it results in the goldstone boson getting a non-zero mass, and is called a pseudo-goldstone boson.

1.4.1 Scalar field in FRW metric

The action for a real scalar field ϕ [289] is given as,

$$S = \int \sqrt{-g}\, d^4x \left[\frac{1}{2} g^{\mu\nu}\partial_\mu\phi\partial_\nu\phi - V(\phi)\right], \tag{1.4.1}$$

where, $V = \frac{1}{2}m^2\phi^2 + \frac{1}{2}\xi R\phi^2$, which for minimally coupled field will be $\xi = 0$ and conformally coupled field will be $\xi = 1/6$. We will further restrict ourselves to $\xi = 0$ case. The equation of motion is given by

$$g^{\alpha\beta}\partial_\alpha\partial_\beta\phi + \frac{1}{\sqrt{-g}}\partial_\alpha(g^{\alpha\beta}\sqrt{-g})\partial_\beta\phi + \frac{\partial V}{\partial\phi} = 0. \tag{1.4.2}$$

For the case of FRW metric, we have

$$ds^2 = dt^2 - a^2(t)dx^2. \tag{1.4.3}$$

In order to see the fact that FRW is conformally flat, we introduce the conformal time as $d\eta = \frac{dt}{a(t)}$. Thus, the line element becomes,

$$ds^2 = a^2(\eta)(d\eta^2 - dx^2). \tag{1.4.4}$$

This looks exaclty like the Minkoswki metric, with an overall scaling. Thus, the metric tensor is given as, $g_{\mu\nu} = a^2\eta_{\mu\nu}$, $\sqrt{-g} = a^4$ and $g^{\mu\nu} = \frac{\eta^{\mu\nu}}{a^2}$. The equation of motion then simplifies to

$$\phi'' + 2\frac{a'}{a}\phi' - \nabla^2\phi + m^2\phi = 0, \tag{1.4.5}$$

where $' \equiv \frac{\partial}{\partial\eta}$. We can define an auxiliary field $\chi = a\,\phi$, which simplifies the equation to

$$\chi'' - \nabla^2\chi + m_{eff}^2\chi = 0,\ m_{eff}^2 = m^2a^2 - \frac{a''}{a}. \tag{1.4.6}$$

Above equation looks exactly like the Klein Gordon equation in Minkowski spacetime, albeit with the different m_{eff}^2 which now depends on the scale factor. The action also takes the form of the scalar field in flat spacetime(with the effective mass),

$$S = \int d^3x\, d\eta \left[\frac{\chi'^2}{2} - \frac{(\nabla\chi)^2}{2} - \frac{m_{eff}^2(\eta)\chi^2}{2}\right]. \tag{1.4.7}$$

Even though the equations look quite similar to the usual KG case, the time dependent action implies that the energy would not be conserved, and there is a possibility of gravitational production of particles, with their energy sourced by the gravitational field in the background.

The next order of business is to derive equations in terms of their Fourier modes, where the spatial part of the Fourier transform will be same as Minkowski, and all the time dependence will be in the Fourier coefficient:

$$\chi(\vec{x},\eta) = \int \frac{d^3k}{(2\pi)^{3/2}} \chi_k(\eta) e^{i\vec{k}.\vec{x}}, \tag{1.4.8}$$

and the equation of motion is,

$$\chi_k'' + \omega_k^2(\eta)\chi_k = 0,\ \omega_k^2(\eta) = k^2 + m^2a^2 - \frac{a''}{a}. \tag{1.4.9}$$

As this is a second order differential equation, any general solution can be expressed in terms of a combination of two linearly independent solutions. The condition for any two solutions to be linearly independent is that they have a non-zero Wronskian, i.e., let $y_{k,1}, y_{k,2}$ be two linearly independent solutions of the same mode equation so that $W[y_{k,1}, y_{k,2}] \neq 0$. Define $v_k(\eta) = y_{k,1} + iy_{k,2}$, then $v_k(\eta)$ and $v_k^*(\eta)$ will be two linearly independent solutions as well, since $W[v_k, v_k^*] = v_k' v_k^* - v_k^{*'} v_k = -2i\, W[y_{k,1}, y_{k,2}] \neq 0$. We can also choose a normalization via, $W[v_k, v_k^*] = 2i$, which will prove useful later when we define the commutation relations. It implies that the general solution, χ_k can be expanded as a linear combination of $v_k(\eta), v_k^*(\eta)$, and this can be used to re-express the Fourier transform as

$$\chi(\vec{x},\eta) = \int \frac{d^3k}{(2\pi)^{3/2}} \frac{1}{\sqrt{2}} \left[a_k^- v_k^*(\eta) e^{i\vec{k}.\vec{x}} + a_k^+ v_k(\eta) e^{-i\vec{k}.\vec{x}} \right], \tag{1.4.10}$$

where, $a_k^- = \sqrt{2}\, \frac{W[v_k,\chi_k]}{W[v_k,v_k^*]}$ and $a_k^+ = a_k^{-*}$, both of which are independent of η.

1.4.2 Quantization of scalar field

Employing the standard trick of promoting the integration constants a_k to operators as $\hat{a}_k$, we get

$$\hat{\chi}(\vec{x},\eta) = \int \frac{d^3k}{(2\pi)^{3/2}} \frac{1}{\sqrt{2}} \left[\hat{a}_k^- v_k^*(\eta) e^{i\vec{k}.\vec{x}} + \hat{a}_k^+ v_k(\eta) e^{-i\vec{k}.\vec{x}}\right], \tag{1.4.11}$$

where the operators satisfy the usual equal time commutation relations,

$$[a_k^-, a_q^+] = \delta^3(\vec{k}-\vec{q}), \quad [a_k^-, a_q^-] = [a_k^+, a_q^+] = 0. \tag{1.4.12}$$

where the normalization is, $W[v_k, v_k^*] = 2i$. The quantum Hamiltonian is given as

$$\hat{H} = \int \frac{d^3x}{2} \left(\hat{\pi}^2 + (\nabla\hat{\chi})^2 + m_{eff}^2 \chi^2\right), \tag{1.4.13}$$

where, $\hat{\pi} = \frac{d\hat{\chi}}{d\eta}$ and it satisfies the equal time commutation relation $[\hat{\chi}(\vec{x},\eta), \hat{\pi}(\vec{y},\eta)] = i\,\delta^3(\vec{x}-\vec{y})$. The creation annihilation operators can be thought in terms of the operators $\hat{a}^{\pm}$, with $\hat{a}_k^- \mid 0\rangle = 0$ and $\hat{a}_k^+ \mid 0\rangle = \mid k\rangle$.

1.4.3 Bogolyubov transformations

Bogolyubov transformation are a useful set of transformations which help in relating the mode decomposition of the field in different Hilbert spaces. This is quite useful, since the idea of particle in curved space is not global, but rather observer-dependent. This implies we need to specify the basis we are working in, to give meaning to what we mean by particle density and so on.

Consider, two sets of solutions, u_k, v_k of the mode equation 1.4.9. Then, because we can always express a solution in terms of the linear independent basis, thus,

$$v_k^* = \alpha_k u_k^* + \beta_k u_k,\ \alpha_k, \beta_k \in \mathbb{C}. \tag{1.4.14}$$

Using the normalization definition, we get $\alpha_k^2 - \beta_k^2 = 1$ and for the stability of the transformations, one can show that $\beta_k k^3 \xrightarrow{k\to\infty} 0$.

By expanding χ in terms of mode functions u_k, schematically as $\chi \sim u^* b^- + u b^+$and then equating it to the one in terms of v_k, we can derive relations between the creation annihilation operators as,

$$\hat{b}_k^- = \alpha_k \hat{a}_k^- + \beta_k^* \hat{a}_k^+, \; \hat{b}_k^+ = \alpha_k^* \hat{a}_k^+ + \beta_k \hat{a}_k^-. \tag{1.4.15}$$

This means we have two sets of vacuum states as well as Hilbert spaces which can be created by applying the creation annihilation operators. The Bogolyubov coefficients α_k, β_k are generally calculated at some value of time, say η_0 by equating the different mode functions. It is given as

$$\alpha_k = \frac{u_k' v_k^* - u_k v_k^{*'}}{2i} \mid_{\eta_0} ; \beta_k^* = \frac{u_k' v_k - u_k v_k^{'}}{2i} \mid_{\eta_0} . \tag{1.4.16}$$

As an example, the work to be discussed in chapter five, we have the transition from inflation to radiation dominated cosmology, which means that the mode equations will be different on the both sides of the transition. Thus, if we choose the mode functions to be continuous at the boundary, then it is useful to use the Bogolyubov transformations to relate the late time Hilbert spaces in terms of the initial *in* state (which is in the Bunch-Davies vacuum).

An important quantity which is calculated using this transformation is the number density. E.g., consider particles in b-state, $N_k^{(b)} = \hat{b}_k^+ \hat{b}_k^-$, in terms of the a-state eigensystem, i.e.,

$$\langle {}_a 0 \mid N_k^{(b)} \mid_a 0 \rangle = \langle {}_a 0 \mid \hat{b}_k^+ \hat{b}_k^- \mid_a 0 \rangle = \beta_k^2 \delta^3(0), \tag{1.4.17}$$

with the $\delta^3(0)$ factor coming from taking infinite volume limit. Hence the number density is given by, $n_k = \beta_k^2$, giving the mean density of b-particles with momentum k in χ field.

The idea of vacuum and particles is not global and unambiguous in curved spaces, but is rather an approximate concept. It depends on the observer, as can be seen in the above result, where the vacuum in state a had number density of b-particles. What is unambiguous are the ones which can be defined in terms of field operators, like the expectation value in some state [309]. Still, one can do analysis by defining instantaneous vacuum via minimizing the energy, or by defining the vacuum over short distances. Sometimes, it is also possible to do a WKB like analysis, in terms of small quantities, e.g., $\omega'/\omega^2 \ll 1$ in radiation dominated era.

1.5 A short introduction to thermal field theory

Our study of the Standard Model was based on the zero temperature QFT, since most of the particle interactions we study today, and test in the particle colliders occur at zero temperature, which means that the thermal effects will be highly suppressed. But this is not true in the early universe, where the thermal effects are quite important, and one needs to use Finite Temperature Field Theory in order to compute observables, e.g., Higgs/scalar vev in the presence of a thermal bath, understanding phase transitions, neutron star formation etc. Another scenario at today's temperatures, involving the theoretical framework of thermal field theory is for the heavy ion collision experiments, where quark-gluon plasma is formed and thermal effects start to play an important role [352, 287, 148, 302].

1.5.1 Preliminaries

We will first review some formulae from statistical mechanics, and then introduce the imaginary time formalism. There are two important thermal ensemble which are central to any discussion involving thermal effects : the canonical ensemble, which describes a system in contact with its surrounding at a fixed temperature, where there is non-zero energy flow but the particle number and volume remains fixed and the grand canonical ensemble corresponds to the situation where both energy and particles can interchange between system and surroundings, keeping the chemical potential and volume fixed. The partition function, which is a fundamental quantity in statistical mechanics, is defined in terms of the density operator ρ,

$$Z = \mathrm{Tr}\,\rho; \quad \rho = \exp(-\beta H), \tag{1.5.1}$$

where, $\beta = 1/T$, T being the temperature of the system and H is the hamiltonian of the system. The other thermodynamical quantities can be related to the partition function, e.g., the number density given as,

$$N = T\frac{\partial \ln Z}{\partial \mu}. \tag{1.5.2}$$

The thermal average of any operator can also expressed in terms of the partition function as

$$\langle \hat{O} \rangle = \frac{\Sigma_m \langle m|\hat{O}|m\rangle e^{-\beta H}}{Z} = \frac{\mathrm{Tr}\left(e^{-\beta H}\hat{O}\right)}{Z} = \frac{\mathrm{Tr}\left(\rho\,\hat{O}\right)}{\mathrm{Tr}\,\rho}. \tag{1.5.3}$$

An important corollary which can be derived from the above definition is the famous "Kubo-Martin-Scwinger relation" (KMS relation). In principle, it relates the shift in the imaginary time by β in the two point correlation functions as [352],

$$\langle \phi(\vec{x},\tau)\phi(\vec{y},0)\rangle = \langle \phi(\vec{y},\beta)\phi(\vec{x},\tau)\rangle. \tag{1.5.4}$$

This yields a periodic relation in terms of the imaginary time with β as the period

$$\phi(\vec{x},0) = \pm\phi(\vec{x},\beta). \tag{1.5.5}$$

where the $+$ corresponds to bosons and $-$corresponds to the fermions. Thus, the Fourier transform will consist of a series of discretised frequencies, called as "Matsubara frequencies",

$$\phi(\vec{x},t) = \sum_l \phi(\vec{x},\omega_l)e^{i\omega_l\tau}, \tag{1.5.6}$$

where the frequencies are given as

$$\omega_l = \begin{cases} \frac{2\pi l}{\beta} & \text{bosons} \\ \frac{2\pi(l+1)}{\beta} & \text{fermions} \end{cases} \tag{1.5.7}$$

and $l \in \mathbb{Z}$. It is often useful to employ the path integral formalism, in which the partition function can be written as,

$$Z = \int D\phi \langle \phi|e^{-\beta H}|\phi\rangle = \int D\phi \exp\left[-\int_0^\beta d\tau \mathcal{L}(\tau)\right]. \tag{1.5.8}$$

1.5.2 Effective potential

One-loop thermal effects can be analysed by employing the framework of effective potential. We can either use the imaginary time formalism introduced in the previous subsection or we can follow a simpler approach discussed at length in Ref.[287], which will be summarized below.

Let's consider a real scalar field Φ, with self interactions and a mass term,

$$\mathcal{L} = \frac{1}{2}\partial_\mu \Phi \partial^\mu \Phi - V(\Phi). \tag{1.5.9}$$

The equation of motion will be,

$$D^\mu D_\mu \Phi + \frac{\partial V(\Phi)}{\partial \Phi} = 0. \tag{1.5.10}$$

We can decompose the field in terms of it's homogeneous and non-homogeneous component, as

$$\Phi(t, \vec{x}) = \bar{\Phi}(t) + \phi(t, \vec{x}); \qquad \langle \phi(t, \vec{x}) \rangle_{spatial} = 0 \tag{1.5.11}$$

We can plug this back into the equation, take a spatial average and expand the potential, to get the resultant equation for $\bar{\Phi}$, which corresponds to the "one-loop approximation",

$$D^\mu D_\mu \bar{\Phi} + V'(\bar{\Phi}) + \frac{1}{2} V'''(\bar{\Phi}) \langle \phi^2 \rangle = 0. \tag{1.5.12}$$

Now, we will show that $V'(\bar{\Phi}) + \frac{1}{2} V'''(\bar{\Phi}) \langle \phi^2 \rangle \equiv V'_{eff}(\bar{\Phi}, T)$. To begin with, we need the value of $\langle \phi^2 \rangle$. At the lowest order, we have

$$D^\mu D_\mu \phi + V''(\bar{\Phi}) \phi = 0. \tag{1.5.13}$$

The solution is

$$\phi(\vec{x}, t) = \int \frac{d^3k}{(2\pi)^{3/2}} \frac{1}{\sqrt{2\omega_k}} (e^{-i\omega_k t + i\vec{k}.\vec{x}} a^-_{\vec{k}} + c.c), \tag{1.5.14}$$

where we defined

$$\omega_k = \sqrt{k^2 + m_\phi^2}, \quad m_\phi^2 = V''(\bar{\phi}). \tag{1.5.15}$$

Once we quantise this theory, the integration constants $a_{\vec{k}}^{\pm}$ will become creation annihilation operators satisfying the equal time commutation relations:

$$[\hat{a}_k^-, \hat{a}_q^+] = \delta^3(\vec{k} - \vec{q}), \ [\hat{a}_k^-, \hat{a}_q^-] = [\hat{a}_k^+, \hat{a}_q^+] = 0. \tag{1.5.16}$$

The total number of particles can be calculated from the number operator, $\hat{N}_{\vec{k}} = \hat{a}_k^+ \hat{a}_k^-$ acting on the state vector $|n_{\vec{k}}\rangle = \frac{(a_{\vec{k}}^+)^n}{\sqrt{n!}}|0\rangle$, as $\hat{N}_{\vec{k}}|n_{\vec{k}}\rangle = \delta(0) n_{\vec{k}}|n_{\vec{k}}\rangle$ where $\delta(0)$ is the infinite volume. Here, the $n_{\vec{k}}$ is the occupation number , and is equal to the number of particles per unit volume. Using eq. 1.5.14, we can calculate

$$\langle \phi^2(\vec{x}) \rangle = \frac{1}{2\pi^2} \int dk \frac{k^2}{\sqrt{k^2 + m_\phi^2(\bar{\Phi})}} (\frac{1}{2} + n_k) \tag{1.5.17}$$

This implies that in our eq.1.5.12, we will have

$$\frac{1}{2} V'''(\bar{\Phi}) \langle \phi^2(\vec{x}) \rangle = \frac{V'''(\bar{\Phi})}{4\pi^2} \int dk \frac{k^2}{\sqrt{k^2 + m_\phi^2(\bar{\Phi})}} (\frac{1}{2} + n_k). \tag{1.5.18}$$

The first term, comes purely from the vacuum fluctuations (can be seen by setting $n_k = 0$). It is clearly divergent as $k \to \infty$, and hence one can use cut-off regularization scheme. Thus, for the first term, we have

$$\frac{1}{2} V'''(\bar{\Phi}) \langle \phi^2 \rangle_{vac} = \frac{1}{8\pi^2} \frac{\partial m_\phi^2(\bar{\Phi})}{\partial \bar{\Phi}} \int_0^\Lambda dk \frac{k^2}{\sqrt{k^2 + m_\phi^2(\bar{\Phi})}} \equiv \frac{\partial V_{CW}}{\partial \bar{\Phi}}, \tag{1.5.19}$$

where the Coleman-Weinberg term [135] is simply the energy density of the vacuum fluctuations, and is given as,

$$V_{CW} = \frac{1}{4\pi^2} \int_0^\Lambda k^2 dk \sqrt{k^2 + m_\phi^2(\bar{\Phi})} = \frac{\mathcal{I}(m_\phi(\bar{\Phi}))}{4\pi^2}, \tag{1.5.20}$$

where we have expressed it in terms of a standard integral,

$$I(m) = \frac{\Lambda^4}{8} \left[(2 + \frac{m^2}{\Lambda^2}) \sqrt{1 + \frac{m^2}{\Lambda^2}} + (\frac{m}{\Lambda})^4 \ln \left(\frac{m/\Lambda}{1 + \sqrt{1 + m^2/\Lambda^2}} \right) \right]. \tag{1.5.21}$$

In the limit of $\Lambda \to \infty$, we get the standard Coleman-Weinberg term,

$$V_{CW} = V_{div} + \frac{m^4(\bar{\Phi})}{64\pi^2} \ln \frac{m_\phi^2(\bar{\Phi})}{\mu^2}, \tag{1.5.22}$$

with the divergent parts of the potential can be reabsorbed into the counter terms for the bare masses and couplings.

For the thermal contribution, we have

$$\begin{aligned}\langle\phi^2(\vec{x})\rangle_T &= \frac{1}{2\pi^2}\int dk \frac{k^2}{\sqrt{k^2+m_\phi^2(\bar{\Phi})}} n_k \\ &= \frac{1}{2\pi^2}\int_0^\infty dk \frac{k^2}{\omega_k(e^{\frac{\omega_k}{T}}-1)} = \frac{T^2}{4\pi^2} J_-^{(1)}(\frac{m_\phi(\bar{\Phi})}{T}),\end{aligned}$$

where $n_k = \frac{1}{(e^{\frac{\omega_k}{T}}-1)}$ for bosons and we have re-expressed the expression in terms of another integral,

$$J_-^{(1)}(\kappa) = \int_\kappa^\infty \frac{(x^2-\kappa^2)^{1/2}dx}{e^x-1}. \tag{1.5.23}$$

Plugging it back into our eq.1.5.12, we have,

$$\frac{1}{2}V'''(\bar{\Phi})\langle\phi^2(\vec{x})\rangle_T = \frac{\partial m_\phi^2}{\partial\bar{\Phi}}\frac{T^2}{8\pi^2}J_-^{(1)}(\frac{m_\phi(\bar{\Phi})}{T}) = \frac{\partial V_\phi^{th}}{\partial\bar{\Phi}}, \tag{1.5.24}$$

where the thermal potential is given by

$$V_\phi^{th} \equiv \frac{T^4}{2\pi^2}J_B[\frac{m_\phi^2(\bar{\Phi})}{T^2}], \tag{1.5.25}$$

where,

$$J_B(y^2) = \int_0^\infty dx\, x^2 \log[1-\exp\Big(-\sqrt{x^2+y^2}\Big)]. \tag{1.5.26}$$

We can now collect our results, to get the overall 1-loop thermal and quantum correction to the potential, given by,

$$V_{eff} = V + \frac{m_\phi^4(\bar{\Phi})}{64\pi^2}\ln\frac{m_\phi^2(\bar{\Phi})}{\mu^2} + \frac{T^4}{2\pi^2}J_B[\frac{m_\phi^2(\bar{\Phi})}{T^2}]. \tag{1.5.27}$$

Although we restricted our derivation to the case of a scalar field, one can generalise it and do a similar calculation for vectors and fermions. We will quote the results for the effective potential, with

$$V_{th}(m_i,T) = (-1)^\eta g_i \frac{T^4}{2\pi^2}J_{B/F}[\frac{m_i^2}{T^2}], \tag{1.5.28}$$

where g_i is the number of degree of freedom of the field, B/F corresponds to bosons or fermions, and the $\eta = \pm$, with $+$ for bosons and $-$ for fermions. The thermal function for fermionic field is given as

$$J_F(y^2) = \int_0^\infty dx\, x^2 \log[1 + \exp\Big(-\sqrt{x^2 + y^2}\Big)]. \tag{1.5.29}$$

The thermal functions become less and less important as the argument increases (or the temperature decreases), going to zero as $T = 0$. We can expand in terms of Bessel functions of the second kind, truncating the series at only two or three terms giving a very good agreement with the exact function.

$$J_B^{low-T}(y^2) = -\sum_{n=1}^{l} \frac{1}{n^2} y^2 K_2(yn),\ |y^2| \gg 1 \tag{1.5.30}$$

$$J_F^{low-T}(y^2) = -\sum_{n=1}^{l} \frac{(-1)^n}{n^2} y^2 K_2(yn),\ |y^2| \gg 1. \tag{1.5.31}$$

On the other hand, the thermal contributions will be very important in the high temperature limit, and we can write approximate expressions for the functions :

$$J_B^{high-T}(y^2) \approx -\frac{\pi^4}{45} + \frac{\pi^2}{12} y^2 - \frac{\pi}{6} y^3 - \frac{y^4}{32} \log\left(\frac{y^2}{c_b}\right) + ...,\ |y^2| \ll 1 \tag{1.5.32}$$

$$J_F^{high-T}(y^2) \approx \frac{7\pi^4}{360} - \frac{\pi^2}{24} y^2 - \frac{y^4}{32} \log\left(\frac{y^2}{c_f}\right) + ...,\ |y^2| \ll 1, \tag{1.5.33}$$

where, $c_b = \pi^2 e^{(3/2 - 2\gamma_E)}$ and $c_f = 16\, c_b$.

1.5.3 Thermal Resummation of the masses

We need to address one caveat in the discussion for the thermal contributions to our tree-level potential. As the temperature increases(e.g. in early universe), the thermal corrections become more and more important, ultimately overwhelming the tree-level potential itself. As an example, during Electroweak phase transition, the wine bottle potential looses its shape once the temperature dependent contribution changes the sign of the mass term, making the Higgs vev to be zero. Another way to say it is that the symmetry is restored at high temperatures. But in principle this should signal a breakdown in our fixed order perturbation theory, since the 1-loop effects are overpowering the zeroth order terms. This implies the existence of another scale in the problem, T in addition to the mass scale, m. Generally, for $T/m > 1$, one needs to resum the loop corrections, see, e.g., Ref. [148]. In this thesis, we will concisely portray the picture and give a generic formula, without bothering too much about technicalities, as they are beyond the scope of our work.

Consider a real massive scalar field with self interaction, with it's potential given as,

$$V_0 = -\frac{m^2\phi^2}{2} + \frac{1}{4}\lambda\phi^4 \tag{1.5.34}$$

The introduction of the self interaction leads to possibility of loop corrections to the mass term. There are essentially four different kind of loop diagrams, which gives correction, and a systematic resummation leads to a controlled inclusion of the loops. In Figure 2, we have showcased the two dominant set of diagrams, namely:

- 1-loop mass correction : This is the standard diagram which is quadratically dependent on Temperature, yielding correction to the mass term and scaling as λT^2.
- Daisy diagrams: These become more and more relevant at high temperatures, with

$$\delta m^2_{n-loop\,daisy} \sim m^2\lambda^n(\frac{T}{m})^{2n-1}, n \geq 2. \tag{1.5.35}$$

Thus, in order to make the expansion reliable, we need to resum the thermal mass by including a temperature dependent term in the tree level mass, schematically given as

$$m^2(\phi, T) = m_0^2(\phi) + \Pi(\phi, T),\ \Pi(\phi, T) \sim \frac{\partial V_{th}}{\partial\phi} \sim \lambda T^2 + ... \tag{1.5.36}$$

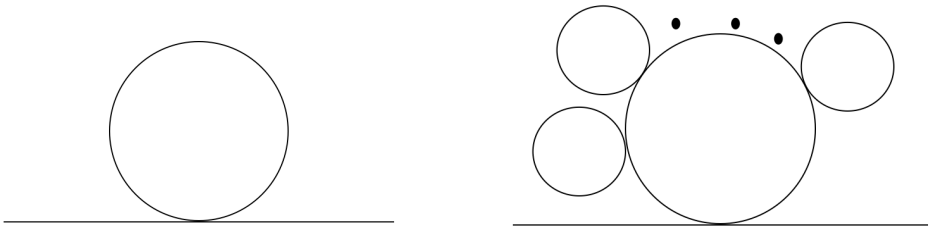

Figure 2: Relevant thermal loops, with the left diagram corresponds to the quadratic correction to the mass term, and the right sided figure corresponds to the daisy diagrams, with number of bubbles corresponding to the order of the diagram. [148]

The way to implement it is via the resummed masses in the one-loop effective potentials, which is also called "dressed" effective potential,

$$V_{eff} = V_0(m^2(\phi)) + V_{CW}(m^2(\phi, T)) + V_{th}(m^2(\phi, T)) \tag{1.5.37}$$

This method, also known as Parwani scheme [298] in the literature, directly takes into account the daisy contributions to all orders, giving rise to a reliable pertubative expansion, as long as [8]

$$\lambda \ll 1, \quad \frac{\lambda T}{m} \ll 1. \tag{1.5.38}$$

This has been a brief introduction of the topics which will be the launching pad for the forthcoming chapters. This doctoral thesis is a two-pronged effort that seeks a deeper understanding of nature and aims at trying to resolve some of the important open questions plaguing the Standard Model, specifically focusing on Dark Matter Physics. One path follows a phenomenological enquiry including the proposal of new signatures and experimental strategies, the interpretation of data from frontier experiments, and the construction of new models and mechanisms (Chapter 2-4). The other explores fundamental conceptual and

[8]The fermionic masses do not require any thermal resummation, owing to a lack of IR divergences in the fermionic propagator [173].

technical aspects of quantum cosmology with applications to dark matter physics, infrared divergences and dressed states, entanglement entropy and interactions in curved space-time background (Chapter 5-7).

2.0 Dark Scalars and Heavy Neutral Leptons at DarkQuest

2.1 Introduction

The hypothesis of a light, weakly coupled 'dark' or 'hidden' sector has received considerable attention in recent years. Though neutral under the Standard Model (SM) gauge group, dark sectors may exhibit rich dynamics, such as new forms of matter, new dark symmetries and forces, confinement, or spontaneous symmetry breaking, that could address some of the deficiencies of the SM. For example, the dark matter may be part of such a sector, communicating with the visible sector through a weakly coupled mediator, or the neutrino mass generation could be connected to new gauge singlet fermions within a dark sector.

A vibrant experimental program to search for light weakly coupled particles has emerged over the last decade and promises to be a fertile area of research for many years to come; for a recent summary of existing and planned efforts, see the community studies [29, 71, 72, 28]. Among the critical components of this program, particularly in exploring GeV scale dark states, are proton beam fixed target experiments [207, 68, 174]. In these experiments, an intense proton beam impinges on a target, producing a torrent of SM particles alongside a smaller flux of relativistic dark sector particles. Due to their suppressed coupling to the SM, once produced these dark particles can travel macroscopic distances before decaying downstream into visible particles. Given a suitable detector apparatus, the visible decay products can then be identified, characterized, and discriminated from potential background sources, which provides a promising means to probe and discover new light weakly coupled states.

One particularly promising experiment is DarkQuest, a mild augmentation of the SeaQuest and SpinQuest experiments [22]. The proposed DarkQuest upgrade entails the addition of an electromagnetic calorimeter (ECAL) to the existing SeaQuest muon spectrometer, which will extend the physics capabilities of the experiment. These new capabilities will allow for DarkQuest to produce a suite of sensitive searches for dark particles decaying to a wide variety of SM final states such as electrons, muons, charged hadrons, and pho-

tons [193, 79, 80, 125, 159, 338, 152]. The experiment's high luminosity coupled with its short baseline would allow for sensitivity to both fairly short-lived particles ($c\tau \lesssim 1\,\mathrm{m}$) and more weakly-coupled particles with fairly low production rates. Although a variety of other experimental proposals targeting dark sectors exist, DarkQuest is exceptional because most of the detector and infrastructure currently exists, is one of the few beam dump experiments with access to a high energy proton beam, would have an impressive range of sensitivity, and could provide novel results in comparatively short timescale.

In this chapter, we will study the potential sensitivity of DarkQuest to two highly motivated dark sector particles – dark scalars and heavy neutral leptons (HNLs). Dark scalars that mix through the Higgs portal provide one of the simplest extensions the SM and may be connected to a variety of puzzles such as dark matter [254], inflation [86], and naturalness [211]. Heavy neutral leptons (also called right-handed neutrinos or sterile neutrinos) are strongly motivated by the observation of neutrino masses [280, 350, 198, 200, 284, 314] and GeV-scale HNLs may also play a role in the generation of the matter-antimatter asymmetry [24, 51]. As we will demonstrate, DarkQuest has excellent prospects to explore substantial new regions of parameter space in these scenarios. Along with previous studies targeting a variety of dark sector models [193, 79, 80, 125, 159, 338, 152], our results lend further strong motivation for the DarkQuest ECAL upgrade, which will provide the basis for a rich and exciting experimental search program in the coming 5-10 years.

2.2 The DarkQuest Experiment

The E906/E1039 SeaQuest/SpinQuest experiment is a proton fixed target beam dump spectrometer experiment on the neutrino-muon beam line of the Fermilab Accelerator Complex [22]. A schematic layout of the experiment is shown in Figure 3. A high-intensity beam of 120 GeV protons (center of mass energy $\sqrt{s} \simeq 15$ GeV) is delivered to a thin nuclear target. The target is situated ~ 1 m upstream of a 5 m long, closed-aperture, solid iron dipole focusing magnet ("FMAG"), which magnetically deflects soft SM radiation and also functions as a beam dump for the large majority of protons that do not interact in the target.

This effectively allows only high energy muons, neutral kaons, and neutrinos to traverse the FMAG. The spectrometer consists of a high precision tracking system (St-1/2/3 tracking) and a muon identification system (absorber and St-4 muon ID). An additional 3 m long open-aperture magnet ("KMAG") is positioned at $z = (9 - 12)$ m and delivers a transverse momentum impulse of $\Delta p_T^{\rm KMAG} \sim 0.4$ GeV, enabling accurate momentum reconstruction of charged particles. In addition, in 2017 displaced vertex trigger hodoscopes were installed on both sides of the KMAG (see Figure 3), allowing for the detection of muons originating from the decays of exotic light long-lived particles after the dump. The experiment has been approved to collect $\sim 10^{18}$ protons on target in the coming two years, until 2023.

On the horizon, there are plans to install a refurbished electromagnetic calorimeter (ECAL) from the PHENIX experiment [40] between St-3 and the absorber wall (see brown region in Figure 3). This will allow the upgraded experiment, DarkQuest, to search for a much broader set of dark sector displaced signatures, including electrons, charged pions and kaons, and photons. The DarkQuest experiment has a relatively compact geometry, making it well-suited to search for dark particles with $\mathcal{O}(10\,\text{cm} - 1\,\text{m})$ lifetimes that are currently hidden to previous beam dump experiments with a much longer baseline.

Additional possible upgrades of the experiment ("LongQuest") have been also proposed [338]. This includes additional trackers and calorimeters after station 4 of the SeaQuest spectrometer.

The ultimate detectability of long lived dark particles at DarkQuest depends on several key factors. These include the production rate and kinematical properties of dark particles, their decay properties including branching ratios to final states containing charged particles and lifetime, the detector acceptance, and any potential SM background processes. In the remainder of this section we provide a brief discussion of these issues, which will motivate us to define two distinct run scenarios to be used later in our sensitivity projections for HNLs and dark scalars.

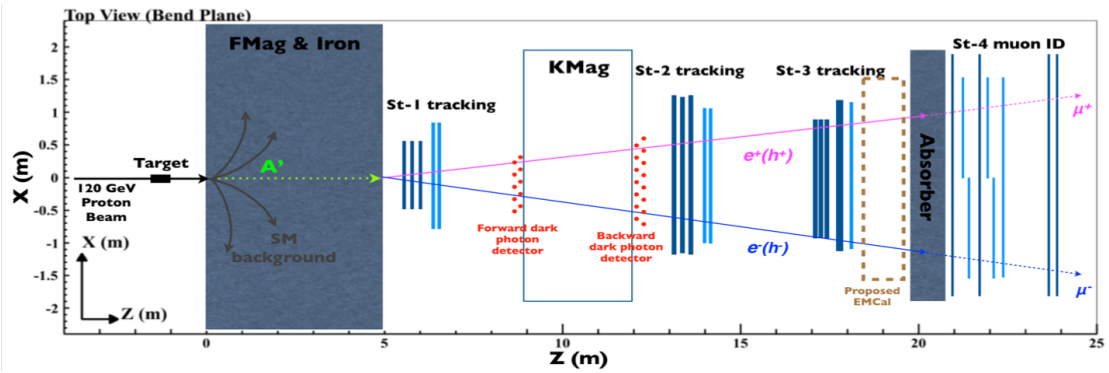

Figure 3: Layout of the DarkQuest experiment. The SeaQuest experiment has the same layout, except for the ECAL (dashed brown region located near $z \sim 19$ m), figure taken from [62].

2.2.1 DarkQuest luminosity scenarios, Phase I and Phase II

At DarkQuest both HNLs and dark scalars can be produced in meson decays (e.g., K, D, and B mesons), while scalars can also be produced in the primary proton interactions through the proton bremsstrahlung and gluon fusion processes. Assuming every proton interacts in the dump, an estimate of the effective integrated luminosity at DarkQuest is given by[1]

$$\mathcal{L} \simeq \frac{N_p}{\sigma_{pN}} \simeq \frac{N_p A}{\sigma_{p\mathrm{Fe}}} \simeq N_p A\, \lambda_{\mathrm{int}}\, \frac{\rho\, N_A}{A} = 79\ \mathrm{ab}^{-1} \left(\frac{N_p}{10^{18}}\right), \tag{2.2.1}$$

where N_p is the total number of protons on target, $\lambda_{\mathrm{int}} = 16.77$ cm is the nuclear interaction length in iron, $\rho = 7.87$ g cm^{-3} is the density of iron, and N_A is the Avogadro's number. In the second equality, we assume the per nucleon cross-section is the total cross-section on iron times the mass number, $A = 56$. A related quantity often seen in the literature is the the total hadronic cross per nucleon, which in iron is given by $\sigma_{pN} \equiv (\lambda_{\mathrm{int}}\, \rho\, N_A)^{-1} \simeq 12.6$ mb.

We will consider two benchmark luminosity scenarios in our projections below: a "Phase

[1] An earlier study [80] used the effective luminosity for proton-proton collision within a single nuclear collision length of iron, $35\mathrm{ab}^{-1} \left(\frac{N_p}{1.44\times 10^{18}}\right)$.

I" corresponding to $N_p = 10^{18}$ ($\mathcal{L} \sim 79$ ab^{-1} of integrated luminosity) which can be achieved on the couple of years time scale, and a "Phase II" scenario corresponding to $N_p = 10^{20}$ ($\mathcal{L} \sim 7.9$ zb^{-1} of integrated luminosity) which could potentially be collected over a longer time frame [318].

2.2.2 Meson production at DarkQuest

Given the considerable energy of the Main Injector protons and the substantial anticipated luminosity, mesons such as kaons, D-mesons, and B-mesons, as well as τ-leptons, are abundantly produced at DarkQuest. Much of hidden sector particle production at DarkQuest thus occurs through the decays of these SM states. Here we discuss our approach to modeling meson production at DarkQuest.

Kaons have an enormous production rate in primary proton collisions at DarkQuest, with an order one number of kaons produced per proton on target. However, since kaons are long lived and typically produced with boosts of order 10, their lab frame decay length is generally much longer than the characteristic hadronic interaction length, causing a significant attenuation of the kaon flux as they traverse the dump. Taking this into account, the number of kaons that decay before the first interaction length can serve as a useful proxy for the opportunities to produce hidden sector particles,

$$N_{K_i \text{decay}} \approx N_p \, n_{K_i} \, \Gamma_{K_i} \langle \gamma_K^{-1} \rangle \, \lambda_K \, , \tag{2.2.2}$$

where $\lambda_K \approx 20$ cm is the kaon interaction length$n_{K_i} \sim 0.2$ is the number of kaons produced per proton on target at DarkQuest for each of K^+, K^-, K_L^0, and K_S^0, and $\langle \gamma_K^{-1} \rangle \sim 0.1$ is the mean inverse Lorentz boost. Both n_{K_i} and $\langle \gamma_K^{-1} \rangle$ were estimated using PYTHIA 8 [328]. The values for $N_{K^\pm}$, $N_{K_L^0}$, and $N_{K_S^0}$ that decay before the first interaction length are shown in Table 1. As expected, the number of K_S^0 is much larger than the number of K_L^0 and $K^\pm$ due to their much shorter lifetime.

For D-meson production, we follow an approach that is similar to the one used by the SHiP experiment at CERN [21]. We compute the $pp \to D^0, \bar{D}^0$ production cross section as a function of $\sqrt{s}$, using PYTHIA 8 [328] with CTEQ6 LO parton distribution functions

Table 1: Number of mesons and τs produced for $N_p = 10^{18}$.

	K mesons*		D mesons		B mesons		Leptons
$K^\pm$	$\sim 1.8 \times 10^{15}$	$D^\pm$	$\sim 6.8 \times 10^{14}$	$B^\pm$	$\sim 5.3 \times 10^{7}$	$\tau^\pm$	$\sim 4.7 \times 10^{10}$
K_L^0	$\sim 2.2 \times 10^{14}$	$D_s^\pm$	$\sim 2.0 \times 10^{13}$	$B_d, \bar{B}_d$	$\sim 5.3 \times 10^{7}$	$\tau_{D_s}^\pm$	$\sim 1.1 \times 10^{12}$
K_S^0	$\sim 1.2 \times 10^{17}$	$D^0, \bar{D}^0$	$\sim 1.3 \times 10^{14}$				

(PDFs) [301]. We rescale these cross sections to match the cross sections measured in the interval $\sqrt{s} = (20 - 40)$ GeV [157, 272]. Using this rescaling, we estimate $\sigma(D^0, \bar{D}^0) \sim 1\,\mu$b at $\sqrt{s} = 15$ GeV. Using the fragmentation fractions for charm production, we obtain a charm production cross section $\sigma_{cc} = \sigma(D^0, \bar{D}^0)/f(c \to D^0) \sim 1.6\,\mu$b. To estimate the fragmentation fractions, we generate hard $c\bar{c}$ processes in PYTHIA 8 [328] at the DarkQuest energy and extract the ratios. As a cross check, we have also used PYTHIA 8 to estimate the B and D fragmentation fractions at SHiP and LHC energies, finding relatively good agreement with the values quoted in Ref. [98]. The number of charm mesons produced for $N_p = 10^{18}$ is shown in Table 1 for $D^\pm$, D^0 and $\bar{D}^0$, and $D_s^\pm$.

We follow a similar procedure to compute the production rate of B-mesons. In Table 1, we report the number of mesons produced for $N_p = 10^{18}$. Due to $2m_B + 2m_p \sim \sqrt{s}$, there is substantial uncertainty on σ_{bb} at DarkQuest beam energies. In particular, Monte Carlo estimates with differing PDF choices can result in largely different values for the projected cross-section. This can be primarily understood from the high uncertainty at large momentum fraction. Unlike in the case of charm, we do not have empirical data to extrapolate from in a controlled manner. Through exploring a variety of PDF choices, we found roughly an order of magnitude discrepancy for the projected cross-sections $\sigma(pp \to b\bar{b}) \sim 0.5 - 5$ pb. Given this range, we choose $\sigma(pp \to b\bar{b}) = 1$ pb throughout this work.

In addition to meson decays, $\tau^\pm$ decays can produce dark sector particles. At DarkQuest, the primary way of producing a τ lepton is through the decay of a D_s meson with $\text{Br}(D_s \to \tau^\pm \nu_\tau) = (5.55 \pm 0.24)\%$ [332], which provides over an order of magnitude more τs than the

direct electroweak production (see Table 1, where the first entry represents the number of $\tau^{\pm}$ directly produced through electroweak processes).

We can compare the numbers in Table 1 to the numbers obtained for higher energy proton beams as, for example, the 400 GeV SPS proton beam. The number of kaons [206], D-mesons [98], and taus [118] produced per proton on target is suppressed only by roughly an order of magnitude at the Fermilab Main Injector. A much larger suppression applies to B-meson production [98], for which the Main Injector loses roughly three orders of magnitude. For this reason, we generally expect DarkQuest to achieve a similar reach for dark sector states produced from light meson or tau decays.

Importantly, with the exception of D-mesons, most of these estimates consider only the particles produced in the incident protons primary interaction. Secondary interactions of hard particles and beam remnants within the beam dump can also produce additional kaons and taus, which could potentially enhance the flux of dark particles. The differential rates for these secondaries should be carefully evaluated in order for DarkQuest to most precisely state their sensitivity to a variety of models. In this sense, our estimate of the reach should be considered conservative.

2.2.3 Detector acceptance of DarkQuest

Next, we turn to the issue of the detector acceptance. Our considerations and approach to modeling the effect of the KMAG magnetic field and acceptance closely follows Ref. [80].

A Monte Carlo simulation is used to compute the total detection efficiency. In particular, we will consider signal events to be those in which the dark particle decays to final states containing two quasi-stable charged particles (i.e., electrons, muons, charged pions, and charged kaons) within a fiducial decay region at position $z \in (z_{\rm min}, z_{\rm max})$, located downstream of the FMAG. The daughter charged particles are then required to intersect tracking station 3, assumed to be a 2 m $\times$ 2 m square centered about the beam line and located approximately 18.5 m downstream of the dump (see Figure 3). We also model the effect of the KMAG magnetic field on charged particles trajectories by an instantaneous transverse momentum impulse of $\Delta p_T = 0.4\,{\rm GeV} \times (\Delta z_K/3{\rm m})$ applied in the $\hat{x}$ direction halfway through the

particle's KMAG traverse, where Δz_K is the distance traveled by the daughter particles through the KMAG[2]. The total detection efficiency is then estimated according to [80]

$$\text{eff} = m\,\Gamma \int_{z_{\text{min}}}^{z_{\text{max}}} dz \sum_{\text{events}\,\in\,\text{geom.}} \frac{e^{-z\,(m/p_z)\,\Gamma}}{N_{\text{MC}}\,p_z}\ , \tag{2.2.3}$$

where m, Γ, and p_z are the mass, width, and $\hat{z}$-component of the momentum of the dark particle, respectively. The sum in (2.2.3) is carried out over those events falling within the geometric acceptance as described above, and N_{MC} represents the total number of simulated events.

We will define two fiducial decay regions for our study that will be associated with our near future and long term run scenarios. As we will discuss in Secs. 2.3.3, 2.4.3, the detection efficiency for the two fiducial decay regions is relatively sizable, ranging from $\sim$ few $\times 10^{-2}$ to ~ 1, depending on the particular production and decay mode of the dark particle.

For our Phase I scenario, we require that the dark particle decays within the 5 m $-$ 6 m region immediately downstream of the FMAG. The main advantages of this choice are that the charged daughter particles are tracked in Station I and their trajectories are bent by the KMAG magnetic field, making accurate momentum reconstruction feasible and greatly helping with particle identification, vertex reconstruction, and background rejection.

For our Phase II scenario we will consider the longer fiducial decay region of 7 m $-$ 12 m. Given the higher luminosity in our Phase II scenario, we expect more background events, e.g., from K_L^0 particles which pass through the FMAG and decay semileptonically. As discussed in Ref. [80], these backgrounds could be further mitigated with additional shielding in the 5 m $-$ 7 m region, partially explaining the motivation of the 7 m $-$ 12 m fiducial region. In addition, the 7 m $-$ 12 m fiducial region would increase the geometric acceptance. While this choice allows for an appreciable enhancement of the overall signal rate and for additional suppression of backgrounds, it is not without additional challenges. For example, momentum reconstruction will be more challenging since the daughter particles would not pass through the first tracking station.

Our benchmark scenarios discussed here should be considered as preliminary, and a dedicated study of the potential backgrounds and signal region optimization is warranted.

[2]Note that Ref. [80] applied the p_T kick at the end of the KMAG.

The DarkQuest collaboration is currently investigating the several sources of backgrounds, with a focus on the e^+e^- signature characteristic of dark photons. While awaiting a definitive study from the collaboration, a crude estimate suggests that it will be possible to observe signals over the K_L^0 decay backgrounds. For the signatures investigated in this paper, the dominant sources come from the production of K_L^0 with subsequent semi-leptonic $K_L^0 \to \pi^\pm e^\mp \nu$, $K_L^0 \to \pi^\pm \mu^\mp \nu$ or purely hadronic $K_L^0 \to \pi^+\pi^-\pi^0$, $K_L^0 \to \pi^+\pi^-$ decays. Roughly 10^{17} K_L^0 will be produced in the beam dump during Phase I. Taking the kaon interaction length in iron to be ~ 20 cm, we expect approximately $\sim 10^6$ kaons to escape FMAG, and $\mathcal{O}(10^4)$ of which will decay in 5 m - 6 m. Accounting for branching ratios and geometric acceptance, we find that, depending on the particular final state, $\mathcal{O}(100 - 1000)$ K_L^0 will decay in the fiducial region with decay products detected by DarkQuest. Despite the substantial increase in luminosity, the situation during Phase II can be much improved over Phase I provided additional shielding is in place between 5 m - 7 m. While approximately $\sim 10^{19}$ K_L^0 will be produced in Phase II, a similar estimate as given for Phase I suggests that depending on the specific final state, $\mathcal{O}(1 - 10)$ K_L^0 will traverse 7 m of iron, decay in the 7 m - 12 m fiducial region, and will lead to detectable decay products. Depending on the final state signature, additional handles can be utilized to further mitigate these backgrounds. In Secs. 2.3.4, 2.4.4, we will estimate how many of these K_L^0 will result in background events for the several signatures. When discussing the DarkQuest reach for dark scalars and HNLs, we will require 10 signal events, but the true requirement against background may be more or less depending on the expected background population specific to the mass and decay paths.

2.3 Heavy Neutral Leptons

Heavy neutral leptons (HNL), $\hat{N}_i$, can interact with the SM neutrinos through the neutrino portal operator

$$-\mathcal{L} \supset \lambda_N^{ij}\, \hat{L}_i\, H \hat{N}_j + \text{H.c.}\,, \tag{2.3.1}$$

where H is the SM Higgs doublet and $\hat{L}_i = (\nu_i, \ell_i)^T$ is the SM lepton doublet of flavor i. Because of these operators, after electroweak symmetry breaking, the HNLs will mix with

the SM neutrinos. We will refer to the unhatted fields ν_i and N_i as the corresponding mass eigenstates of the light SM neutrinos and HNLs, respectively, and the relation between the flavor and mass bases is described by a mixing matrix, U. The phenomenology of HNLs largely follows from their induced couplings to electroweak bosons, which in the limit of small mixing angles are given by

$$\mathcal{L} \supset \frac{g}{\sqrt{2}} U_{ij} W^-_\mu \, \ell_i^\dagger \, \overline{\sigma}^\mu N_j + \frac{g}{2c_W} U_{ij} \, Z_\mu \, \nu_i^\dagger \, \overline{\sigma}^\mu N_j + \text{H.c.} \tag{2.3.2}$$

Additionally, we will assume that N is a Majorana particle throughout this work. Majorana HNLs are particularly motivated as they arise in the Type-I seesaw mechanism for neutrino mass generation. While the Type-I seesaw naively leads to mixing angles of parametric size $\sim \sqrt{m_\nu/m_N}$, which is extremely small for GeV-scale HNLs, we note that there are schemes such as the inverse seesaw [282, 283, 81] and linear seesaw [277] where the mixing angles can be much larger. For the purposes of characterizing the DarkQuest sensitivity, we will take a phenomenological approach, as is commonly done in the literature, assuming the existence of a single HNL state, N, in the mass range of interest, which dominantly mixes with a particular neutrino flavor, i.e., dominant electron-, muon-, or tau- flavor mixing. In this case, the phenomenology is dictated by the HNL mass, m_N, and mixing angle, denoted by U_e, U_μ, or U_τ, respectively, for the three mixing scenarios. If these assumptions were relaxed, we expect the phenomenological implications relevant for DarkQuest are typically only slightly different than in a flavor-aligned case.

2.3.1 HNL production

As a consequence of the interactions in (2.3.2), HNLs can be copiously produced at DarkQuest through the decays of mesons and τ leptons. Meson and τ production at DarkQuest is discussed in Sec. 2.2.1 and summarized in Table 1. For example, HNLs can be produced in the two body decays of charged pseudoscalar mesons, $P \to \ell_i N$. In the regime $m_\ell \ll m_N \ll m_P$, the branching ratio is given by [97]

$$\text{Br}(P \to \ell_i N) \simeq \tau_P \frac{G_F^2}{8\pi} \, f_P^2 \, m_P \, m_N^2 \, |V_{\alpha\beta}|^2 \, |U_i|^2, \tag{2.3.3}$$

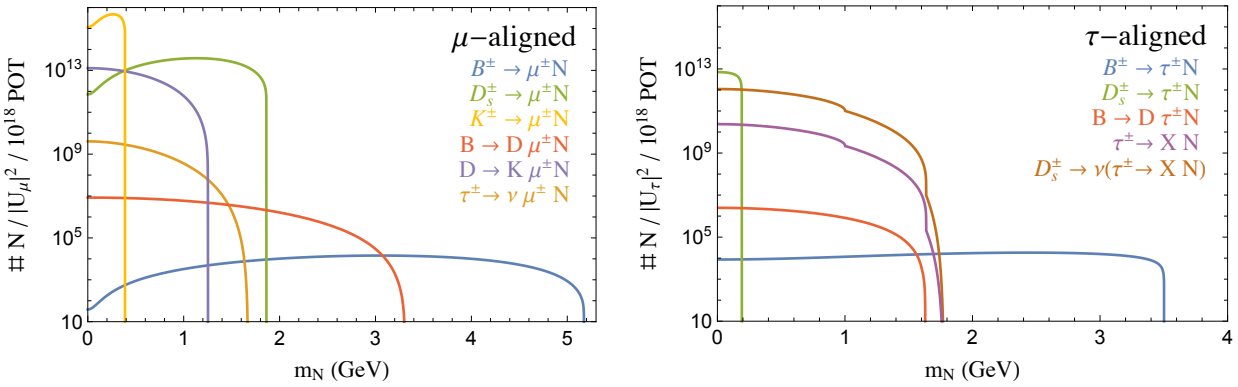

Figure 4: Number of μ-aligned (left) and τ-aligned (right) HNLs produced through meson and lepton decays, using 10^{18} protons on target and mixing angle equal to 1. The e-aligned scenario is nearly identical to μ-aligned one. For this reason, we do not show it here. The most important channels are $B^{\pm} \to \ell^{\pm} N$ (blue), $D_s^{\pm} \to \ell^{\pm} N$ (green), B mesons decaying to a charm meson and ℓN (red, denoted as $B \to D\ell^{\pm} N$), D mesons decaying to a strange meson and μN (purple, denoted as $D \to K\mu^{\pm} N$, left figure only), $\tau^{\pm} \to \nu\mu^{\pm} N$ (yellow, left figure only), $\tau^{\pm} \to XN$ (purple, right figure only), and $D_s^{\pm} \to \nu(\tau^{\pm} \to XN)$ (brown, right figure only). , figure taken from [62].

where τ_P, f_P, and m_P are the meson lifetime, decay constant, and mass, respectively, and the CKM matrix element, $V_{\alpha\beta}$, is dictated by the valence quark content of P (e.g., V_{cd} for $D^{\pm}$, etc.). The two body decay rates (2.3.3) scale as m_N^2 as a consequence of the chirality flip, and are thus enhanced for heavier HNLs.

Three body decays of mesons to HNLs are also important and can even be the dominant production mechanism depending on the HNL mass. Although phase space suppressed, the three body meson decay rates do not suffer from the CKM or chirality flip suppressions characteristic of the two body decays in (2.3.3). HNLs can furthermore be produced through τ decays (e.g., two body decays involving hadronic resonances, or three body leptonic decays) and are subject to similar considerations.

For all meson and τ branching ratios, we use the expressions in Ref. [97]. The total number of HNLs produced at DarkQuest through different pathways is summarized in Figure 4, where we utilized a luminosity of 10^{18} protons on target.

2.3.2 HNL decays

Once produced at DarkQuest, HNLs will decay through the weak interactions (2.3.2) to a variety of SM final states. Since their decays proceed through an off-shell heavy electroweak boson, GeV-scale HNLs are generically long lived and can easily traverse the beam dump at DarkQuest before decaying. There is a rich variety of HNL decay modes, including a pseudo-scalar meson and a lepton, a vector meson and a lepton, a lepton and two or more pions, or three leptons (including three neutrinos). We note that there is some disagreement in the literature about the corresponding rates. We have verified the results of Refs. [97, 55], and utilize these expressions for the neutrino decays.

In Figure 5 we show the branching ratios of HNLs in the $e-$aligned, $\mu-$aligned, and $\tau-$aligned case (left, center, and right panel, respectively). For HNL masses below 1.5 GeV, we determine the total hadronic rate as the sum of exclusive meson decay rates, while above 1.5 GeV, we switch to using the inclusive $N \to q\bar{q}'\ell$ rate, assuming exclusive rates are contained within this value. As we can observe from the figure, the branching ratio into the invisible $\nu\nu\nu$ final state (in blue in the figure) is quite subdominant as long as the HNL

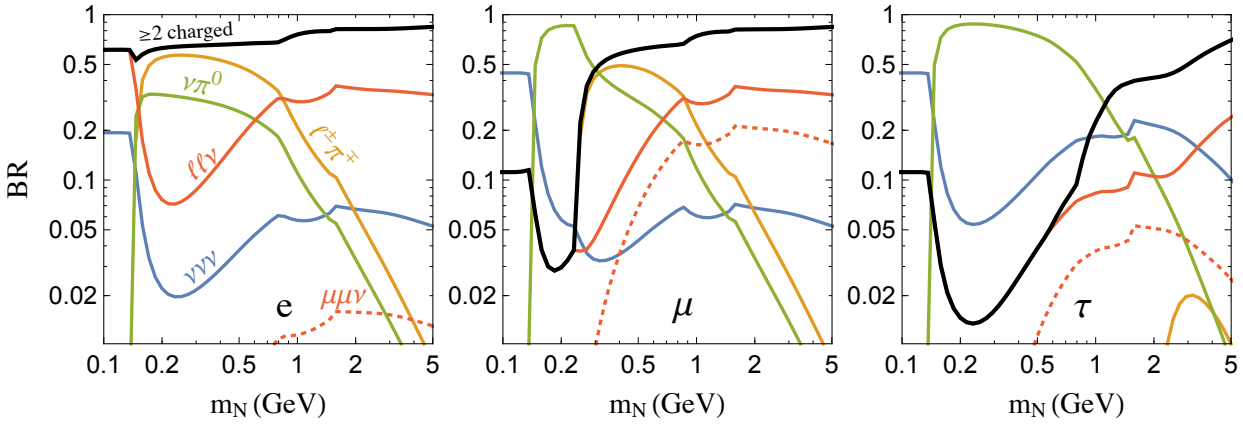

Figure 5: Branching ratios of the HNLs. The three panels represent HNLs mixed either with the electron (left panel), muon (middle panel), or tau (right panel) neutrinos. In each figure, we show the branching ratios into three SM neutrinos $\nu\nu\nu$ (blue), $e^{\pm}\pi^{\mp}$ or $\mu^{\pm}\pi^{\mp}$ (gold), $\nu\pi^0$ (green), one neutrino and two charged leptons of any flavors (red), and one neutrino and two muons (dotted red). The thick black curve represents the sum of the branching ratios into two or more charged tracks. Figure taken from [62]

has a mass above the pion mass. The other channels presented in the figure contain visible particles that are in principle observable by DarkQuest. The red dotted curve represents the decay into one neutrino and two muons. The corresponding branching ratio is also relatively suppressed, especially in the $e-$aligned, and $\tau-$aligned scenarios. This is the only channel that can be easily identified now by the SeaQuest experiment, without the ECAL upgrade.

Provided the ECAL upgrade is installed, DarkQuest will have the capability to also search for a variety of HNL decays containing multiple charged particles in addition to muons. Among all visible channels, the $\pi^0\nu$ channel is likely to be the most difficult one because of the challenging π^0 identification and large sources of backgrounds arising e.g., from the SM $K_L^0 \to 3\pi^0, K_S^0 \to \pi^0\pi^0$ processes, where some of the pions are missed or misidentified by the detector. For this reason, in the calculation of the DarkQuest reach on HNLs, we conservatively do not include this channel. The bold black line in Figure 5 shows the observable branching ratio used in this work, which is obtained by summing all branching ratios resulting in at least two charged particles.

In estimating the sensitivity below we will require 10 signal events, working under the assumption that backgrounds can be brought down to the level of a few events. The FMAG, i.e., the 5 m magnetized beam dump, serves to mitigate most of the backgrounds by sweeping away charged particles and largely blocking the most dangerous neutrals. Several potential sources remain and the ultimate size of these is the subject of current study. One of the most relevant backgrounds comes from K_L^0 particles that penetrate the dump and decay in the fiducial region. As we discussed in Sec. 2.2.3, we expect $\mathcal{O}(100-1000)$ of such K_L^0 in Phase I and $\mathcal{O}(1-10)$ in Phase II. The decay $K_L^0 \to \pi^\pm e^\mp \nu$ will be background to the $N \to e^+e^-\nu$ and $N \to e^\pm\pi^\mp$ signatures presented in Figure 5. For the former, a pion rejection factor of order $\sim 1\%$ will be sufficient to suppress the $K_L^0 \to \pi^\pm e^\mp \nu$ background to $\mathcal{O}(10)$ (< 1) events for Phase I (Phase II). This level of electron-pion discrimination should be feasible with the planned ECAL upgrade [40]. For the latter signal, the background could be suppressed through suitable kinematic cuts such as a cut on the $m_{e\pi}$ invariant mass. However, a detailed study of these possibilities requires a careful modeling of K_L^0 production in the FMAG, which is beyond our current scope. For signatures involving muons, the existing SeaQuest spectrometer already has the capability to distinguish muons, which pass through

the absorber and are detected in the Muon-ID system (see Figure 3), from charged hadrons, which do not penetrate the absorber. As above, muonic backgrounds to the $N \to \mu^{\pm}\pi^{\mp}$ signature can arise from decays such $K_L^0 \to \pi^{\pm}\mu^{\mp}\nu$, while the $N \to \mu^{+}\mu^{-}\nu$ channel should have very small backgrounds.

2.3.3 Detector acceptance

We follow the procedure outlined in Sec. 2.2.3 to compute the geometric acceptance for HNLs at DarkQuest. To reduce the complexity for a clear presentation, we show in Figure 6 the normalized geometric efficiency in the large lifetime limit. To compute these curves, we consider the μ-aligned scenario and the large lifetime regime, i.e., we assume that the HNL decay length is much larger than the detector size so that the differential probability to decay is a constant with distance, and normalize to only the particles that decay within the fiducial region. This limit is relevant for small mixing angles. The different colored curves in Figure 6 correspond to several representative production and decay modes of the HNL. The lighter (darker) curves represent the acceptance for Phase I (5 m - 6 m) (Phase II (7 m - 12 m)). Overall, the acceptance is relatively large, ranging from a few % to $\sim$ 20% depending on the HNL production/decay mode, and is fairly constant with the HNL mass. As expected, the acceptance for Phase I is somewhat smaller than that for Phase II, since for Phase II the HNLs decay typically closer to tracking station 3.

2.3.4 The DarkQuest reach for HNLs

With our estimates for HNL production, decays, and experimental acceptance in hand, we can compute the total number of signal events in the SM final state i expected at DarkQuest according to

$$N_{\text{signal}} = N_N \times \text{Br}_i \times \text{eff}_i \,. \tag{2.3.4}$$

Here N_N is the number of HNLs produced in a given production channel (see Section 2.3.1 and Figure 4), Br_i is the branching ratio for $N \to i$ (see Section 2.3.2, and Figure 5), and eff_i is the experimental efficiency to detect the final state i, computed using (2.2.3).

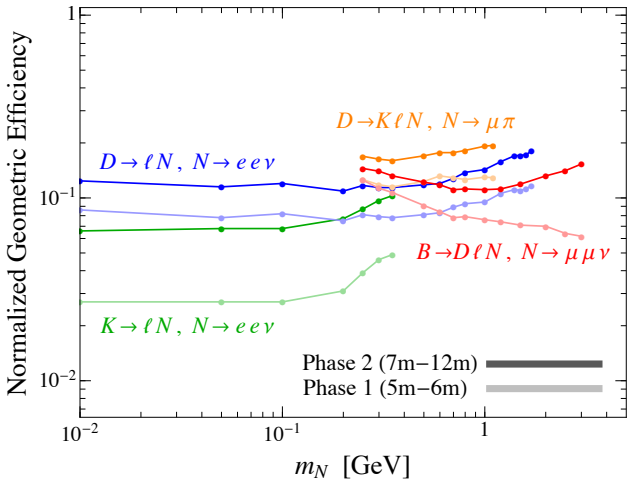

Figure 6: Geometric acceptance as a function of the HNL mass normalized to the number of HNLs decaying within the fiducial decay region in the large lifetime limit (i.e., the HNL decay length is much larger than the detector size). We show separately the efficiency for HNLs that are produced and decay through several representative channels, including $K \to \ell N, N \to ee\nu$ (green), $D \to \ell N,\ N \to ee\nu$ (blue), $D \to K\ell N, N \to \mu\pi$ (orange) and $B \to D\ell N, N \to \mu\mu\nu$ (red), and for two run scenarios: Phase II, 5m - 6m (lighter darker), Phase II, 7m - 12m, (darker color). Figure taken from [62]

A summary of the projected reach is shown in Figure 7 for μ- and τ-flavored HNLs decaying inclusively to final states containing two or more detected charged tracks. The solid black (dashed black) contour specifies the HNL mass - squared mixing angle parameters leading to 10 signal events according to (2.3.4) for the Phase I (Phase II) run scenario. We note that the projected reach for e-aligned HNLs is very similar to the μ-aligned reach shown in Figure 7. For this reason, we do not show the e-aligned scenario in the figure. We also show in the shaded gray regions the existing experimental or observational limits, including CHARM [78], PS191 [82], DELPHI [16], NuTeV [339], E949 [47], MicroBooNE [280], T2K [11], ATLAS [5], Belle [271], and Big Bang Nucleosynthesis (BBN) [107][3] (see e.g., Ref. [72] for a thorough discussion of these limits). For comparison, we also display the projected sensitivities to HNLs from several proposed experiments, including NA62++[164], FASER [246], CODEX-b [23], MATHUSLA [147] and SHiP [27]. For additional proposals to probe GeV-scale HNLs see e.g., Refs. [56, 55, 72, 84, 141, 140, 230].

We conclude that DarkQuest Phase I can probe a significant region of currently unexplored parameter space for τ-aligned HNLs. For the Phase II scenario, DarkQuest will be able to extend the sensitivity by more than one order of magnitude in the squared mixing angle compared to Phase I, while also covering new regions of parameter space in the μ-aligned scenario which are presently unconstrained.

2.4 Dark Scalars

We now consider dark scalars interacting through the Higgs portal. A new singlet scalar can couple to the SM Higgs through two renormalizable portal couplings,

$$-\mathcal{L} \supset (A\hat{S} + \lambda\hat{S}^2)\hat{H}^\dagger\hat{H}. \tag{2.4.1}$$

The dark scalar may acquire a small coupling to SM fermions and gauge bosons through its mass mixing with the Higgs, which will occur if the $A \neq 0$ in (2.4.1) or if the dark scalar obtains a non-zero vacuum expectation value. Then, in the physical basis, the phenomenology

[3] We cut off the BBN constraints above $|U| = 10^{-5}$ to match the information presented in Ref. [107], but naturally expect the limits to extend above this range.

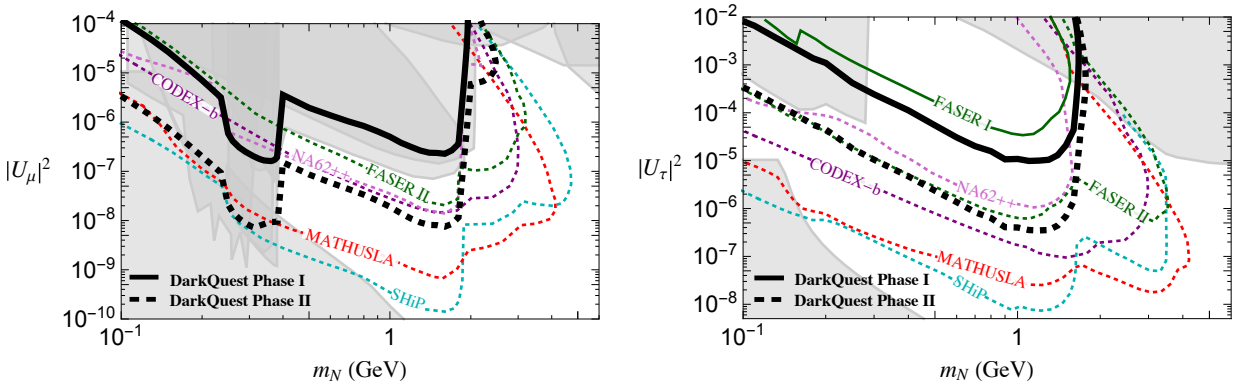

Figure 7: Projected reach for μ-flavored HNLs (left panel) and τ-flavored HNLs (right panel) in the m_N vs $|U_{\mu,\tau}|^2$ plane. DarkQuest Phase I is represented by the black solid line, and Phase II by the black dashed line. Current limits (gray) and limits from proposed future experiments (colored dashed) are also displayed for comparison; see the text for a details. Limits are set requiring 10 signal events. Figure taken from [62].

at DarkQuest is governed by the dark scalar mass, m_S, and the scalar-Higgs mixing angle, θ:

$$\mathcal{L} \supset -\frac{1}{2}\, m_S^2 S^2 + \theta\, S \left(\frac{2m_W^2}{v} W_\mu^+ W^{\mu-} + \frac{m_Z^2}{v} Z_\mu Z^\mu - \sum_f \frac{m_f}{v} \bar{f} f \right). \tag{2.4.2}$$

Given the experimental constraints on the mixing angle for dark scalars at the GeV-scale, we will always be working in the regime $\theta \ll 1$. We will not study the phenomenological consequences of additional couplings between the scalar and the Higgs, such as the cubic interaction hSS. While such a coupling can lead to additional scalar production processes such as $B \to KSS$, these are typically not as important at DarkQuest as processes involving singly produced scalars. Such coupling also leads to Higgs exotic decays of the type $h \to SS$ [146] that can be searched for at the LHC. We do not include the corresponding bounds in our summary plot in Figure 11, since these bounds depend on the hSS coupling that is independent from the mixing angle θ. We now discuss in more detail the production of scalars, their decays, the experimental acceptance, and the DarkQuest reach.

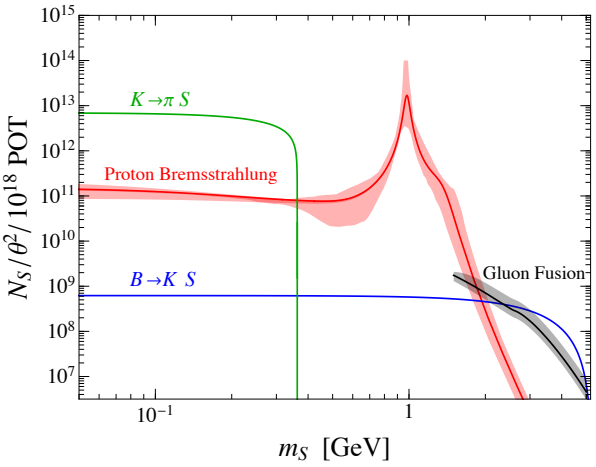

Figure 8: Number of scalars produced at DarkQuest for $K \to \pi S$ (green), $B \to KS$ (blue), proton bremsstrahlung (red), and gluon fusion (black), assuming 10^{18} protons on target and a mixing angle equal to 1. Figure taken from [62].

2.4.1 Scalar production at DarkQuest

At DarkQuest scalars are produced through three main processes: meson decays, proton bremsstrahlung, and gluon-gluon fusion. The sensitivity of DarkQuest to scalars produced through B meson decays was already studied in Ref. [80]. In this work we will also examine the potential additional sensitivity from scalars produced through kaon decays, proton bremsstrahlung, and gluon-gluon fusion.

Figure 8 shows the number of dark scalars produced through these three production channels as a function of the scalar mass, assuming 10^{18} protons on target. Low mass scalars are dominantly produced in kaon decays. Above the $m_K - m_\pi$ threshold and in the vicinity of $m_S \sim 1$ GeV, proton bremsstrahlung dominates, while heavier scalars can be produced through B-meson decays and gluon fusion.

2.4.1.1 Meson decays

We first consider scalar production through meson decays. We refer the reader to Sec. 2.2.1 and Table 1 for a summary of meson production at the DarkQuest. We first consider scalars produced through kaon decays, $K \to \pi S$, which is especially relevant for lighter scalars. The partial decay width for $K^\pm \to \pi^\pm S$ is [347, 266, 86, 240, 349]

$$\Gamma(K^\pm \to \pi^\pm S) \simeq \frac{\theta^2}{16\pi m_K}\left|\frac{3G_F\sqrt{2}V_{td}^* V_{ts} m_t^2 m_s}{16\pi^2 v}\right|^2 \left(\frac{1}{2}\frac{m_K^2 - m_\pi^2}{m_s - m_d} f_K\right)^2 \lambda^{1/2}\left(1, \frac{m_S^2}{m_K^2}, \frac{m_\pi^2}{m_K^2}\right), \tag{2.4.3}$$

with $\Gamma(K_L^0 \to \pi^0 S) \simeq \Gamma(K^\pm \to \pi^\pm S)$.[4] Using these partial widths and (2.2.2), the number of scalars produced from kaon decays in a thick target can be estimated as [349]

$$N_S = N_p\, n_K\, \Gamma(K \to \pi S)\, \lambda_K \langle \gamma_K^{-1} \rangle \sim 10^{13} \times \theta^2 \left(\frac{N_p}{10^{18}}\right) \qquad \text{(kaon decays)}, \tag{2.4.4}$$

where $n_K \sim 0.6$ is the number of $K^\pm$ and K_L^0 produced per proton on target.

Next, we consider scalars produced through B meson decays, which proceeds through $b - s - S$ penguin transitions. The inclusive branching ratio for $B \to X_s S$ can be written as [176, 203, 215] (see also [69, 349] for exclusive B decays)

$$\frac{\mathrm{Br}(B \to X_s\, S)}{\mathrm{Br}(B \to X_c\, e\, \nu)} \simeq \theta^2\, \frac{27\sqrt{2}\, G_F\, m_t^4}{64\pi^2\, \Phi\, m_b^2}\left|\frac{V_{ts}^* V_{tb}}{V_{cs}}\right|^2 \left(1 - \frac{m_S^2}{m_b^2}\right)^2, \tag{2.4.5}$$

where $\Phi \approx 0.5$ is a phase space factor. Using the measured inclusive rate for $B \to X_c\, e\, \nu$ [332], we obtain $\mathrm{Br}(B \to X_s\, S) \simeq 6.2 \times \theta^2 (1 - m_S^2/m_b^2)^2$. Since B-mesons decay promptly, we can estimate the number of scalars produced in their decays as

$$N_S = N_p\, n_B\, \mathrm{Br}(B \to X_s\, S) \sim 10^9 \times \theta^2 \left(\frac{N_p}{10^{18}}\right) \qquad (B \text{ meson decays}), \tag{2.4.6}$$

where $n_B \sim 10^{-10}$ is the number of B mesons produced per proton on target at DarkQuest.

[4] Although the branching fractions are different, the partial widths are very similar, and the total width cancels out of the estimate (2.2.2) as long as $\lambda_K \ll \langle \gamma_K^{-1} \rangle c\tau_i$. In fact, K_S^0 has $\lambda_K \sim \langle \gamma_K^{-1} \rangle c\tau_{K_S}$ suggesting its total width could also cancel out of the expression (up to an $\mathcal{O}(1)$ factor). However, K_S^0 is not included in our analysis since the partial width $\Gamma(K_S^0 \to \pi^0 S) \ll \Gamma(K_L^0 \to \pi^0 S)$, so it can be neglected for that reason.

2.4.1.2 Proton bremsstrahlung

Next, we turn to scalars produced through proton bremsstrahlung, $p + p \to S + X$. The cross section is obtained following the calculation in Ref. [94], which is based on the generalized Weizsacker-Williams method [244]. Specifically, scalar events are generated by sampling the differential cross section $d\sigma_{\rm brem}/dz\, dp_T^2$, where $z \equiv p_S/p_p$ is the fraction of the proton beam momentum, p_p, carried by the emitted scalar, with p_S the scalar momentum, and p_T is the scalar transverse momentum. The validity of the Weizsacker-Williams approach relies on the kinematic conditions $p_p,\ p_S,\ p_p - p_S \gg m_p,\ |p_T|$. To satisfy these conditions for DarkQuest that uses 120 GeV protons, we follow Ref. [80] and restrict the phase space to the range $z \in (0.1, 0.9)$ and $p_T < 1$ GeV. We note that these conditions are slightly more restrictive than those used in Ref. [94], leading to an integrated cross section that is smaller by an order one factor.

The total bremsstrahlung cross section is estimated to be

$$\sigma_{\rm brem} \sim \sigma_{pp} \times \left(\frac{g_{SNN}^2 \theta^2}{8\pi^2} |F_S(m_S^2)|^2 \right), \tag{2.4.7}$$

where $\sigma_{pp} \approx 40$ mb is the total inelastic proton-proton cross section and the factor in parentheses gives the approximate integrated probability of scalar emission. The parameter g_{SNN} is the zero momentum scalar nucleon coupling (for $\theta = 1$) and $F_S(p_S^2)$ is a time-like scalar-nucleon form factor. Including order one factors arising from phase space integration, we estimate the total number of scalars produced in proton bremsstrahlung to be

$$N_S \sim 10^{11}\, \theta^2 \left(\frac{N_p}{10^{18}} \right) \qquad \text{(Proton Bremsstrahlung)}. \tag{2.4.8}$$

Figure 8 shows the total number of scalars produced at DarkQuest as a function of the scalar mass. The large resonant enhancement near $m_S \sim 1$ GeV is a consequence of mixing with the narrow $f_0(980)$ scalar resonance, while the bremsstrahlung cross section drops steeply for $m_S \gtrsim 1$ GeV due to the form factor suppression. It is likely that the zoo of heavy f_0 resonances would belay this high mass suppression, but we make no attempt to model that here. The uncertainty band is obtained by varying the lower integration limit for z between 0.05 and 0.2 as well as the scalar resonance masses and widths in the form factor $F_S(p_S^2)$.

We note that the rates for scalar production from bremsstrahlung have a rather mild dependence on the proton beam energy, and thus the production rate at higher energy facilities such as the CERN SPS (400 GeV protons) is very similar to that at DarkQuest.

2.4.1.3 Gluon fusion

The final process we consider is scalar production via gluon fusion. As in the case of the SM Higgs boson, this process proceeds at one loop through the heavy quark triangle diagrams. We restrict our analysis to scalar masses above $\mathcal{O}(1\,\text{GeV})$ where the perturbative QCD computation is valid. In this mass range, the cross section is of order $\sigma_{ggS} \sim 30\,\text{pb} \times \theta^2\,(m_S/1\text{GeV})^{-2}$, and the number of scalars produced is therefore

$$N_S \sim 10^9 \times \theta^2 \left(\frac{1\,\text{GeV}}{m_S}\right)^2 \left(\frac{N_p}{10^{18}}\right) \qquad \text{(Gluon Fusion)}. \tag{2.4.9}$$

As in the case of the SM Higgs boson, we expect higher order corrections to enhance the rate by an order one factor, although we are not aware of an existing calculation in the literature that can be applied to such light scalars. While it would be interesting to study this question further, we will simply apply a K-factor equal to 1.5 in our estimate of the rate, which is similar to that of the SM Higgs boson. For our simulation, we use the HEFT model in MadGraph5_aMC@NLO [33] to generate scalar events, which are then passed to PYTHIA 8 [328] for showering. While we find that gluon fusion is generally subdominant to other production mechanisms (see the black curve in Figure 8), it can give some additional sensitivity in the 1-2 GeV scalar mass range, particularly for the Phase II scenario. For comparison, we find that the scalar production via gluon fusion is only about a factor of 2 larger at the higher energy CERN SPS.

2.4.2 Scalar decays

Through its mixing with the Higgs, the scalar will decay to SM final states. For example, the dark scalar can decay to charged leptons with a partial decay width, $\Gamma_{S\to\ell^+\ell^-} \simeq \theta^2 m_\ell^2 m_S/(8\pi v^2)$.

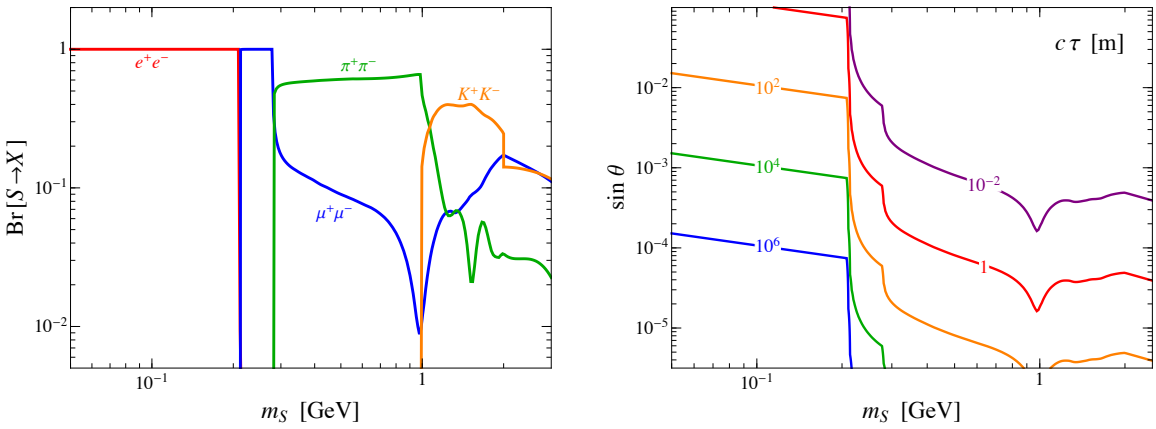

Figure 9: Left panel: Scalar branching ratios in the e^+e^- (red), $\mu^+\mu^-$ (blue), $\pi^+\pi^-$ (green), in the K^+K^- (orange) final state channels. Note that the branching ratios are independent of $\sin\theta$. Right panel: Isocontours of the scalar decay length in units of meter in the m_S - $\sin\theta$ plane. Figure taken from [62].

Above the two pion threshold the scalar can also decay to hadronic final states. The theoretical description of such decays is complicated by strong interaction effects, leading to significant uncertainties in the predictions for masses of order 1 GeV. In our study we will use the results and prescriptions from the recent study in Ref. [349]. In particular, for relatively low scalar masses in the few hundred MeV range, the hadronic decays are well described using Chiral Perturbation Theory [341, 163]. At higher masses, $m_S \gtrsim 2$ GeV, the perturbative spectator model can be used to compute the decay rates to quarks and gluons [217]. In the intermediate regime of $m_S \sim 1 - 2$ GeV an analysis based on dispersion relations can be employed to estimate the partial decay widths for scalar decays to pairs of pions and kaons [303, 337, 163, 285, 349]. Furthermore, Ref. [349] includes an additional contribution to the scalar decay width to account for other hadronic channels above the 4π threshold. Despite the formidable calculations involved in estimating the decays in these regimes, these are uncontrolled approximations and should be viewed with healthy skepticism [87]. The scalar branching ratios in the e^+e^-, $\mu^+\mu^-$, $\pi^+\pi^-$, and K^+K^- channels, as well as the scalar

decay length, are shown in Figure 9.

As with our HNL projections presented in Sec. 2.3.4, we will require 10 signal events in our dark scalar sensitivity estimates. The considerations leading to this assumption are similar to those outlined in Secs. 2.2.3 and 2.3.2. In particular, for the signatures arising from scalar decays to leptons, $S \to \ell^+\ell^-$, there can be backgrounds from K_L^0 that pass through the FMAG and decay via $K_L^0 \to \pi^\pm \ell^\pm \nu$, though we expect that detector level pion-lepton discrimination can be used to bring these backgrounds at the level of $\mathcal{O}(10)$ (< 1) events for Phase I (Phase II). For the hadronic scalar signatures such as $S \to \pi^+\pi^-, K^+K^-$, there are backgrounds from the decays $K_L^0 \to \pi^-\pi^+\pi^0$ and $K_L^0 \to \pi^+\pi^-$. The corresponding background rates, particularly for the two pion decay, are further suppressed by the small branching ratios ($\mathrm{BR}(K_L^0 \to \pi^+\pi^-) \sim 2 \times 10^{-3}$), and we expect that kinematic information will be helpful in distinguishing the signal, though this remains to be studied in detail.

2.4.3 Detector acceptance

We follow the procedure discussed in Sec. 2.2.3 to account for the geometric acceptance of the experiment, with the total detector efficiency computed according to Eq. (2.2.3).

In Figure 10 we display the geometric acceptance as a function of scalar mass in the infinite lifetime limit, normalized to the number of scalars decaying within the fiducial decay region. This limit is of practical importance for much of the small θ parameter space. Several notable features can be observed in Figure 10. First, the overall efficiency is higher for dark scalars produced in proton bremsstrahlung compared to those from B and kaon decays. This is due to the larger typical Lorentz boosts of scalars originating in the former process, which inherit an order one fraction of the beam energy. Second, an increase in the efficiency is typically observed as m_S increases beyond the dimuon threshold. Due to phase space suppression, heavier particles produced through scalar decays will typically be more collinear with the parent scalar, which leads to a higher overall acceptance. Furthermore, in the decays to electrons, the emitted particles are highly relativistic in the scalar rest frame and the fraction emitted towards the negative z direction can have a small lab frame longitudinal momentum. Such electrons can be swept out of the detector as they pass

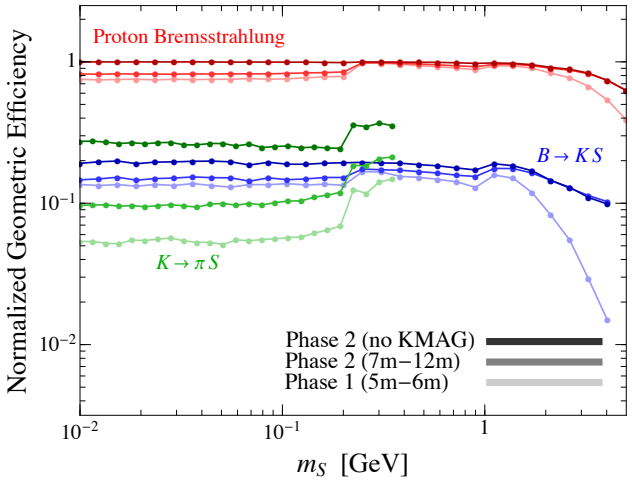

Figure 10: Geometric acceptance as a function of scalar mass normalized to the number of scalars decaying within the fiducial decay region in the infinite lifetime limit. We show separately the efficiency for scalars produced via proton bremsstrahlung (red), B decays (blue), and kaon decays (green), and for three run scenarios: Phase I, 5 m $-$ 6 m (light shading), Phase II, 7 m $-$ 12 m, (medium shading) and Phase II, 7 m $-$ 12 m, without the KMAG (dark shading). The acceptance combines the e^+e^-, $\mu^+\mu^-$, $\pi^+\pi^-$, and K^+K^- final states weighted by their relative decay rates. Figure taken from [62].

through the KMAG, explaining in the lower observed efficiency when the KMAG is present. Furthermore, we see that for heavy scalars produced via bremsstrahlung and B-meson decays, the efficiency tends to decrease as the the scalar mass increases beyond $\mathcal{O}(1\,\text{GeV})$ since in this regime the daughter particle p_T inherited from the scalar mother increases approximately in proportion to m_S and is generally larger than that imparted by the KMAG. Another trend observed in all production channels is the increased efficiency in Phase II (medium shading) over that in Phase I (lighter shading), which stems from the fact that for the Phase II scenario the scalars decay closer to tracking station 3.

Finally, we have displayed the efficiency for an alternate Phase II scenario in which the KMAG is removed and the charged daughters are not deflected. In this case, the daughter particles have a smaller characteristic transverse momentum, leading to a higher geometric acceptance as seen in Figure 10. However, it should also be emphasized that in this run scenario particle momenta measurement capability is likely to be significantly degraded. In fact, the magnetic field strength of the KMAG is tunable and could impart a smaller p_T kick than the 0.4 GeV used in this work. It would be interesting to study in detail its impact on the geometric acceptance and reconstruction capabilities.

2.4.4 DarkQuest sensitivity to dark scalars

Given the scalar production rates, decay branching ratios, lifetime, and experimental efficiency, we can now estimate the total number of signal events in the SM final state i according to the formula

$$N_{\text{signal}} = N_S \times \text{Br}_i \times \text{eff}_i \,, \tag{2.4.10}$$

where N_S is the number of scalars produced in a given production channel (see Eqs. (2.4.4, 2.4.6, 2.4.8, 2.4.9) for the number of scalars produced via K decay, B decay, bremsstrahlung, and gluon fusion, respectively). In Figure 11 we show the projected per-production-channel sensitivity of DarkQuest Phase I for scalars decaying inclusively to pairs of charged particles, specifically e^+e^-, $\mu^+\mu^-$, $\pi^+\pi^-$, and K^+K^-. Each contour indicates the scalar mass - mixing angle parameters predicting 10 signal events according to (2.4.10). We show three contours corresponding to distinct scalar production mechanisms, including kaon decays, B-meson

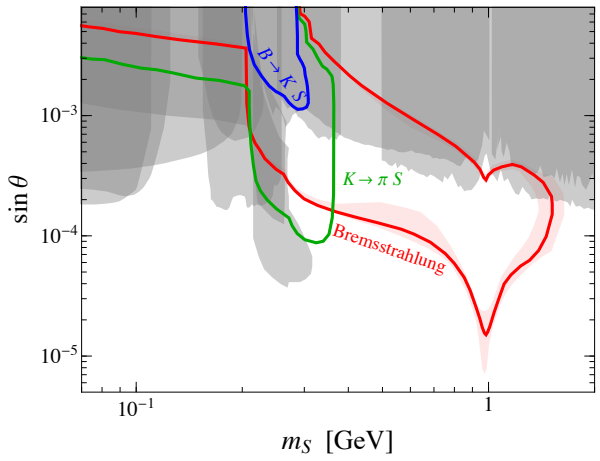

Figure 11: DarkQuest Phase I sensitivity to dark scalars corresponding to $N_p = 10^{18}$ and 5 m - 6 m decay region. The contours correspond to 10 signal events as obtained by adding the e^+e^-, $\mu^+\mu^-$, $\pi^+\pi^-$, K^+K^- channels, for dark scalars produced via $K \to \pi S$ (green), $B \to KS$ (blue), and proton bremsstrahlung (red). The gray shaded regions correspond to existing limits from past experiments. Figure taken from [62].

decays, and proton bremsstrahlung. No sensitivity is obtained from the gluon fusion process alone in the Phase I run scenario. The gray shaded regions indicate parameter points that are excluded by past experiments, which will be discussed in more details below. We observe from Figure 11 that DarkQuest Phase I (5m - 6m, $N_p = 10^{18}$) will be able to explore a significant new region of parameter space, in particular for scalars produced through kaon decays and proton bremsstrahlung.

Next, in Figure 12 we show the full DarkQuest sensitivity to scalars decaying inclusively to pairs of charged particles, now combining all S production channels, for both Phase I (solid, black) and Phase II (dashed, black) scenarios. In comparison to Ref. [80], which studied scalars produced only in B-decays, we find that the additional scalar production from kaon decays and proton bremsstrahlung can significantly expand the parameter space that can be probed by DarkQuest. [5] In the figure, we also show the current experimental

[5] We have compared our projections with Ref. [80] for scalars produced via B decays and find good

bounds on dark scalar parameter space, including those from CHARM [77, 349], LSND [185], E787/E949 [48, 46], LHCb [6, 7], and NA62. In addition, we also display sensitivity projections from several ongoing or proposed future experiments, including NA62 [96, 72], SBND and ICARUS [61], Belle II [238] (see also Ref. [181]), FASER [178], CODEX-b [203], MATH-USLA [147] and SHiP [27]. See also e.g., Refs. [72, 84, 286, 42] for further proposals to probe Higgs portal scalars in this mass range.[6] We observe that DarkQuest Phase I has the potential to cover a significant region of unexplored parameter space for scalar masses between about 200 MeV and 2 GeV. Phase II will probe angles as small as $\theta \gtrsim 5 \times 10^{-6}$ and as large as $\theta \lesssim 10^{-3}$.

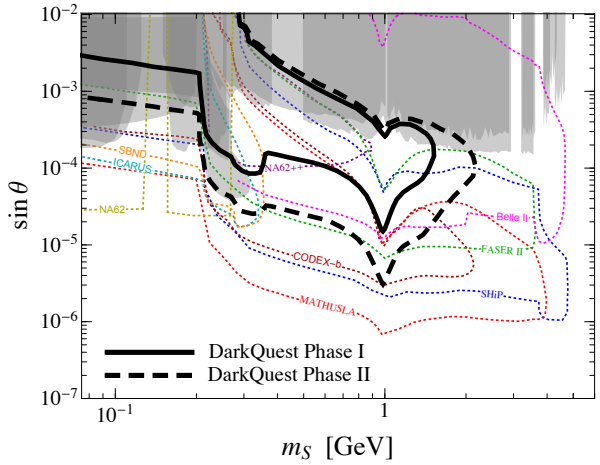

Figure 12: DarkQuest sensitivity to dark scalars. The contours correspond to 10 signal events as obtained by adding the e^+e^-, $\mu^+\mu^-$, $\pi^+\pi^-$, K^+K^- channels, for combined dark scalar production via meson decay, proton bremsstrahlung and gluon fusion. We display both the DarkQuest Phase I sensitivity (solid, black) corresponding to $N_p = 10^{18}$ and 5 m - 6 m decay region, as well as the DarkQuest Phase II sensitivity (dashed, black) corresponding to $N_p = 10^{20}$ and 7 m - 12 m decay region. The gray shaded regions correspond to existing limits and dashed lines corresponds to upcoming limits. Figure taken from [62].

agreement.

[6] We also note that a recent excess observed by the KOTO experiment can be explained in this scenario for scalar masses $m_S \sim 150$ MeV and mixing angles $\theta \sim$ few $\times 10^{-4}$ [167].

2.5 Summary

We have investigated the sensitivity of the Fermilab DarkQuest experiment to two simple and well-motivated dark sector scenarios, heavy neutral leptons and Higgs-mixed scalars. The proposed DarkQuest ECAL upgrade will allow for sensitive searches to a variety of displaced final states containing charged particles and photons, which arise in the models considered here from the decay of long lived HNLs or scalars. We have carefully estimated the production and decay rates of these dark sector particles as well as the detector acceptance to derive projections under two benchmark run scenarios. During the Phase I scenario based on 10^{18} protons on target and a 5m - 6m fiducial decay region, DarkQuest will be able to explore significant new parameter space for τ-mixed HNLs and dark scalars in the mass range of a few hundred MeV - 2 GeV. It is conceivable that this could be achieved on the 5 year time scale, putting DarkQuest on a competitive footing with other proposed experiments. Looking down the road, a potential Phase II scenario with 10^{20} protons on target and a 7m-12m fiducial decay region would allow for improvements by more than one order of magnitude in terms of the interaction rates with SM particles (proportional to squared mixing angle). Our results build on past phenomenological studies [193, 79, 80, 125, 159, 338, 152] and provide further motivation for the DarkQuest ECAL upgrade. This upgrade can be realized with a relatively modest investment and will leverage the existing experimental infrastructure already in place to build an exciting dark sector physics program at Fermilab.

3.0 Renormalizable Models of Flavor-Specific Scalars

3.1 Introduction

Light dark sectors that couple weakly to the Standard Model (SM) may address some of the key open questions in particle physics today [29, 71, 72]. For instance, dark matter may reside in a dark sector, possibly along with other states that are SM gauge singlets, and communicate with the SM through a light mediator particle. One commonly investigated model employs a singlet scalar as the mediator interacting through the Higgs portal [319, 279, 119, 254]. In this scenario, the singlet scalar inherits its interactions with SM matter via mixing with the Higgs boson, thereby coupling preferentially to the heavy third generation fermions and massive electroweak bosons. This leads to a characteristic phenomenology for a light scalar mediator with masses in the MeV-GeV range, with the best probes typically coming from penguin-induced rare meson decays and exotic Higgs decays; see, for example, Ref. [254].

While the Higgs portal provides a well-motivated and popular benchmark, it is of interest to explore other models with qualitatively distinct patterns of mediator couplings to the SM. Such investigations are warranted by the prospect of novel phenomena and new experimental opportunities to probe dark sectors. For scalar mediators in particular, an immediate obstacle is the specter of new dangerous flavor changing neutral currents (FCNCs). Unlike the Higgs portal, which automatically respects Minimal Flavor Violation [151], there is no built-in protection mechanism against large FCNCs for general scalar mediators. From a bottom-up perspective, one can circumvent this issue by appealing to a flavor hypothesis on the structure of the scalar mediator couplings, devised so as to suppress FCNCs at tree level. In this regard, scalar mediators respecting the *flavor-specific* hypothesis provide an interesting alternative to the Higgs portal [63] (for related work, see Ref. [166, 168]). Under this hypothesis, the scalar couples to one (or a few) SM fermion mass eigenstate(s) in the physical basis. Particularly if the singlet couples preferentially to first or second generation states, this scenario leads to a distinctive phenomenology compared to the Higgs portal model. This

point has been illustrated in previous studies of light hadrophilic dark matter based on an up-specific scalar mediator [64] and a possible explanation of the muon anomalous magnetic moment discrepancy [76, 13] based on a muon-specifc scalar mediator [63].

Open questions in this framework related to the short distance structure of the theory remain. Unlike the renormalizable Higgs portal, the flavor specific hypothesis is necessarily formulated in an effective field theory (EFT) setting, where the coupling of interest emerges from a dimension-five operator. Particularly for sizable scalar mediator couplings to matter, we anticipate the presence of new SM-charged degrees of freedom near the weak scale. It is therefore important to study concrete renormalizable completions of flavor-specific EFTs as they can point to additional constraints and experimental prospects associated with the new heavy states.

In this work we study renormalizable completions of flavor-specific EFTs, focusing for concreteness on models realizing up-quark specific couplings. We study two simple completions of this model, one involving a vector-like quark (VLQ) and another involving a second scalar doublet in addition to the Higgs. We consider the implications of naturalness on the couplings of the light scalar mediator and constraints on the models from electroweak precision observables, flavor- and CP-violation, CKM unitarity, and searches for new particles at the LHC. We demonstrate that these additional tests, while being model-dependent, can probe new regions of the low energy EFT scalar mass–coupling parameter space. This study therefore builds on and is highly complementary to the previous flavor specific-EFT studies of Refs. [63, 64].

Another important open structural question pertains to the ultraviolet dynamics generating the flavor-specific coupling structure. In all likelihood, the resolution of this issue must be tied to the origin of SM flavor, itself a challenging open question. We do not address this issue in this work, but instead focus on the more tractable problem of realizing the flavor-specific EFT in simple renormalizable models and studying their phenomenology.

3.2 Effective field theory of flavor-specific scalar

In this section, we review the EFT framework describing a new light scalar S with *flavor-specific* couplings, meaning that the scalar predominantly couples to a particular SM fermion mass eigenstate [63]. To understand the flavor-specific hypothesis, it is useful to start from the Yukawa interactions in the SM quark sector:

$$\mathcal{L}_{\rm SM} = i\overline{Q}_L \not{D} Q_L + i\overline{u}_R \not{D} u_R + i\overline{d}_R \not{D} d_R - \left(\overline{Q}_L Y_u u_R H_c + \overline{Q}_L Y_d d_R H + \text{h.c.}\right), \tag{3.2.1}$$

where $Q_L^\top = (u_L, d_L)$ and H is the Higgs doublet with $H_c = i\sigma^2 H^*$. The Yukawa interactions in (3.2.1) break the large $U(3)_Q \times U(3)_U \times U(3)_D$ global flavor symmetry down to baryon number $U(1)_B$. In many extensions of the SM there are new couplings that also break the flavor symmetry, leading to the dangerous prospect of new large FCNCs. It is common to invoke a flavor hypothesis that restricts the form of these new couplings in such a way that new FCNCs are adequately suppressed. The most common choice is MFV [151], which states that the Yukawa couplings Y_u, Y_d are the only flavor-breaking spurions present in the theory, such that all new couplings that break flavor are constructed out of Y_u and Y_d.

The flavor-specific hypothesis takes a different route from MFV to ensure the suppression of new FCNCs. To build up to the flavor-specific hypothesis, one can first understand how the quark flavor symmetry is broken if only one of the Yukawas (up or down) are nonvanishing. In the case of $Y_u \neq 0$ and $Y_d \to 0$, the $U(3)_D$ symmetry is unbroken, while a general Y_u results in the breaking pattern

$$U(3)_Q \times U(3)_U \to U(1)_u \times U(1)_c \times U(1)_t \qquad (Y_u \neq 0, Y_d = 0). \tag{3.2.2}$$

Similarly, in the case $Y_u \to 0$ and $Y_d \neq 0$, the $U(3)_U$ symmetry is respected, while general Y_d breaks the symmetry according to

$$U(3)_Q \times U(3)_D \to U(1)_d \times U(1)_s \times U(1)_b \qquad (Y_u = 0, Y_d \neq 0), \tag{3.2.3}$$

In the case of the SM, both Y_u and Y_d are non-vanishing and the CKM matrix is nontrivial. Hence the separate $U(1)^3$ quark flavor symmetries preserved by Y_u (in Eq. (3.2.2)) and Y_d (in Eq. (3.2.3)) are different, and only the full $U(1)_B$ baryon number symmetry remains.

With this understanding, we now consider an EFT containing a real SM singlet scalar S that dominantly interacts with the SM through a dimension-five operator contained in the Lagrangian

$$\mathcal{L}_S = \frac{1}{2}\partial_\mu S \partial^\mu S - \frac{1}{2} m_S^2 S^2 - \left(\frac{c_S}{M} S \overline{Q}_L u_R H_c + \text{h.c.} \right). \tag{3.2.4}$$

Under the flavor-specific hypothesis, the coupling c_S only involves a single up-type quark in the mass basis. As an interesting example which we will study throughout this paper, consider the case of an up-specific hypothesis, so that $c_S \propto \text{diag}(1,0,0)$ in the mass basis. The $U(3)^3$ flavor symmetry is then broken by c_S according to the pattern

$$U(3)_Q \times U(3)_U \to U(1)_u \times U(2)_{ctL} \times U(2)_{ctR}. \tag{3.2.5}$$

In particular, simultaneous diagonalization of c_S and Y_u implies that the $U(1)_u$ factor in Eq. (3.2.5) is the same as the one left unbroken by Y_u in Eq. (3.2.2). We note that the flavor-specific hypothesis can be viewed as a special case of alignment.

The EFT framework provides a good starting point for phenomenological investigations of light flavor-specific scalars, as illustrated by the studies of Ref. [63, 64]. However, two basic open questions related to the UV structure of the theory remain. First, Eq. (3.2.4) should emerge from a renormalizable theory containing new SM-charged states near the UV scale $\Lambda \sim M$. Importantly, such completions predict a host of additional phenomena that, while being model-dependent, are not captured by the low-energy EFT. Particularly for light scalars with sizable effective Yukawa couplings, $g_u \equiv c_S v/(\sqrt{2}M)$, the new states cannot be too far above the weak scale, leading to additional experimental constraints and opportunities. The goal of this work is to investigate these issues within the context of two simple completions, one involving a VLQ and another with a second scalar doublet. For concreteness we focus on completions of the up quark-specific couplings.

A second, more challenging question concerns the UV origin of the flavor-specific coupling structure. It should be stressed that the symmetry breaking pattern in Eq. (3.2.5) is a hypothesis on the form of the low energy EFT. As discussed Ref. [63], this assumption is self-consistent in that there are no large radiatively generated deviations from the flavor-specific structure, but its UV origin remains obscure. We do not endeavor here to construct explicit flavor models that naturally enforce flavor-specific couplings, but leave this important open

question to future work. See also Refs. [248, 32] for some potential model-building approaches along this direction.

Flavor-specific scalars may have any number of phenomenological applications, including as a possible new physics explanation for certain experimental anomalies (e.g., the muon anomalous magnetic moment discrepancy [63]) or as a mediator between the SM and a dark sector. The latter application was considered in detail in Ref. [64], which studied a light sub-GeV "hadrophilic" dark sector consisting of a Dirac fermion dark matter, χ, coupled to an up quark-specific scalar mediator. Restricting ourselves here to real couplings for simplicity, the dominant low energy interactions in this scenario are

$$\mathcal{L} \supset -g_u S\bar{u}u - g_\chi S\overline{\chi}\chi, \tag{3.2.6}$$

where the effective scalar-up quark coupling g_u originates from the dimension-five operator in Eq. (3.2.4),

$$g_u \equiv \frac{c_S\, v}{\sqrt{2}M}, \tag{3.2.7}$$

with $v = 246$ GeV being the SM Higgs vacuum expectation value (vev). Through these couplings, the dark matter can obtain the correct relic abundance via thermal freeze-out of its annihilation either directly to hadrons or to scalar mediators. This scenario presents a rich low energy phenomenology, both for the case of visible scalar decays to hadrons (or photons if $m_S < 2m_\pi$) and the case of invisible decays of scalars to dark matter particles. As we will demonstrate below in Secs. 3.3 and 3.4, the additional signatures predicted by the specific UV completions studied in this work can provide complementary constraints on this parameter space.

Starting from the EFT (3.2.4) defined at the UV scale M, one can estimate the expected radiative size of other couplings in the EFT, which has implications for the naturalness of the light singlet scalar and its phenomenology. Concerning naturalness, for example, the two loop correction to the scalar mass and the shift to the up quark mass generated by the S vev are small provided

$$\begin{aligned} c_S &\lesssim (16\pi^2)\,\frac{m_S}{M} \approx 0.08\left(\frac{m_S}{1\,\text{GeV}}\right)\left(\frac{2\,\text{TeV}}{M}\right), \\ \implies \quad g_u &\lesssim \frac{16\pi^2}{\sqrt{2}}\,\frac{m_S v}{M^2} \approx 0.007\left(\frac{m_S}{1\,\text{GeV}}\right)\left(\frac{2\,\text{TeV}}{M}\right)^2. \end{aligned} \tag{3.2.8}$$

As another example, there can be new loop-level contributions to FCNCs in the EFT. Considering the case of neutral kaon mixing, we find a three loop contribution described by the effective lagrangian

$$\mathcal{L} \supset C^{ds}[\bar{d}_L \gamma^\mu s_L][\bar{d}_L \gamma^\mu s_L] + \text{h.c.}, \tag{3.2.9}$$

where the Wilson coefficient is estimated to be

$$C^{ds} \sim \frac{|c_S|^4 (V_{ud}^* V_{us})^2}{(16\pi^2)^3 M^2}. \tag{3.2.10}$$

The current bound on this coupling is given by $\text{Re}[C^{ds}] \lesssim (10^3\,\text{TeV})^{-2}$ [95], leading to a rather mild constraint

$$c_S \lesssim 4 \left(\frac{M}{2\,\text{TeV}}\right)^{1/2} \quad \Longrightarrow \quad g_u \lesssim 0.4 \left(\frac{M}{2\,\text{TeV}}\right)^{-1/2}. \tag{3.2.11}$$

As we will see, corrections to the scalar mass and kaon mixing operators arise already at one loop in the UV completions we study, which can lead to stronger conditions than shown in Eqs. (3.2.8,3.2.11). These examples highlight how the UV theory can provide complementary information on the theoretically favored or experimentally allowed model parameter space.

With this introduction, in the next sections, we will analyze renormalizable models that lead to the low energy EFT in Eq. (3.2.4), focusing on the case of the up-specific hypothesis for concreteness. Two simple completions of the dimension-five operator involve a new VLQ or scalar doublet at the scale M. For each of these possibilities, we will study the implications of the new high-scale physics for the radiatively generated corrections to the Lagrangian, as well as for phenomenology. We will find that naturalness and experimental constraints on the UV theories are in some cases stronger than in the the effective theory and probe complementary regions of low energy scalar mass–coupling parameter space. This suggests that only considering limits in the EFT does not provide a complete picture of the status of flavor-specific scalar theories.

3.3 Vector-like Quark Completion

In this section we consider a renormalizable completion of the flavor-specific EFT in Eq. (3.2.4) involving a VLQ. In what follows, we begin by presenting the model and then consider the natural expected radiative size of the scalar potential and other couplings in the theory, which will lead to a set of naturalness criteria. Following this, we discuss the transition to the physical basis including the interactions and decays of the VLQ. We then study the phenomenology of the model, including the impact of CKM unitarity, FCNCs, EWPTs, CP violation, and searches at the LHC. At the end of this section we present a summary of these constraints and also illustrate how these bounds probe the low-energy EFT parameter space of a light up-philic scalar.

3.3.1 Model

We add to the SM a real gauge singlet scalar S and a VLQ with the same quantum numbers as the SM right-handed up quark, $U'_{L,R} \sim (\mathbf{3}, \mathbf{1}, \frac{2}{3})$. The Lagrangian of the model is

$$\begin{aligned}\mathcal{L}_{\rm VLQ} = \mathcal{L}_{\rm SM} + \frac{1}{2}\partial_\mu S \partial^\mu S - \frac{1}{2} m_S^2 S^2 + \overline{U}' i\gamma^\mu D_\mu U' - M\,\overline{U}' U' \\ - \left[\, y_i\, \overline{Q}_L^i U'_R\, H_c + \lambda^i\, \overline{U}'_L u_{Ri}\, S + \text{h.c.}\,\right]\end{aligned} \tag{3.3.1}$$

Here $i = 1, 2, 3$ is a generation index and M is the VLQ mass. Integrating out the VLQ leads to an effective Lagrangian, with the leading terms appearing at the dimension 5 level:

$$\mathcal{L} \supset \frac{y_i\, \lambda^j}{M} S\, \overline{Q}_L^i\, u_{Rj}\, H_c + \text{h.c.} \tag{3.3.2}$$

Comparing this with the Wilson coefficient of the effective operator in Eq. (3.2.4), we thus identify the VLQ mass M as the new UV physics scale and $(c_S)_i^j \equiv -y_i\, \lambda^j$. The up-specific hypothesis corresponds to $y_i \propto \delta_{i1}$ and $\lambda^i \propto \delta^{i1}$ in the quark flavor basis in which Y_u is diagonal.

It is important to note that the new physics couplings in Eq. (3.3.1) are not the most general ones allowed by the gauge symmetries. To realize the flavor-specific hypothesis in the low-energy EFT, an extended flavor hypothesis must be made in the renormalizable completion. This entails specifying the spurion quantum numbers of Y_u, Y_d, y, λ, and M under the enlarged quark flavor symmetry and how their background values break this symmetry. Once this hypothesis is made, the Lagrangian in the basis (3.3.1) is obtained through suitable quark flavor rotations.

In addition, the symmetries of the model admit additional renormalizable terms beyond those listed in Eq. (3.3.1), such as a $S\overline{U}U$ Yukawa couplings, S self-couplings, and interactions between S and H. For simplicity, we assume that these are small, comparable to their radiatively induced contributions (see below) which provide a rough lower bound on the sizes of these couplings in the absence of fine-tuning.

3.3.2 Naturalness considerations

We are interested in the phenomenology of a light singlet scalar, $m_S \ll v$, with sizable couplings to the up quark. To achieve this, the UV model couplings y, λ in Eq. (3.3.1) must not be too small given the expectation that $M \sim \mathcal{O}(\text{TeV})$. However, it is of interest to know if the required magnitudes of these and other couplings in the theory are technically natural, i.e., that radiatively induced corrections to the Lagrangian parameters in (3.3.1) are comparable to or smaller than the physical values of these parameters.

The technical naturalness of y and λ in (3.3.1) can be derived in terms of discrete symmetries [63]. Here, we estimate the size of radiative corrections to other couplings in the theory to obtain order-of-magnitude naturalness "bounds", using a factor $(16\pi^2)^{-1}$ for each loop and counting the relevant coupling and scale factors. For the latter, all mass scales that are parametrically smaller than M can be neglected (such as all SM masses).

The most important corrections are those to the scalar masses, which arise at one loop in the renormalizable VLQ completion. In particular, the coupling λ leads to a correction to the S mass, $\delta m_S^2 \sim \text{Tr}(\lambda^*\lambda)M^2/16\pi^2$, where we have defined the matrix $(\lambda^*\lambda)^i_j = \lambda^*_i\lambda^j$ and its trace $\text{Tr}\,\lambda^*\lambda = \lambda^*_i\lambda^i$. Demanding this is less than the S squared mass leads to the

condition

$$\lambda^i \lesssim 4\pi \frac{m_S}{M} \simeq (6 \times 10^{-3}) \left(\frac{m_S}{1\,\text{GeV}}\right) \left(\frac{2\,\text{TeV}}{M}\right). \tag{3.3.3}$$

In addition, there is a correction to the Higgs mass term originating from the y coupling, $\delta m_H^2 \sim \text{Tr}(yy^*)M^2/16\pi^2$. Requiring that this is smaller than the square of the electroweak vev gives the naturalness condition

$$y_i \lesssim 4\pi \frac{v}{M} \simeq 2 \left(\frac{2\,\text{TeV}}{M}\right). \tag{3.3.4}$$

Combining Eqs. (3.3.3) and (3.3.4) we obtain a bound on the Wilson coefficient c_S defined in Eqs. (3.2.4,3.3.2):

$$(c_S)_i^j \lesssim 16\pi^2 \frac{v\, m_S}{M^2} \simeq 0.01 \left(\frac{m_S}{1\,\text{GeV}}\right) \left(\frac{2\,\text{TeV}}{M}\right)^2. \tag{3.3.5}$$

We note that this condition is stronger than the one obtained in the EFT, Eq. (3.2.8), by a factor v/M. Eq. (3.3.5) confirms the general expectation that a light scalar with substantial couplings is in tension with naturalness considerations.

The Higgs portal operator $S^2|H|^2$ will also give a correction to the S mass term after electroweak symmetry breaking. The radiative size of this operator is estimated to be $\delta_{S^2H^2} \sim \text{Tr}[(y\lambda)(y\lambda)^\dagger]/16\pi^2 = \text{Tr}(c_S c_S^\dagger)/16\pi^2$, and the correction to the scalar mass is thus $\delta m_S^2 \sim \text{Tr}(c_S c_S^\dagger)v^2/16\pi^2$. The corresponding naturalness bound is thus $(c_S)_i^j \lesssim 4\pi\, m_S/v$, which is a weaker bound than Eq. (3.3.5) so long as $M \gtrsim 2\sqrt{\pi}v \sim$ TeV.

Besides the scalar masses, there are other corrections to the scalar potential that must be taken into account. In particular, there is an S tadpole generated at two loops with size $\delta_S \sim \text{Tr}(y\lambda\, Y_u^\dagger)M^3/(16\pi^2)^2 = \frac{\text{Tr}(c_S\, Y_u^\dagger)M^3}{(16\pi^2)^2}$. Provided the naturalness bounds in Eqs. (3.3.3,3.3.4) are satisfied, it is straightforward to show that the tadpole and mass terms dominate the S potential; for a detailed argument in the EFT context, see Ref. [63]. In the presence of the tadpole, the scalar develops a vev of characteristic size $v_S \simeq \delta_S/m_S^2 = \text{Tr}(c_S\, Y_u^\dagger)M^3/(16\pi^2)^2 m_S^2$, which in turn gives an effective contribution to the up quark Yukawa through the effective operator in Eq. (3.3.2) equal to $(\delta Y_u)_i^j \simeq (c_S)_i^j\, \text{Tr}(c_S\, Y_u^\dagger)M^2/(16\pi^2)^2 m_S^2$. Specializing to the flavor-specific hypothesis and demanding this correction is small compared to the SM Yukawa yields another naturalness condition, $c_S \lesssim 16\pi^2\, m_S/M$. This bound is clearly weaker than the one given in Eq. (3.3.5).

The other corrections to the scalar potential terms, such as the cubic interactions, S^3 and $S|H|^2$, and the quartic interactions S^4 and $|H|^4$, can be estimated in a similar manner. In particular, we note that $S|H|^2$ will induce mass mixing between the Higgs and the singlet scalars. However, as already mentioned, it can easily be seen that the expected radiative sizes of these couplings and the resulting Higgs-scalar mixing angle are tiny once the naturalness conditions (3.3.3,3.3.4) are met, and as such they will not play a role in our phenomenological considerations below.

Besides the scalar potential, there are other couplings involving the quarks and scalar that are radiatively generated. The parametric dependence of the radiative sizes of these terms on the tree-level couplings follows from symmetry considerations [63]. For instance, at one loop a mass mixing term between the VLQ and SM up quark of the form $\mathcal{L} \supset -m\,\overline{U}'_L\,u_R + \text{h.c.}$ is generated with an expected radiative size $m \sim y\,Y_u\,M/16\pi^2$. This is smaller than 1 MeV for $y = 1$, $(Y_u)^1_1 \sim 10^{-5}$, and $M = 2$ TeV. Therefore, no large tuning of the physical up quark mass is caused by this effect. Similarly, at one loop the coupling $\mathcal{L} \supset -\lambda'\,\overline{U}'_L U'_R\,S + \text{h.c.}$ is generated with size $\lambda' \sim y\lambda Y_u/16\pi^2$, which is tiny if the naturalness bounds discussed above hold.

Given the considerations above, the dominant naturalness constraints come from the conditions on y and λ given in Eq. (3.3.3,3.3.4), which taken together lead to the bound on c_S given in Eq. (3.3.5).

3.3.3 Mixing, mass eigenstates, and interactions

We now discuss the fermion mass diagonalization and the resulting interactions in the physical basis that will play an important role in our phenomenological considerations below. We start from the interactions of the VLQ, Eq. (3.3.1), and the SM Yukawa couplings, Eq. (3.2.1). Without loss of generality we may start from the flavor basis in which Y_u is real and diagonal. Furthermore, invoking the up-specific hypothesis, the couplings y and λ in Eq. (3.3.1) take the form $y_i = y\,\delta_{i1}$, $\lambda^i = \lambda\,\delta^{i1}$ in this basis. After electroweak symmetry

breaking, there is mass mixing between the u and U' quark fields,

$$-\mathcal{L} = \begin{pmatrix} \overline{u}_L & \overline{U}'_L \end{pmatrix} \begin{pmatrix} \frac{y_u v}{\sqrt{2}} & \frac{yv}{\sqrt{2}} \\ \lambda v_S & M \end{pmatrix} \begin{pmatrix} u_R \\ U'_R \end{pmatrix} + \text{h.c.} \tag{3.3.6}$$

where y, λ and M are complex parameters in general, while y_u is real and positive in this basis. Through suitable phase rotations of the quark fields, it can be shown that there is one new physical phase if all of y_u, y, λ, and M are non-vanishing. In the limit that any one of these couplings is zero, the phase can be rotated away. Here, we instead consider the limit $y_u v, \lambda v_S \ll yv < M$, which is motivated by the fact that $y_u \ll y$ and the naturalness considerations regarding y, λ, v_S discussed in Sec. 3.3.2. In this regime the system is diagonalized by a rotation of the left handed quarks,

$$\begin{aligned} u_L &\to \cos\theta\, u_L + \sin\theta\, U'_L, \qquad & U'_L &\to \cos\theta\, U'_L - \sin\theta\, u_L, \\ \cos\theta &= \frac{M}{m_{U'}}, & \sin\theta &= \frac{yv}{\sqrt{2}\, m_{U'}}. \end{aligned} \tag{3.3.7}$$

where $m_{U'} = \sqrt{M^2 + y^2 v^2/2}$ is the physical mass of the heavy VLQ.

This mixing plays an important role in VLQ phenomenology due to the modifications of the SM interactions and the couplings induced between the VLQ and light SM fields. For example, the W boson couplings involving the SM up quark and VLQ are

$$\mathcal{L} \supset \frac{g}{\sqrt{2}} W^+_\mu \left(\cos\theta\, V_{1i}\, \overline{u}_L \gamma^\mu d_{Li} + \sin\theta\, V_{1i}\, \overline{U}'_L \gamma^\mu d_{Li} \right) + \text{h.c.}, \tag{3.3.8}$$

where V is unitary and $i = 1, 2, 3$ runs over the three SM generations. The first term implies that the effective SM CKM matrix is no longer unitary, while the second term leads to the decay $U' \to d_i W^+$. The couplings in Eq. (3.3.8) also give rise to $\Delta S = 2$ transitions. The dominant contributions to such processes will be computed below in Section 3.3.5. Furthermore, the Z boson couplings involving the up quark and VLQ include

$$\mathcal{L} \supset g_{uL} Z_\mu\, \overline{u}_L \gamma^\mu u_L + \left(\frac{g}{2c_W} \sin\theta \cos\theta\, Z_\mu\, \overline{u}_L \gamma^\mu U'_L + \text{h.c.} \right). \tag{3.3.9}$$

The Z coupling to left-handed up quarks g_{uL} is shifted from its SM value as a result of u–U' mixing, while the right-handed up quark coupling g_{uR} is unaffected by this mixing:

$$g_{uL} = g_{uL}^{\rm SM} + \delta g_{uL}, \qquad \delta g_{uL} = \sin^2\theta (g_{uR}^{\rm SM} - g_{uL}^{\rm SM}) \approx \frac{y^2 v^2}{2M^2}(g_{uR}^{\rm SM} - g_{uL}^{\rm SM}) \tag{3.3.10}$$
$$g_{uL}^{\rm SM} = \frac{g}{c_W}\Big(\frac{1}{2} - \frac{2}{3}s_W^2\Big), \qquad g_{uR}^{\rm SM} = -\frac{2g s_W^2}{3c_W}.$$

As we will discuss below, such shifts can be probed by electroweak precision tests. Furthermore, the second term in Eq. (3.3.9) above leads to the decay $U' \to uZ$. Finally, there are interactions between the scalars and quarks, the most important of which are

$$-\mathcal{L} \supset \cos\theta \frac{y}{\sqrt{2}}\, h\, \overline{u}_L\, U'_R - \sin\theta\, \lambda\, S\, \overline{u}_L\, u_R + \cos\theta\, \lambda\, S\, \overline{U}'_L\, u_R + \text{h.c.} \tag{3.3.11}$$

The first and third terms above lead to the VLQ decays $U' \to uh$ and $U' \to uS$, respectively. The second term is the induced coupling of S to up quarks, which in the limit of large M reproduces the EFT result discussed earlier in Eqs. (3.2.6,3.2.7).

3.3.3.1 VLQ and singlet scalar decays

From the couplings of U' to vector and scalar bosons given above, Eqs. (3.3.8,3.3.9,3.3.11), we obtain the partial decay widths of the VLQ:

$$\Gamma(U' \to uS) = \cos^2\theta\, \frac{\lambda^2\, m_{U'}}{32\,\pi}\left(1 - \frac{m_S^2}{m_{U'}^2}\right)^2 \simeq \frac{\lambda^2 M}{32\,\pi}, \tag{3.3.12}$$

$$\Gamma(U' \to uh) = \sin^2\theta \cos^2\theta\, \frac{G_F\, m_{U'}^3}{16\sqrt{2}\,\pi}\left(1 - \frac{m_h^2}{m_{U'}^2}\right)^2 \simeq \frac{y^2 M}{64\,\pi}, \tag{3.3.13}$$

$$\Gamma(U' \to uZ) = \sin^2\theta \cos^2\theta\, \frac{G_F\, m_{U'}^3}{16\sqrt{2}\,\pi}\left(1 - \frac{m_Z^2}{m_{U'}^2}\right)^2\left(1 + \frac{2m_Z^2}{m_{U'}^2}\right) \simeq \frac{y^2 M}{64\,\pi}, \tag{3.3.14}$$

$$\Gamma(U' \to dW) = \sin^2\theta\, \frac{G_F\, m_{U'}^3}{8\sqrt{2}\,\pi}\left(1 - \frac{m_W^2}{m_{U'}^2}\right)^2\left(1 + \frac{2m_W^2}{m_{U'}^2}\right) \simeq \frac{y^2 M}{32\,\pi}, \tag{3.3.15}$$

where the u–U' mixing angle θ is defined in Eq. (3.3.7). We have also provided approximate expressions for the decay widths in the limit $M \gg v$, from which is it is evident that the U' decays to electroweak bosons respect the Goldstone Equivalence Theorem. Given the naturalness considerations discussed earlier, which suggest $\lambda \ll y$, we typically expect the U' decays to electroweak bosons to dominate. As we will discuss in detail below, this suggests

that LHC searches for VLQs with couplings to the first generation are a promising way to test this completion.

However, it is also possible in principle that U' could dominantly decay to a scalar S and an up quark, provided $y \lesssim \lambda$. In such a situation, the VLQ signature will depend in detail on how S decays. If there are no additional light states present in the theory, S will decay to pairs of up quarks [or to exclusive hadronic modes for $m_S \sim \mathcal{O}(1\text{ GeV})$]. This decay width is controlled by the effective scalar-up quark coupling g_u defined in Eqs. (3.2.6,3.2.7). If S is even lighter, with mass below the two-pion threshold, it will decay to a pair of photons at one loop, and is naturally long-lived. Alternatively, if there are additional light degrees of freedom with sizable couplings to S, the scalar may dominantly decay to such states. For example, in the case of a coupling to light dark matter as in Eq. (3.2.6), the scalar can decay invisibly via $S \to \chi\overline{\chi}$.

We now turn to the phenomenology of the model.

3.3.4 CKM constraints

Due to the mixing of the up quark with the VLQ, the effective 3×3 CKM matrix describing the mixing of the SM quarks is no longer unitary. This is clearly seen in Eq. (3.3.8), where the elements of the unitary matrix V_{1i} are multiplied by the prefactor $\cos\theta$. This model therefore predicts that the top-row CKM unitarity triangle relation is modified and no longer equal to unity. The current experimental determination of the top-row CKM unitarity relation is [357]

$$\left[|\tilde{V}_{ud}|^2 + |\tilde{V}_{us}|^2 + |\tilde{V}_{ub}|^2 \right]\Big|_{\text{exp}} = 0.9985(3)_{V_{ud}}(4)_{V_{us}}, \tag{3.3.16}$$

where the dominant uncertainties from V_{ud} and V_{us} are indicated. Here $\tilde{V}_{ij}$ are the apparent CKM matrix elements when assuming the SM. Interestingly, the current determination (3.3.16) displays a 3σ deviation from unitarity. Such a deviation is a natural consequence of our model, which gives the prediction

$$|\tilde{V}_{ud}|^2 + |\tilde{V}_{us}|^2 + |\tilde{V}_{ub}|^2 = \cos^2\theta \left[|V_{ud}|^2 + |V_{us}|^2 + |V_{ub}|^2 \right] = \cos^2\theta, \tag{3.3.17}$$

where we have used the unitarity of V in the second step. This is to be compared with Eq. (3.3.16). The model can therefore provide an explanation of this discrepancy provided the mixing angle is in the range

$$0.032 < |\sin\theta| < 0.045, \tag{3.3.18}$$

which brings the theory prediction and experimental determination into agreement at the 1σ level. Explaining this discrepancy with VLQ was also recently studied in Refs. [73, 74, 109].

Beyond a possible explanation of this discrepancy, Eq. (3.3.16) can be used to place a conservative bound on the mixing angle. Requiring that the theory prediction is within 3σ of the experimental determination, we find the constraint $\sin\theta \lesssim 0.055$, which can be phrased as the following bound on the model parameters using Eq. (3.3.7):

$$y \lesssim 0.6 \left(\frac{M}{2\,\text{TeV}}\right). \tag{3.3.19}$$

3.3.5 FCNCs

Although the flavor-specific hypothesis generally provides strong protection against FCNCs, there can still be important effects if the VLQ is light enough and its couplings are relatively large. Here we consider the contributions to neutral kaon mixing, which generally provides the strongest FCNC constraints. In particular, working in the unbroken electroweak theory there is a one loop box diagram resulting from U' and Higgs doublet exchange, which leads to an effective operator with four Q_L fields. The resulting effective Lagrangian reads

$$\mathcal{L} \supset -\frac{y_i y^{\dagger j} y_k y^{\dagger \ell}}{128\pi^2 M^2} [\overline{Q}^i \gamma^\mu P_L\, Q_j][\overline{Q}^k \gamma^\mu P_L\, Q_\ell]. \tag{3.3.20}$$

Going to the physical basis, $d_L \to V d_L$, and specializing to the up-specific hypothesis, we find a contribution that mediates neutral kaon mixing, described by the effective Lagrangian (3.2.9) with the Wilson coefficient

$$C^{ds} = -\frac{y^4 |V_{ud}^* V_{us}|^2}{128\pi^2 M^2}. \tag{3.3.21}$$

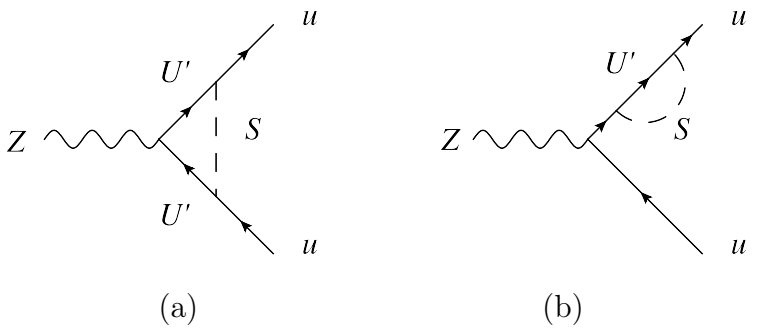

Figure 13: Loop diagrams contributing to the hadronic Z width in the VLQ completion, figure taken from Ref.[65].

Current limits restrict $\mathrm{Re}[C^{ds}] \lesssim (10^3\,\mathrm{TeV})^{-2}$ [95], leading to the constraint

$$y \lesssim 0.6 \left(\frac{M}{2\,\mathrm{TeV}}\right)^{1/2}. \tag{3.3.22}$$

We emphasize that it is the exchange of the charged Higgs Goldstone bosons and U' that generate FCNCs in the neutral kaon system.

3.3.6 Electroweak precision bounds

The heavy VLQ modifies the partial width of Z to hadrons in two ways: through u–U' mixing and through the loop diagrams in Figure 13 (a,b). Additional diagrams suppressed by both a loop factor and the mixing angle θ exist but will be neglected. The main observable to constrain modifications of the hadronic Z width is the hadron-to-lepton branching ratio, $R_\ell \equiv \frac{\Gamma[Z\to\mathrm{had.}]}{\Gamma[Z\to\ell^+\ell^-]}$. The current experimental data and SM theory prediction give $R_\ell^{\mathrm{exp}} - R_\ell^{\mathrm{SM}} = 0.034 \pm 0.025$ [332]. For general shifts in the Z boson coupling to up and down quarks, $\delta g_{uL,R}$, $\delta g_{dL,R}$, the modification to this observable is given by

$$\delta R_\ell \simeq \frac{2N_c\,\mathrm{Re}(g_{uL}^{\mathrm{SM}}\,\delta g_{uL} + g_{uR}^{\mathrm{SM}}\,\delta g_{uR} + g_{dL}^{\mathrm{SM}}\,\delta g_{dL} + g_{dR}^{\mathrm{SM}}\,\delta g_{dR})}{(g_{\ell L}^{\mathrm{SM}})^2 + (g_{\ell R}^{\mathrm{SM}})^2}, \tag{3.3.23}$$

where $N_c = 3$ and $g_{fL}^{\mathrm{SM}} = \frac{g}{c_W}(T_f^3 - Q_f s_W^2)$, $g_{fR}^{\mathrm{SM}} = \frac{g}{c_W}(-Q_f s_W^2)$ are the Z boson couplings to fermions f in the SM.

The largest effect comes from the mixing in (3.3.7), which leads to a tree-level shift of the $Z\bar{u}_L u_L$ coupling, given above in Eqs. (3.3.9,3.3.10). Plugging these shifts into Eq. (3.3.23) we obtain

$$\delta R_\ell \simeq -\frac{3(\frac{1}{2}-\frac{2}{3}s_W^2)}{(-\frac{1}{2}+s_W^2)^2+(s_W^2)^2}\sin^2\theta \simeq -8.3\sin^2\theta \tag{3.3.24}$$

This leads to the bound

$$|\sin\theta| \lesssim 0.044. \tag{3.3.25}$$

For $v \ll M$, the bound can also be stated as $|yv/M| < 0.063$.

This bound could be improved at a future high-luminosity e^+e^- collider running on the Z-pole, such as CEPC [162] or FCC-ee [8]. With the expected FCC-ee precision, $\delta R_\ell^{\text{exp.}} = 0.001$ [92], one would be able to constrain $|yv/M| < 0.022$.

At the one-loop level, the diagrams Figure 13 (a,b) generate a correction to the $Z\bar{u}_R u_R$ coupling. In the limit $M \gg v \gg m_S$, it is given by

$$\delta g_{uR} \approx g_{uR}^{\text{SM}} \frac{7\lambda^2}{576\pi^2}\frac{m_Z^2}{M^2} \tag{3.3.26}$$

For $M = 1$ TeV and $\lambda \sim \sqrt{4\pi}$ near its perturbative limit, the shift in R_ℓ from (3.3.26) is less than 10^{-3} and thus phenomenologically irrelevant.

3.3.7 CP violation

If the couplings M, y, λ are complex we may expect new CP-violating phenomena including a potentially large neutron electric dipole moment. Separate rephasings of $u_{L,R}$ and $U'_{L,R}$ leave invariant

$$\phi_{\text{CP}} \equiv \arg\left[y_u M\,(y\lambda)^*\right], \tag{3.3.27}$$

and all CP-violating effects are proportional to $\sin\phi_{\text{CP}}$. The dominant contribution in the VLQ model arises due to an effective CP-violating four up quark operator mediated by the exchange of the scalar S,

$$\mathcal{L} \supset C'_u\,\bar{u}i\gamma^5 u\,\bar{u}u, \tag{3.3.28}$$

where the Wilson coefficient is

$$C'_u = \frac{\text{Re}(Y_{S\bar{u}u})\text{Im}(Y_{S\bar{u}u})}{m_S^2} \simeq -\frac{y^2\lambda^2 v^2}{4M^2 m_S^2}\sin 2\phi_{\text{CP}}. \tag{3.3.29}$$

The final expression in Eq. (3.3.29) holds provided $y_u M \gg y\lambda v_S$, which is always satisfied in the natural region of parameter space. The effective operator, Eq. (3.3.28), is then matched to CP-violating interactions in the chiral Lagrangian, from which the relevant hadronic matrix elements can be estimated. For this we use the results of Ref. [36], which derives a prediction for the neutron EDM in terms of the Wilson coefficient,

$$d_n = 0.182\, e\, C'_u\, \text{GeV} \simeq 3.6 \times 10^{-15}\, e\, \text{cm}\, C'_u\, \text{GeV}^2. \tag{3.3.30}$$

The current leading upper limit on the neutron EDM is $|d_n| < 1.8 \times 10^{-26} e$ cm (90% C.L.) from Ref. [12]. Using Eqs. (3.3.29,3.3.30) we can express this as a limit on the effective coupling of the scalar to up quarks ($g_u \simeq y\lambda v/\sqrt{2}M$),

$$|g_u| \sqrt{\sin 2\phi_{\text{CP}}} < 3 \times 10^{-6} \left(\frac{m_S}{1\,\text{GeV}}\right) \tag{3.3.31}$$

A one-loop contribution to the neutron EDM also arises due to pion-scalar mixing which leads to a CP-violating pion-nucleon coupling. The bound that results from this process is [317]

$$|g_u| \sqrt{\sin 2\phi_{\text{CP}}} < 1 \times 10^{-5} \left(\frac{m_S}{1\,\text{GeV}}\right), \tag{3.3.32}$$

which is quantitatively similar to that in Eq. (3.3.31).[1]

Other contributions to the neutron EDM are subdominant to the four up-quark CP odd operator (3.3.28). For example, a one-loop penguin-type diagram with the scalar S entering in the loop, gives a contribution to the up quark EDM of

$$d_u \simeq \frac{3eQ_u}{32\pi^2} |g_u|^2 \sin 2\phi_{\text{CP}} \frac{m_u}{m_S^2} \left[1 + \frac{4}{3} \log\left(\frac{\Lambda_{\text{IR}}}{m_S}\right)\right], \tag{3.3.33}$$

where we have taken the large M limit and $\Lambda_{\text{IR}} \simeq 300$ MeV is an IR cutoff on the loop. The neutron EDM induced by the up-quark EDM is $d_n = 0.784(28) d_u$ [218]. We thus obtain a bound,

$$|g_u| \sqrt{\sin 2\phi_{\text{CP}}} < 3.2 \times 10^{-4} \left(\frac{m_S}{1\,\text{GeV}}\right) \tag{3.3.34}$$

[1] Note that Ref. [63] also included an estimate of the one-loop contribution to the neutron EDM in the presence of pion-scalar mixing (see Eq. (35) in that reference) by matching to the chiral Lagrangian and cutting the loop off at the neutron mass. The resulting contribution to d_n from this process in [63] is larger by a factor $\left(2\frac{m_\pi^2}{m_N^2} \log \frac{m_N^2}{m_\pi^2}\right)^{-1} \simeq 6$ than that in Ref. [317] which involves a detailed treatment of heavy baryon chiral perturbation theory.

which is significantly weaker than the one given in Eq. (3.3.31). A similar diagram leads to an up quark chromo-EDM, leading to a comparable limit to that in Eq. (3.3.34) from the mercury EDM limit of $|d_{\rm Hg}| < 7.4 \times 10^{-30}\, e\,{\rm cm}$ [213].

In Figure 16, we show the leading limit on g_u from Eq. (3.3.31) fixing $\phi_{\rm CP} = \pi/4$. Since the estimates in this section all assume that m_S is larger than the hadronic scale, we only display this limit for $m_S > 1$ GeV.

3.3.8 Collider phenomenology

We now discuss the collider phenomenology of the VLQ completion. Pair production of U' at hadron colliders proceeds through the strong interaction, while single electroweak production is also possible through mixing. Unlike top partners, the U' decays only to light flavor quarks, so typical VLQ searches requiring b-tagged jets in the final state do not apply. Instead, we consider collider searches for VLQs decaying to light quarks. Motivated by the naturalness constraints on λ, Eq. (3.3.3), we will initially focus on the small λ limit, where the $U' \to Su$ decay can be neglected and VLQ decays to a first generation quark and an electroweak boson dominates, see Eqs. (3.3.12-3.3.15). The ATLAS and CMS collaborations performed light-flavor VLQ searches only with 8 TeV data to date. ATLAS considered pair production of U' followed by the decay $U' \to Wd$ in the single-lepton final state [3]. CMS considered both pair production and single production, including the decay modes $U' \to Wd, Zu, hu$ in final states involving one or more leptons [320]. We will follow CMS, performing an analysis similar to their search for pair production of VLQs decaying to two leptons, jets and missing energy.

Before turning to our recast analysis, we briefly mention the other channels studied by CMS in Ref. [320]. First, in principle both pair production and single production of the U' is possible. However, single production requires mixing between the U' and the SM quarks, which is strongly constrained. CMS searched for single production of down-type VLQ decaying to $W^- u$ or Zd. The latter decay mode is relevant to the present case of up-type VLQ, and in this channel the effective limit on the mixing angle is $\mathcal{O}(1)$ across the mass range considered. Since the single production cross-section goes as the square of the mixing

angle and constraints from CKM and EW precision observables limit $\sin^2\theta \lesssim 10^{-3}$, single production is not competitive with pair production in the allowed regions of parameter space. Turning to pair production, CMS performed searches for $U'\bar{U}'$ in single lepton, dilepton, and multilepton (3 or 4) final states. In the Goldstone equivalence limit where the ratio of the U' decays to W, Z, and h is 2:1:1 (see Eqs. (3.3.13,3.3.14,3.3.15)), the single lepton analysis is the strongest of these searches owing to the high W branching fraction. However, this channel involves a kinematic fit of each event to the hypothesis that it contains two W bosons, one W and one Z, or one W and one h. Events are considered under each hypothesis based on the χ^2 of this fit, which is difficult to estimate. We thus choose to focus on the next most constraining channel, the dilepton final state. The multilepton search has much lower statistics.

For the signal, we simulate pair production of the U' with MadGraph [33], Pythia [327] and Delphes [153], using the UFO [31, 155] model for a singlet VLQ [114]. We also simulate the dominant backgrounds in the CMS search, which are top pair production and Z + jets. We stay close to the cuts of the signal region aimed at the $WqWq$ final state, which enjoys the highest statistics due to the large $U' \to Wd$ branching fraction. Specifically, we require:

- Exactly two opposite-sign leptons with $p_T > 30, 20$ GeV respectively and $|\eta| < 2.5$
- At least two jets with $p_T > 200, 100$ GeV and $|\eta| < 2.4$ that do not pass a b-tag with efficiency 84% and fake rate 10%
- No same-flavor lepton pair within 7.5 GeV of the Z mass
- Missing transverse energy (MET) > 60 GeV
- $S_T > 1000$ GeV, where S_T is the scalar sum of the lepton p_T, jet p_T and MET

Most of these cuts are very similar to those of CMS, except that while they set limits using the full S_T distribution, we simply perform a cut-and-count analysis with a minimum S_T requirement. Prior to this cut, our signal and background event counts are in agreement with CMS. We then estimate 2σ limits on the production cross-section as a function of $m_{U'}$, considering statistical uncertainties only.

We perform this search with 20 fb^{-1} of integrated luminosity at 8 TeV as a check of our analysis, and then repeat it assuming 3000 fb^{-1} at 14 TeV. Our results are shown in Figure 14.

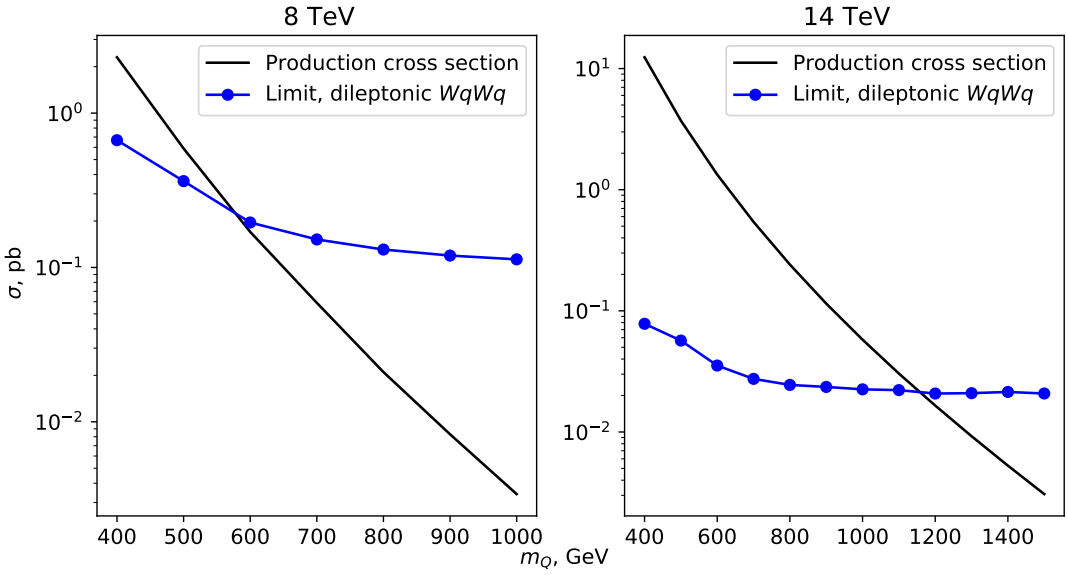

Figure 14: Estimated limits on the U' pair production cross-section from a search for a final state with two leptons, jets and missing energy, figure taken from Ref.[65].

The expected 8 TeV limit on $m_{U'}$ is approximately 575 GeV. For comparison, CMS combines several dilepton and multilepton search channels to obtain a limit of 585 GeV when the branching fractions of U' to Wd, Zu, and Hu are 50%, 20%, and 30%, respectively. At 14 TeV with the full HL-LHC dataset, we estimate that the limit from the dilepton channel alone could approach 1150 GeV. This represents a significant increase over the limit of 685 GeV reported by CMS in Ref. [320] for a U' which decays with the branching ratios expected by Goldstone equivalence, when combining searches in multiple pair production final states. It would be of interest, then, to see updated light-flavor VLQ searches with the latest LHC dataset. While we have considered only the dilepton final state, it is quite possible that a combination of searches, including the high statistics single-lepton channel, could do even better than our projection.

Next, we consider the case where the $U' \to Su$ decay is important. The relevant coupling λ is limited by Eq. (3.3.3) if it is natural, which for light scalars S is typically much smaller than the effective $\bar{Q}U'H_c$ coupling allowed by the indirect constraints from CKM unitarity, FCNCs and EWPT in Eqs. (3.3.19), (3.3.22) and (3.3.25) respectively. However, if y is even smaller than required by these indirect constraints, the $U' \to Su$ decay could dominate. For visibly decaying S, the pions produced in the S decay would be highly collimated if S were light. Consequently, strong production of U' could be probed by searches for pair production of dijet resonances. A reinterpretation [165] of a 13 TeV ATLAS paired dijet resonance search [2] found that for light S, the limit on the VLQ mass is approximately 700 GeV. For invisibly decaying S, searches for jets plus missing energy would apply, which tend to give considerably stronger limits [325, 5].

Finally, the light scalar can also be directly produced in hadron collisions, but the bounds on the effective scalar-up quark coupling g_u are generally quite weak. For visible S decays there are constraints from di-jet+photon searches in the mass range 10 GeV $\lesssim m_s \lesssim$ 100 GeV, which lead to a bound $g_u \lesssim 0.3$ [322]. For invisible decays of S, one can look for a mono-jet signature. A bound $g_u \lesssim 0.1$ was derived previously in Ref. [64].

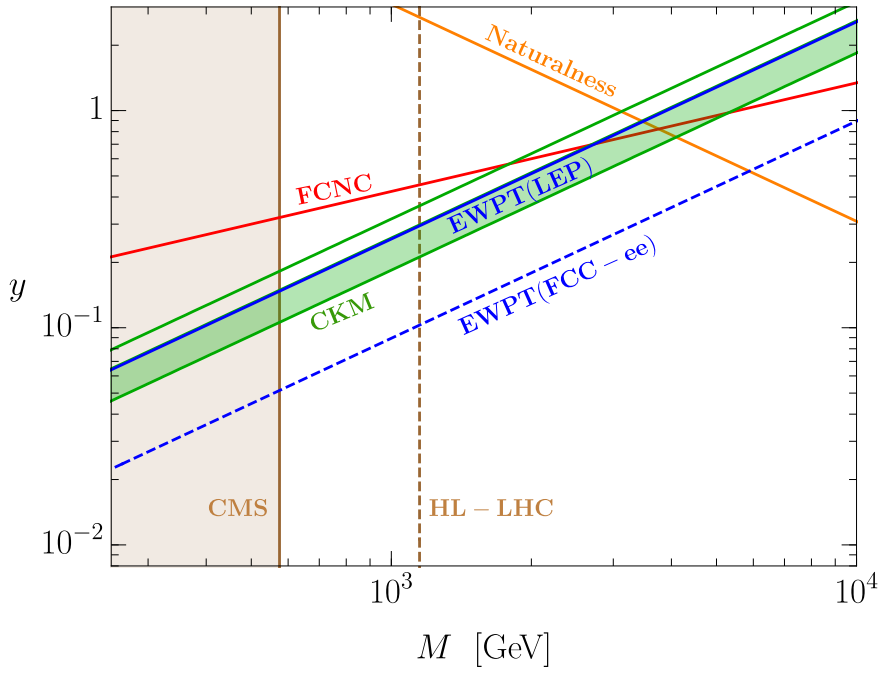

Figure 15: Constraints on the VLQ model in the $M - y$ plane. Shown are current bounds from neutral kaon mixing (red solid line), CKM unitarity (green solid line), the Z boson hadronic-to-leptonic branching ratio R_ℓ (blue solid line), and a direct VLQ search from CMS (brown shaded region). Regions above the lines are excluded. We also indicate the parameter space where the model can explain the $\sim 3\sigma$ discrepancy in CKM top row unitarity triangle determination (green shaded band). The expected future reach from precision measurements of R_ℓ at FCC-ee (blue dashed line) and a direct VLQ search at the HL-LHC (brown dashed line) are also indicated. Large couplings and VLQ masses do not satisfy the naturalness condition (3.3.4) (orange solid line). This plot assumes $\lambda \ll y$, which is typically the case in this plane for light scalars, $m_S \lesssim$ GeV, and natural values of λ, as suggested by Eq. (3.3.3), figure taken from Ref.[65].

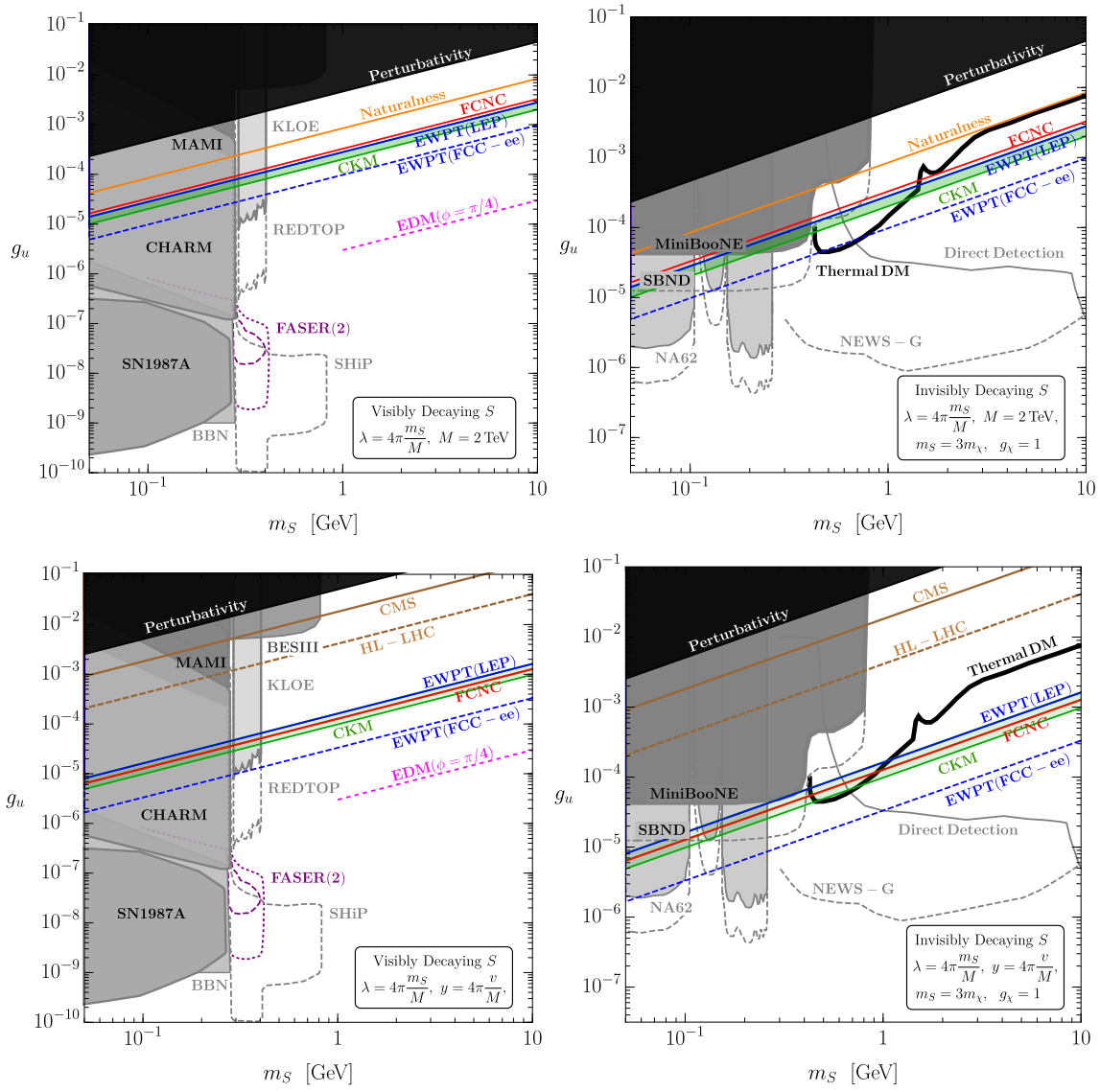

Figure 16: The up-specific scalar EFT parameter space shown in the $m_S - g_u$ plane. The left panels assume the scalar decays visibly to hadrons, while the right panels assume the scalar decays invisibly to dark matter with $g_\chi = 1$ and $m_S = 3m_\chi$. In the top panels, y is varied while the VLQ mass is fixed to $M = 2$ TeV and λ is chosen to saturate the naturalness condition (3.3.3). In the bottom panels, M is varied while both λ and y are chosen to saturate their naturalness bounds (3.3.3,3.3.4). In all panels we show several model-independent constraints from Ref. [64] on the EFT parameter space, which depend only on g_u and m_S. In addition, constraints from the VLQ model are shown under the stated assumptions for each plot, figure taken from Ref.[65]

3.3.9 Summary

Here we summarize the current bounds and future expected sensitivities in the VLQ completion of the light up-specfic scalar. As argued above in Sec. 3.3.2, for a light scalar satisfying naturalness conditions (3.3.3,3.3.4), we typically expect $\lambda \ll y$. In this situation, the strongest constraints on the UV completion pertain to the coupling y and the VLQ mass $m_{U'} \simeq M$. These limits are summarized in Figure 15, where we show the constraints from FCNCs in the neutral kaon system, CKM-top row unitarity, Z boson hadronic width, and direct searches at the LHC. The LHC constraint relies on QCD production and thus is not sensitive to the precise value of the coupling y, again provided that $\lambda \ll y$. The indirect bounds from FCNCs, CKM unitarity, and EWPT all probe similar regions of parameter space and are generally more stringent for lighter VLQs. As discussed in Sec. 3.3.4, the model can explain the $\sim 3\sigma$ discrepancy in the CKM top row unitarity determination for couplings $y \sim 0.1 - 1$ in the mass range 600 GeV $\lesssim M \lesssim$ 5 TeV, as indicated by the green band in Figure 15. This region can be probed further at the HL-LHC and definitively tested by a future FCC-ee measurement of R_ℓ.

The bounds on the UV completion shown in Figure 15 can also be interpreted within the up-specific scalar EFT mass – coupling parameter space. Several such interpretations are presented in Figure 16, which shows a variety of constraints in the $m_S - g_u$ plane. In particular, we show both the model-independent constraints relying only on g_u and m_S derived previously in Ref. [64] (see the next paragraph for details), along with the constraints depending on the VLQ UV completion. The left panels assume the scalar decays visibly to hadrons, while the right panels assume the scalar decays invisibly to dark matter with $g_\chi = 1$ and $m_S = 3m_\chi$. In the top panels, y is varied while the VLQ mass is fixed to $M = 2$ TeV and λ is chosen to saturate the naturalness condition (3.3.3). Therefore, the top panels always satisfy the direct constraints from the LHC on VLQs, but can only satisfy the naturalness conditions if the scalar is sufficiently weakly coupled. In contrast, in the bottom panels M is varied while both y and λ are chosen to saturate their naturalness bounds (3.3.3,3.3.4). With these assumptions, all parameters shown in the the bottom panels are natural, but LHC VLQ searches rule out low mass, strongly coupled scalars. Regions shown in black

correspond to nonpertubative values of the coupling, $y > 4\pi$. One observes that bounds from the VLQ completion uniquely probe certain regions of the light scalar parameter space. These bounds are therefore highly complementary to those obtained in the EFT analysis [64].

Finally, we provide a brief summary of the constraints on the low energy scalar EFT appearing in Figure 16; see Ref. [64] for more details. We first discuss the case of visible scalar decays (left panels). Scalars lighter than the di-pion threshold will decay radiatively to a pair of photons and tend to be long-lived for natural values of the coupling. This low mass region is tightly constrained by fixed target experiments (CHARM [77]), rare pion decays (MAMI [290]), Big Bang nucleosynthesis, and supernova data. For masses $m_S > 2m_\pi$, there are constraints from rare η (KLOE [37]) and η' (BESII [14]) decay searches, while future η decay searches at REDTOP [197, 192] will test a currently viable and natural region of parameter space. In addition, searches for long-lived scalars at FASER/FASER2 [247, 177] and the proposed SHiP experiment [27] can probe very feeble couplings. Finally, if there is a new $\mathcal{O}(1)$ CP-violating phase in the theory, the neutron EDM constraint discussed in Section 3.3.7 provides the strongest bound today for $m_S > 2m_\pi$.

For the case of invisible scalar decays to dark matter particles (right panels), searches for the rare kaon decay, $K \to \pi S, S \to$ invisible, at NA62 [144, 143] provide the best constraint at low masses, while substantial improvements are anticipated in the near future with the full NA62 dataset. The MiniBooNE beam dump dark matter search and a future beam dump run at SBND can provide powerful tests in the several hundred MeV mass range [19, 20, 340]. At larger masses of order GeV and above, direct detection experiments such as CRESST-III [10], DAMIC [18], XENON1T [41], PandaX [145], and in the future NEWS-G [45, 71], will provide the leading constraints in this simple hadrophilic dark matter model. Also shown in the right panels of Figure 16 are the parameters leading to the correct dark matter thermal relic abundance through freezeout of dark matter annihilation to hadrons. We observe that low-energy EFT probes as well as a number of measurements unique to the VLQ completion can provide complementary tests of the cosmologically motivated region of parameter space.

3.4 Scalar Doublet Completion

In this section we investigate a second renormalizable completion of the flavor-specific EFT involving an additional scalar electroweak doublet. After presenting the model, we discuss the expected radiative contributions to the couplings and the ensuing naturalness criteria. We then study the minimization of the potential, the passage to the physical basis, and the decays of the new scalar doublet states. A study of the phenomenology follows, including the predictions and constraints from electroweak precision tests, FCNCs, CP violation, and searches for the the new scalars at the LHC. Finally, we conclude this section with a summary of these bounds along with several interpretations in the low-energy scalar EFT parameter space.

3.4.1 Model

We consider a model with a singlet scalar S and a heavy scalar mediator with the same quantum numbers as the Higgs, $H' \sim (\mathbf{1}, \mathbf{2}, \frac{1}{2})$. The minimal Lagrangian is given by

$$\begin{aligned}\mathcal{L}_{\rm sd} = \mathcal{L}_{\rm SM} &+ \frac{1}{2}\partial_\mu S \partial^\mu S - \frac{1}{2} m_S^2 S^2 + (D_\mu H')^\dagger D^\mu H' - M^2 H'^\dagger H' \\ &- \left[y'^j_i \, \overline{Q}^i_L \, u_{Rj} \, H'_c + \kappa \, M \, S \, H^\dagger H' + \text{h.c.} \right] + \text{quartic scalar couplings}, \end{aligned} \tag{3.4.1}$$

where $i = 1, 2, 3$ is a generation index and M is the mass of the scalar doublet. To render κ dimensionless, the scalar triple coupling has been re-scaled with M. Integrating out the scalar doublet at tree-level, we obtain the leading effective interactions at dimension 4 and 5:

$$\mathcal{L} \supset |\kappa|^2 S^2 |H|^2 + \frac{\kappa \, y'^j_i}{M} S \, \overline{Q}^i_L \, u_{Rj} \, H_c + \text{h.c.} \tag{3.4.2}$$

The first term in (3.4.2) is the Higgs portal operator, which we will return to in the next subsection when we discuss the scalar potential. The second term in (3.4.2) gives rise to the scalar-quark coupling of interest. Thus, we can identify M with the new scale and $(c_S)^j_i = -\kappa \, y'^j_i$, respectively, in the effective operator (3.2.4). In the flavor basis in which the SM up quark Yukawa couplings are diagonal, the up-specific hypothesis corresponds to $y'^j_i \propto \delta_{i1}\delta^{j1}$.

Similar to the VLQ model in Eq. (3.3.1), the Lagrangian in Eq. (3.4.1) could be extended by additional renormalizable scalar potential terms involving S, H and/or H'. In the absence of fine-tuning, small but non-zero coefficients of these terms are induced radiatively, as will be discussed below. However, we will assume that they do not receive any tree-level contribution that is parametrically larger than these loop effects. We note that the technical naturalness of the couplings in (3.4.1) can be established with discrete symmetries, e.g. y' is a spurion that breaks a Z_2 under which S is odd.

3.4.2 Naturalness considerations

We now consider the implications of naturalness on the scalar potential, following the same philosophy and approach used for the VLQ model; see Sec. 3.3.2. Our aim is to estimate the expected radiative sizes of the various scalar interactions generated by the couplings of S and H to the heavy scalar doublet H' in (3.4.1). As in Sec. 3.3.2, the size of the loop corrections are estimated by including factors of $(16\pi^2)^{-1}$ for each loop and counting the pertinent coupling and scale factors, the latter of which are taken to be M.

For interactions of even or odd numbers of the scalar S one thus finds

$$\delta_{S^{2k}} \sim \frac{|\kappa|^{2k}}{16\pi^2} M^{4-2k}, \qquad \delta_{S^{2k+1}} \sim \frac{|\kappa|^{2k}\,\mathrm{Re}\{\kappa\,\mathrm{Tr}(y' y_u^\dagger)\}}{(16\pi^2)^2} M^{3-2k}, \tag{3.4.3}$$

from the one- and two-loop diagrams in Figure 17 (a) and (b), respectively. The case $k = 1$ corresponds to a correction to the mass parameter, m_S^2, given by $\delta m_S^2 \sim |\kappa|^2 M^2/16\pi^2$. Requiring δm_S^2 to be less than the physical mass m_S^2 leads to the bound

$$|\kappa| \lesssim 4\pi \frac{m_S}{M} \simeq (6 \times 10^{-3}) \left(\frac{m_S}{1\,\mathrm{GeV}}\right) \left(\frac{2\,\mathrm{TeV}}{M}\right). \tag{3.4.4}$$

This can be compared to the tree-level contribution from the Higgs portal operator, which arises from integrating out the heavy scalar doublet, Eq. (3.4.2). After electroweak symmetry breaking, this gives a correction to the scalar mass, $\delta m_S^2 \sim |\kappa|^2 v^2$, leading to the naturalness condition

$$|\kappa| \lesssim \frac{m_S}{v} \simeq (4 \times 10^{-3}) \left(\frac{m_S}{1\,\mathrm{GeV}}\right). \tag{3.4.5}$$

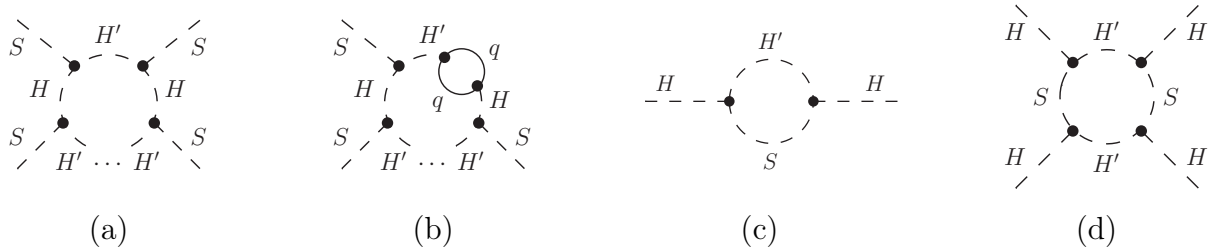

Figure 17: Loop-induced contributions to scalar self-couplings in the scalar doublet UV completion, figure taken from Ref.[65]

This condition is stronger than (3.4.4) unless $M \gtrsim 4\pi v$. We note that there is no analogous one-loop naturalness condition on the coupling y'. However, at two loops there is a contribution to the S mass depending on both κ and y', which precisely corresponds to the two-loop correction in the EFT that was mentioned in Eq. (3.2.8).

Similarly to the singlet scalar, the one-loop diagrams in Figure 17 (c) and (d) lead to corrections to the SM Higgs mass and self-coupling,

$$\delta\mu^2 \sim \frac{|\kappa|^2}{16\pi^2} M^2, \qquad\qquad \delta\lambda \sim \frac{|\kappa|^4}{16\pi^2}. \tag{3.4.6}$$

Demanding that $\delta\mu^2 \lesssim \mu^2 = m_h^2/2$ leads to the bound $\kappa \lesssim 2^{3/2}\pi\, m_h/M$, which is a weaker bound than (3.4.4) for $m_S \sim \mathcal{O}(\text{GeV})$.

In addition, (3.4.3) generates a number of scalar self-interaction terms that were not present in the original Lagrangian (3.4.1):

$$\mathcal{L} \supset -\delta_S S - a_3 S^3 - a_4 S^4, \tag{3.4.7}$$

$$\delta_S \sim \frac{\text{Re}\{\kappa\, \text{Tr}\big(y' y_u^\dagger\big)\}}{(16\pi^2)^2} M^3, \tag{3.4.8}$$

$$a_3 = \frac{|\kappa|^2\, \text{Re}\{\kappa\, \text{Tr}\big(y' y_u^\dagger\big)\}}{(16\pi^2)^2} M, \qquad a_4 = \frac{|\kappa|^4}{16\pi^2}. \tag{3.4.9}$$

The presence of the tadpole term δ_S causes S to develop a vev, v_S. The couplings a_3 and a_4 also have an influence on the value of v_S, but it is subdominant given the radiative estimates in Eq. (3.4.9) for values of κ that satisfy the naturalness bound in Eqs. (3.4.4,3.4.5).

In a similar fashion, there are radiatively generated $S|H|^2$, $S^2|H|^2$, $S|H'|^2$, $S^2|H'|^2$ and $|H'|^4$ terms, which can be neglected to first approximation in phenomenological applications. More relevant is the loop-induced mixing mass term

$$\mathcal{L} \supset \delta\mu'^2\, H'^\dagger H + \text{h.c.}, \qquad\qquad \delta\mu'^2 \sim \frac{\text{Tr}\big(y' y_u^\dagger\big)}{16\pi^2} M^2. \tag{3.4.10}$$

3.4.3 Mixing and mass eigenstates

3.4.3.1 Scalar potential

Including the leading radiatively induced tadpole and mass terms from the previous subsection, but neglecting the loop corrections to 3- and 4-point interactions, the scalar potential takes the form

$$V \supset -\mu^2(H^\dagger H)+\lambda(H^\dagger H)^2+\delta_S S+\frac{m_S^2}{2}S^2+M^2(H'^\dagger H')+\big[-\delta\mu'^2 H'^\dagger H+\kappa M(H'^\dagger H)S+\text{h.c.}\big] \tag{3.4.11}$$

In general, the neutral components of all three scalar fields produce vevs, for which we introduce the following notation: $\langle S\rangle = v_S$, $\langle H\rangle = (0, v_0/\sqrt{2})^\top$, $\langle H'\rangle = (0, v'/\sqrt{2})^\top$. Minimizing the scalar potential, we can solve for the vevs for S and H' to get

$$v' = \frac{v_0\,(\delta_S\,\kappa M + m_S^2\,\delta\mu'^{\,2})}{M^2\,(m_S^2-\kappa^2 v_0^2)}, \qquad\qquad v_S = -\frac{\delta_S M + \kappa\,\delta\mu'^{\,2} v_0^2}{M\,(m_S^2-\kappa^2 v_0^2)}. \tag{3.4.12}$$

One can reduce the number of independent parameters by using the radiative estimates $\kappa \lesssim 4\pi m_S/M$, $\delta_S \sim \frac{M^3\kappa}{(16\pi^2)^2}\,\text{Tr}(y' y_u)$, $\delta\mu'^2 \sim \frac{M^2}{16\pi^2}\,\text{Tr}(y' y_u)$ from section 3.4.2. The outcome depends on the relative sign between δ_S and $\delta\mu'^2$ (which in general is unknown since both terms can receive additional tree-level contributions). However, in the limit of large M the expressions simplify to

$$\left|\frac{v'}{v_0}\right| \sim \frac{y'\,y_u}{16\pi^2} \sim 10^{-7}, \qquad\qquad \left|\frac{v_S}{v_0}\right| \sim \frac{y'\,y_u M^2}{64\pi^3 m_S v_0} \sim 10^{-4} \tag{3.4.13}$$

where we have specialized to the up-specific scenario and assumed $y' \sim \mathcal{O}(1)$, $m_S \sim \mathcal{O}(\text{GeV})$ and $M > 1$ TeV for the numerical estimates.

Similar to the 2HDM, it is useful to rotate the doublets to the "Higgs basis", where only one of the doublets develops a vev, while the singlet remains unchanged, viz. :

$$\begin{pmatrix} \hat{H} \\ \hat{H}' \end{pmatrix} = \begin{pmatrix} \cos\beta & \sin\beta \\ -\sin\beta & \cos\beta \end{pmatrix} \begin{pmatrix} H \\ H' \end{pmatrix}, \tag{3.4.14}$$

where $\tan\beta \equiv v'/v_0$. The fields can be decomposed according to

$$\hat{H} = \begin{pmatrix} G^+ \\ \frac{1}{\sqrt{2}}(v + \phi_1 + iG^0) \end{pmatrix}, \qquad \hat{H}' = \begin{pmatrix} H^+ \\ \frac{1}{\sqrt{2}}(\phi_2 + iA^0) \end{pmatrix}, \qquad S = v_S + \phi_3, \tag{3.4.15}$$

where $v = 246$ GeV. The CP-even scalar fields ϕ_1, ϕ_2, ϕ_3 will mix with each other. Diagonalizing their 3×3 mass matrix $\mathcal{M}_\phi^2$ leads to three mass eigenstates h, h', s,

$$R^T \mathcal{M}_\phi^2 R = \text{diag}\{m_h^2, m_{h'}^2, m_s^2\}, \tag{3.4.16}$$

where h corresponds to the SM-like Higgs boson discovered at the LHC. For $\tan\beta \ll 1$, we can approximately write

$$\mathcal{M}_\phi^2 \simeq \begin{pmatrix} 2\lambda v^2 & -2\lambda v^2 \tan\beta & 2\kappa M v \tan\beta \\ -2\lambda v^2 \tan\beta & M^2 & \kappa M v \\ 2\kappa M v \tan\beta & \kappa M v & m_S^2 \end{pmatrix} \tag{3.4.17}$$

Since the off diagonal terms are small, the rotation matrix takes the approximate form

$$R \simeq \begin{pmatrix} 1 & \theta_{12} & \theta_{13} \\ -\theta_{12} & 1 & \theta_{23} \\ -\theta_{13} & -\theta_{23} & 1 \end{pmatrix}, \qquad \text{with} \qquad \begin{aligned} \theta_{12} &\simeq -2\lambda v^2 \tan\beta / M^2, \\ \theta_{13} &\simeq \kappa M \tan\beta / \lambda v, \\ \theta_{23} &\simeq -\kappa v / M, \end{aligned} \tag{3.4.18}$$

where we have kept the leading contributions to the mixing angles in the limit $m_S^2 \ll \lambda v^2 \ll M^2$ and $\tan\beta \ll 1$. Similarly, one finds that the CP-even scalar masses are approximately given by

$$m_h^2 \simeq 2\lambda v^2, \qquad m_{h'}^2 \simeq M^2, \qquad m_s^2 \simeq m_S^2 - \kappa^2 v^2. \tag{3.4.19}$$

Note that the second contribution to the light singlet squared mass eigenstate comes from the Higgs portal operator in Eq. (3.4.2). We will always impose $|\kappa| < m_S/v$ such that $m_s^2 > 0$ in what follows. The masses of A^0 and $H^\pm$ are given by

$$m_{A^0, H^\pm}^2 = \frac{M^2}{\cos^2\beta} \approx M^2. \tag{3.4.20}$$

3.4.3.2 Scalar decays

It is straightforward to work out the interaction Lagrangian in the mass basis. However, since the expectation is that the mixing between the scalar doublets is small, i.e., $\tan\beta \ll 1$, many of the phenomenological consequences can be extracted directly from our starting Lagrangian, Eq. (3.4.1). Here we consider the decays of the heavy scalar. While in general 2HDMs gauge interactions often mediate decays of a heavy scalar doublet component into a lighter doublet component and an electroweak boson (W, Z, h), such two-body decays are typically kinematically forbidden in our scenario due to the approximate mass degeneracy of the doublet components (see Eqs. (3.4.19,3.4.20)). The leading decays of the scalar doublet then arise from the new couplings y' and κ in Eq. (3.4.1). These lead to the partial widths

$$\Gamma(h' \to u\bar{u}) = \Gamma(A^0 \to u\bar{u}) = \Gamma(H^+ \to u\bar{d}) \simeq \frac{3y'^2 M}{16\pi}, \tag{3.4.21}$$

$$\Gamma(h' \to sh) = \Gamma(A^0 \to sZ) = \Gamma(H^+ \to sW^+) \simeq \frac{\kappa^2 M}{16\pi}. \tag{3.4.22}$$

These expressions are valid in the limit $\tan\beta \ll 1$ and $M \gg v$. In natural regions of parameter space, we expect that κ satisfies the conditions (3.4.4,3.4.5) and is typically much smaller than y', which is not subject to any analogous naturalness condition. In this case, the decays of the doublet to first-generation quarks will dominate. This will lead to a dijet resonance signature at the LHC, which we will discuss in more detail below.

For completeness, it should be noted that other decays are possible due to mixing of the scalar doublets. In particular, there can be decays of heavy scalar doublet components into pairs of lighter electroweak, Higgs, and singlet bosons. The corresponding partial widths scale as $\tan^2\beta$ and are thus expected to be highly suppressed in natural regions of parameter space. As for the light singlet scalar s, it will predominantly decay visibly to pairs of up quarks if there are no lighter hidden sector states. Alternatively, if the scalar couples strongly to light dark matter, it may decay via $s \to \chi\overline{\chi}$. See also the discussion in Sec. 3.3.3.

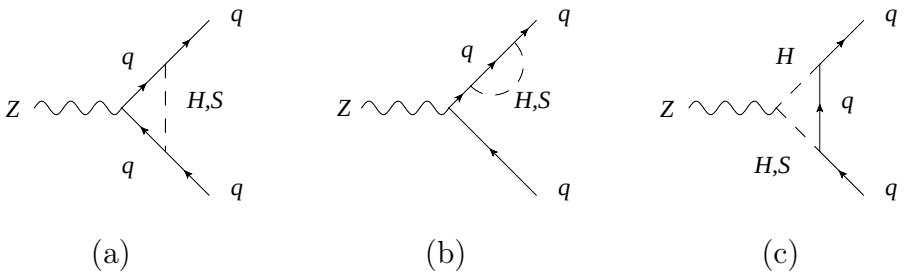

Figure 18: Loop diagrams contributing to the hadronic Z width in the scalar doublet UV completion, figure taken from Ref.[65].

3.4.4 Electroweak precision bounds

Similar to the VLQ model, the scalar doublet model modifies the partial width of the Z boson to hadrons. The leading correction is given by the loop diagrams in Figure 18. In the limit $M \equiv M_{H'} \gg v \gg m_S$, these yield the following shifts to the Z couplings:

$$\delta g_{uR} \approx g_{uR}^{\rm SM}\left\{\frac{y'^2\, m_Z^2}{48\pi^2\, M^2}\left[\frac{5}{6} - \ln\Big(-\frac{m_Z^2+i\epsilon}{M^2}\Big)\right]\right. \tag{3.4.23}$$
$$\left. + \frac{y'^2\kappa^2 v^2}{128\pi^2 M^2}\left[-\frac{1}{2} - \frac{9}{8s_W^2} + \Big(1-\frac{3}{4s_W^2}\Big)\ln\Big(-\frac{m_Z^2+i\epsilon}{M^2}\Big) + \ln\frac{M^2}{m_S^2}\right]\right\},$$
$$\delta g_{uL} \approx g_{uL}^{\rm SM}\left\{\frac{y'^2\, m_Z^2}{(18-24s_W^2)\pi^2\, M^2}\left[\frac{1}{8} - \frac{s_W^2}{3} + s_W^2\ln\Big(-\frac{m_Z^2+i\epsilon}{M^2}\Big)\right]\right. \tag{3.4.24}$$
$$\left. + \frac{y'^2\kappa^2 v^2}{128\pi^2 M^2}\left[-\frac{6-2s_W^2}{3-4s_W^2} - \frac{4s_W^2}{3-4s_W^2}\ln\Big(-\frac{m_Z^2+i\epsilon}{M^2}\Big) + \ln\frac{M^2}{m_S^2}\right]\right\},$$
$$\delta g_{dL} \approx g_{dL}^{\rm SM}\,\frac{y'^2\, m_Z^2}{(18-12s_W^2)\pi^2\, M^2}\left[\frac{1}{8} + \frac{s_W^2}{12} - s_W^2\ln\Big(-\frac{m_Z^2+i\epsilon}{M^2}\Big)\right]. \tag{3.4.25}$$

The second lines in (3.4.23) and (3.4.24) are additionally suppressed by κ^2 but they are enhanced by the logarithm $\ln M^2/m_S^2$.

Plugging Eqs. (3.4.23,3.4.24,3.4.25) into Eq. (3.3.23), we obtain the correction to the Z boson hadronic-to-leptonic branching ratio R_ℓ. For $M = 1\,\text{TeV}$, $m_S = 1\,\text{GeV}$ and $y' = \kappa = \sqrt{4\pi}$ one finds that R_ℓ is shifted by 0.83, which is excluded by current data, $R_\ell^{\rm exp} - R_\ell^{\rm SM} = 0.034 \pm 0.025$ [332]. For $y' = \kappa = 1$, the shift is instead 5.5×10^{-3}, which is currently not excluded and can be probed only marginally by FCC-ee, with an expected 1σ precision of $\delta R_\ell^{\rm exp.} = 0.001$ [92].

3.4.5 FCNCs

Similar to the FCNC we discussed in the VLQ section, there is a one loop box diagram resulting from H' and up quark exchange, which leads to an effective operator with four Q_L fields given by

$$\mathcal{L} \supset -\frac{(y'y'^{\dagger})^j_i (y'y'^{\dagger})^l_k}{128\pi^2 M^2} [\overline{Q}^i \gamma^\mu P_L Q_j][\overline{Q}^k \gamma^\mu P_L Q_l]. \tag{3.4.26}$$

With the up-specfic hypothesis and moving to the physical basis, we obtain a contribution to neutral Kaon mixing, described by the operator in Eq. (3.2.9) with Wilson coefficient $C^{ds} = -(y')^4 |V^*_{ud} V_{us}|^2/(128\pi^2 M^2)$. Applying the bound $\mathrm{Re}[C^{ds}] \lesssim (10^3\,\mathrm{TeV})^{-2}$ [95], we obtain the constraint

$$y' \lesssim 0.6 \left(\frac{M}{2\,\mathrm{TeV}}\right)^{1/2}, \tag{3.4.27}$$

similar to Eq. (3.3.22) for the VLQ model.

3.4.6 CP violation

In the scalar doublet completion, the basis independent CP-violating phase is

$$\phi_{\mathrm{CP}} = \arg\left(y_u y'^* \kappa\right) \tag{3.4.28}$$

Separate rephasings of $u_{L,R}$ and H' leave this quantity invariant. If ϕ_{CP} is nonvanishing, a nonzero neutron EDM will develop. This occurs in much the same way as in the VLQ completion, namely through a CP-violating four up quark operator mediated by S exchange. This operator is defined in Eq. (3.3.28). In this model, the corresponding Wilson coefficient is

$$C'_u \simeq -\frac{y'^2 \kappa^2 v^2}{4M^2 m_S^2} \sin 2\phi_{\mathrm{CP}}. \tag{3.4.29}$$

Using Eqs. (3.3.30,3.4.29) we can express this as a limit on the effective coupling of the scalar to up quarks ($g_u \simeq y'\kappa v/\sqrt{2}M$). We obtain the same bound as in the VLQ model given in Eq. (3.3.31).

3.4.7 Collider phenomenology

We next discuss signatures of the heavy scalar doublet at the LHC. Motivated by the naturalness conditions (3.4.4,3.4.5), we typically expect $\kappa \ll y$, in which case the scalar doublet will decay to first-generation quarks through the y' coupling; see Eqs. (3.4.21) for the partial decay widths. This makes it challenging to probe the scalar doublet through its electroweak pair production process at the LHC, given the low production rate and large QCD backgrounds. On the other hand, if y' is large enough the heavy scalar doublet can be produced singly in quark-antiquark annihilation and decays into a di-jet final state. Since all physical eigenstates of the heavy doublet have masses that are very close to each other, $m_{h'} \approx m_{A^0,H^\pm} \approx M$, and they all decay dominantly into quarks, they would manifest as a single narrow[2] di-jet resonance. The influence of the mixing angle β is very small and can be safely neglected in this context.

Both ATLAS and CMS have conducted searches for di-jet resonances at $\sqrt{s} = 13$ TeV and presented bounds in terms of several representative models [4, 321, 324]. We use the published bounds for hadro-philic Z' models to derive corresponding limits for the heavy scalar doublet. For this purpose, we have computed fiducial cross-sections for both the Z' model and the scalar doublet model with CalcHEP 3.4.6 [75], for a grid of different resonance masses ranging from 100 GeV to 7 TeV. Since both cases are $q\bar{q}$ initiated, one may expect that the K-factor from QCD corrections is similar for both models and cancels when taking the ratio of the cross-sections. We then used these cross-section ratios to re-scale the coupling limits for the Z' model reported in Refs. [4, 321, 324]. For the low-mass region, below 500 GeV, a boosted di-jet search by CMS can be utilized [323]. Furthermore, the HL-LHC will be able to extend the reach to di-jet resonances, particularly in the high mass region. We have translated one such HL-LHC projection from ATLAS to the scalar doublet model [1]. This translation depends on the K-factor for $pp \to H'$, which is currently unknown. For simplicity, we have used $K = 1$, which is supported by the fact that the closely related Drell-Yan (see e.g. Ref. [99]) and scalar diquark production [221] processes have small K-factors of about 1.2. The resulting limits and projections on the Yukawa coupling y', as a function

[2]Here "narrow" means that the physical decay width of all heavy scalars is smaller than the experimental resolution.

of the mass M, are shown in Figure 19.

Let us also make a few comments about the scenario that $y' < \kappa$. In this case the scalar doublet decays predominantly to an electroweak or Higgs boson and s, see Eq. (3.4.22). Furthermore, the condition $y' < \kappa$ combined with the naturalness constraints on κ suggest that y' is relatively small in this scenario, such that the single production process $q\bar{q} \to H'$ is suppressed. In this case heavy scalar pair production, mediated by electroweak gauge interactions, may be more promising. $H^\pm h'$ and $H^\pm A^0$ production, followed by the decays $H^\pm \to sW^\pm$, $h' \to sh$ and $A^0 \to sZ$, leads to final states with several leptons and/or a $b\bar{b}$ pair. If s decays into light dark matter particles, these signatures are very similar to gaugino pair production processes in the MSSM. Thus we expect that heavy scalar masses $M \lesssim \mathcal{O}(\text{TeV})$ are excluded by $\tilde{\chi}_1^\pm \tilde{\chi}_2^0$ searches at ATLAS and CMS [**?**, 136, 326], but the details of this bound depend on the different production cross-sections in the MSSM and our scalar doublet model. If instead s decays visibly into hadrons, the signature is very similar to the VLQ searches discussed in section 3.3.8, with the main difference that the heavy scalar pair production is an electroweak rather than a strong process. As a result, we expect somewhat weaker limits than those reported for VLQs in section 3.3.8.

Finally, as in the VLQ model, the singlet scalar s can be produced directly at the LHC and show up as either a di-jet resonance if it decays visibly or as a mono-jet if it decays invisibly. In both cases the limit on the effective coupling g_u is rather weak. For further details, see the earlier discussion in Sec. 3.3.8.

3.4.8 Summary

Here we summarize the experimental constraints and prospects in the scalar doublet completion of the light up-specfic scalar. As discussed earlier in Sec. 3.3.2, for a light scalar satisfying naturalness conditions (3.4.4,3.4.5), we typically expect $\kappa \ll y'$. In this case, the strongest bounds on the UV completion are on the coupling y' and the scalar doublet mass M. These limits are compiled in Figure 19, where we show the constraints from FCNCs in the neutral kaon system and direct searches for dijet resonances at the LHC. We also display the projected reach of precision measurments of the Z boson hadronic width at FCC-ee and

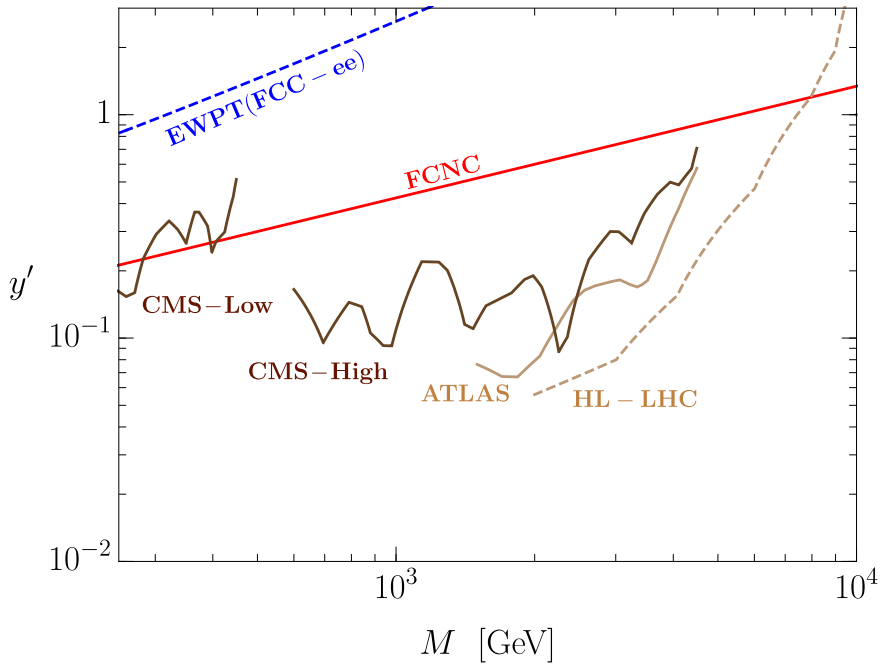

Figure 19: Constraints on scalar doublet completion in the $M - y'$ plane. Shown are current bounds from neutral kaon mixing (red solid line) and dijet searches search at the LHC (brown solid lines), including high mass dijet searches ("ATLAS" and "CMS-High") [4, 321, 324] and a low mass boosted dijet search ("CMS-Low") [323]. The expected future reach from precision measurements of R_ℓ at FCC-ee (blue dashed line) and high mass dijet searches at the HL-LHC [1] (brown dashed line) are also indicated. The trilinear scalar coupling κ is chosen to saturate its naturalness condition, which is the minimum of either Eqs. (3.4.4) and (3.4.5), while the physical singlet scalar mass is set $m_s = 1$ GeV, figure taken from Ref.[65]

high-mass dijet searches at the HL-LHC.

As was done for the VLQ completion, we interpret the bounds on the scalar doublet completion within the up-specific scalar EFT mass–coupling parameter space. Two interpretations are presented in Figure 20, where a number of bounds and projections are displayed in the m_S–g_u plane. In particular, we show the model-independent constraints relying only on g_u and m_S derived previously in Ref. [64]; we refer the reader to Sec. 3.3.9 for further details. Furthermore, we display the additional constraints that arise in the scalar doublet completion. The left panel assumes the scalar decays visibly to hadrons, while the right panel assumes the scalar decays invisibly to dark matter with $g_\chi = 1$ and $m_S = 3m_\chi$. In both plots, y' is varied while the scalar doublet mass is fixed to $M = 3$ TeV and κ is chosen to saturate the naturalness condition (3.4.5). We see that the bounds from the scalar doublet completion cover interesting regions of the light scalar parameter space and as such complement those obtained by only considering up-specific EFT [64].

3.5 Conclusions

In this work we have studied two simple renormalizable completions of flavor-specific scalar mediators. While for concreteness we have focused on the up quark-specific coupling, similar models can straightforwardly be constructed for other flavor-specific couplings. In the first completion, a new VLQ mediates interactions between the light quarks, Higgs, and scalar singlet. In the second model, the interactions occur via a second scalar electroweak doublet. In both models we have studied the implications of naturalness on the size of the scalar potential and other couplings in the theory. A sizeable effective singlet–Higgs–quark coupling implies that the mediators (VLQ or scalar doublet) cannot be arbitrarily heavy, which opens new opportunities for experimental tests. We have derived bounds from the hadronic decay width of the Z boson, FCNCs in the neutral kaon system, the neutron EDM, deviations in CKM unitarity, and direct searches for the new SM-charged states at the LHC. These models can be further tested at the HL-LHC and at future colliders. The bounds we derived can also be interpreted within the low energy flavor-specific EFT and are found

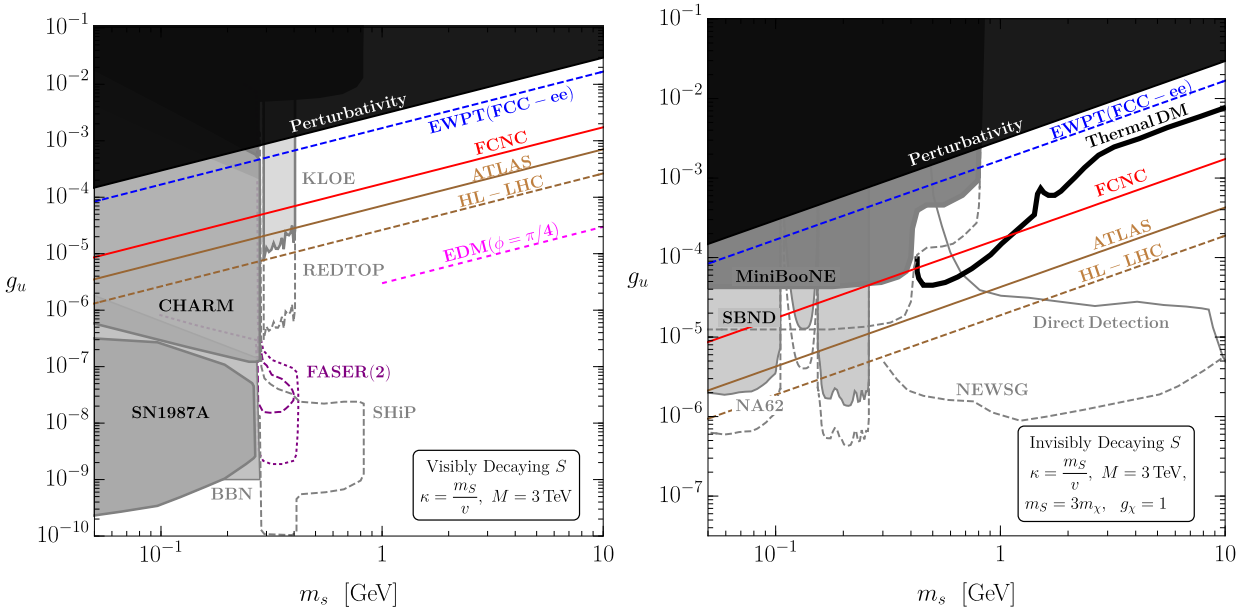

Figure 20: The up-specific scalar EFT parameter space shown in the $m_s - g_u$ plane. The left panel assumes the scalar decays visibly to hadrons, while the right panels assume the scalar decays invisibly to dark matter with $g_\chi = 1$ and $m_s = 3m_\chi$. In both panels the coupling y' is varied while the scalar doublet mass is fixed to $M = 3$ TeV and κ is chosen to saturate the naturalness condition (3.4.5). In both panels we show several model-independent constraints from Ref. [64] on the EFT parameter space, which depend only on g_u and m_s. In addition, constraints from the scalar doublet completion are shown under the stated assumptions for each plot, figure taken from Ref.[65]

to probe new regions in the scalar mass – effective coupling plane. This underscores the general expectation that renormalizable completions can provide complementary constraints and new experimental opportunities to probe flavor-specific scalars.

Looking ahead, there is significant scope for further phenomenological exploration within the flavor-specific framework. Investigations of other flavor-specifc couplings beyond the up quark-specific one studied here and in [64] and the muon-specific one studied in [63] would be valuable and are likely to present new opportunities for model building (e.g., as a mediator to dark matter) and novel experimental prospects. In addition, it would be interesting to consider the UV origin of the flavor specific hypothesis, which may ultimately be tied to the dynamics underlying the SM flavor structure.

4.0 Dynamics of Dark Matter Misalignment Through the Higgs Portal

4.1 Introduction

Understanding the nature of the cosmic dark matter (DM), which constitutes roughly a quarter of the energy density in the universe [17], is among the most pressing problems in particle physics and cosmology today. Despite its clear influence on a host of astrophysical and cosmological phenomena, the most basic properties of DM remain mysterious, including it fundamental dynamics (spin, mass, interactions, etc.) as well as its origin during the earliest epochs of the universe.

One particularly compelling idea is that DM is an ultra-light, feebly-coupled scalar field ϕ [39]. As is well-known, such scalar field DM is generically created in the early universe through the misalignment mechanism [300, 9, 158]. The scalar field starts from some initial field value at the end of inflation that is misaligned with respect to its eventual potential minimum (i.e., its vacuum expectation value (VEV)). In the early stages of the radiation-dominated era, the scalar field is held up by Hubble friction and, notably, does not experience any additional dynamical misalignment during this epoch. As the universe expands, the scalar field eventually begins oscillating once the Hubble expansion rate drops below its mass. The oscillating scalar field subsequently forms a pressureless, non-relativistic fluid and thus has the desired bulk properties of cold DM. Thus, in this *standard misalignment* scenario, the DM density today is controlled by the initial value ϕ_i and does not depend at all on the coupling of ϕ to the Standard Model (SM).

A simple model realization of ultra-light bosonic DM consists of a real singlet scalar field coupled to the SM through the super-renormalizable Higgs portal, $A\phi H^\dagger H$, as first proposed more than a decade ago by Piazza and Pospelov [299]. This model is attractive from several perspectives. First, it is among the most minimal, UV-complete extensions of the SM, with the cosmology (up to initial conditions) and phenomenology determined by two parameters, namely, the mass of the scalar, m_ϕ and its Higgs portal coupling A. Second, the feebleness of this coupling allows the light scalar mass (and scalar potential) to be stable

against radiative corrections. Furthermore, the model has a distinctive phenomenology, with a variety of existing probes from both terrestrial experiments and astrophysical observations, and has served as a well-motivated benchmark model for several proposed ultralight scalar DM detection concepts; see, e.g., Refs. [210, 49, 39].

On the other hand, the cosmology of this simple model remains relatively underexplored, and it is the primary aim of this work to fill that gap. As our study will make clear, the cosmology of the scalar field in the Higgs portal model is not generally encapsulated by the standard misalignment scenario discussed above. In contrast to the standard misalignment scenario, the scalar field undergoes a nontrivial evolution during the radiation era by which new sources of misalignment are dynamically generated, impacting the scalar relic abundance in an essential way. In particular, we will investigate two distinct dynamical misalignment mechanisms that are inherent in the Higgs portal model: (i) *thermal misalignment*, and (ii) *VEV misalignment*.

The thermal misalignment mechanism was recently explored in detail in Ref. [66] (see also Refs. [126, 113] for related work) in the context of simple Yukawa-type theory, but the essential aspects of the mechanism carry over to the Higgs portal model. In the earliest stages of the radiation era, the scalar field responds to a finite-temperature correction to its effective potential, associated with the free energy density of the Higgs degrees of freedom in the thermal bath to which the scalar is feebly coupled. This tends to drive the scalar field toward its high-temperature minimum at large field values, thus generating misalignment. As we will demonstrate below, thermal misalignment dominates for scalar masses larger than a few meV. Furthermore, provided the initial field value ϕ_i at the end of inflation is small (in magnitude) in comparison to the displacement generated by thermal misalignment, the late-time scalar oscillation amplitude and associated relic density are insensitive to initial conditions, instead being tightly controlled by the DM mass and Higgs portal coupling. Thus, a sharp prediction can be made for the model parameters (scalar mass and Higgs portal coupling) yielding the observed relic abundance through thermal misalignment, providing a cosmologically motivated target that can be compared with experimental tests.

VEV misalignment is a second source of dynamical misalignment which is built in to the Higgs portal model. It arises as a consequence of the electroweak phase transition (EWPT),

during which the Higgs field quickly turns on as electroweak symmetry is broken and induces a rapid shift in the ϕ potential minimum towards its zero-temperature VEV. As we will see, VEV misalignment dominates for scalar masses below about 10^{-5} eV. For this region of parameter space, we will find that the scalar oscillation amplitude and corresponding relic abundance sensitively depends on the initial field value ϕ_i, in particular, whether the scalar field is initially close to its zero temperature VEV or far away from it.

In the intermediate scalar mass range, an intricate interplay between thermal misalignment and VEV misalignment leads to a novel forced resonance effect, with the scalar oscillation amplitude experiencing either an enhancement or suppression following the EWPT depending on the ϕ mass. This manifests as a striking series of peaks and valleys in the relic density target line as the scalar mass is varied.

Our main results are presented in Figure 21 as contours in the mass-coupling parameter space yielding the observed DM relic abundance, providing cosmologically motivated targets for experiments searching for ultralight scalar DM. In view of this, we also compile the existing bounds and sensitivity projections for a variety of experimental and astrophysical probes of the model, including equivalence principle and inverse square law tests, stellar cooling, resonant molecular absorption, and observations of extra-galactic background light and diffuse X-ray backgrounds. Still, much of the parameter space remains unexplored, and we hope our results will stimulate new innovative experimental concepts for ultra-light DM searches.

It is important to note that the potential impact of the finite-temperature effects and the EWPT on the scalar field evolution and relic abundance were discussed in the original study of Ref. [299]. The effect of the EWPT on scalar field misalignment in Higgs portal models was also investigated in Ref. [44], though thermal effects were not considered in that work. We believe our study elucidates the dynamics of the scalar field during the radiation era by including both the thermal misalignment and VEV misalignment effects, discerning the regions of parameter space where each is relevant, and exploring the role of and sensitivity to initial conditions. In particular, we have carefully derived estimates of the scalar relic density, both by numerically solving its equation of motion during the radiation era through the EWPT and by developing various approximate solutions as appropriate for the region of

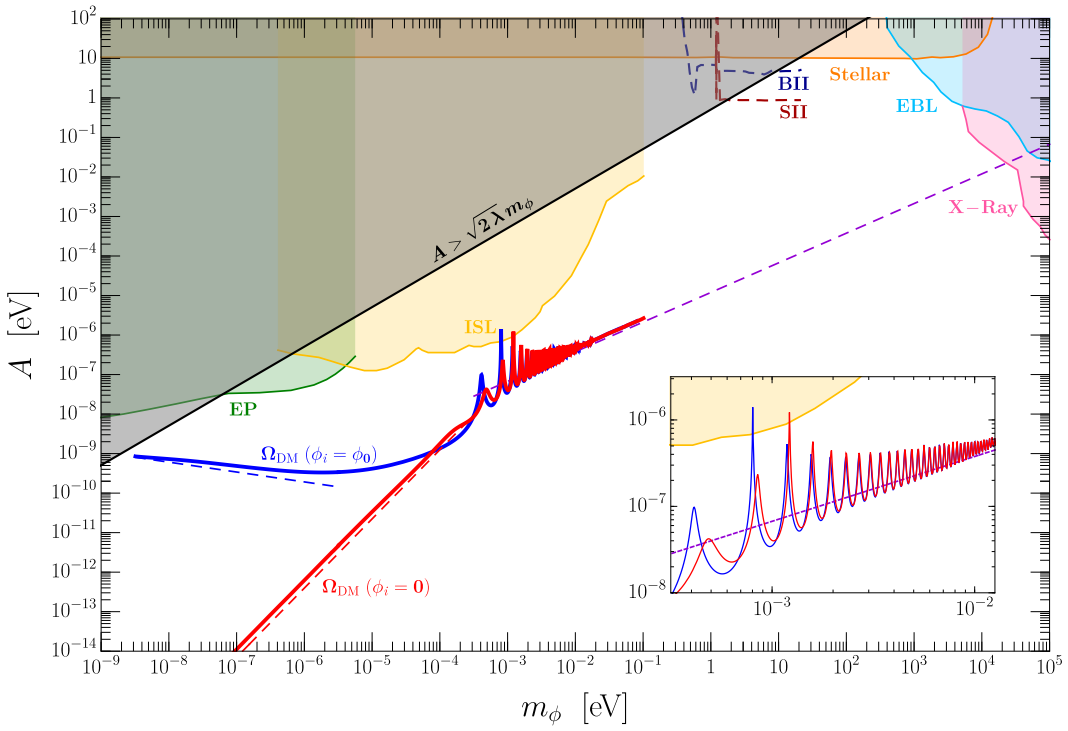

Figure 21: DM relic abundance predictions along with constraints and projections displayed in the $m_\phi - A$ (mass-coupling) plane. Parameter choices leading to the observed relic abundance, $\Omega_{\phi,0} = \Omega_{\rm DM} = 0.26$, computed by numerically evolving Eq. (4.3.14) and using Eq. (4.3.15), are shown for two choices of initial conditions: $\phi_i = \phi_0$ (blue solid) and $\phi_i = 0$ (red solid). Colored regions show a variety of current constraints, while the black region is theoretically unviable. Figure taken from [67].

parameter space, cosmological epoch, and initial conditions under consideration. Both our numerical and analytical results are shown in Figure 21 and are in good agreement.

4.2 Super-Renormalizable Higgs Portal Model

We consider the model of Ref. [299] which contains a real singlet scalar field ϕ that couples to the SM via the super-renormalizable Higgs portal. The scalar potential to be

considered is

$$V = -\mu^2 H^\dagger H + \lambda (H^\dagger H)^2 + \frac{1}{2} m_\phi^2 \phi^2 + A \phi H^\dagger H \,, \tag{4.2.1}$$

where the first two terms constitute the usual SM Higgs potential, m_ϕ is the scalar mass parameter, and A is a dimensionful coupling of the scalar to the Higgs. Note that we have omitted a potential linear term in ϕ, which can always be achieved by performing a field redefinition.

We will mainly be interested in feeble couplings such that $A \ll m_\phi$. This implies that the light scalar mass is technically natural, with loops generating $\delta m_\phi^2 \sim A^2/(16\pi^2) \log \Lambda_{\rm UV} \ll m_\phi$. This is one of the attractive features of the super-renormalizable portal. Furthermore, radiatively generated nonlinear potential terms such as ϕ^3 and ϕ^4 are also small and will be neglected for the remainder of this work.

4.2.1 Zero temperature vacuum and spectrum

We first consider the theory at zero temperature. The background Higgs field is parameterized as $H^T = (0, \frac{1}{\sqrt{2}} h)$. The potential then reads

$$V_0(\phi, h) = -\frac{1}{2} \mu^2 h^2 + \frac{1}{4} \lambda h^4 + \frac{1}{2} m_\phi^2 \phi^2 + \frac{1}{2} A \phi h^2 \,. \tag{4.2.2}$$

Minimizing the potential, we obtain the vacuum expectation values (VEVs) for the scalar fields $\langle h \rangle = v$ and $\langle \phi \rangle = \phi_0$, given by

$$v^2 = \frac{\mu^2}{\lambda - A^2/2m_\phi^2} \,, \qquad \phi_0 = -\frac{A v^2}{2 m_\phi^2} \,, \tag{4.2.3}$$

with $v = 246$ GeV. It can be seen from Eq. (4.2.3) that a viable electroweak vacuum is obtained only for

$$\frac{A^2}{2 \lambda m_\phi^2} < 1 \,. \tag{4.2.4}$$

To study the spectrum at zero temperature, we replace $h \to v + \tilde{h}$ and $\phi \to \phi_0 + \tilde{\phi}$ in the potential, Eq. (4.2.2), where $\tilde{h}$ and $\tilde{\phi}$ represent the fluctuations about the vacuum.

Expanding the potential to quadratic order, we find that there is mass mixing between the scalars,

$$V \supset \frac{1}{2}(2\lambda v^2)\tilde{h}^2 + \frac{1}{2}m_\phi^2\,\tilde{\phi}^2 + A\,v\,\tilde{h}\,\tilde{\phi}\,. \tag{4.2.5}$$

We move to the physical basis by performing a rotation,

$$\begin{bmatrix} \tilde{h} \\ \tilde{\phi} \end{bmatrix} = \begin{bmatrix} \cos\theta & \sin\theta \\ -\sin\theta & \cos\theta \end{bmatrix} \begin{bmatrix} h \\ \phi \end{bmatrix}, \tag{4.2.6}$$

where, in an abuse of notation, h and ϕ represent the physical scalar fluctuations in the mass basis. The mixing angle θ in (4.2.6) is given by

$$\tan 2\theta = \frac{2Av}{2\lambda v^2 - m_\phi^2}\,. \tag{4.2.7}$$

The mass eigenvalues are

$$M_{h,\phi}^2 = \frac{1}{2}\left[2\lambda v^2 + m_\phi^2 \pm \sqrt{(2\lambda v^2 - m_\phi^2)^2 + 4A^2v^2}\right]\,. \tag{4.2.8}$$

As we will always be working in the regime $A^2 \leq 2\lambda m_\phi^2 \ll \lambda v^2$, the approximate expressions for the mixing angle and mass eigenvalues are

$$\theta \sim \frac{A}{2\lambda v} \simeq \frac{Av}{M_h^2}\,, \qquad M_h^2 \simeq 2\lambda v^2 + \frac{A^2}{2\lambda}\,, \qquad M_\phi^2 \simeq m_\phi^2 - \frac{A^2}{2\lambda}\,. \tag{4.2.9}$$

Note that the correction to the Higgs mass is always negligible and thus $M_h^2 \simeq 2\lambda v^2 \equiv m_h^2 = (125\ \text{GeV})^2$ as in the SM. Furthermore, we will find that in most of the cosmologically interesting parameter space, $A \ll m_\phi$, such that $M_\phi^2 \simeq m_\phi^2$. Note that very close to the boundary where the electroweak vacuum is viable (see Eq. (4.2.4)), $A^2/(2\lambda m_\phi^2) \lesssim 1$, and only in this very small region of parameter space is the physical scalar mass is substantially modified from m_ϕ^2.

The electroweak vacuum condition, Eq. (4.2.4) (gray shaded region in Figure 21), could be relaxed in a scenario with additional scalar potential terms. However, in this case the light scalar mass M_ϕ would require fine-tuning, as can be seen from Eq. (4.2.9) above. In this work, we will restrict our investigation of the scalar cosmology to parameters satisfying Eq. (4.2.4).

4.3 Cosmology

In this section, we describe the cosmological evolution of the scalar ϕ before and through the EWPT until it oscillates about its late time potential minimum and behaves as DM. We will assume that the universe reheats to a temperature much larger than the electroweak scale ($T_{\rm RH} \gg v$). We begin by describing the contribution to the scalar potential from the thermal bath. We will then describe the EWPT experienced by the Higgs, which can significantly impact the dynamics of ϕ in certain regions of parameter space. We describe the sources of misalignment and detail the initial conditions assumed for the scalar at the end of inflation. We then describe the final equation of motion that governs the scalar evolution and numerically estimate the relic ϕ abundance. We also derive approximate analytic estimates of the relic density and compare them with our numerical results.

4.3.1 Effective Potential

Our analysis begins in the radiation-dominated era during which the Hubble parameter is given by $H = 1/2t = \gamma T^2/M_{\rm pl}$, where t is the cosmic time, T is the temperature of the SM thermal bath, $M_{\rm pl} = 2.43 \times 10^{18}$ GeV is the reduced Planck mass, and $\gamma(T) \equiv \sqrt{\pi^2 g_*(T)/90}$ with $g_{*(S)}$ the effective number of relativistic (entropy) degrees of freedom. During this epoch, the effective potential of the scalar fields is given by

$$V_{\rm eff}(\phi, h, T) = V_0(\phi, h) + V_{\rm CW}(\phi, h) + V_T(\phi, h, T)\,. \tag{4.3.1}$$

The first piece is the tree-level potential given in Eq. (4.2.1). The second term represents the zero-temperature correction to the effective potential, i.e., the Coleman-Weinberg potential [135], which we will comment on shortly. The final term in (4.3.1) is the finite-temperature correction associated with the thermal free energy density of the SM particles in the plasma [161, 346]. The expression for the finite-temperature potential in Landau

gauge is [302]

$$V_T(\phi,h,T) \supset \frac{1}{2\pi^2}T^4 J_B\left[\frac{m_h^2(\phi,h,T)}{T^2}\right] + \frac{3}{2\pi^2}T^4 J_B\left[\frac{m_\chi^2(\phi,h,T)}{T^2}\right] + \frac{4}{2\pi^2}T^4 J_B\left[\frac{m_{W_T}^2(h)}{T^2}\right] + \frac{2}{2\pi^2}T^4 J_B\left[\frac{m_{Z_T}^2(h)}{T^2}\right] + \frac{2}{2\pi^2}T^4 J_B\left[\frac{m_{W_L}^2(h,T)}{T^2}\right] + \frac{1}{2\pi^2}T^4 J_B\left[\frac{m_{Z_L}^2(h,T)}{T^2}\right] + \frac{1}{2\pi^2}T^4 J_B\left[\frac{m_{A_L}^2(h,T)}{T^2}\right] - \frac{12}{2\pi^2}T^4 J_F\left[\frac{m_t^2(h)}{T^2}\right], \tag{4.3.2}$$

where the $J_{B,F}$ functions are defined as

$$J_{B,F}(w^2) = \int_0^\infty dx\, x^2\, \log\left[1 \mp \exp\left(-\sqrt{x^2+w^2}\right)\right]. \tag{4.3.3}$$

The thermal squared masses, $m_i^2(\phi,h,T)$, entering in the arguments of these functions depend in general on both the background field fields ϕ and h and the temperature. To obtain a reliable perturbative expansion near the EWPT, we follow the prescription for daisy resummation of Ref. [298], writing the thermal squared mass as sum of a tree-level term field-dependent term, $m_{0,i}^2(\phi,h)$, and a temperature-dependent self-energy term $\Pi_i(T)$,

$$m_i^2(\phi,h,T) = m_{0,i}^2(\phi,h) + \Pi_i(T)\,. \tag{4.3.4}$$

In particular, for the self-energies we retain the leading contributions in the high temperature expansion. The subscripts $(h,\chi,W_T,Z_T,W_L,Z_L,A_L,t)$ in these functions refer to the Higgs, Nambu-Goldstones, transverse and longitudinal gauge bosons, and top quark. The prefactors in front of the $J_{B,F}$ functions account for the degrees of freedom of the corresponding field.

It is important to emphasize that ϕ itself is not in thermal equilibrium for the feeble values of Higgs portal coupling A considered in this work, and as such there is no term associated with ϕ in the finite temperature potential (4.3.2). Rather, the finite temperature potential is due to the SM degrees of freedom in thermal equilibrium. It is a function of the background value for ϕ via the dependence of the squared mass parameters on ϕ.

For simplicity, we will neglect the Coleman-Weinberg (CW) contribution $V_{\rm CW}(\phi,h)$ to the effective potential (4.3.1) in our numerical analysis below. The correction to the ϕ potential from $V_{\rm CW}$ is negligible in the viable region of parameter space (Eq. (4.2.4)) due to the feeble coupling A, as already alluded to at the beginning of Sec. 6.2. Furthermore, as we will see below, for large scalar masses the misalignment is generated at high temperatures (thermal

misalignment) where $V_T(\phi, h, T)$ dominates and $V_{\rm CW}$ is negligible. For lower scalar masses, the misalignment is a result of the induced scalar VEV triggered by the EWPT. Even in this case, $V_{\rm CW}$ does not qualitatively alter the behavior of the scalar potential and the nature of the EWPT, and will only lead to relatively small numerical differences in our results.

Note that Eq. (4.3.2) is appropriate for temperatures above the QCD phase transition. For lower temperatures, an alternative description in terms of light hadronic states would be required. However, we will see the onset of scalar oscillations in the parameter space we consider occurs at temperatures well above the QCD scale, so that a description at lower temperatures is not required to calculate the relic abundance. For similar reasons, the quarks lighter than the top quark as well as leptons will not influence our results.

We will find it convenient to work with the following set of dimensionless parameters:

$$y \equiv \frac{T}{\mu}\,, \qquad \hat{\phi} \equiv \frac{\phi}{M_{\rm pl}}\,, \qquad \hat{h} \equiv \frac{h}{\mu}\,, \qquad \kappa \equiv \frac{m_\phi M_{\rm pl}}{\mu^2}\,, \qquad \beta \equiv \frac{A M_{\rm pl}}{\mu^2}\,. \tag{4.3.5}$$

In particular, the parameter y is a proxy for the temperature, with $y \sim \mathcal{O}(1)$ for temperatures near the electroweak scale. Furthermore, $\hat{\phi}$ and $\hat{h}$ are simply the ratios of the field variables to their respective characteristic scales. Finally, the scalar mass m_ϕ and Higgs portal coupling A are expressed in terms of the dimensionless variables κ and β, respectively.

Combining the V_0 and V_1^T in Eqs. (4.2.1,4.3.2) and writing the effective potential in terms of dimensionless quantities ($\hat{V}_{\rm eff} = V_{\rm eff}/\mu^4$), we obtain

$$\begin{aligned}\hat{V}_{\rm eff} = &-\frac{1}{2}\hat{h}^2(1-\beta\hat{\phi}) + \frac{1}{4}\lambda\hat{h}^4 + \frac{1}{2}\kappa^2\hat{\phi}^2 + \frac{y^4}{2\pi^2}\Big\{ J_B[\eta_h(\hat{\phi},\hat{h},\hat{y})] + 3J_B[\eta_\chi(\hat{\phi},\hat{h},\hat{y})] + 4J_B[\eta_{W_T}(\hat{h})] \\ &+ 2J_B[\eta_{Z_T}(\hat{h})] + 2J_B[\eta_{W_L}(\hat{h},\hat{y})] + J_B[\eta_{Z_L}(\hat{h},\hat{y})] + J_B[\eta_{A_L}(\hat{h},\hat{y})] - 12J_F[\eta_t(\hat{h},\hat{y})]\Big\}\,,\end{aligned} \tag{4.3.6}$$

where we have defined the dimensionless arguments of the $J_{B,F}$ functions, $\eta_i(\hat{\phi},\hat{h},y) \equiv m_i^2(\phi,h,T)/T^2$.

4.3.2 Higgs field and Electroweak Phase Transition

We first discuss the evolution of the Higgs field h, which serves as the order parameter for the EWPT. In the SM, the EWPT is a smooth crossover [239] characterized by the critical temperature $T_c \sim \mathcal{O}(v)$ ($y_c \equiv T_c/\mu \sim \mathcal{O}(1)$). The feeble portal coupling between ϕ and h will not alter the nature of the phase transition, at least in the $\beta\hat{\phi} \ll 1$ regime of primary relevance for this work. The Higgs field is assumed to track the potential minimum throughout the phase transition, starting at $h = 0$ at high temperatures ($y \gg y_c$), then taking nonzero values for $y < y_c$, and finally settling at $h = v$ at low temperatures ($y \ll 1$).

Thus, for temperatures below y_c, the evolution of $\hat{h}(\hat{\phi}, y)$ is determined by the minimization condition $\partial\hat{V}_{\rm eff}/\partial\hat{h} = 0$, with $\hat{V}_{\rm eff}$ given in Eq. (4.3.6):

$$0 = \lambda\hat{h}^2 - (1-\beta\hat{\phi}) + \frac{y^2}{2\pi^2}\Big\{6\lambda(J'_B[\eta_h] + J'_B[\eta_\chi]) + g^2\left(2J'_B[\eta_{W_T}] + J'_B[\eta_{W_L}]\right) \\ + (g^2+g'^2)J'_B[\eta_{Z_T}] + 2y^2\frac{\partial\eta_{Z_L}}{\partial\hat{h}^2}J'_B[\eta_{Z_L}] + 2y^2\frac{\partial\eta_{A_L}}{\partial\hat{h}^2}J'_B[\eta_{A_L}] - 12y_t^2J'_F[\eta_t]\Big\}. \tag{4.3.7}$$

Here g, g', and y_t are the $SU(2)_L$ gauge coupling, $U(1)_Y$ gauge coupling, and top Yukawa coupling, respectively. Note that the η_i are functions of $(\hat{\phi}, \hat{h}, y)$. Our procedure is to solve Eq. (4.3.7) for $\hat{h}(\hat{\phi}, y)$ and then use this solution in equation of motion of $\hat{\phi}$, to be discussed below in Sec. 4.3.4. In principle, Eq. (4.3.7) can be solved numerically. However, since $\beta\hat{\phi} \ll 1$ for essentially all of our parameter space, in practice we will treat $\beta\hat{\phi}$ as a perturbation. We therefore define $\hat{h}_0(y)$ as the solution to Eq. (4.3.7) with $\beta\hat{\phi} = 0$. Including the $\beta\hat{\phi}$ dependence will change the evolution and y_c slightly ($\propto \mathcal{O}(\beta\hat{\phi})$). The evolution of $\hat{h}_0(y)$ is shown in Figure 22.

4.3.3 Sources of Misalignment and Initial Conditions

Before we study the evolution of the scalar field ϕ in detail, it is worth discussing the various sources of misalignment that contribute to the late-time ϕ oscillation amplitude and associated relic density. To gain insight, it is helpful to examine the minimum of the effective

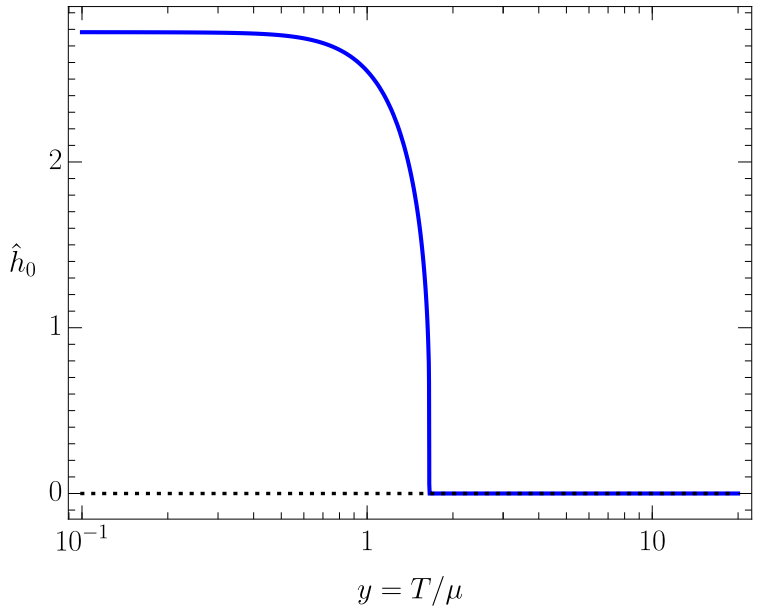

Figure 22: Dimensionless Higgs profile $\hat{h}_0 = \hat{h}(\hat{\phi} = 0, y)$ as a function of $y = T/\mu$. The critical temperature corresponding to the EWPT can be seen at $y_c \simeq 1.6$, figure taken from [67].

potential with respect to $\hat{\phi}$ as a function of temperature, $\hat{\phi}_{\rm min}(y)$, which can be obtained from Eq. (4.3.6) by setting $\partial \hat{V}_{\rm eff}/\partial\hat{\phi} = 0$. The solution can be written as

$$\hat{\phi}_{\rm min} = -\frac{\beta}{2\kappa^2}\left[\hat{h}^2 + \frac{y^2}{\pi^2}\left(J'_B[\eta_h] + 3J'_B[\eta_\chi]\right)\right] . \tag{4.3.8}$$

Since $\beta\hat{\phi} \ll 1$ for the bulk of our parameter space, it is typically a good approximation to neglect this dependence in $\eta_{h,\chi}$ and $\hat{h}$ which enter in the r.h.s. of Eq. (4.3.8). In Figure 23 we show the variation of $\hat{\phi}_{\rm min}(y)$ with $y = T/\mu$ for a representative benchmark model. We see that at high temperatures, $y \gg y_c$, the minimum is located at large (negative) scalar field values, reflecting the dominance of the second term in Eq. (4.3.8). As the temperature drops, the minimum decreases as $|\hat{\phi}_{\rm min}| \propto y^2$ until the EWPT at y_c. At this point, the Higgs field turns on and the $\hat{\phi}$ potential minimum rapidly transitions to its zero temperature value, Eq. (4.2.3), or in terms of the dimensionless variables,

$$\hat{\phi}_0 = -\frac{\beta}{2\lambda\kappa^2 - \beta^2} \simeq -\frac{\beta}{2\lambda\kappa^2} . \tag{4.3.9}$$

The qualitative behavior of $\hat{\phi}_{\rm min}$ is similar to that in Figure 23 for other parameter choices.

As we now discuss, there are three qualitatively distinct contributions to the misalignment of $\hat{\phi}$:

- **Misalignment due to initial conditions -** This contribution is given by the value $\hat{\phi}_i$ the scalar field takes at the end of inflation.
- **Thermal misalignment -** At temperatures much larger than the temperature of EWPT, $y \gg y_c$, the scalar experiences a finite-temperature contribution to the effective potential due to its feeble coupling to the thermalized Higgs degrees of freedom given by Eq. (4.3.2). This causes the scalar to roll towards the high-temperature minimum set by Eq. (4.3.8) and illustrated in Figure 23, dynamically generating misalignment. We refer to this contribution as thermal misalignment, $\hat{\phi}_T$, and we will show below in Sec. 4.3.5.1 that

$$\hat{\phi}_T \propto \frac{\beta}{\kappa} . \tag{4.3.10}$$

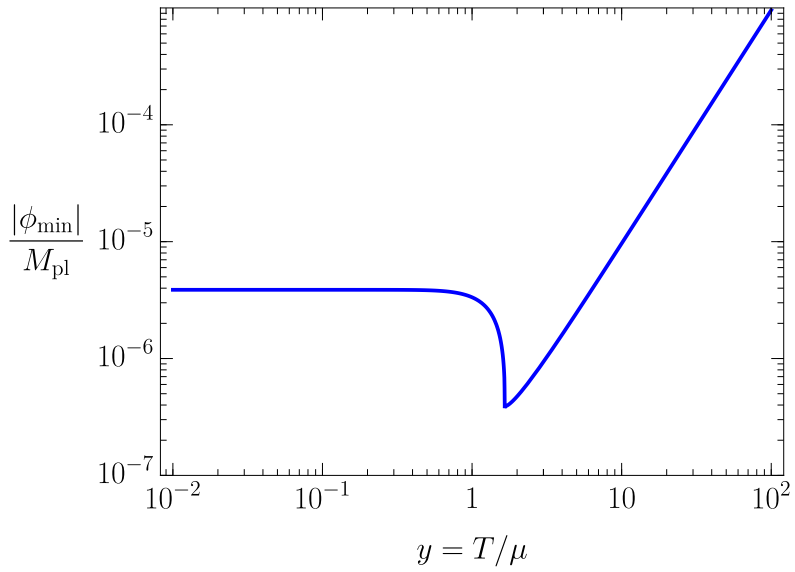

Figure 23: Evolution of the temperature-dependent scalar field minimum $|\hat{\phi}_{\rm min}(y)|$ as a function of $y = T/\mu$ for the benchmark $\kappa = 10^3$, $\beta = 1$. The ϕ minimum is controlled by the finite-temperature contribution to the effective potential for $y > y_c$, while instead for $y < y_c$ it transitions quickly towards its zero temperature value induced by the the Higgs VEV, Eq. (4.2.3). We have used $\hat{h}_0 = \hat{h}(\hat{\phi} = 0, y)$ as a function of $y = T/\mu$, figure taken from [67].

- **VEV misalignment -** Below the temperature of the EWPT, $y < y_c$, the Higgs field switches on and induces a rapid shift in the minimum of the scalar field $\hat{\phi}$ (see Figure 23) to its zero temperature VEV (4.3.9). This dynamically generates and additional source of misalignment, $\hat{\phi}_V$, which we refer to as VEV misalignment.

The final misalignment is in general influenced by all of the above contributions. Note that both thermal misalignment and VEV misalignment are dynamical processes occurring during the radiation era. As we will see, these sources of misalignment depend on the DM model parameters, i.e., the mass m_ϕ (or equivalently κ) and the coupling A (or equivalently β). On the other hand, the initial value $\hat{\phi}_i$ after reheating depends on the detailed dynamics during inflation and can in principle be arbitrary. An important question then is to what extent the relic abundance prediction depends on the assumed initial condition. If the relic density prediction is insensitive to the initial conditions and only depends on the DM model parameters, this opens up the exciting prospect of confronting the cosmological production mechanism with experiments, since the signatures and predictions for the latter are determined by the same model parameters (mass and coupling).

As we will show in detail in Sec. 4.3.5.1, for larger scalar masses, $m_\phi \gtrsim$ few meV ($\kappa \gtrsim 10^3$), thermal misalignment dominates over VEV misalignment, $\hat{\phi}_T \gg \hat{\phi}_V$. Then provided $\hat{\phi}_i \ll \hat{\phi}_T$, which can be satisfied for a broad range of conceivable initial field values given Eq. (4.3.10), the thermal misalignment generated during the radiation era will overwhelm (or "erase") the contribution from the initial field value. If this condition holds, the late-time oscillation amplitude and resulting scalar relic abundance is controlled entirely by the DM model parameters. We can then define a relic density target corresponding to a line in the $m_\phi - A$ plane yielding a DM abundance in accord with the measured value, $\Omega_{\rm DM} \simeq 0.26$ [17]. Modulo fine tuning of initial conditions, parameters above the relic density target line will lead to even larger scalar oscillation amplitudes generated by thermal misalignment and would thus overclose the universe. These features, such as correlations between DM relic density and its mass and coupling, as well as insensitivity to initial conditions and UV physics, are reminiscent of similar attractive aspects found in models of weakly-interacting-massive particle (WIMP) DM.

For lower masses, $m_\phi \lesssim 10^{-5}$ eV ($\kappa \lesssim 1$), VEV misalignment dominates over thermal

misalignment, $\phi_V \gg \phi_T$. As will be clearly shown in Sec. 4.3.5, the insensitivity of the scalar relic density to the initial field value $\hat{\phi}_i$ does not carry over to this lower mass regime.

Below we will detail two choices of initial conditions that will be used in our numerical and analytic estimates in the coming sections. These two choices will allow us to demonstrate the insensitivity of the relic density to initial conditions for scalars with relatively large masses where thermal misalignment dominates, as well as study the impact of different initial conditions for scalars with relatively low masses where VEV misalignment is important.

- $\phi_i = \phi_0$:

  In this case, the scalar is initially at its zero-temperature VEV, ϕ_0, given by Eq. (4.2.3). This initial condition is naturally realized through a sufficiently long enough period of inflation with a low enough inflationary Hubble parameter, $H_I \ll v$. In this case, electroweak symmetry is broken during inflation, the Higgs is close to its VEV v, and the ϕ potential minimum is approximately at ϕ_0. Given a long enough period of inflation the distribution of ϕ will relax to the average $\langle\phi\rangle|_{H_I} = \phi_i = \phi_0$. This relaxation will take order $\mathcal{N} \sim H_I^2/m_\phi^2$ e-folds, and the variance of ϕ will be given by $\sigma_{\phi_i} = 3H_I^4/(8\pi m_\phi^2)$. Note that H_I cannot be arbitrarily low if thermal misalignment is to be important, which requires the reheat temperature to satisfy $T_{\rm RH} \gg v$, though this condition can easily be met. We also require $\sigma_{\phi_i} \ll \phi_T$, (ϕ_V) for the thermal (VEV) misalignment to be important. We note that a low inflationary Hubble scale naturally suppresses scalar fluctuations (see, e.g., Refs. [212, 331, 333]), thus easing otherwise stringent CMB constraints on isocurvature perturbations [25].

  As emphasized above, for heavier scalars the displacement generated by thermal misalignment overwhelms the initial field value assumed here. On the other hand, for lighter scalars thermal misalignment is negligible and VEV misalignment operates, though we must carefully consider the impact of the assumed initial condition. The scalar is held fixed by Hubble friction for some time near its initial value, $\hat{\phi}_i \sim \hat{\phi}_0$. Then at temperatures just above the EWPT, the $\hat{\phi}$ potential minimum adjusts to field values that are much smaller than its initial value $\hat{\phi}_0$, as can be seen in in Figure 23. At this stage, the scalar field slow-rolls away from its initial position, generating misalignment. After the EWPT, the location of the $\hat{\phi}$ minimum quickly transitions to its zero-temperature VEV

$\hat{\phi}_0$, and eventually oscillations commence after the expansion rate drops below the scalar mass. It will be shown that the parametric dependence of the VEV misalignment for this inital condition is

$$\hat{\phi}_V \propto \beta, \qquad (\hat{\phi}_i = \hat{\phi}_0)\,. \tag{4.3.11}$$

A more thorough treatment of this dynamics will be presented in Sec. 4.3.5.3.

- $\phi_i = 0$:

  This initial condition is chosen as a representative example of the general situation where $|\phi_i|$ is vastly different than $|\phi_0|$. For larger scalar masses, thermal misalignment again dominates the evolution and the scalar relic abundance is insensitive to the assumed initial field value. In contrast, for smaller scalar masses, VEV misalignment dominates over thermal misalignment, although we must again understand the role of the initial condition. In fact, the evolution of the scalar field in this case is quite simple. Initially, the scalar is held at its initial location at the origin by Hubble friction. The EWPT triggers a shift in the ϕ potential minimum to its zero-temperature value ϕ_0, generating VEV misalignment of parametric size (see Sec. 4.3.5.3):

$$\hat{\phi}_V \simeq -\frac{\beta^2}{2\kappa^2\lambda} \qquad (\hat{\phi}_i = 0)\,. \tag{4.3.12}$$

  At some later time the Hubble rate falls below the scalar mass and oscillations begin.

It can be seen in Figure 21 that the relic density lines in the lower scalar mass region are strongly sensitive to the initial field value, while instead those in the higher scalar mass range are the same for both assumed initial conditions.

4.3.4 Scalar field dynamics

We are now ready to discuss the evolution of the scalar field ϕ, which is governed by the following equation of motion during the radiation-dominated era

$$\ddot{\phi} + 3H\dot{\phi} + \frac{\partial V_{\rm eff}}{\partial \phi} = 0\,, \tag{4.3.13}$$

where again $V_{\rm eff} = \mu^4 \hat{V}_{\rm eff}$ is given in Eqs. (4.3.1,4.3.6) and the Hubble parameter H has been defined at the beginning of Sec. 4.3.1.

For simplicity, we will ignore the small time variation of g_* during the initial phase of the ϕ evolution until ϕ oscillations begin, fixing it to the high temperature SM value of $g_*^{\rm SM} = 106.75$ ($\gamma = \sqrt{\pi^2 g_*/90} \simeq 3.4$). For large scalar masses, oscillations begin well before the EWPT, and as such $g_* = g_*^{\rm SM}$ is exactly correct. Instead, for smaller masses, oscillations begin below the EWPT and g_* starts to decreases as t, W, Z, h fall out of thermal equilibrium, giving for example $g_* \sim 80$ at $y \sim 0.01$. Thus for smaller masses our constant $g_* = g_*^{\rm SM}$ approximation will result in a $\mathcal{O}(10\%)$ error in the relic abundance prediction.

Let us also briefly discuss a potential additional source of scalar field damping. As the scalar field evolves, the effective mass of the Higgs particles in the bath changes though their momenta does not, causing a small deviation in the Higgs phase space distribution from its equilibrium value. This can manifest as an additional effective friction term in the scalar equation of motion; see e.g., Ref. [354]. However, the Higgs quickly relaxes toward equilibrium through fast number changing processes, such that this source of damping is much smaller than the other terms in Eq. (4.3.13). See also Ref. [93] for discussion.

We can re-express the ϕ equation of motion (4.3.13) in terms of the dimensionless variables defined in Eq. (4.3.5), with independent variable of time t traded for $y = T/\mu$. We obtain

$$\hat{\phi}'' + \frac{1}{\gamma^2 y^6}\left[\kappa^2 \hat{\phi} + \frac{\beta \hat{h}^2}{2} + \frac{\beta y^2}{2\pi^2}\left(J_B'[\eta_h] + 3J_B'[\eta_\chi]\right)\right] = 0\,. \tag{4.3.14}$$

Here, $\hat{h} = \hat{h}(\hat{\phi}, y)$ is the solution to Eq. (4.3.7), as discussed in detail in Sec. 4.3.2. We then solve the $\hat{\phi}$ equation of motion (4.3.14) subject to the initial conditions as described in the previous section. These are defined at $y_i = T_i/\mu$, where $y_i \gg 1$ corresponds to some suitably

early time well before the scalar starts to oscillate. The scalar field is evolved until $y_f = T_f/\mu$ corresponding to some suitable time after it begins oscillating and redshifts as matter. From this time on, the ϕ comoving energy density, ρ_ϕ/s, where ρ_ϕ is the ϕ energy density and $s(T) = (2\pi^2/45)g_{*S}(T)T^3$ is the total entropy density of the plasma, is conserved. Using this fact, we then arrive at our estimate for the ϕ energy density in the present epoch,

$$\rho_{\phi,0} = \frac{g_{*S}(y_0)}{g_{*S}(y_f)} \left(\frac{y_0}{y_f}\right)^3 \rho_\phi(y_f)\,, \tag{4.3.15}$$

where $y_0 = T_0/\mu$ with $T_0 \simeq 2.7$ K. We use $g_{*S}(y_f) = 106.75$ and $g_{*S}(y_0) \simeq 3.91$ in our estimate. Expressing the relic density in terms of the density parameter $\Omega_{\phi,0} = \rho_{\phi,0}/\rho_{c,0}$, with $\rho_{c,0} = 3M_{\rm pl}^2 H_0^2$ the critical density today, we show the parameters leading to the observed DM relic abundance, $\Omega_{\phi,0} = \Omega_{\rm DM} \simeq 0.26$ [17] in Figure 21.

Before discussing these results and comparing with the various experimental probes of the model, it is valuable to gain analytical insight into the ϕ evolution and resulting relic density estimate, which we explore in the next section.

4.3.5 Relic Density Estimation

As the universe expands, the Hubble parameter decreases until it eventually falls below the effective ϕ mass, marking the onset of scalar oscillations. This can be quantified by the condition $[3H(y_{\rm osc})]^2 = m_\phi^2(y_{\rm osc}) \simeq m_\phi^2$, which gives the oscillation temperature as

$$y_{\rm osc} = \frac{T_{\rm osc}}{\mu} = \sqrt{\frac{\kappa}{3\gamma}}\,. \tag{4.3.16}$$

Here we have used the fact that the effective squared scalar mass is dominated by the tree-level contribution m_ϕ^2 over the entire parameter space we consider and for all temperatures. Several epochs after the oscillations begin, we can safely calculate the energy density stored in the scalar field and then redshift it to present times, which will yield the ϕ relic density given by Eq. (4.3.15). Typically, once the scalar starts to oscillate, it behaves like DM with an oscillation amplitude set by

$$\phi_{\rm osc} \equiv \phi(y_{\rm osc})\,, \tag{4.3.17}$$

i.e., the scalar amplitude at the beginning of oscillations. To determine $\phi_{\rm osc}$ we must study the evolution of the scalar field during the radiation era up until the onset of oscillations. As discussed at length in Sec. 4.3.3, there are additional dynamical sources of misalignment present in the Higgs portal model and contribute to the oscillation amplitude. For large scalar masses, thermal misalignment provides the main contribution, while for small scalar masses VEV misalignment (along with initial conditions) is dominant. In the intermediate mass range, both effects are important. In the following, we will therefore divide the parameter space into distinct regions characterized by which sources of misalignment dominate and then develop a suitable analytic estimate for the ϕ evolution and relic abundance. These estimates will be compared with our relic density prediction obtained from the exact numerical solution of the ϕ equation of motion (4.3.13), as described in the previous section.

4.3.5.1 Region I ($\kappa \gtrsim 10^3,\ m_\phi \gtrsim 3\times 10^{-3}\,\text{eV}$)

Region I is defined to be the region of large scalar masses m_ϕ (large κ). In this region, the the amplitude of oscillations at y_c due to thermal misalignment dominates over the "kick" imparted to the scalar resulting from the EWPT (VEV misalignmnet). To understand this point, we first need to estimate the thermal misalignment generated at high temperatures by considering Eq. (4.3.14). For $y \gg y_{\rm osc} \gg y_c$, $\hat{h}(\hat{\phi}, y) = 0$ and we can ignore the $\kappa^2\hat{\phi}$ term since it is subdominant to the finite-temperature contribution to the equation of motion. Hence, in this regime, Eq. (4.3.14) takes the approximate form

$$\begin{aligned} \hat{\phi}''(y) + \frac{\beta}{2\pi^2\gamma^2 y^4}\left(J_B'[\eta_h] + 3(J_B'[\eta_\chi]\right) = 0, \\ \implies \quad \hat{\phi}''(y) + \frac{\beta}{\pi^2\gamma^2 y^4} = 0\,, \end{aligned} \tag{4.3.18}$$

where in the second line we have used the fact that $J_B'[\eta_h] + 3J_B'[\eta_\chi] \approx 2$ for $y \gg y_c$. (The solution to Eq. (4.3.18), assuming negligible initial field velocity, is

$$\hat{\phi}(y) = -\frac{\beta}{6\pi^2\gamma^2 y^2} + \hat{\phi}_i\,, \tag{4.3.19}$$

where the first term represents the thermal misalignment, $\hat{\phi}_T(y) = -\beta/(6\pi^2\gamma^2 y^2)$, while the second is the initial condition $\hat{\phi}_i$. As the temperature drops below $y_{\rm osc} = \sqrt{\kappa/3\gamma}$, the mass

term $(\kappa^2\hat{\phi})$ in Eq. (4.3.14) begins to dominate over the thermal contribution and the scalar starts to oscillate and redshift like DM. Plugging $y = y_{\rm osc}$ into Eq. (4.3.19), we find the scalar amplitude at the onset of oscillations is given by

$$\hat{\phi}_{\rm osc} = \hat{\phi}(y_{\rm osc}) = -\frac{\beta}{2\pi^2\gamma\kappa} + \hat{\phi}_i \,. \tag{4.3.20}$$

For the first initial condition $\hat{\phi}_i = \hat{\phi}_0 \simeq -\beta/(2\lambda\kappa^2)$ motivated in Sec. 4.3.3, we observe that thermal misalignment $\hat{\phi}_T$ dominates over $\hat{\phi}_i = \hat{\phi}_0$ for $\kappa \gtrsim \pi^2\gamma/\lambda \approx 300$. Thus, our definition of Region I, $\kappa > 10^3$, satisfies this criterion.

In Figure 24 we display the numerical evolution of $\hat{\phi}(y)$ relative to its temperature-dependent Higgs-induced minimum, $\delta\phi(y) \equiv \hat{\phi}(y) - [-\beta\hat{h}_0^2(y)/(2\kappa^2)]$, for two benchmark models in Region I and the initial conditions $\hat{\phi}_i = \hat{\phi}_0$ and $\hat{\phi}_i = 0$ discussed in Sec. 4.3.3. This quantity provides a convenient visualization of both the thermal misalignment generated at high temperatures as well as the negligible impact of VEV misalignment for $y < y_c$. The temperature-dependent Higgs-induced minimum, $[-\beta\hat{h}_0^2(y)/(2\kappa^2)]$, is simply the first term in the full temperature-dependent minimum $\hat{\phi}_{\rm min}$ in Eq. (4.3.8), which dominates the expression at low temperatures, i.e.,

$$\hat{\phi}_{\rm min}(y) \simeq -\frac{\beta\hat{h}_0^2(y)}{2\kappa^2} \qquad (y \lesssim y_c). \tag{4.3.21}$$

This is also clear from Figure 23. The dominance of thermal misalignment and the independence of the the oscillation amplitude on the initial conditions are clearly seen in Figure 24.

We will now justify the condition $\kappa \gtrsim 10^3$ used to define Region I. For $\kappa \gtrsim 10^3$, oscillations of the scalar field around its high temperature minimum begin at $y_{\rm osc} \gg y_c$. The amplitude of the oscillations then decreases with temperature as $y^{3/2}$ (i.e., ϕ redshifts like matter) until $y = y_c$. At y_c the Higgs field transitions nearly instantaneously, causing a shift in the minimum of $\hat{\phi}$ from the its minimum at $y > y_c$ to $\hat{\phi}_0$. If the change in the $\hat{\phi}$ minimum near $y = y_c$ within one oscillation time period is larger than the oscillation amplitude, then the relic density is controlled by VEV misalignment. Conversely, if the oscillation amplitude at $y = y_c$ is much larger than the shift in the $\hat{\phi}$ minimum due to the EWPT, then thermal misalignment dominates. For large κ (large m_ϕ), the latter scenario of thermal

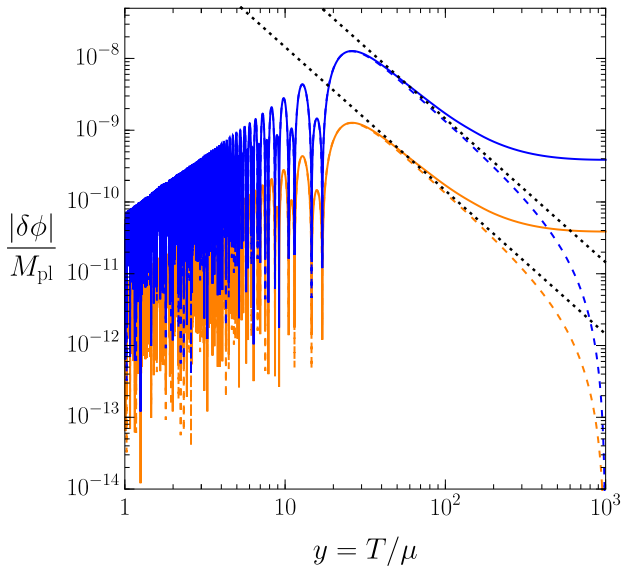

Figure 24: Scalar field evolution $\hat{\phi}(y)$ relative to its temperature-dependent Higgs-induced minimum, $\delta\phi(y) \equiv \hat{\phi}(y) - [-\beta\hat{h}_0^2(y)/(2\kappa^2)]$ for two benchmark models in Region I: $\beta = 10^{-2}, \kappa = 10^4$ (blue) and $\beta = 10^{-3}, \kappa = 10^4$ (orange). The black dotted lines show the corresponding approximate initial thermal misalignment trajectories of Eq. (4.3.20). The β^2 scaling due to thermal misalignment is clearly observed. The evolution is shown for the two choices of initial conditions discussed in Sec. 4.3.3: $\hat{\phi}_i = \hat{\phi}_0$ (solid) and $\hat{\phi} = 0$ (dashed). It is evident that the late time $\hat{\phi}$ evolution is independent of the initial value of the scalar field for these choices, figure taken from [67].

misalignment applies. In what follows, we will derive a lower bound on κ above which the thermal misalignment dominates (defined to be Region I) and then develop an analytical approximation for the ϕ relic density.

At y_c, the minimum of $\hat{\phi}$ transitions from being governed by the thermal contribution to the potential to being controlled by the Higgs VEV $\hat{h}$ (see Figure 23). In this region, the $\hat{\phi}$ minimum swiftly changes according $\hat{\phi}_{\rm min}$ given in Eq. (4.3.21). This rapid shift in $\hat{\phi}_{\rm min}$ provides a "kick" by effectively changing the amplitude of the oscillation. The magnitude of this kick is the variation of $\hat{\phi}_{\rm min}$ within one half oscillation of the scalar field i.e. within $\Delta t = \pi/m_\phi$. It can be shown that this time period corresponds to $\Delta y = -y_c^3\gamma\pi/\kappa$. The change in the $\hat{\phi}$ minimum is then given by

$$\begin{aligned}\Delta\hat{\phi}_{\rm min} &\simeq \frac{\partial\hat{\phi}_{\rm min}}{\partial y}\Delta y = -\frac{\beta}{2\kappa^2}\frac{\partial\hat{h}^2}{\partial y}\Delta y \\ &\simeq -\frac{\pi\gamma y_c^4\beta}{2\lambda\kappa^3},\end{aligned} \tag{4.3.22}$$

where in the last line we have used $\partial\hat{h}^2/\partial y \simeq -y_c/\lambda$ (this can be seen from the evolution equation for $\hat{h}^2$ in Eq. (4.3.7)). This is to be compared to the oscillation amplitude near y_c due to thermal misalignment, which is given by

$$\hat{\phi}_{\rm osc}(y_c) = \hat{\phi}(y_{\rm osc})\left(\frac{y_c}{y_{\rm osc}}\right)^{3/2} = -\frac{(\sqrt{3}y_c)^{3/2}\beta}{2\pi^2\gamma^{1/4}\kappa^{7/4}}\,, \tag{4.3.23}$$

where we have used Eq. (4.3.20) and redshifted it to y_c. For Region I, we require thermal misalignment to dominate over the "kick", taking as our criterion $\hat{\phi}_{\rm osc}(y_c) > 3\Delta\hat{\phi}_{\rm min}$. Using Eqs. (4.3.22,4.3.23) we find that this is satisfied for

$$\kappa > \gamma y_c^2\left(\frac{3\pi^{12}}{\lambda^4}\right)^{1/5} \simeq 10^3\,. \tag{4.3.24}$$

In practice we find that numerically we agree well with the estimates of Region I for $\kappa > 10^3$. We thus take $\kappa = 10^3$ as the boundary for Region I.

Having established that thermal misalignment dominates in Region I, $\kappa \geq 10^3$, we are now ready to provide an analytic estimate of the ϕ relic abundance. We use Eq. (4.3.15) to estimate $\rho_{\phi,0}$, the ϕ energy density today. As input to this equation, we take $y_f = y_{\rm osc}$ as the temperature at which oscillations begins, with $y_{\rm osc}$ given by Eq. (4.3.16). We also use

$\rho(y_f) = \rho(y_{\rm osc}) \simeq \frac{1}{2} m_\phi^2 \phi(y_{\rm osc})^2$, with $\phi(y_{\rm osc})$ given by the first term in Eq. (4.3.20). Other inputs needed are described below Eq. (4.3.15). Putting everything together, we arrive at the following estimate for the DM density parameter,

$$\begin{aligned}\Omega_{\phi,0} &\simeq \frac{g_{*S}^0}{g_{*S}^{\rm osc}} \frac{y_0^3 \mu^4}{\rho_{c,0}} \frac{3^{3/2}}{8\pi^4} \frac{\beta^2}{\gamma^{1/2}\kappa^{3/2}} \\ &\simeq 0.26 \left(\frac{\beta}{0.05}\right)^2 \left(\frac{1000}{\kappa}\right)^{3/2} . \end{aligned} \tag{4.3.25}$$

Parameters leading to the observed DM abundance according to the approximate analytic estimate, Eq. (4.3.25), are displayed as a dashed line in the $m_\phi - A$ plane in Figure 21 for $m_\phi \gtrsim 10^{-3}$ eV, agreeing well with the calculation using the exact numerical solution to the ϕ equation of motion (4.3.13) in Region I. Eq. (4.3.25) (and the associated numerical estimate) represents one of the most important results of this work, providing a prediction for the observed DM relic density in terms of only the DM model parameters (m_ϕ and A) which is insensitive to initial conditions provided $|\phi_i| \ll |\phi_T|$, as discussed in Sec. 4.3.3. In particular, note that for parameters above the relic density line in Figure 21, initial conditions with $|\phi_i| \gg |\phi_T|$ will overclose the universe. Since thermal misalignment is unavoidable given a standard radiation dominated cosmology and a high enough reheating temperature $T_{RH} \gg v$, this gives a cosmologically motivated target in the parameter space for experiments to pursue. In fact, requiring DM not to overclose the universe currently provides the best constraint on the model (with the caveats mentioned above) over the vast majority of the parameter space.

4.3.5.2 Region II ($10 \lesssim \kappa \lesssim 10^3$, $3 \times 10^{-5} \lesssim m_\phi \lesssim 3 \times 10^{-3}$eV)

We now move to Region II, corresponding to the intermediate mass range ($10 \lesssim \kappa \lesssim 10^3$, $3 \times 10^{-5} \lesssim m_\phi \lesssim 3 \times 10^{-3}$eV). In this region, the final misalignment amplitude is influenced in an important way by the change in the minimum of ϕ triggered by the EWPT at $y = y_c$.

Notably, for masses near the upper end of Region II, $m_\phi \sim \mathcal{O}(10^{-3}\text{eV})$, a competition between thermal misalignment and VEV misalignment leads to a novel forced resonance phenomena which impacts the relic abundance in a rather dramatic fashion. At the EWPT,

the Higgs field rapidly moves from the origin towards $h = v$, simultaneously inducing a shift the ϕ potential minimum towards its zero-temperature value ϕ_0. The acts as a step-like forcing term in the ϕ equation of motion (4.3.14), causing a suppression or enhancement in the oscillation amplitude depending on the relative phase between the oscillations and Higgs source term, which in turn depends on the the scalar mass. For instance, if the scalar is near its oscillation maximum as this shift happens, the effective oscillation amplitude is reduced, thus requiring a larger coupling β to produce the observed DM abundance. This behavior is shown in Figure 25 for one example benchmark point. A striking series of recurring peaks and valleys in the coupling β yielding the correct DM abundance is observed as the scalar mass is varied, as shown the inset of Figure 21.

For masses near the lower end of Region II, VEV misalignment dominates and the predicted DM abundance starts to be sensitive to initial conditions, which is also evident from Figure 21. The impact of VEV misalignment and the role of the initial conditions for the low mass scalars will be clarified in the next through our analysis of Region III.

4.3.5.3 Region III ($\kappa \lesssim 1, m_\phi \lesssim 3 \times 10^{-6}\,\text{eV}$)

Finally, we come to Region III, which may roughly be defined by the condition that oscillations begin below the EWPT, $y_{\text{osc}} \lesssim 1 \implies \kappa \lesssim 3\gamma$. We will simply take $\kappa \lesssim 1$ ($m_\phi \lesssim 3 \times 10^{-6}\,\text{eV}$) for concreteness. In this low mass regime, VEV misalignment caused by the EWPT dominates over thermal misalignment. However, the final ϕ misalignment and number density depends sensitively on the initial conditions (see Figure 21). In the following, we will examine two distinct choices for the initial condition, $\hat{\phi}_i = \hat{\phi}_0$ and $\hat{\phi}_i = 0$, as discussed in Sec. 4.3.3.

(i) $\hat{\phi}_i = \hat{\phi}_0$: Let us first consider the initial condition $\hat{\phi}_i = \hat{\phi}_0 \simeq -\beta/(2\lambda\kappa^2)$. Examining the $\hat{\phi}$ equation of motion (4.3.14) for $\hat{\phi} \approx \hat{\phi}_0$, we observe that the mass term $\kappa^2\hat{\phi}$ dominates over the thermal term for $\frac{y^2}{2\pi^2}\beta\left(J'_B[\eta_h] + 3J'_B[\eta_\chi]\right)$ for $y^2 \lesssim \pi^2/(2\lambda)$. Thus, the scalar field first experiences thermal misalignment $\hat{\phi}_T \sim -\lambda\beta/(3\pi^4\gamma^2)$, where we have used Eq. (4.3.20) and $y^2 \sim \pi^2/(2\lambda)$. However, we note that the displacement of the scalar from $\hat{\phi}_0$ generated by thermal misalignment is minuscule, $|\hat{\phi}_T| \ll \hat{\phi}_0$, since $\kappa \lesssim 1$ in this

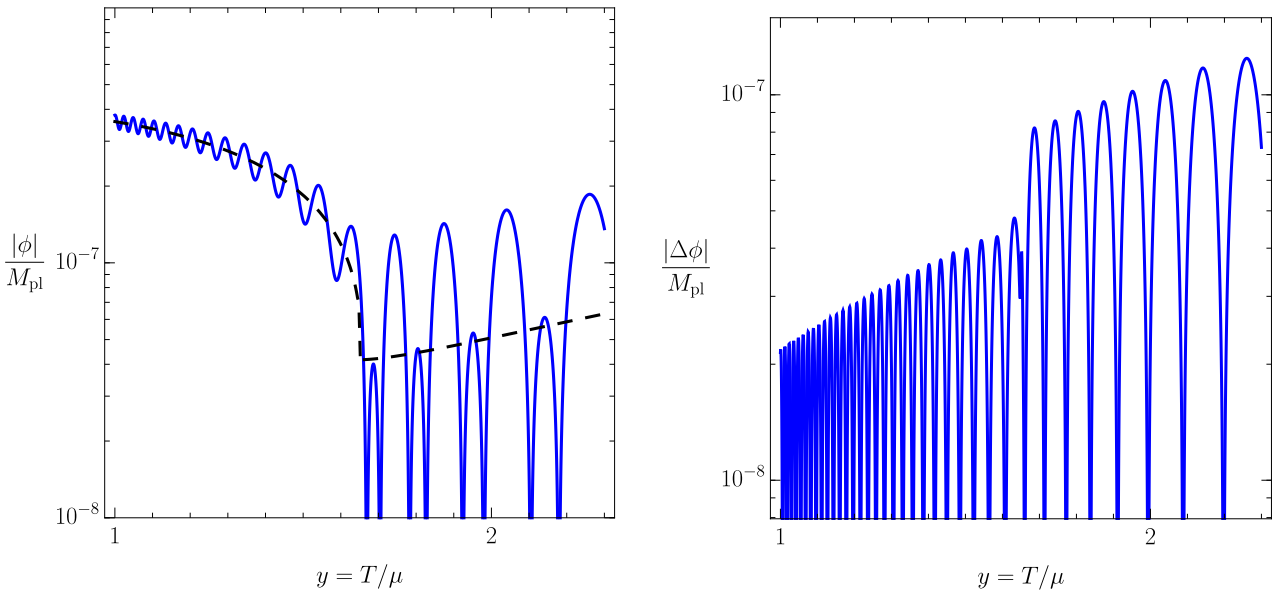

Figure 25: **Left panel:** The evolution of ϕ (blue) along with the progression of the temperature-dependent minimum of ϕ (black dashed) during the EWPT. The true minimum jumps quickly after the transition, reducing the effective oscillation amplitude. **Right panel:** This amplitude reduction is clearly seen in $\Delta\phi(y) \equiv \phi(y) - \phi_{\rm min}(y)$, which shows the oscillations relative to the temperature dependent ϕ minimum, Eq. (4.3.21). In both plots we have chosen the benchmark parameters $\kappa = 10^{2.985}$, $\beta = 10^{-1}$, figure taken from [67].

region. For $y_c < y \lesssim \sqrt{\pi^2/(2\lambda)} \simeq 7$ the mass term dominates and the equation of motion becomes

$$\begin{aligned} &\hat{\phi}''(y) + \frac{1}{\gamma^2 y^6}\left(\kappa^2\hat{\phi}\right) = 0\,, \\ \Longrightarrow \quad &\hat{\phi}''(y) - \frac{\beta}{2\gamma^2\lambda}\frac{1}{y^6} = 0\,, \end{aligned} \tag{4.3.26}$$

where in the second line we have assumed $\hat{\phi} \simeq \hat{\phi}_0$. The solution to this equation is given by

$$\hat{\phi}(y) = \frac{1}{y^4}\frac{\beta}{40\gamma^2\lambda} + \hat{\phi}_0\,. \tag{4.3.27}$$

The trajectory of $\hat{\phi}$ follows Eq. (4.3.27) until $y \sim 1$ at which point the contribution from $\beta\hat{h}^2/2$ in Eq. (4.3.14) turns on and, to a good approximation, cancels the $\kappa^2\hat{\phi}$ term. At this point, all source terms in Eq. (4.3.27) are negligible and the evolution is dictated by $\hat{\phi}''(y) = 0$. This has the solution

$$\hat{\phi}(y) = \hat{\phi}'(1)(y-1) + \hat{\phi}(1)\,, \tag{4.3.28}$$

where the initial conditions for the field and its velocity are obtained by matching the solution in Eq. (4.3.27) at $y = 1$. We find $\hat{\phi}'(1) = -\beta/(10\gamma^2\lambda)$ and $\hat{\phi}(1) = \beta/(40\gamma^2\lambda) + \hat{\phi}_0$. Then for small y, before beginning of oscillations, we obtain the asymptotic value of $\hat{\phi}(y \ll 1) = 5\beta/(40\gamma^2\lambda) + \hat{\phi}_0$, where the first term is the amplitude of oscillations. The evolution of the scalar field for $\hat{\phi}_i = \hat{\phi}_0$ is displayed for a representative benchmark model in the left panel of Figure 26.

With an estimate for the oscillation amplitude, $\hat{\phi}(y_{\rm osc}) \simeq 5\beta/(40\gamma^2\lambda)$, we are now in a position to compute the ϕ relic abundance, following similar steps to those used earlier in Region I. In particular, we employ Eq. (4.3.15) to estimate $\rho_{\phi,0}$, taking $y_f = y_{\rm osc} = \sqrt{\kappa/(3\gamma)}$, Eq. (4.3.16), as the temperature corresponding to the onset of oscillations. Furthermore, we use $\rho(y_f) = \rho(y_{\rm osc}) \simeq \frac{1}{2}m_\phi^2\phi(y_{\rm osc})^2$. Collecting the other inputs described around Eq. (4.3.15), we obtain

$$\begin{aligned} \Omega_{\phi,0} &\simeq \frac{g_{*S}^0}{g_{*S}^{\rm osc}}\frac{y_0^3\,\mu^4}{\rho_{c,0}}\frac{3^{3/2}}{128}\frac{\beta^2\,\kappa^{1/2}}{\gamma^{5/2}\,\lambda^2} \\ &\simeq 0.26\left(\frac{\beta}{10^{-4}}\right)^2\left(\frac{\kappa}{4\times10^{-2}}\right)^{1/2}\,. \end{aligned} \tag{4.3.29}$$

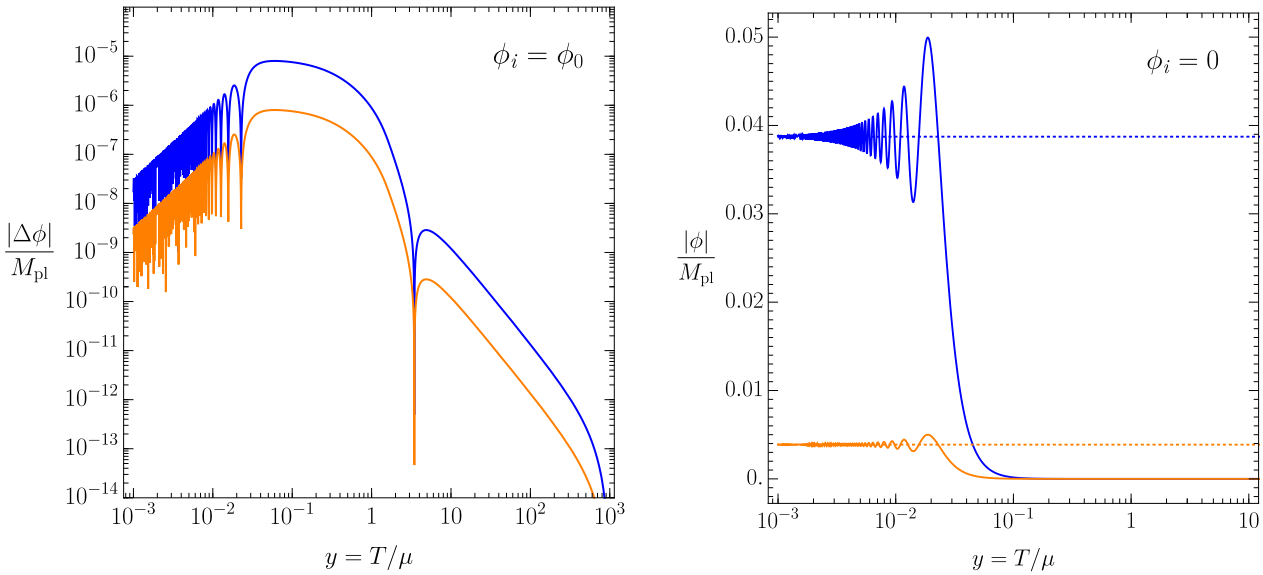

Figure 26: Scalar field evolution in Region III, where VEV misalignment is important, for two choices of initial conditions. **Left panel:** The initial condition is chosen to be $\phi_i = \phi_0$. The evolution $\Delta\phi(y) \equiv \phi(y) - \phi_0$ is shown for two benchmark models: $\kappa = 10^{-2}$, $\beta = 10^{-4}$ (blue curves), and $\kappa = 10^{-2}$, $\beta = 10^{-5}$ (orange curves). **Right panel:** The initial condition is chosen to be $\phi_i = 0$. The evolution $\phi(y)$ is shown for two benchmark models: $\kappa = 10^{-2}$, $\beta = 10^{-6}$ (blue curves), and $\kappa = 10^{-2}$, $\beta = 10^{-7}$ (orange curves). The dotted lines show the corresponding zero temperature minima ϕ_0. Figure taken from [67].

It should be noted that since the amplitude of oscillations is comparatively small for $\phi_i = \phi_0$, a much larger value of β is needed to obtain the correct relic density. This initial condition is representative of an optimistic scenario for experimental detection of low mass scalars.

(ii) $\hat{\phi}_i = 0$: Next, we consider the initial condition $\hat{\phi}_i = 0$. It is far more straightforward to estimate the scalar relic density in this case. Thermal misalignment is again negligible, and in the earliest stages of its evolution the scalar is held near at its initial value by Hubble friction until the EWPT at y_c. At this point, the $\hat{\phi}$ VEV rapidly evolves to its zero temperature value $\hat{\phi}_0$, triggering VEV misalignment of the scalar, until eventually oscillations begin (see Figure 26 right panel). The oscillation amplitude is therefore given by $\hat{\phi}(y_{\rm osc}) \simeq \hat{\phi}_0 \simeq -\beta/(2\lambda\kappa^2)$. Thus the ϕ density parameter today is given by

$$\begin{aligned}\Omega_{\phi,0} &\simeq \frac{g_{*S}^0}{g_{*S}^{\rm osc}} \frac{y_0^3\,\mu^4}{\rho_{c,0}} \frac{3^{3/2}}{8} \frac{\gamma^{3/2}\beta^2}{\lambda^2\,\kappa^{7/2}} \\ &\simeq 0.26 \left(\frac{\beta}{3\times 10^{-10}}\right)^2 \left(\frac{10^{-2}}{\kappa}\right)^{7/2} . \end{aligned} \tag{4.3.30}$$

For this initial condition, we note the drastically lower values of β required to get the correct relic density. Thus the initial condition $\phi_i = 0$ is representative of low mass scalar scenario that is challenging to probe experimentally.

4.3.6 Summary of Results

A summary of our results is presented in Figure 21, which shows contours leading to the observed relic abundance in the $m_\phi - A$ plane for the two choices of initial conditions, $\phi_i = \phi_0$ and $\phi_i = 0$. Both the numerical results from solving Eq. (4.3.14) and using Eq. (4.3.15) (solid lines), as well as the analytic estimates, Eqs. (4.3.25,4.3.29,4.3.30) (dashed lines) are presented and agree well.

4.4 Constraints

We now discuss the existing experimental constraints and future prospects for the ultra-light Higgs portal DM model. These bounds are shown in the $m_\phi - A$ plane and can be

compared with our numerical and analytic predictions for the relic abundance lines ($\Omega_{\phi,0} = \Omega_{\rm DM} = 0.26$) in Figure 21. We now provide a brief overview for each of these bounds.

4.4.1 Equivalence Principle and Inverse Square Law Tests

The light scalar mixes with the Higgs and thus couples to ordinary matter, leading to an additional Yukawa-like potential between nucleons. This additional force can be constrained by experiments searching for violations of the gravitational inverse square law (ISL) or tests of the equivalence principle (EP).

For the ISL bounds, we follow the approach of Ref. [299]. The potential between two test bodies (labeled 1 and 2) is given by

$$V(r) = -\frac{G m_1 m_2}{r}\left(1 + \alpha_1 \alpha_2\, e^{-m_\phi r}\right) . \tag{4.4.1}$$

We will assume that the scalar has the same coupling to protons and neutrons, with the scalar-nucleon coupling given by

$$g_{\phi NN} = g_{hNN}\,\frac{A\,v}{m_h^2} \simeq 10^{-3}\,\frac{A\,v}{m_h^2}\,, \tag{4.4.2}$$

where $g_{hNN} \simeq 10^{-3}$ is known with order one uncertainty [210]. The scalar coupling to the test body i is given by

$$\frac{\alpha_i}{\sqrt{2}M_{\rm pl}} = \frac{d\ln m_N(\phi)}{d\phi} = \frac{g_{\phi NN}}{m_N}\,. \tag{4.4.3}$$

We can then translate constraints reported on ISL tests. The constraints are typically reported on the product $\tilde{\alpha} = \alpha_1\alpha_2$, which in terms of our model parameters is given by

$$\tilde{\alpha} = \alpha_1\alpha_2 = 10^{-6}\,\frac{2M_{\rm pl}^2}{m_N^2}\left(\frac{A\,v}{m_h^2}\right)^2 = \left(\frac{A}{1.7\times 10^{-5}\,{\rm eV}}\right)^2 . \tag{4.4.4}$$

The constraints from ISL tests from Refs. [233, 351] are shown in Figure 21. As can be seen in the inset, the ISL tests are already beginning to probe interesting regions of the parameter space due to the resonance effects discussed in Sec. 4.3.5.2.

Constraints from violation of EP are more involved. We follow Ref. [210] in the following. EP constraints involve measurements of differential accelerations in test bodies which have

different charge-to-mass ratios, i.e., the ratio of the scalar coupling strength to the mass of a given atom ($\Delta_{\phi H^2}$). The EP violation constraints on a mediator coupled to a $B-L$ charge obtained by measuring the differential acceleration between Beryllium (Be) and Aluminium (Al) were derived in Ref. [342]. Translating these bounds to our model, we can write

$$A = 4.4 \times 10^{13}\text{eV}\, g_{B-L} \sqrt{\frac{\Delta_{B-L}}{\Delta_{\Phi h^2}}}\,, \tag{4.4.5}$$

where g_{B-L} is the the coupling strength of the scalar to $B-L$ charge and Δ_{B-L} is the differential charge-to-mass ratio between Be and Al. We use $\Delta_{B-L} = 0.037$ and $\Delta_{\phi H^2} = 4 \times 10^{-4}$ [210]. The EP constraints on the Higgs portal model are shown in Figure 21.

4.4.2 Stellar Cooling Bounds

For the Higgs portal, the stellar cooling bounds primarily arise from the effective coupling of ϕ to electrons [224]. The dominant constraints on the model come from red giant (RG) and horizontal branch (HB) stars. In red giant cores, the dominant energy loss mechanism is neutrino production. Any additional stronger energy loss mechanism will delay the onset of helium fusion in cores of RG stars. Since this is not observed, it implies a constraint on the Higgs-scalar mixing angle $\sin\theta \simeq Av/m_h^2 \leq 3 \times 10^{-10}$ for $m_\phi < 2$ keV [224]. For HB stars, any additional strong energy loss mechanism causes the cores to contract and heat up, increasing the rate of helium fusion and shortening the lifetime of the stars, which is not observed. The combined constraints from RG and HB stars are shown in Figure 21.

4.4.3 Resonant Absorption in Molecules

Resonant absorption of ϕ by polyatomic molecules has been proposed as a DM detection concept in Ref. [49]. The basic idea is to search for DM absorption via the subsequent transition of these molecules from the excited to ground state through the emission of photons. Concerning the Higgs portal model, this technique is most sensitive to the effective coupling of ϕ to electrons, which in terms of the coupling A is given by

$$g_{\phi ee} = \frac{A\,v}{m_h^2} y_e = \frac{A\,m_e}{m_h^2}. \tag{4.4.6}$$

The approach has the potential to probe scalar DM coupled to electrons in the mass range $0.2\,\mathrm{eV} \lesssim m_\phi \lesssim 20\,\mathrm{eV}$. In the parameterization employed in [49], the constraint is given by $d_{m_e} \lesssim 10^5$ where $d_{m_e} = \sqrt{2} g_{\phi ee} M_{\rm pl}/m_e \simeq 2.2 \times 10^5 \times (A/\mathrm{eV})$.

We show projections corresponding to a phase II 'bulk' (BII) and 'stack' (SII) experimental configurations in Figure 21; for more details we refer the reader to Ref. [49].

4.4.4 Extragalactic Background Light and Reionization Constraints

For larger masses and couplings, the scalar ϕ can decay into photons on cosmological time scales. The decay rate of the scalar to photons is given by [186]

$$\Gamma_{\phi\gamma\gamma} = \frac{\theta^2 \alpha^2}{256\pi^2} \frac{m_\phi^3}{v^2} |C|^2 \tag{4.4.7}$$

where $\theta \simeq Av/m_h^2$ and the factor $C \simeq 50/27$ accounts for the charged particles running in the loop. Decay of scalars would contribute to the extragalactic background light (EBL). EBL constraints have been calculated in [121, 43] and recast for a Higgs portal in [183]. Note that these constrains are calculated assuming a given present day DM density $Y_\phi = n_\phi/s_\gamma$, where $s_{\gamma,0}$ is the entropy density of photons today. The actual parameter constrained is $m_\phi n_\phi \Gamma_\phi$ as a function of m_ϕ. We rescale our constraints assuming $\Omega_\phi = \Omega_{DM} \simeq 0.26$ i.e. $Y_\phi = 0.26 \frac{\rho_c}{s_{\gamma,0}} m_\phi$, where ρ_c is the critical energy density of universe today.

4.4.5 X-ray Constraints

For $m_\phi \gtrsim$ few keV, the scalar decay to photons on cosmological time scales is constrained by the HEAO [216] and INTEGRAL [100] satellites. The data from these satellites was translated into lifetime of scalar decaying into photons in [175] and we use translate these constraints on the lifetime of our scalar $\tau_\phi = \Gamma^{-1}_{\phi\gamma\gamma}$ given by Eq. (4.4.7).

4.4.6 Other Probes

There are other constraints that we have not shown because they lie outside the shown mass range, or lie in the forbidden region $A > \sqrt{2\lambda} m_\phi$. These include atomic and nuclear clocks, atomic interferometers, mechanical resonators, superradiance etc. A comprehensive summary of all constraints can be found in [39].

4.5 Conclusions

In this work we have revisited the cosmology of a light scalar feebly coupled to the SM through the super-renormalizable Higgs portal. This is among the most minimal UV complete extensions of the SM and is described by only two additional parameters, the scalar mass m_ϕ and its dimensionful coupling to the Higgs A. The scalar field in this model can naturally be light due to its feeble super-renormalizable coupling. Despite being minimal, the model presents a rich cosmology, with the scalar field experiencing a non-trivial dynamical evolution during the radiation era before and/or during scalar oscillations. This generates two additional dynamical sources of misalignment, which we have referred to as thermal misalignment and VEV misalignment, beyond that from its initial field value at the end of inflation. We have studied the evolution of the scalar field both numerically and analytically over a broad range of scalar masses and couplings, delineating the parameters in the $m_\phi - A$ plane that are consistent with the observed DM relic density. We have also investigated two qualitatively distinct choices of initial scalar field values in order to discern the role played by initial conditions. Our main results are presented in Figure 21.

For large masses, the scalar field evolution is mainly governed by thermal misalignment. The finite-temperature contribution to the effective potential drives the scalar towards large field values at high temperatures, dynamically generating misalignment. Provided the initial scalar field value is smaller in magnitude than its displacement caused by thermal misalignment, the scalar relic density in this higher mass range is insensitive to the initial conditions. The scalar abundance today is then tightly controlled by the model parameters m_ϕ and A.

Therefore, parameters in the mass-coupling plane yielding the observed relic abundance then provide a robust target that can be compared against experimental searches for ultra-light scalar DM. Furthermore, the relic density line in this mass range can be viewed as an upper bound on the scalar-Higgs coupling assuming a standard cosmology with a high enough reheat temperature, as any larger coupling would overclose the universe. These features are quite similar in character to those of the popular WIMP DM scenario, in which the relic abundance is insensitive to initial conditions and UV dynamics, instead being set by the WIMP mass and its couplings to SM particles through the mechanism of thermal freeze-out. The insensitivity to initial conditions in the high scalar mass range is evident from Figure 21.

For lower scalar masses, the impact of the EWPT on the scalar field evolution is important. The phase transition leads to a rapid shift in the scalar field potential minimum towards its zero-temperature VEV, generating VEV misalignment. However, in this regime the oscillation amplitude and corresponding relic density is also sensitive to the initial conditions and depends on whether the scalar field is initially in close proximity to its zero temperature minimum or not. In the former case, which can be naturally realized for a long period of inflation with a low inflationary Hubble parameter (smaller than the electroweak scale v), relatively large couplings are needed to significantly displace the field from its minimum and produce the observed DM abundance, thus offering more promising detection prospects. Instead, if the field is initially distant from its zero temperature VEV, the required coupling can be extremely small while still leading to a consistent DM cosmology.

In the intermediate mass range we have discovered a novel forced resonance phenomena resulting from a competition between thermal misalignment and VEV misalignment. This causes enhancements or suppressions in the oscillation amplitude depending on the scalar mass, thus requiring smaller or larger couplings, respectively, to achieve the correct DM abundance. This is reflected by a series of peaks and valleys in the DM relic density contours as the scalar mass varies; see Figure 21.

We have also compared our relic density predictions with constraints and projections from a variety of terrestrial and astrophysical probes, including the equivalence principle and inverse square law tests, stellar cooling, resonant molecular absorption, and observations of extra-galactic background light and diffuse X-ray backgrounds. While some parts of the

parameter space are starting to be explored, new experimental ideas are needed to probe the cosmologically motivated regions of parameter space. We hope our results will provide the impetus for new creative approaches to ultralight scalar DM detection.

5.0 On the origin of entropy of gravitationally produced dark matter: the entanglement entropy.

5.1 Introduction

The convergence of evidence for dark matter (DM) from cosmic microwave background (CMB) anisotropies, galactic rotation curves, gravitational lensing, Bullet cluster, large scale surveys and numerical evolution of galaxy formation is very compelling. It is also evident from its properties that a particle physics candidate must be sought in extensions beyond the Standard Model (SM). However, a multi decade effort for its direct detection has not yet led to an unambiguous identification of a (DM) particle[85, 137]. A suitable particle physics candidate must feature a production mechanism yielding the correct abundance and equation of state, and satisfy the cosmological and astrophysical constraints with a lifetime of at least the age of the Universe. So far, all of the available evidence is consistent with dark matter interacting solely with gravity.

Among the various production mechanisms, particle production as a consequence of cosmological expansion is a remarkable phenomenon that has been studied in pioneering work in refs.[294, 184, 214, 89, 189, 297, 288]. An important aspect of this mechanism is that if the particle interacts only with gravity and no other degrees of freedom, its abundance is determined solely by the particle mass, its coupling to gravity, and the expansion history, independently of hypothetical couplings beyond the (SM). As such, production via cosmological expansion provides a baseline for the abundance and clustering properties of dark matter candidates.

Gravitational production has been studied for various candidates and different cosmological settings: heavy particles produced adiabatically during inflation[130, 127, 129, 256, 257, 128, 170, 169, 281], or via inflaton oscillations[312], during reheating[225, 259, 30, 242, 34], or via cosmological expansion during an era with a particular equation of state[260]. More recently the non-adiabatic cosmological production of ultralight bosonic particles[226] and heavy fermionic particles [103] were studied during inflation followed by a radiation domi-

nated era. This chapter is based on Ref. [304].

Motivations, main objectives and brief summary of results.

Non-adiabatic gravitational production of both ultra light bosonic dark matter and a heavier fermionic dark matter species were studied in references[226, 103] with initial "in" conditions during inflation with the respective fields in their Bunch-Davies vacuum state, evolving to asymptotic "out" particle states in the radiation dominated (RD) era. The asymptotic "out" particle states feature pair correlations and the distribution function is obtained from the Bogoliubov coefficients relating the "in" to the "out" states which were obtained in these references. Well after the transition from inflation to (RD) and well before matter radiation equality, when the scale factor $a_{eq} \simeq 10^{-4} \gg a(t) \gg 10^{-17}/\sqrt{m/(\mathrm{eV})}$ there ensues an adiabatic regime during which the Hubble expansion rate $H(t)$ is much smaller than the mass m of the dark matter particle. It is shown in these references that during the adiabatic regime, and after averaging rapid oscillations in interference terms, the energy momentum tensor of these dark matter particles feature the kinetic-fluid form. Furthermore, in the case of fermionic dark matter, ref.[103] found that the distribution function features an unexpected near thermality.

These results motivate the main questions addressed in this chapter: a kinetic-fluid description in terms of a distribution function typically also includes the entropy[83], which along with the energy density and pressure provide an effective statistical description of the "fluid", as in thermodynamics. In this study we address the *origin of entropy* associated with this kinetic fluid description.

At *prima facie* the question of entropy within the context of gravitational production seems surprising because the "in" state of dark matter is the vacuum state during inflation, therefore the density matrix describes a pure state with vanishing entropy. While this is true, the study in refs.[226, 103] revealed that during the adiabatic regime and in the basis of asymptotic "out" particles, the energy momentum tensor features contributions that evolve on widely different time scales: a slow time scale associated with the cosmological expansion $\simeq 1/H(t)$ and a fast time scale $\simeq 1/m$ associated with the dynamics of the "out" particle states. The latter one is manifest in specific interference terms in pair correlations which *dephase* on the rapid time scale $\simeq 1/m$. As shown explicitly in refs.[226, 103], the kinetic-fluid

form emerges upon *averaging* these rapidly varying correlations on the longer time scales. The wide separation of these two time scales is precisely the hallmark of the adiabatic regime that sets in well before matter radiation equality. In this chapter we study whether and how this rapid dephasing phenomena stemming from interference in the asymptotic "out" state heralds a decoherence mechanism, and how such mechanism entails loss of information and a non-vanishing entropy.

Brief summary of results: Following up on the study of refs.[226, 103], we consider the non-adiabatic gravitational production of an ultra light complex scalar field minimally coupled to gravity and a heavier fermionic Dirac field under the same set of minimal assumptions considered in these references. The cosmological expansion results in the production of *entangled* correlated asymptotic "out" particle-antiparticle pairs of vanishing total momentum.

During the adiabatic regime, we introduce an effective Schroedinger picture that implements a separation of the widely different time scales, the rapid time scale is included in the time evolution of the density matrix, whereas the slow time scale is associated with operators. The Bogoliubov transformation that relates the "in" to the "out" states relates the Schroedinger picture density matrix in the "in" basis to the "out" basis. Off-diagonal density matrix elements in the "out" basis feature fast dephasing on short time scales $\simeq 1/m$, leading to decoherence and information loss, effectively reducing the density matrix to a diagonal form in this basis, and consequently to a non-vanishing von Neumann entropy. This rapid dephasing and decoherence in the density matrix is a direct manifestation of the interference terms in the energy momentum tensor in the out basis and the emergence of its kinetic fluid form.

We show that because gravitational production results in correlated particle-antiparticle pairs, the von Neumann entropy resulting from dephasing and decoherence is precisely the *entanglement entropy* obtained by tracing the density matrix over one member of the pairs. Remarkably, the entanglement entropy is similar to the quantum kinetic expression in terms of the distribution function with noteworthy differences arising from the intrinsic pair correlations in the out states. We find that the comoving entropy density in terms of the

distribution function of produced particles, N_k, is given by

$$\mathcal{S} = \pm \frac{1}{2\pi^2} \int_0^\infty k^2 \Big\{ (1 \pm N_k)\, \ln(1 \pm N_k) \mp N_k\, \ln N_k \Big\} dk\,,$$

where $(+)$ is for *real or complex* bosons and $(-)$ is for each spin/helicity of *Dirac or Majorana* fermions. If the "out" states were *independent* particles and/or antiparticles, complex bosons and Dirac fermions would have twice the number of degrees of freedom of real bosons and Majorana fermions and the entropy would feature an extra factor 2 when particles are different from antiparticles. The fact that the entropy is the same regardless of whether particles are the same as antiparticles or not is a consequence of the *pair correlations* of the "out" state. These pairs are entangled in momentum (and spin/helicity for fermions), tracing out any member of the pair yields the same entanglement entropy regardless of whether the member is a particle or an antiparticle. Therefore, the von Neumann-entanglement-entropy and the kinetic fluid form of the energy momentum are all a direct consequence of decoherence of the density matrix in the out basis by dephasing.

We discuss the role of the "out" particle basis as a privileged or "pointer" basis, to describe the statistical aspects of dark matter, it is preferred by the measurement of the properties of dark matter "particles".

For a minimally coupled ultra light scalar field gravitational production yields a distribution function that is strongly peaked in the infrared[226]. In this case we find that the specific entropy (entropy per particle) is vanishingly small, this is a hallmark of a *condensed phase* albeit with a vanishing expectation value of the field. For fermionic dark matter, the distribution function is nearly thermal[103] and the specific entropy is $\mathcal{O}(1)$ in agreement with a nearly thermal (but cold) dark matter candidate.

Although we have studied the origin of entropy within these two specific examples, we argue that the emergence of entropy in the production of dark matter from the time evolution of an initial pure state is more generally valid and the mechanism of decoherence by dephasing is common to several alternative proposed mechanisms of particle production in cosmology.

We note that cosmological particle production and entanglement entropy have previously been considered for inflationary perturbations[195, 194, 196, 111, 110, 108, 265, 101], in cosmological particle production[268], and as scenarios of quantum information concepts

applied to model cosmologies[278, 54, 188, 275]. However, to the best of our knowledge the origin of entropy has not yet been addressed for non-adiabatic gravitational production of dark matter during inflation followed by a post inflation radiation dominated cosmology, which is the focus of our study.

For self-consistency, completeness and continuity of presentation, sections (5.3) and (5.4) include some of the most relevant technical aspects that are discussed in greater detail in refs.([226, 103]).

5.2 Preliminaries:

We consider a similar cosmological setting as in refs.[226, 103], namely a spatially flat Friedmann-Robertson-Walker cosmology in conformal time η with metric

$$g_{\mu\nu}(\eta) = a^2(\eta)\,\mathrm{diag}(1,-1,-1,-1)\,. \tag{5.2.1}$$

The assumptions adopted from these references are: **i:)** the dark matter particle only interacts with gravity but no other degrees of freedom and the dark matter field does not develop an expectation value, **ii:)** instantaneous transition from inflation to a post-inflation radiation dominated era, motivated by the consideration of modes that are super-Hubble at the end of inflation, **iii:)** we take the cosmological dynamics as a *background*: during inflation it is determined by the inflaton field, and during radiation domination (RD) by the more than $\simeq 100$ degrees of freedom of the (SM) (and beyond), **iv:)** we take all dark matter fields to be in their (Bunch-Davies) vacuum state during inflation.

The inflationary stage is described by a de Sitter space time (thereby neglecting slow roll corrections) with a scale factor

$$a(\eta) = -\frac{1}{H_{dS}(\eta - 2\eta_R)}\,, \tag{5.2.2}$$

where H_{dS} is the Hubble constant during de Sitter and η_R is the (conformal) time at which the de Sitter stage transitions to the (RD) stage.

During the (RD) stage

$$H(\eta) = \frac{1}{a^2(\eta)}\frac{da(\eta)}{d\eta} = 1.66\sqrt{g_{eff}}\,\frac{T_0^2}{M_{Pl}\,a^2(\eta)}\,, \tag{5.2.3}$$

where g_{eff} is the effective number of ultrarelativistic degrees of freedom, which varies in time as different particles become non-relativistic. We take $g_{eff} = 2$ corresponding to radiation today. As discussed in references [226, 103] by taking $g_{eff} = 2$ for a fixed dark matter particle mass, one obtains a *lower bound* on the (DM) abundance and equation of state, differing by a factor of $\mathcal{O}(1)$ from the abundance if the (RD) era is dominated only by (SM) degrees of freedom. This discrepancy is not relevant for our study on the origin of entropy.

With this approximation the scale factor during radiation domination is given by

$$a(\eta) = H_R\,\eta\,, \tag{5.2.4}$$

with

$$H_R = H_0\,\sqrt{\Omega_R} \simeq 10^{-35}\,\text{eV}\,, \tag{5.2.5}$$

and matter radiation equality occurs at

$$a_{eq} = \frac{\Omega_R}{\Omega_M} \simeq 1.66\,\times 10^{-4}\,. \tag{5.2.6}$$

The result (5.2.5) corresponds to the value of the fraction density Ω_R *today*, thereby neglecting the change in the number of degrees of freedom contributing to the radiation density fraction. For g_{eff} effective ultrarelativistic degrees of freedom, eqn. (5.2.5) must be multiplied by $\sqrt{g_{eff}/2}$. However, as discussed in references[226, 103] accounting for ultrarelativistic degrees of freedom of the (SM) at the time of the transition between inflation and (RD) modifies the final abundance by a factor of $\mathcal{O}(1)$ and affects the entropy only at a quantitative level by factors of $\mathcal{O}(1)$.

We require that the scale factor and the Hubble rate be continuous across the transition from inflation to (RD) at conformal time η_R, and assume (self-consistently) that the transition occurs deep in the (RD) era so that $a(\eta_R) = H_R\,\eta_R \ll a_{eq}$. Continuity of the scale factor and Hubble rate at the instantaneous reheating time results in that the energy density is continuous at the transition[226, 103].

Using $H(\eta) = a'(\eta)/a^2(\eta)$, continuity of the scale factor and Hubble rate at η_R imply that

$$a_{dS}(\eta_R) = \frac{1}{H_{dS}\,\eta_R} = H_R\,\eta_R \quad ; \quad H_{dS} = \frac{1}{H_R\,\eta_R^2}\,, \tag{5.2.7}$$

yielding

$$\eta_R = \frac{1}{\sqrt{H_{dS}\,H_R}}\,. \tag{5.2.8}$$

Constraints from Planck[26] on the tensor-to-scalar ratio yield the following upper bound on the scale of inflation H_{dS},

$$H_{dS}/M_{Pl} < 2.5 \times 10^{-5} \quad (95\%)\,\mathrm{CL}\,. \tag{5.2.9}$$

We take as a representative value $H_{dS} = 10^{13}\,\mathrm{GeV}$, from which it follows that

$$a_{dS}(\eta_R) = H_R\,\eta_R = \sqrt{\frac{H_R}{H_{dS}}} \simeq 10^{-28} \ll a_{eq}\,, \tag{5.2.10}$$

consistently with our assumption that the transition from inflation occurs deep in the (RD) era.

With $H_{dS} \simeq 10^{13}\,\mathrm{GeV}, H_R \simeq 10^{-35}\,\mathrm{eV}$ it follows that $\eta_R \simeq 10^6/(\mathrm{eV})$. In our analysis we will consider solely modes that are super-Hubble at the end of inflation, namely with comoving wavevectors k such that

$$k\,\eta_R \ll 1\,, \tag{5.2.11}$$

corresponding to comoving wavelengths $\lambda \gg$ few mts. Therefore, all scales of cosmological relevance today correspond to super-Hubble wavelengths at the end of inflation.

The consideration of solely super-Hubble modes provides an *a priori* justification for the assumption of an instantaneous transition from inflation to (RD). These modes feature very slow dynamics and in principle are causally disconnected from microphysical processes, such as collisional thermalization, occurring on sub-Hubble scales. These considerations suggest that these cosmologically relevant modes are insensitive to the reheating dynamics post-inflation, thereby bypassing the model dependence of reheating mechanisms[30, 34] and the rather uncertain dynamics of thermalization of (SM) degrees of freedom, which depends on couplings and non-equilibrium aspects.

5.3 Complex Scalar Fields

We begin by considering an ultra light complex scalar field ϕ minimally coupled to gravity, generalizing the study in ref.[226]. The action in comoving coordinates is given by

$$S = \int d^3x dt \sqrt{-g} \left\{ \frac{\partial \phi^\dagger}{\partial t} \frac{\partial \phi}{\partial t} - \frac{1}{a^2} \nabla\phi^\dagger \nabla\phi - m^2 \phi^\dagger \phi \right\}. \tag{5.3.1}$$

Changing coordinates to conformal time η with metric (5.2.1), conformally rescaling the scalar field

$$\phi(\vec{x}, \eta) = \frac{\chi(\vec{x}, \eta)}{a(\eta)}, \tag{5.3.2}$$

and after discarding a total surface term the action becomes

$$S = \int d^3x d\eta \left\{ \chi^{\dagger\prime} \chi' - \nabla\chi^\dagger \nabla\chi - M^2(\eta) \chi^\dagger \chi \right\} \tag{5.3.3}$$

where $' \equiv \frac{d}{d\eta}$, and

$$M^2(\eta) = m^2 a^2(\eta) - \frac{a''(\eta)}{a(\eta)}. \tag{5.3.4}$$

Quantization of the complex scalar field in a comoving volume V is achieved by writing

$$\chi(\vec{x}, \eta) = \frac{1}{\sqrt{V}} \sum_{\vec{k}} \left[a_{\vec{k}}\, g_k(\eta)\, e^{-i\vec{k}\cdot\vec{x}} + b^\dagger_{\vec{k}}\, g^*_k(\eta)\, e^{i\vec{k}\cdot\vec{x}} \right], \tag{5.3.5}$$

where the mode functions $g_k(\eta)$ obey the equations of motion

$$g''_k(\eta) + \left[k^2 + m^2\, a^2(\eta) - \frac{a''(\eta)}{a(\eta)} \right] g_k(\eta) = 0, \tag{5.3.6}$$

and satisfy the Wronskian conditions

$$g'_k(\eta)\, g^*_k(\eta) - g_k(\eta)\, g'^*_k(\eta) = -i, \tag{5.3.7}$$

which imply canonical commutation relations for the annihilation and creation operators in the expansion (5.3.5).

5.3.1 "In-out" states, adiabatic mode functions and particle states.

The mode equation (5.3.6) can be written in the more familiar form as

$$-\frac{d^2}{d\eta^2}\, g_k(\eta) + V(\eta) g_k(\eta) = k^2 g_k(\eta) \quad ; \quad V(\eta) = -m^2 a^2(\eta) + \frac{a''(\eta)}{a(\eta)}\,, \tag{5.3.8}$$

namely a Schroedinger equation for a wave function g_k with a potential $V(\eta)$ and "energy" k^2. The potential $V(\eta)$ and/or its derivative are discontinuous at the transition η_R; however $g_k(\eta)$ and $g'_k(\eta)$ are continuous at η_R. Defining

$$g_k(\eta) = \begin{cases} g_k^{<}(\eta) \;\; ; \;\; \text{for} \;\; ; \;\; \eta < \eta_R \\ g_k^{>}(\eta) \;\; ; \;\; \text{for} \;\; ; \;\; \eta > \eta_R \end{cases}\,, \tag{5.3.9}$$

the matching conditions are

$$\begin{aligned} g_k^{<}(\eta_R) &= g_k^{>}(\eta_R) \\ \frac{d}{d\eta} g_k^{<}(\eta)\Big|_{\eta_R} &= \frac{d}{d\eta} g_k^{>}(\eta)\Big|_{\eta_R}\,. \end{aligned} \tag{5.3.10}$$

As discussed in ref.[226] these continuity conditions on the mode functions, along with the continuity of the scale factor and Hubble rate ensure that the energy density is *continuous* at the transition from inflation to (RD).

5.3.1.1 Inflationary stage:

We consider that the (DM) scalar field is in the Bunch-Davies vacuum state during the inflationary stage, which corresponds to the mode functions $g_k(\eta)$ fulfilling the boundary condition

$$g_k(\eta) \quad \xrightarrow[\eta\to-\infty]{} \quad \frac{e^{-ik\eta}}{\sqrt{2k}}\,, \tag{5.3.11}$$

and the Bunch-Davies vacuum state $|0_I\rangle$ is such that

$$a_{\vec{k}}\,|0_I\rangle = 0 \quad ; \quad b_{\vec{k}}\,|0_I\rangle = 0 \;\forall \vec{k}\,. \tag{5.3.12}$$

We refer to this vacuum state as the *in* vacuum.

During the de Sitter stage ($\eta < \eta_R$), with the scale factor given by eqn. (5.2.2), the mode equation becomes

$$\frac{d^2}{d\tau^2}\,g^<_k(\tau) + \left[k^2 - \frac{\nu^2 - 1/4}{\tau^2}\right] g^<_k(\tau) = 0\,, \tag{5.3.13}$$

where

$$\tau = \eta - 2\eta_R \quad ; \quad \nu^2 = \frac{9}{4} - \frac{m^2}{H^2_{dS}}\,. \tag{5.3.14}$$

The solution with the boundary condition (5.3.11) fulfilling the Wronskian condition (5.3.7) is given by

$$g^<_k(\tau) = \frac{1}{2}\,\sqrt{-\pi\tau}\; e^{i\frac{\pi}{2}(\nu+1/2)}\, H^{(1)}_\nu(-k\tau) \tag{5.3.15}$$

where $H^{(1)}_\nu$ is a Hankel function. For ultra light dark matter with the correct abundance, the result of ref.[226] yields $m \simeq 10^{-5}\,(\text{eV})$, therefore, with $H_{dS} \simeq 10^{13}\,\text{GeV}$ it follows that $m/H_{dS} \ll 1$, hence we can take $\nu = 3/2$, yielding

$$g^<_k(\tau) = \frac{e^{-ik\tau}}{\sqrt{2k}}\left[1 - \frac{i}{k\tau}\right]. \tag{5.3.16}$$

As mentioned in the previous section, we consider only comoving wavelengths that are *well outside* the Hubble radius at the end of inflation, namely fulfilling the condition (5.2.11), these describe all the relevant astrophysical scales today.

In summary, the "*in*" state is the Bunch-Davies vacuum defined by equation (5.3.12) and the mode functions (5.3.16) during the de Sitter inflationary stage.

5.3.1.2 Radiation dominated era:

During the radiation era for $\eta > \eta_R$, with $a(\eta) = H_R \eta$ we set $a'' = 0$, and the mode equation (5.3.6) becomes

$$\frac{d^2}{d\eta^2} g_k^>(\eta) + \left[k^2 + m^2 H_R^2 \eta^2\right] g_k^>(\eta) = 0\,, \tag{5.3.17}$$

the general solutions of which are linear combinations of parabolic cylinder functions[226, 209, 15, 293, 70, 276]. As "out" boundary conditions, we consider particular solutions that describe asymptotically positive frequency "particle" states, their complex conjugate describe antiparticles. This identification relies on a Wentzel-Kramers-Brillouin (WKB) form of the asymptotic mode functions.

Let us consider a particular solution of (5.3.17) of the WKB form[89]

$$f_k(\eta) = \frac{e^{-i\int_{\eta_R}^{\eta} W_k(\eta')\, d\eta'}}{\sqrt{2\, W_k(\eta)}}\,. \tag{5.3.18}$$

Upon inserting this ansatze in the mode equation (5.3.17) one finds that $W_k(\eta)$ obeys

$$W_k^2(\eta) = \omega_k^2(\eta) - \frac{1}{2}\left[\frac{W_k''(\eta)}{W_k(\eta)} - \frac{3}{2}\left(\frac{W_k'(\eta)}{W_k(\eta)}\right)^2\right], \tag{5.3.19}$$

where

$$\omega_k^2(\eta) = k^2 + m^2 H_R^2 \eta^2\,. \tag{5.3.20}$$

When $\omega_k(\eta)$ is a slowly-varying function of time the WKB eqn. (6.2.24) may be solved in a consistent *adiabatic expansion* in terms of derivatives of $\omega_k(\eta)$ with respect to η divided by appropriate powers of the frequency, namely

$$W_k^2(\eta) = \omega_k^2(\eta)\left[1 - \frac{1}{2}\frac{\omega_k''(\eta)}{\omega_k^3(\eta)} + \frac{3}{4}\left(\frac{\omega_k'(\eta)}{\omega_k^2(\eta)}\right)^2 + \cdots\right]. \tag{5.3.21}$$

We refer to terms that feature n-derivatives of $\omega_k(\eta)$ as of n-th adiabatic order. During the time interval of rapid variations of the frequencies the concept of particle is ambiguous, but at long time the frequencies evolve slowly and the concept of particle becomes clear[226].

We want to identify "particles" (dark matter "particles") near the time of matter radiation equality, so that entering in the matter dominated era when $a(\eta) \simeq a_{eq} \simeq 10^{-4}$, we can extract the energy momentum tensor associated with these *particles*.

The condition of adiabatic expansion relies on the ratio

$$\frac{\omega_k^{'}(\eta)}{\omega_k^2(\eta)} \ll 1\,. \tag{5.3.22}$$

An upper bound on this ratio is obtained in the very long wavelength (superhorizon) limit, taking $\omega_k(\eta) = m\,a(\eta)$, in a (RD) cosmology the adiabaticity condition (5.3.22) leads to

$$\frac{a'(\eta)}{m\,a^2(\eta)} = \frac{H_R}{m\,a^2(\eta)} \ll 1 \Longrightarrow a(\eta) \gg \frac{10^{-17}}{\sqrt{m/(eV)}}\,. \tag{5.3.23}$$

Therefore, for $m \simeq 10^{-5}\,\text{eV}$ corresponding to $a(\eta) \simeq 10^{-14}$ there is a long period of *non-adiabatic* evolution since the end of inflation $a(\eta_R) \simeq 10^{-29} \ll 10^{-14}$, during which the $\omega_k(\eta)$ varies *rapidly*. However, even for an ultra-light particle with $m \simeq 10^{-5}\,(\text{eV})$ the adiabaticity condition is fulfilled well before matter-radiation equality.

The adiabaticity condition (5.3.23) has an important physical interpretation. Since $a'/a^2 = H(t) = 1/d_H(t)$ is the Hubble expansion rate with d_H the Hubble radius (both in comoving time) it follows that the condition (5.3.23) implies that

$$\frac{H(t)}{m} \ll 1 \;\text{ or }\; \frac{\lambda_c}{d_H(t)} \ll 1\,, \tag{5.3.24}$$

where λ_c is the Compton wavelength of the particle. During radiation or matter domination $d_H(t)$ is proportional to the physical particle horizon, therefore the adiabaticity condition is the statement that the Compton wavelength of the particle is much smaller than the physical particle horizon. The adiabaticity condition becomes less stringent for $k \gg m\,a(\eta)$, in which case it implies that the comoving de Broglie wavelength is much smaller than the particle horizon. The evolution of the mode functions is non-adiabatic during inflation and for a period after the transition to (RD)[226, 103], but becomes adiabatic well before matter radiation equality.

During the adiabatic regime the WKB mode function (6.2.23) asymptotically becomes

$$f_k(\eta) \to \frac{e^{-i\int^\eta \omega_k(\eta')\,d\eta'}}{\sqrt{2\,\omega_k(\eta)}}\,. \tag{5.3.25}$$

We refer to the mode functions with this asymptotic boundary condition that fulfill the Wronskian condition

$$f_k^{'}(\eta)\, f_k^{*}(\eta) - f_k(\eta)\, f_k^{'*}(\eta) = -i\,, \tag{5.3.26}$$

as "out" particle states. As discussed in refs.[226, 103] this criterion is the closest to the particle characterization in Minkowski space-time.

The general solution of equation (5.3.17) is a linear combination

$$g_k^{>}(\eta) = A_k\, f_k(\eta) + B_k\, f_k^{*}(\eta)\,, \tag{5.3.27}$$

where $f_k(\eta)$ are the solutions of the mode equation (5.3.17) with the asymptotic boundary conditions (6.2.21) and A_k and B_k are Bogoliubov coefficients. Since $g_k^{>}(\eta)$ obeys the Wronskian condition (5.3.7) and so does $f_k(\eta)$, it follows that the Bogoliubov coefficients obey

$$|A_k|^2 - |B_k|^2 = 1\,. \tag{5.3.28}$$

Using the Wronskian condition (5.3.26) and the matching condition (5.3.10), the Bogoliubov coefficients are determined from the following relations,

$$\begin{aligned} A_k &= i\Big[g_k^{'<}(\eta_R)\, f_k^{*}(\eta_R) - g_k^{<}(\eta_R)\, f_k^{'*}(\eta_R)\Big] \\ B_k &= -i\Big[g_k^{'<}(\eta_R)\, f_k(\eta_R) - g_k^{<}(\eta_R)\, f_k^{'}(\eta_R)\Big]\,. \end{aligned} \tag{5.3.29}$$

Since the mode functions $g_k^{<}(\eta)$ also fulfill the Wronskian condition (5.3.7), it is straightforward to confirm the identity (5.3.28).

For $\eta > \eta_R$ the field expansion (5.3.5) yields

$$\chi(\vec{x},\eta) = \frac{1}{\sqrt{V}}\sum_{\vec{k}}\Big[a_{\vec{k}}\, g_k^{>}(\eta)\, e^{i\vec{k}\cdot\vec{x}} + b^{\dagger}_{\vec{k}}\, g_k^{*>}(\eta)\, e^{-i\vec{k}\cdot\vec{x}}\Big] = \frac{1}{\sqrt{V}}\sum_{\vec{k}}\Big[c_{\vec{k}}\, f_k(\eta)\, e^{i\vec{k}\cdot\vec{x}} + d^{\dagger}_{\vec{k}}\, f_k^{*}(\eta)\, e^{-i\vec{k}\cdot\vec{x}}\Big]\,, \tag{5.3.30}$$

where

$$c_{\vec{k}} = a_k\, A_k + b^{\dagger}_{-\vec{k}}\, B_k^{*} \;\;;\;\; d^{\dagger}_{\vec{k}} = b^{\dagger}_{\vec{k}}\, A_k^{*} + a_{-\vec{k}}\, B_k\,. \tag{5.3.31}$$

We refer to $c_{\vec{k}}, d_{\vec{k}}$ and $c^{\dagger}_{\vec{k}}, d^{\dagger}_{\vec{k}}$ as the annihilation and creation operators of *out particle and antiparticle* states respectively and the mode functions $f_k(\eta)$ as defining the out basis. These operators obey canonical quantization conditions as a consequence of the relation (5.3.28) and

are time independent because the mode functions $f_k(\eta)$ are exact solutions of the equations of motion. The expectation values of bilinears in c, d in the Bunch-Davies vacuum state $|0_I\rangle$ (5.3.12) are obtained from the relations (5.3.31), we find

$$\langle 0_I|\, c^\dagger_{\vec{k}}\, c_{\vec{k}'}\, |0_I\rangle = |B_k|^2\, \delta_{\vec{k},\vec{k}'} \quad ; \quad \langle 0_I|\, d^\dagger_{\vec{k}}\, d_{\vec{k}'}\, |0_I\rangle = |B_k|^2\, \delta_{\vec{k},\vec{k}'} \quad ; \quad \langle 0_I|\, c^\dagger_{\vec{k}}\, d^\dagger_{-\vec{k}'}\, |0_I\rangle = B_k\, A^*_k\, \delta_{\vec{k},\vec{k}'} \tag{5.3.32}$$

with all others vanishing. In particular the number of *out*-particles and anti-particles are given by

$$N_k = \langle 0_I|\, c^\dagger_{\vec{k}}\, c_{\vec{k}}\, |0_I\rangle = |B_k|^2 = \overline{N}_k = \langle 0_I|\, d^\dagger_{\vec{k}}\, d_{\vec{k}}\, |0_I\rangle\ . \tag{5.3.33}$$

We identify $N_k = \overline{N}_k$ with the number of dark matter particles and antiparticles produced *asymptotically* from cosmic expansion. Gravitational production yields the same number of particles as antiparticles. Only in the asymptotic adiabatic regime can N_k be associated with the number of *particles* (for a more detailed discussion on this point see ref.[226]).

It remains to obtain the solutions $f_k(\eta)$ of the mode equations (5.3.17) with asymptotic "out" boundary condition (6.2.21) describing asymptotic particle states.

It is convenient to introduce the dimensionless variables

$$x = \sqrt{2mH_R}\,\eta \quad ; \quad \alpha = -\frac{k^2}{2mH_R}\,, \tag{5.3.34}$$

in terms of which the equation (5.3.17) becomes Weber's equation[15, 293, 70, 276]

$$\frac{d^2}{dx^2}\, f(x) + \Big[\frac{x^2}{4} - \alpha\Big] f(x) = 0\,. \tag{5.3.35}$$

The solution that satisfies the Wronskian condition (5.3.26) and features the asymptotic "out-state" behavior (6.2.21) with $\omega^2_k(\eta) = \frac{x^2}{4} - \alpha$, has been obtained in ref.([226]) in terms of Weber's function $W[\alpha; x]$[209, 15, 293]. It is given by

$$f_k(\eta) = \frac{1}{(8mH_R)^{1/4}} \Big[\frac{1}{\sqrt{\kappa}}\, W[\alpha; x] - i\sqrt{\kappa}\, W[\alpha; -x]\Big] \quad ; \quad \kappa = \sqrt{1 + e^{-2\pi|\alpha|}} - e^{-\pi|\alpha|}\,. \tag{5.3.36}$$

The Bogoliubov coefficients are obtained from eqns. (5.3.29), where the mode functions during the de Sitter era, $g^<_k(\eta)$, are given by eqn. (5.3.16) (with $\tau = \eta - 2\eta_R$). Here we just quote the result for $|B_k|^2$ referring the reader to [226] for details. In terms of the variable

$$z = \frac{k}{[2mH_R]^{1/2}}\,, \tag{5.3.37}$$

it is given by

$$N_k = |B_k|^2 \simeq \frac{1}{16\sqrt{2}} \left(\frac{H_{dS}}{m}\right)^2 \frac{D(z)}{z^3} \,. \tag{5.3.38}$$

where

$$D(z) = \sqrt{1+e^{-2\pi z^2}} \left| \frac{\Gamma\left(\frac{1}{4} - i\frac{z^2}{2}\right)}{\Gamma\left(\frac{3}{4} - i\frac{z^2}{2}\right)} \right| . \tag{5.3.39}$$

This function is analyzed in ref.[226] but the only properties that are relevant for our discussion are that $D(0) \simeq 4.2$ and that $D(z) \to \sqrt{2}/z$ for $z \gg 1$. The infrared enhancement of $N_k \propto 1/k^3$ and the prefactor $H_{dS}/m \gg 1$ are both consequences of a minimally coupled light scalar field during inflation[226] and results in a distribution function that is strongly peaked with $N_k \gg 1$ for $z \ll \sqrt{H_{dS}/m}$.

5.3.2 Heisenberg vs. adiabatic Schrodinger pictures

In the adiabatic regime the mode functions $f_k(\eta)$ with "out" boundary conditions can be written as

$$f_k(\eta) = \frac{e^{-i\int^\eta \omega_k(\eta')d\eta'}}{\sqrt{2\omega_k(\eta)}} \mathcal{F}_k(\eta) \quad ; \quad f_k'(\eta) = -i\omega_k(\eta) \frac{e^{-i\int^\eta \omega_k(\eta')d\eta'}}{\sqrt{2\omega_k(\eta)}} \mathcal{G}_k(\eta) \,, \tag{5.3.40}$$

where

$$\mathcal{F}_k(\eta) = e^{-i\left(\xi^{(1)}(\eta)+\xi^{(2)}(\eta)+\cdots\right)} \left[1 + \mathcal{F}_k^{(1)}(\eta) + \mathcal{F}_k^{(2)}(\eta) + \cdots\right] , \tag{5.3.41}$$

$$\mathcal{G}_k(\eta) = e^{-i\left(\xi^{(1)}(\eta)+\xi^{(2)}(\eta)+\cdots\right)} \left[1 + \mathcal{G}_k^{(1)}(\eta) + \mathcal{G}_k^{(2)}(\eta) + \cdots\right] . \tag{5.3.42}$$

The functions $\xi^{(n)}$ are real, and $\xi^{(n)}\,;\, \mathcal{F}_k^{(n)}\,;\, \mathcal{G}^{(n)}$ are of n-th adiabatic order and vanish in the asymptotic long time limit. During the adiabatic regime $\xi^{(n)}\,;\, \mathcal{F}(\eta)\,;\, \mathcal{G}(\eta)$ are *slowly varying* functions of η, whereas the phase $e^{-i\int^\eta \omega_k(\eta')d\eta'}$ varies rapidly during a Hubble time. To appreciate this latter point more clearly, consider the $k = 0$ case for which the phase is given in comoving time by $mt \simeq m/H(\eta) = m\,a^2/a' \gg 1$, were the last equality follows from the adiabaticity condition (5.3.23) during (RD). The important point is that during the adiabatic regime there is a wide separation of time scales: the expansion time scale $1/H(t)$ is much longer than the microscopic time scale $1/m$, namely $H(t)/m \ll 1$ which is precisely the adiabaticity condition.

This important point is at the heart of decoherence of the density matrix by dephasing discussed below.

With the slow-fast expansion of the out basis modes (5.3.40) the expansion of the complex field (5.3.30) in this basis in the Heisenberg representation is given by

$$\chi(\vec{x},\eta) = \sum_{\vec{k}} \frac{1}{\sqrt{2\omega_k(\eta)\,V}} \left[c_{\vec{k}}\, \mathcal{F}_k(\eta)\, e^{-i\int_{\eta_i}^{\eta} \omega_k(\eta')d\eta'}\, e^{i\vec{k}\cdot\vec{x}} + d^{\dagger}_{\vec{k}}\, \mathcal{F}^{*}_k(\eta)\, e^{i\int_{\eta_i}^{\eta} \omega_k(\eta')d\eta'}\, e^{-i\vec{k}\cdot\vec{x}} \right], \tag{5.3.43}$$

where η_i is some (arbitrary) early scale but well within the adiabatic regime. We note that a change of η_i may be absorbed into a canonical transformation of $c_{\vec{k}}, d_{\vec{k}}$. Let us introduce the *zeroth order* adiabatic Hamiltonian in the out basis

$$H_0(\eta) = \sum_{\vec{k}} \left[c^{\dagger}_{\vec{k}}\, c_{\vec{k}} + d^{\dagger}_{\vec{k}}\, d_{\vec{k}} \right] \omega_k(\eta)\,. \tag{5.3.44}$$

It follows that

$$[H_0(\eta), c_{\vec{k}}] = -\omega_k(\eta)\, c_{\vec{k}} \quad ; \quad [H_0(\eta), d_{\vec{k}}] = -\omega_k(\eta)\, d_{\vec{k}}\,. \tag{5.3.45}$$

Although $H_0(\eta)$ depends explicitly on time, it fulfills

$$[H_0(\eta), H_0(\eta')] = 0 \quad \forall \eta, \eta'\,. \tag{5.3.46}$$

Therefore, associated with H_0 we introduce the unitary time evolution operator

$$U_0(\eta,\eta_i) = e^{-i\int_{\eta_i}^{\eta} H_0(\eta')\, d\eta'}\,, \tag{5.3.47}$$

and from the commutation relations (5.3.45) it follows that

$$U_0^{-1}(\eta,\eta_i)\; c_{\vec{k}}\; U_0(\eta,\eta_i) = c_{\vec{k}}\, e^{-i\int_{\eta_i}^{\eta} \omega_k(\eta')d\eta'} \quad ; \quad U_0^{-1}(\eta,\eta_i)\; d_{\vec{k}}\; U_0(\eta,\eta_i) = d_{\vec{k}}\, e^{-i\int_{\eta_i}^{\eta} \omega_k(\eta')d\eta'}\,. \tag{5.3.48}$$

We can now write the Heisenberg picture field operator in the out basis (5.3.43) as

$$\chi(\vec{x},\eta) = U_0^{-1}(\eta,\eta_i)\; \chi_S(\vec{x},\eta)\; U_0(\eta,\eta_i)\,, \tag{5.3.49}$$

with the *adiabatic Schroedinger* picture field

$$\chi_S(\vec{x},\eta) = \sum_{\vec{k}} \frac{1}{\sqrt{2\omega_k(\eta)\,V}} \left[c_{\vec{k}}\, \mathcal{F}_k(\eta)\, e^{i\vec{k}\cdot\vec{x}} + d^{\dagger}_{\vec{k}}\, \mathcal{F}^{*}_k(\eta)\, e^{-i\vec{k}\cdot\vec{x}} \right]. \tag{5.3.50}$$

Similarly with the expansion (5.3.40) we find

$$\chi'(\vec{x},\eta) = U_0^{-1}(\eta,\eta_i)\ \Pi_S(\vec{x},\eta)\ U_0(\eta,\eta_i)\,, \tag{5.3.51}$$

where

$$\Pi_S(\vec{x},\eta) = \sum_{\vec{k}} \frac{-i\,\omega_k(\eta)}{\sqrt{2\omega_k(\eta)\,V}} \left[c_{\vec{k}}\,\mathcal{G}_k(\eta)\,e^{i\vec{k}\cdot\vec{x}} - d^\dagger_{\vec{k}}\,\mathcal{G}^*_k(\eta)\,e^{-i\vec{k}\cdot\vec{x}}\right]. \tag{5.3.52}$$

This is the Schroedinger picture version of the adiabatic expansion, $\chi_S(\vec{x},\eta)\,;\,\Pi_S(\vec{x},\eta)$ evolve slowly, on time scales $\simeq 1/H(t)$ in the adiabatic regime, whereas the exponential phases evolve fast, on time scales $1/m$.

In the Heisenberg picture operators depend on time but states and the density matrix do not. Consider a Heisenberg picture operator $\mathcal{O}(\vec{x},\eta)$ and its expectation value in the Bunch-Davis "in" state $|0_I\rangle$,

$$\langle 0_I|\,\mathcal{O}(\vec{x},\eta)\,|0_I\rangle = \langle 0_I|\,U_0^{-1}(\eta,\eta_i)\ \mathcal{O}_S(\vec{x},\eta)\ U_0(\eta,\eta_i)\,|0_I\rangle \equiv \mathrm{Tr}\Big[\rho_S(\eta)\ \mathcal{O}_S(\vec{x},\eta)\Big]\,, \tag{5.3.53}$$

where we have introduced the adiabatic Schroedinger picture density matrix

$$\rho_S(\eta) = U_0(\eta,\eta_i)\,|0_I\rangle\,\langle 0_I|\,U_0^{-1}(\eta,\eta_i)\,. \tag{5.3.54}$$

Obviously this density matrix describes a pure state since $\rho_S^2(\eta) = \rho_S(\eta)$. This adiabatic Schroedinger picture effectively separates the fast time evolution, now encoded in the density matrix, from the slow time evolution of the field operators $\mathcal{O}_S(\vec{x},\eta)$.

In Minkowski space time the Schroedinger picture operators $\mathcal{O}_S(\vec{x},\eta)$ do not evolve in time whereas the states and the density matrix evolves in time with the usual time evolution operator e^{-iHt}. During the adiabatic regime in (RD) cosmology the equivalent Schroedinger picture operators feature a slow residual adiabatic time evolution on the time scales of cosmological expansion.

5.3.3 Energy Momentum Tensor

For a minimally coupled complex scalar field, the energy momentum tensor is given by

$$T_{\mu\nu} = \partial_\mu\phi^\dagger\partial_\nu\phi + \partial_\nu\phi^\dagger\partial_\mu\phi - g_{\mu\nu}\left[g^{\alpha\beta}\partial_\alpha\phi^\dagger\partial_\beta\phi - m^2|\phi|^2\right]. \tag{5.3.55}$$

In conformal time and after the conformal rescaling of the field (5.3.2) we find (space-time arguments are implicit)

$$T^0_0 = \frac{1}{a^4}\left[(\chi' - \frac{a'}{a}\chi)^\dagger(\chi' - \frac{a'}{a}\chi) + \nabla\chi^\dagger\cdot\nabla\chi + m^2a^2|\chi|^2\right], \tag{5.3.56}$$

along with

$$T^\mu_\mu = \frac{2}{a^4}\left[2m^2a^2|\chi|^2 - (\chi' - \frac{a'}{a}\chi)^\dagger(\chi' - \frac{a'}{a}\chi) + \nabla\chi^\dagger\cdot\nabla\chi\right]. \tag{5.3.57}$$

The Bunch-Davies "in" vacuum state is homogeneous and isotropic therefore the expectation value of the energy momentum tensor in this state features the ideal fluid form $\langle 0_I|\, T^\mu_\nu\, |0_I\rangle = \mathrm{diag}\big(\overline{\rho}(\eta), -\overline{P}(\eta), -\overline{P}(\eta), -\overline{P}(\eta)\big)$. It proves convenient to extract the homogeneous and isotropic components of the energy momentum tensor as an operator, this is achieved by its averaging over the comoving volume V, namely

$$\frac{1}{V}\int d^3x\, T^0_0(\vec{x},\eta) = \widehat{\overline{\rho}}(\eta) \quad ; \quad \frac{1}{V}\int d^3x\, T^\mu_\mu(\vec{x},\eta) = \widehat{\overline{\rho}}(\eta) - 3\,\widehat{\overline{P}}(\eta)\,, \tag{5.3.58}$$

where the hat refers to the operator. Since we are interested in the energy momentum tensor near matter radiation equality well within the adiabatic regime, we obtain these volume averages by implementing two steps: **i:)** the field χ is written in the "out" basis, namely in terms of the mode functions $f_k(\eta)$ as in eqn. (5.3.30), **ii:)** these mode functions are written by separating the slow and fast parts as in eqns. (5.3.40,5.3.43), we find

$$\widehat{\overline{\rho}}(\eta) = \frac{1}{2\,V\,a^4(\eta)}\sum_{\vec{k}}\Bigg\{\Bigg[1 + c^\dagger_{\vec{k}}\,c_{\vec{k}} + d^\dagger_{\vec{k}}\,d_{\vec{k}}\Bigg]\Bigg[\Big(|\mathcal{F}|^2 + |\mathcal{G}|^2\Big)\,\omega_k(\eta)$$
$$- i\Big(\frac{a'}{a}\Big)\Big(\mathcal{G}^*\,\mathcal{F} - \mathcal{G}\,\mathcal{F}^*\Big) + \Big(\frac{a'}{a}\Big)^2\frac{|\mathcal{F}|^2}{\omega_k(\eta)}\Bigg]$$
$$+ c^\dagger_{\vec{k}}\,d^\dagger_{-\vec{k}}\,e^{2i\int_{\eta_i}^{\eta}\omega_k(\eta')\,d\eta'}\Bigg[\omega_k(\eta)\Big(\mathcal{F}^{*2} - \mathcal{G}^{*2}\Big) - 2i\Big(\frac{a'}{a}\Big)\Big(\mathcal{F}\,\mathcal{G}\Big)^* + \Big(\frac{a'}{a}\Big)^2\frac{\mathcal{F}^{*2}}{\omega_k(\eta)}\Bigg]$$
$$+ c_{\vec{k}}\,d_{-\vec{k}}\,e^{-2i\int_{\eta_i}^{\eta}\omega_k(\eta')\,d\eta'}\Bigg[\omega_k(\eta)\Big(\mathcal{F}^2 - \mathcal{G}^2\Big) + 2i\Big(\frac{a'}{a}\Big)\Big(\mathcal{F}\,\mathcal{G}\Big) + \Big(\frac{a'}{a}\Big)^2\frac{\mathcal{F}^2}{\omega_k(\eta)}\Bigg]\Bigg\}, \tag{5.3.59}$$

and

$$\widehat{\overline{\rho}}(\eta) - 3\,\widehat{\overline{P}}(\eta) = \frac{1}{V\,a^4(\eta)}\sum_{\vec{k}}\Bigg\{\Big(1 + c^\dagger_{\vec{k}}c_{\vec{k}} + d^\dagger_{\vec{k}}d_{\vec{k}}\Big)\Bigg[\frac{m^2a^2(\eta)}{\omega_k(\eta)}\,|\mathcal{F}|^2$$
$$+ \omega_k(\eta)\,\big(|\mathcal{F}|^2 - |\mathcal{G}|^2\big) + i\Big(\frac{a'}{a}\Big)\Big(\mathcal{G}^*\,\mathcal{F} - \mathcal{G}\,\mathcal{F}^*\Big) - \Big(\frac{a'}{a}\Big)^2\frac{|\mathcal{F}|^2}{\omega_k(\eta)}\Bigg]$$
$$+ c^\dagger_{\vec{k}}\,d^\dagger_{-\vec{k}}\,e^{2i\int_{\eta_i}^{\eta}\omega_k(\eta')\,d\eta'}\Bigg[\frac{\mathcal{F}^{*2}}{\omega_k}\big(m^2a^2 + \omega_k^2\big) - \frac{1}{\omega_k}\Big(i\omega\,\mathcal{G}^* - \frac{a'}{a}\mathcal{F}^*\Big)^2\Bigg]$$
$$+ c_{\vec{k}}\,d_{-\vec{k}}\,e^{-2i\int_{\eta_i}^{\eta}\omega_k(\eta')\,d\eta'}\Bigg[\frac{\mathcal{F}^2}{\omega_k}\big(m^2a^2 + \omega_k^2\big) - \frac{1}{\omega_k}\Big(-i\omega\,\mathcal{G} - \frac{a'}{a}\mathcal{F}\Big)^2\Bigg]\Bigg\}. \tag{5.3.60}$$

The expectation values of these operators in the "in" vacuum state are readily obtained from equations (5.3.32).

These expressions show explicitly that the contributions that are diagonal in the "out" basis, namely, $c^\dagger c$; $d^\dagger d$ are slowly varying, whereas the off-diagonal terms $c\,d$; , $c^\dagger d^\dagger$ exhibit the fast varying phases. These rapidly varying terms are a consequence of the interference between particle and antiparticle "out" states, similar to the phenomenon of *zitterbewegung*, and average out over time scales $\gtrsim 1/m$ leaving only the diagonal contributions to the energy

density and pressure[226]. The energy momentum tensor, as an operator, can also be written passing to the adiabatic Schroedinger picture as

$$T^{\mu\nu}(\vec{x},\eta) = U_0^{-1}(\eta,\eta_i)\, T_S^{\mu\nu}(\vec{x},\eta)\, U_0(\eta,\eta_i)\,, \tag{5.3.61}$$

where $U_0(\eta,\eta_i)$ is the time evolution operator (5.3.47) removing the fast varying phases in (5.3.59,5.3.60), and $T_S^{\mu\nu}(\vec{x},\eta)$ is the adiabatic Schroedinger picture operator with slow time evolution in the adiabatic regime. In terms of the adiabatic Schroedinger picture density matrix (5.3.54), it follows that

$$\langle 0_I|\, T^{\mu\nu}(\vec{x},\eta)\, |0_I\rangle = \mathrm{Tr}\Big[\rho_S(\eta)\, T_S^{\mu\nu}(\vec{x},\eta)\Big]\,. \tag{5.3.62}$$

The rapidly varying phases in the particle-antiparticle interference terms in the "out" basis in (5.3.59,5.3.60) suggest that the off diagonal elements of the density matrix $\rho_S(\eta)$ in the "out" basis will also feature these rapidly varying phases from particle-antiparticle interference, which average out on time scales $\gtrsim 1/m$. This averaging suggests a process of *decoherence by dephasing*, which is analyzed in detail in the next section.

5.3.4 Decoherence of the density matrix: von Neumann and entanglement entropy

The 'in" Bunch-Davies vacuum state can be written in terms of the Fock states of the "out" basis as

$$|0_I\rangle = \Pi_{\vec{k}} \sum_{n_{\vec{k}}=0}^{\infty} \mathcal{C}_{n_{\vec{k}}}(k)\, \left|n_{\vec{k}};\overline{n}_{\vec{k}}\right\rangle \quad ; \quad \mathcal{C}_{n_{\vec{k}}}(k) = \frac{\left(e^{2i\varphi_-(k)}\, \tanh(\theta_k)\right)^{n_{\vec{k}}}}{\cosh(\theta_k)}\,, \tag{5.3.63}$$

with

$$|B_k|^2 = \sinh^2(\theta_k) = N_k \quad ; \quad |A_k|^2 = \cosh^2(\theta_k) \quad ; \quad \tanh^2(\theta_k) = \frac{N_k}{1+N_k}\,, \tag{5.3.64}$$

and

$$e^{2i\varphi_-(k)}\, \tanh(\theta_k) = \frac{B_k^*}{A_k^*}\,, \tag{5.3.65}$$

and the correlated Fock pair states

$$\left|n_{\vec{k}};\overline{n}_{-\vec{k}}\right\rangle = \frac{\left(c^{\dagger}_{\vec{k}}\right)^{n_{\vec{k}}}}{\sqrt{n_{\vec{k}}\,!}}\,\frac{\left(d^{\dagger}_{-\vec{k}}\right)^{n_{\vec{k}}}}{\sqrt{n_{\vec{k}}\,!}}\,\left|0_O\right\rangle \quad ; \quad n_{\vec{k}} = 0, 1, 2\cdots , \tag{5.3.66}$$

where the "out" vacuum state $|0_O\rangle$ is such that

$$c_{\vec{k}}\,\left|0_O\right\rangle = d_{\vec{k}}\,\left|0_O\right\rangle = 0\,. \tag{5.3.67}$$

We note that the Fock pair states (5.3.66) are eigenstates of the *pair number operator*

$$\widehat{\mathcal{N}}_{\vec{k}} = \sum_{m_{\vec{k}}=0}^{\infty} m_{\vec{k}}\;\left|m_{\vec{k}};\overline{m}_{-\vec{k}}\right\rangle\left\langle m_{\vec{k}};\overline{m}_{-\vec{k}}\right| , \tag{5.3.68}$$

with

$$\widehat{\mathcal{N}}_{\vec{k}}\;\left|n_{\vec{k}};\overline{n}_{-\vec{k}}\right\rangle = n_{\vec{k}}\;\left|n_{\vec{k}};\overline{n}_{-\vec{k}}\right\rangle \quad ; \quad n_{\vec{k}} = 0, 1, 2\cdots . \tag{5.3.69}$$

In this "out" basis and in the adiabatic regime prior to matter-radiation equality, the density matrix in the Schroedinger picture (5.3.54) becomes

$$\rho_S(\eta) = \Pi_{\vec{k}}\Pi_{\vec{p}}\sum_{n_{\vec{k}}=0}^{\infty}\sum_{m_{\vec{p}}=0}^{\infty}\mathcal{C}^{*}_{m_{\vec{p}}}(p)\;\mathcal{C}_{n_{\vec{k}}}(k)\;\left|n_{\vec{k}};\overline{n}_{-\vec{k}}\right\rangle\left\langle m_{\vec{p}};\overline{m}_{-\vec{p}}\right|\;e^{2i\int_{\eta_i}^{\eta}\left[m_{\vec{p}}\,\omega_p(\eta')-n_{\vec{k}}\,\omega_k(\eta')\right]d\eta'} . \tag{5.3.70}$$

The diagonal density matrix elements both in momentum and number of particles, namely $\vec{k} = \vec{p}\;;\; m_{\vec{p}} = n_{\vec{k}}$ are time independent, these describe the "populations", whereas the off-diagonal elements describe the coherences. These latter matrix elements vary rapidly in time and average out over time scales $\gg 1/m$. To see this aspect more clearly, and recognizing that

$$\int^{\eta}\omega_k(\eta')d\eta' = \int^{t} E_k(t')dt' \quad ; \quad E_k(t) = \sqrt{\frac{k^2}{a^2(t)} + m^2} \tag{5.3.71}$$

let us consider the average

$$\frac{1}{(t_f - t_i)}\int_{t_i}^{t_f} e^{2i\int^{t}\left[m_{\vec{p}}\,E_p(t')-n_{\vec{k}}\,E_k(t')\right]dt'}\,dt \quad ; \quad m(t_f - t_i) \gg 1\,. \tag{5.3.72}$$

For example for $\vec{p} = \vec{k} = 0$ and $m(t_f - t_i) \gg 1$ the integral yields $\delta_{m_{\vec{0}},n_{\vec{0}}}$. Taking the interval $t_f - t_i$ of the order of the Hubble time $\simeq 1/H(t)$, in the adiabatic regime with $H(t)/m \ll 1$ the integral yields $\simeq H/m \ll 1$ for $m_{\vec{0}} \neq n_{\vec{0}}$ and $\mathcal{O}(1)$ for $m_{\vec{0}} = n_{\vec{0}}$. Therefore, the rapidly

varying phases effectively average out the coherences over time scales $\simeq 1/m \ll 1/H(t)$ projecting the density matrix to the diagonal elements in the "out" basis.

In summary: the rapid dephasing of the off-diagonal matrix elements in the out basis in the adiabatic regime average these contributions on time scales of order $1/m$ which are much shorter than the expansion time scale (Hubble scale) in the adiabatic regime. The rapid dephasing leads to *decoherence* in the "out" basis, the time averaging is tantamount to a coarse graining over short time scales leaving effectively a diagonal density matrix in this basis, describing a *mixed state* that evolves slowly on the long time scale,

$$\rho_S^{(d)} = \Pi_{\vec{k}}\big[1-\tanh^2(\theta_k)\big]\sum_{n_{\vec{k}}=0}^{\infty}\Big(\tanh^2(\theta_k)\Big)^{n_{\vec{k}}}\,\big|n_{\vec{k}};\overline{n}_{-\vec{k}}\big\rangle\,\big\langle n_{\vec{k}};\overline{n}_{-\vec{k}}\big|\,. \tag{5.3.73}$$

This density matrix is diagonal in the Fock "out" basis of correlated –entangled– particle-antiparticle pairs, and in $\vec{k}$ space, with the diagonal matrix elements representing the probabilities. We note that $\mathrm{Tr}\,\rho_S^{(d)} = 1$. The entropy associated with this mixed state can be calculated simply by establishing contact between the density matrix $\rho_S^{(d)}$ and that of quantum statistical mechanics in equilibrium described by a fiducial Hamiltonian

$$\widehat{\mathcal{H}} = \sum_{\vec{k}}\mathcal{E}_k\,\widehat{\mathcal{N}}_{\vec{k}}\,, \tag{5.3.74}$$

with $\widehat{\mathcal{N}}_{\vec{k}}$ the pair number operator (5.3.68) with eigenvalues $n_{\vec{k}} = 0, 1, 2\cdots$, and the fiducial energy

$$\mathcal{E}_k = -\ln\big[\tanh^2(\theta_k)\big]\,. \tag{5.3.75}$$

This fiducial Hamiltonian is diagonal in the correlated basis of particle-antiparticle pairs, therefore we identify

$$\rho_S^{(d)} = \frac{e^{-\widehat{\mathcal{H}}}}{\mathcal{Z}} \quad ; \quad \mathcal{Z} = \mathrm{Tr}\,e^{-\widehat{\mathcal{H}}} \equiv e^{-\mathbb{F}}\,, \tag{5.3.76}$$

with $\mathbb{F}$ the fiducial free energy, and

$$\mathcal{Z} = \Pi_{\vec{k}}\mathcal{Z}_{\vec{k}} \quad ; \quad \mathcal{Z}_{\vec{k}} = \frac{1}{\Big[1-e^{-\mathcal{E}_k}\Big]} = \frac{1}{\Big[1-\tanh^2(\theta_k)\Big]}\,. \tag{5.3.77}$$

Obviously the matrix elements of (5.3.76) in the pair basis are identical to those of (5.3.73).

The von Neumann entropy associated with this mixed state is

$$S^{(d)} = -\mathrm{Tr}\,\rho_S^{(d)}\,\ln\rho_S^{(d)}\,. \tag{5.3.78}$$

Since $\widehat{\mathcal{H}}$ is diagonal in the basis of the pair Fock states (5.3.66), so is $\rho_S^{(d)}$. The eigenvalues of $\rho_S^{(d)}$ are the probability for each state of $n_{\vec{k}}$ pairs of momenta $(\vec{k};-\vec{k})$, namely

$$P_{\vec{k};n_{\vec{k}}} = \frac{e^{-\mathcal{E}_k\,n_{\vec{k}}}}{\mathcal{Z}_{\vec{k}}} \quad ; \quad \sum_{n_{\vec{k}}=0}^{\infty} P_{\vec{k};n_{\vec{k}}} = 1\,, \tag{5.3.79}$$

therefore the von Neumann entropy is given by

$$S^{(d)} = -\sum_{\vec{k}}\sum_{n_{\vec{k}}=0}^{\infty} P_{\vec{k};n_{\vec{k}}}\,\ln P_{\vec{k};n_{\vec{k}}}\,. \tag{5.3.80}$$

This is equivalent to a simple quantum statistical mechanics problem. The relation

$$\mathbb{F} = -\ln\mathcal{Z} = U - S^{(d)} \quad ; \quad U = \mathrm{Tr}\rho_S^{(d)}\,\widehat{\mathcal{H}}\,, \tag{5.3.81}$$

is a direct consequence of the expression (5.3.80) for $S^{(d)}$ and the normalized probabilities $P_{\vec{k};n_{\vec{k}}}$ given by (5.3.79). The entropy $S^{(d)}$ is obtained once the fiducial internal energy U is found. It is easily shown to be given by the equivalent form in quantum statistical mechanics

$$U = \sum_{\vec{k}} \frac{\mathcal{E}_k}{e^{\mathcal{E}_k}-1}\,. \tag{5.3.82}$$

Using the identity (5.3.64) and recognizing the following relations

$$\mathcal{E}_k = \ln\left[\frac{1+N_k}{N_k}\right] \quad ; \quad \frac{1}{e^{\mathcal{E}_k}-1} = N_k \tag{5.3.83}$$

we find the von Neumann entropy

$$S^{(d)} = \sum_{\vec{k}}\left\{(1+N_k)\,\ln(1+N_k) - N_k\,\ln N_k\right\}. \tag{5.3.84}$$

5.3.5 Interpretation of $S^{(d)}$ entanglement entropy.

Consider the full density matrix $\rho_S(\eta)$ eqn. (5.3.70). Although it describes a pure state, in the out basis this state is a highly correlated, *entangled state of pairs*, because in this basis the state $|0_I\rangle$ is not a simple product state. Because the members of the particle-anti-particle pairs are correlated, projecting onto a state with $n_{\vec{k}}$ antiparticles of momentum $-\vec{k}$ effectively projects onto the state with $n_{\vec{k}}$ particles with momentum $\vec{k}$. Therefore, consider obtaining a *reduced* density matrix by tracing $\rho_S(\eta)$ over the *anti-particle* states $\overline{p}$. Because the states $\left|n_{\vec{k}};\overline{n}_{-\vec{k}}\right\rangle = \left|n_{\vec{k}}\right\rangle\left|\overline{n}_{-\vec{k}}\right\rangle$ such trace involves terms of the form $\left(\left|n_{\vec{k}}\right\rangle\langle m_{\vec{p}}|\right)\left(\langle\overline{n}_{-\vec{k}}|\overline{m}_{-\vec{p}}\rangle\right) = \left(\left|n_{\vec{k}}\right\rangle\langle m_{\vec{p}}|\right)\delta_{\vec{k},\vec{p}}\,\delta_{n_{\vec{k}},m_{\vec{p}}}$ thereby projecting on particle states diagonal both in number and momentum. Therefore the rapidly varying phases in (5.3.70) vanish *identically*, yielding

$$\rho_S^{(r)}(\eta) = \mathrm{Tr}_{\overline{p}}\,\rho_S(\eta) = \Pi_{\vec{k}}\left[1-\tanh^2(\theta_k)\right]\sum_{n_{\vec{k}}=0}^{\infty}\Big(\tanh^2(\theta_k)\Big)^{n_{\vec{k}}}\left|n_{\vec{k}}\right\rangle\left\langle n_{\vec{k}}\right| . \tag{5.3.85}$$

Note that because the density matrix (5.3.73) is diagonal in the basis of correlated pairs, tracing over one member of the correlated pair, either the particle or the antiparticle keeps the density matrix diagonal with the same probabilities. For example, tracing over the antiparticles reduces (5.3.73) directly to (5.3.85) *with the same eigenvalues, i.e. probabilities.* This observation is yet another manner to interpret the equivalence with the fiducial quantum statistical mechanical example, now with the fiducial Hamiltonian

$$\widehat{\mathcal{H}}^{(r)} = \sum_{\vec{k}}\mathcal{E}_k\,\widehat{\mathcal{N}}_{\vec{k}}^{(r)} , \tag{5.3.86}$$

with the *reduced* number operator

$$\widehat{\mathcal{N}}_{\vec{k}}^{(r)} = \sum_{m_{\vec{k}}=0}^{\infty} m_{\vec{k}}\;\left|m_{\vec{k}}\right\rangle\left\langle m_{\vec{k}}\right| , \tag{5.3.87}$$

namely,

$$\rho_S^{(r)} = \frac{e^{-\widehat{\mathcal{H}}^{(r)}}}{\mathcal{Z}} \quad ; \quad \mathcal{Z} = \mathrm{Tr}\,e^{-\widehat{\mathcal{H}}^{(r)}} \equiv e^{-\mathbb{F}} , \tag{5.3.88}$$

with the same $\mathcal{Z}$ and fiducial free energy $\mathbb{F}$ as for $\rho_S^{(d)}$ eqn. (5.3.73). Hence $\rho_S^{(r)}$ and $\rho_S^{(d)}$ feature the same eigenvalues and yield the same entropy.

The von Neumann entropy associated with the reduced density matrix $\rho_S^{(r)}(\eta)$, i.e.

$$S^{(r)} = -\mathrm{Tr}\,\rho_S^{(r)}\,\ln\rho_S^{(r)}\,, \tag{5.3.89}$$

is the *entanglement entropy*[292]. Therefore, we conclude that decoherence from rapid dephasing of the off diagonal density matrix elements results in a reduction of the density matrix which is diagonal in the correlated pair basis. This reduction is identical to tracing over one member of the correlated pair leading to the entanglement entropy. The equivalence between the entropy resulting from dephasing and decoherence and the entanglement entropy is no accident: it is a direct consequence of the entangled– correlated– particle-antiparticle pairs in the out state and that after decoherence the density matrix is diagonal in this basis of *correlated pairs*. Therefore the diagonal matrix elements, in other words the probabilities, are exactly the same as when one of the members of the pairs is traced over, which yields the entanglement entropy. The result (5.3.84) is remarkably similar to the quantum kinetic form of the entropy in terms of the distribution function[83]. However, there is an important difference: a complex scalar field has two degrees of freedom, corresponding to particles and antiparticles, therefore if the out state were a superposition independent single particles and antiparticles we would expect an extra overall factor 2 multiplying the von Neumann entropy (5.3.84) because of the two independent degrees of freedom. The reason for this discrepancy is that the density matrix is diagonal in the basis of particle-antiparticle *correlated pairs*, not independent particles and antiparticles. Because of the pairing, for each pair there is effectively only one degree of freedom, not two as would be the case for independent particles and antiparticles. This is more evident in the identification of the von Neumann entropy with the entanglement entropy which is obtained by tracing over one member of the pairs either particle or antiparticle.

5.3.6 Energy density, pressure and entropy.

During the adiabatic regime and well before matter radiation equality, the decoherence process via dephasing renders the time dependent density matrix in the Schroedinger picture

diagonal in the "out" basis, namely $\rho_S^{(d)}$. With this density matrix we find

$$\begin{aligned}
&\mathrm{Tr}\, c_{\vec{k}}^\dagger\, c_{\vec{k}}\, \rho_S^{(d)} = \mathrm{Tr}\, d_{\vec{k}}^\dagger\, d_{\vec{k}}\, \rho_S^{(d)} = \sinh^2(\theta_k) = N_k\,, \\
&\mathrm{Tr}\, c_{\vec{k}}^\dagger\, d_{-\vec{k}}^\dagger\, \rho_S^{(d)} = \mathrm{Tr}\, d_{-\vec{k}}\, c_{\vec{k}}\, \rho_S^{(d)} = 0\,,
\end{aligned} \tag{5.3.90}$$

from which we can now obtain the expectation value of the energy momentum tensor, given by eqn. (5.3.62) with $\rho_S(\eta) \equiv \rho_S^{(d)}$. The non-vanishing contributions to the expectation values of the expressions (5.3.59,5.3.60) are those with terms $c^\dagger c, d^\dagger d$, since the off-diagonal terms of the density matrix $\rho_S^{(d)}$ vanish.

Near matter radiation equality when the dark matter contribution begins to dominate, the adiabatic approximation is very reliable, therefore we keep the leading order terms in the adiabatic expansions (5.3.41,5.3.42), namely $|\mathcal{F}| = |\mathcal{G}| = 1$, yielding

$$\overline{\rho}(\eta) = \mathrm{Tr}\, \widehat{\overline{\rho}}(\eta)\, \rho_S^{(d)} = \frac{1}{2\pi^2\, a^4(\eta)} \int_0^\infty k^2 \Big[1 + 2N_k\Big] \omega_k(\eta)\, dk\,, \tag{5.3.91}$$

$$\overline{P}(\eta) = \mathrm{Tr}\, \widehat{\overline{P}}(\eta)\, \rho_S^{(d)} = \frac{1}{6\pi^2\, a^4(\eta)} \int_0^\infty k^2 \Big[1 + 2N_k\Big] \frac{k^2}{\omega_k(\eta)}\, dk\,. \tag{5.3.92}$$

These are precisely the kinetic fluid expressions obtained in ref.[226] after averaging over the rapid phases in the interference terms. Therefore, this averaging in the energy momentum tensor and the emergence of the kinetic fluid form in the adiabatic regime is a direct manifestation of decoherence by dephasing in the density matrix, hence also directly related to the emergence of entropy.

The "1" inside the brackets in (5.3.91,5.3.92) correspond to the zero point energy density and pressure. As explained in detail in refs.[226], these zero point contributions are subtracted by renormalization of the energy momentum tensor[117, 295, 190, 234, 38, 88, 220]. Therefore the contribution from gravitational particle-antiparticle production to the energy

density, pressure and comoving entropy density $\mathcal{S} = S/V$ (V is comoving volume) of dark matter are given by the kinetic-fluid forms

$$\mathcal{N}_{p\bar{p}} = \frac{1}{\pi^2}\int_0^\infty k^2 N_k\, dk \tag{5.3.93}$$

$$\overline{\rho}_{p\bar{p}}(\eta) = \frac{1}{\pi^2\, a^4(\eta)}\int_0^\infty k^2 N_k\, \omega_k(\eta)\, dk \tag{5.3.94}$$

$$\overline{P}_{p\bar{p}}(\eta) = \frac{1}{3\pi^2\, a^4(\eta)}\int_0^\infty \frac{k^4}{\omega_k(\eta)}\, N_k\, dk \tag{5.3.95}$$

$$\mathcal{S}_{p\bar{p}} = \frac{1}{2\pi^2}\int_0^\infty k^2\Big[(1+N_k)\,\ln[1+N_k] - N_k\,\ln N_k\Big]\, dk\,, \tag{5.3.96}$$

where $\mathcal{N}_{p\bar{p}}$ is the total (particles plus antiparticles) comoving number density . It is straightforward to confirm covariant conservation

$$\dot{\overline{\rho}}_{p\bar{p}}(t) + 3\,\frac{\dot{a}}{a}\left(\overline{\rho}_{p\bar{p}}(t) + \overline{P}_{p\bar{p}}(t)\right) = 0\,, \tag{5.3.97}$$

along with the conservation of the comoving entropy density

$$\dot{\mathcal{S}}_{p\bar{p}} = 0\,, \tag{5.3.98}$$

where the dot stands for derivative with respect to comoving time. Although the comoving entropy density is proportional (up to a factor 2) to the quantum kinetic expression, it is not to be identified with a thermodynamic entropy, as shown above it is the entanglement entropy resulting from the loss of information as a consequence of dephasing and decoherence from the interference between particle and antiparticle out states. The equivalence with the entanglement entropy is a consequence of the correlations in the particle-antiparticle pairs, tracing over one member is equivalent to neglecting the off-diagonal matrix elements.

The result (5.3.96) is similar to the expression for the entanglement entropy obtained in ref.[268] for bosonic particle production after tracing one member of the produced pairs from the Wigner distribution function. While in this reference the tracing over one member of the pairs was carried out to obtain the entanglement entropy, we emphasize that in our case, the main origin of entropy is the decoherence via dephasing during the adiabatic regime. The fact that this entropy is exactly the same as the entanglement entropy is an *a posteriori* conclusion on the equivalence between the entropy emerging from the decoherence via dephasing and the entanglement entropy.

5.3.7 Entropy for ultra light dark matter:

In ref.[226] the case of gravitationally produced ultra light dark matter has been studied under the same conditions assumed in this chapter. In this reference it was established that a scalar field minimally coupled to gravity and with mass $m \simeq 10^{-5}\,\text{eV}$ yields the correct dark matter abundance and is a cold dark matter candidate with a very small free streaming length. The distribution function is given by equation (5.3.38). It features an infrared enhancement $\propto 1/k^3$ and the large factor $H_{dS}/m \gg 1$, both consequences of a light scalar minimally coupled to gravity during inflation. Since $D(z) \simeq 1/z$ for $z \gg 1$ the occupation number $N_k \gg 1$ in the region $0 \leq z \ll \sqrt{H_{dS}/m}$.

The comoving number density of gravitationally produced cold dark matter scalar particles has been obtained in ref.[226], it is given by

$$\mathcal{N}_{p\bar{p}} \simeq \left(\frac{H_{dS}}{4\,\pi\,m}\right)^2 \Big(2mH_R\Big)^{3/2}\, D(0)\, \ln\left[\frac{\sqrt{2mH_R}}{H_0}\right]. \tag{5.3.99}$$

The leading contribution to the comoving entropy density (5.3.96) can be extracted by implementing the following steps: a) changing integration variable to z given by (5.3.37) b) taking the limit $N_k \gg 1$ in the region of integration dominated by the infrared $0 \leq z \leq z_c$ where $1 \ll z_c \ll \sqrt{H_{dS}/m}$, yielding

$$\mathcal{S}_{p\bar{p}} \simeq \frac{\big(2\,m\,H_R\big)^{3/2}}{2\pi^2} \int_0^{z_c} z^2 \Big[\,\ln(N_k) + \cdots\Big]\, dz\,, \tag{5.3.100}$$

where the dots stand for subleading terms of order $1/N_k$ for $N_k \gg 1$. It is more instructive to obtain the dimensionless *specific entropy*, namely the entropy per particle $\mathcal{S}_{p\bar{p}}/\mathcal{N}_{p\bar{p}}$. To leading order in $H_{dS}/m \gg 1$ we find

$$\frac{\mathcal{S}_{p\bar{p}}}{\mathcal{N}_{p\bar{p}}} \simeq \frac{16}{3\,D(0)}\, \frac{\ln\big(H_{dS}/m\big)\, z_c^3}{\Big(\frac{H_{dS}}{m}\Big)^2 \ln\Big[\frac{\sqrt{2mH_R}}{H_0}\Big]} \left\{1 - \frac{1}{2\,\ln\big(H_{dS}/m\big)}\left[\ln\Big(8\sqrt{2}\Big) - (4/3 - 4\ln z_c) - \frac{0.17}{z_c^3}\right]\right\}. \tag{5.3.101}$$

For ultra light dark matter with $H_0 \ll m \ll H_{dS}$ (for example with $H_{dS} = 10^{13}\,\text{GeV}, m \simeq 10^{-5}\,\text{eV}$) it follows that the specific entropy

$$\frac{\mathcal{S}_{p\bar{p}}}{\mathcal{N}_{p\bar{p}}} \ll 1\,. \tag{5.3.102}$$

A large occupation number in an narrow momentum region and with a very small specific entropy are all hallmarks of a *condensed state*, these are precisely the conditions of a Bose Einstein Condensate. However, in this case of gravitationally produced particles, this is not a condensate in the usual manner because the expectation value of the field vanishes, therefore it is not described by a coherent state. Instead this a condensed state of correlated pairs entangled in momentum but of total zero momentum in a two-mode squeezed state[58].

For a value of the mass that yields the correct dark matter abundance, $m \simeq 10^{-5}\,\mathrm{eV}$[226], the ratio of the comoving dark matter entropy $\mathcal{S}_{p\bar{p}}$ to that of the (CMB)

$$\mathcal{S}_{cmb} \simeq T_0^3 \quad ; \quad T_0 \simeq 10^{-4}\,\mathrm{eV} \tag{5.3.103}$$

yields,

$$\frac{\mathcal{S}_{p\bar{p}}}{\mathcal{S}_{cmb}} \simeq 10^{-45}\,, \tag{5.3.104}$$

therefore, if ultra light dark matter is gravitationally produced, the entropy of the Universe today is dominated by the (CMB).

5.4 Fermionic Dark Matter

The results obtained above for a complex scalar are, in fact, much more general and apply with few modifications primarily due to the different statistics, to the case of gravitationally produced fermionic dark matter. We analyze this case by briefly summarizing the results of ref.[103] to which we refer the reader for a more comprehensive treatment.

In comoving coordinates, the action for a Dirac field is given by

$$S = \int d^3x\; dt\; \sqrt{-g}\,\overline{\Psi}\Big[i\,\gamma^\mu\;\mathcal{D}_\mu - m\Big]\Psi\,. \tag{5.4.1}$$

Introducing the vierbein field $e^\mu_a(x)$ defined as

$$g^{\mu\,\nu}(x) = e^\mu_a(x)\; e^\nu_b(x)\; \eta^{ab}\,,$$

where $\eta_{ab} = \text{diag}(1, -1, -1, -1)$ is the Minkowski space-time metric, the curved space time Dirac gamma- matrices $\gamma^\mu(x)$ are given by

$$\gamma^\mu(x) = \gamma^a e_a^\mu(x) \quad , \quad \{\gamma^\mu(x), \gamma^\nu(x)\} = 2\, g^{\mu\nu}(x) \,, \tag{5.4.2}$$

where the γ^a are the Minkowski space time Dirac matrices.

The fermion covariant derivative $\mathcal{D}_\mu$ is given in terms of the spin connection by[344, 123, 297, 89]

$$\mathcal{D}_\mu = \partial_\mu + \frac{1}{8}\,[\gamma^c, \gamma^d]\; e_c^\nu \;\left(\partial_\mu e_{d\nu} - \Gamma^\lambda_{\mu\nu}\; e_{d\lambda}\right) \,, \tag{5.4.3}$$

where $\Gamma^\lambda_{\mu\nu}$ are the usual Christoffel symbols.

For a spatially flat Friedmann-Robertson-Walker cosmology in conformal time with metric is given by eqn. (5.2.1) the vierbeins can be obtained easily. Introducing the conformally rescaled fields

$$a^{\frac{3}{2}}(\eta)\, \Psi(\vec{x}, t) = \psi(\vec{x}, \eta) \,, \tag{5.4.4}$$

the action becomes

$$S = \int d^3x\; d\eta\, \overline{\psi}\, \Big[i\; \not{\partial} - M(\eta)\Big]\psi \,, \tag{5.4.5}$$

with

$$M(\eta) = m\, a(\eta) \,, \tag{5.4.6}$$

and the γ^a matrices are the usual Minkowski space time ones taken to be in the standard Dirac representation. We consider the fermion mass m much smaller than the Hubble scale during inflation, namely $m/H_{dS} \ll 1$ but otherwise arbitrary.

The Dirac equation for the conformally rescaled fermi field becomes

$$\Big[i\; \not{\partial} - M(\eta)\Big]\psi = 0 \,, \tag{5.4.7}$$

and expand $\psi(\vec{x}, \eta)$ in a comoving volume V as

$$\psi(\vec{x}, \eta) = \frac{1}{\sqrt{V}} \sum_{\vec{k}, s} \left[b_{\vec{k},s}\, U_s(\vec{k}, \eta) + d^\dagger_{-\vec{k},s}\, V_s(-\vec{k}, \eta)\right]\; e^{i\vec{k}\cdot\vec{x}} \,, \tag{5.4.8}$$

and the spinor mode functions U, V obey the Dirac equations

$$\left[i\,\gamma^0\,\partial_\eta - \vec{\gamma}\cdot\vec{k} - M(\eta) \right] U_s(\vec{k},\eta) = 0 \tag{5.4.9}$$

$$\left[i\,\gamma^0\,\partial_\eta - \vec{\gamma}\cdot\vec{k} - M(\eta) \right] V_s(-\vec{k},\eta) = 0\,. \tag{5.4.10}$$

Finally, the spinor solutions are given by[103]

$$U_s(\vec{k},\eta) = N \begin{pmatrix} \mathcal{F}_k(\eta)\,\xi_s \\ k\,f_k(\eta)\,s\,\xi_s \end{pmatrix}, \tag{5.4.11}$$

$$V_s(-\vec{k},\eta) = N \begin{pmatrix} -k\,f_k^*(\eta)\,s\,\xi_s \\ \mathcal{F}_k^*(\eta)\,\xi_s \end{pmatrix}, \tag{5.4.12}$$

where

$$\mathcal{F}_k(\eta) = i f_k'(\eta) + M(\eta) f_k(\eta)\,, \tag{5.4.13}$$

and the functions $f_k(\eta)$ are solutions of[103]

$$\left[\frac{d^2}{d\eta^2} + k^2 + M^2(\eta) - i\,M'(\eta) \right] f_k(\eta) = 0\,, \tag{5.4.14}$$

with "in" boundary conditions

$$f_k(\eta) \;\rightarrow\; e^{-ik\eta}\,, \tag{5.4.15}$$

as $\eta \rightarrow -\infty$ during inflation[103]. The two component spinors ξ_s are helicity eigenstates, namely

$$\vec{\sigma}\cdot\vec{k}\,\xi_s = s\,k\,\xi_s \quad ; \quad s = \pm 1\,, \tag{5.4.16}$$

and N is a (constant) normalization factor.

The spinor solutions are normalized as follows

$$U_s^\dagger(\vec{k},\eta)\,U_{s'}(\vec{k},\eta) = \delta_{s,s'} \quad ; \quad V_s^\dagger(-\vec{k},\eta)\,V_{s'}(-\vec{k},\eta) = \delta_{s,s'}\,, \tag{5.4.17}$$

yielding

$$|N|^2 \left[\mathcal{F}_k^*(\eta)\,\mathcal{F}_k(\eta) + k^2 f_k^*(\eta)\,f_k(\eta) \right] = 1\,. \tag{5.4.18}$$

With these normalization conditions the operators $b_{\vec{k},s}, d_{\vec{k},s}$ in the field expansion (5.4.8) obey the usual canonical anticommutation relations.

Furthermore, it is straightforward to confirm that

$$U_s^\dagger(\vec{k},\eta)\, V_{s'}(-\vec{k},\eta) = 0 \quad \forall s, s' \,. \tag{5.4.19}$$

The spinors U_s, V_s furnish a complete set of four independent solutions of the Dirac equation.

During the inflationary stage, considered as an spatially flat de Sitter space-time, the functions f_k obey

$$\left[\frac{d^2}{d\tau^2} + k^2 - \frac{\nu^2 - 1/4}{\tau^2}\right] f_k(\tau) = 0 \quad ; \quad \tau = \eta - 2\eta_R \quad ; \quad \nu = \frac{1}{2} + i\,\frac{m}{H_{dS}} \,. \tag{5.4.20}$$

The solution with "in" boundary conditions (5.4.15) is given by

$$f_k(\tau) = \sqrt{-\frac{\pi k \tau}{2}}\; e^{i\pi(\nu+1/2)/2}\; H_\nu^{(1)}(-k\tau) \,, \tag{5.4.21}$$

where $H_\nu^{(1)}$ is a Hankel function. The operators $b_{\vec{k},s}, d_{\vec{k},s}$ in the field expansion (5.4.8) are chosen to annihilate the "in" vacuum state $|0_I\rangle$, namely

$$b_{\vec{k},s}\,|0_I\rangle = 0 \quad ; \quad d_{\vec{k},s}\,|0_I\rangle = 0 \,, \tag{5.4.22}$$

with the mode functions f_k given by (5.4.21), the state $|0_I\rangle$ corresponds to the Bunch-Davies vacuum.

Since we are considering an instantaneous transition between inflation and radiation domination, and because the Dirac equation is first order in time, the matching conditions correspond to the continuity of the spinor wave functions across the transition.

Defining $\psi^<(\vec{x},\eta)$ and $\psi^>(\vec{x},\eta)$ the fermion field for $\eta < \eta_R$ (inflation) and $\eta > \eta_R$ (RD) respectively, the matching condition is

$$\psi^<(\vec{x},\eta_R) = \psi^>(\vec{x},\eta_R) \,. \tag{5.4.23}$$

This continuity condition along with the continuity of the scale factor and Hubble rate at η_R results in that the energy density is *continuous at the transition*[103].

Introducing the Dirac spinors during the inflationary ($\eta < \eta_R$) and (RD) ($\eta > \eta_R$) stages as $U^<$, $V^<$ and $U^>$, $V^>$ respectively, it follows from the matching condition (5.4.23) that

$$U_s^<(\vec{k},\eta_R) = U_s^>(\vec{k},\eta_R)\,, \tag{5.4.24}$$

$$V_s^<(-\vec{k},\eta_R) = V_s^>(-\vec{k},\eta_R)\,. \tag{5.4.25}$$

We define the mode functions during (RD) as $h_k(\eta)$ to distinguish them from the solutions (5.4.21) during inflation. These obey the mode equations

$$\left[\frac{d^2}{d\eta^2} + \omega_k^2(\eta) - i\,mH_R\right] h_k(\eta) = 0 \quad ; \quad \omega_k^2(\eta) = k^2 + m^2H_R^2\eta^2\,. \tag{5.4.26}$$

Similarly to the spinor solutions (5.4.11,5.4.12) we now find

$$\mathcal{U}_s(\vec{k},\eta) = \widetilde{N}\begin{pmatrix} \mathcal{H}_k(\eta)\,\xi_s \\ k\,h_k(\eta)\,s\,\xi_s \end{pmatrix}\,, \tag{5.4.27}$$

$$\mathcal{V}_s(-\vec{k},\eta) = \widetilde{N}\begin{pmatrix} -k\,h_k^*(\eta)\,s\,\xi_s \\ \mathcal{H}_k^*(\eta)\,\xi_s \end{pmatrix}\,, \tag{5.4.28}$$

where we have introduced

$$\mathcal{H}_k(\eta) = ih_k'(\eta) + M(\eta)h_k(\eta)\,, \tag{5.4.29}$$

and $\widetilde{N}$ is a (constant) normalization factor chosen so that

$$\mathcal{U}_s^\dagger(\vec{k},\eta)\,\mathcal{U}_{s'}(\vec{k},\eta) = \delta_{s,s'} \quad ; \quad \mathcal{V}_s^\dagger(-\vec{k},\eta)\,\mathcal{V}_{s'}(-\vec{k},\eta) = \delta_{s,s'}\,, \tag{5.4.30}$$

yielding

$$|\widetilde{N}|^2\Big[\mathcal{H}_k^*(\eta)\mathcal{H}_k(\eta) + k^2h_k^*(\eta)h_k(\eta)\Big] = 1\,. \tag{5.4.31}$$

Again, it is straightforward to confirm that

$$\mathcal{U}_s^\dagger(\vec{k},\eta)\,\mathcal{V}_{s'}(-\vec{k},\eta) = 0\,. \tag{5.4.32}$$

The mode equation (5.4.26) admits a solution of the form[103]

$$h_k(\eta) = e^{-i\int^\eta \Omega_k(\eta')d\eta'}\,, \tag{5.4.33}$$

where $\Omega_k(\eta)$ obeys a differential equation that can be systematically solved in the adiabatic expansion. It relies on the ratio $H(\eta)/m \ll 1$ which during the (RD) era implies that $a(\eta) \gg 10^{-17}/\sqrt{m(\mathrm{eV})}$, for the value $m \simeq 10^8\,\mathrm{GeV}$ which saturates the dark matter bound as found in ref.[103], its range of validity begins well before matter radiation equality at $a_{eq} \simeq 10^{-4}$. We choose the solution of (5.4.26) to feature the asymptotic "out" boundary condition

$$h_k(\eta) \to e^{-i\int^\eta \omega_k(\eta')\,d\eta'}\,. \tag{5.4.34}$$

With this boundary condition, the spinor solutions during the (RD) era (5.4.27,5.4.28) satisfy the asymptotic "out" boundary conditions

$$\mathcal{U}_s(\vec{k},\eta) \to\propto\ e^{-i\int^\eta \omega_k(\eta')\,d\eta'}\ \ ;\ \ \mathcal{V}_s(\vec{k},\eta) \to\propto\ e^{i\int^\eta \omega_k(\eta')\,d\eta'}\,. \tag{5.4.35}$$

therefore describing "out" particle and anti-particle solutions with helicities ± 1, defining a complete set of four solutions of the Dirac equation during (RD).

It is convenient to introduce the following dimensionless combinations,

$$z = \sqrt{mH_R}\,\eta\ \ ;\ \ q = \frac{k}{\sqrt{mH_R}}\ \ ;\ \ \lambda = q^2 - i \tag{5.4.36}$$

in terms of which eqn. (5.4.26) becomes

$$\frac{d^2}{dz^2}h_k(z) + (z^2+\lambda)h_k(z) = 0\,, \tag{5.4.37}$$

the solutions of which are the parabolic cylinder functions[209, 15, 293, 70, 276]

$$D_\alpha[\sqrt{2}e^{i\pi/4}z]\ \ ;\ \ D_\alpha[\sqrt{2}e^{3i\pi/4}z]\ \ ;\ \ \alpha = -\frac{1}{2} - i\,\frac{\lambda}{2} = -1 - i\,\frac{q^2}{2}\,. \tag{5.4.38}$$

The solution that fulfills the "out" boundary condition (5.4.34) (see appendix A in ref.[103]) is given by

$$h_k(\eta) = D_\alpha[\sqrt{2}e^{i\pi/4}z]\,. \tag{5.4.39}$$

The general solution for the spinor wave functions $U^>, V^>$ during the (RD) era are linear combinations of the four independent solutions (5.4.27,5.4.28). In principle, with four independent solutions during inflation matching onto four independent solutions during (RD)

there would be a 4×4 matrix of Bogoliubov coefficients, however, because helicity is conserved, the linear combinations are given by

$$U_s^>(\vec{k},\eta) = A_{k,s}\,\mathcal{U}_s(\vec{k},\eta) + B_{k,s}\,\mathcal{V}_s(-\vec{k},\eta) \tag{5.4.40}$$

$$V_s^>(-\vec{k},\eta) = C_{k,s}\;\mathcal{V}_s(-\vec{k},\eta) + D_{k,s}\,\mathcal{U}_s(\vec{k},\eta)\,. \tag{5.4.41}$$

The Bogoliubov coefficients $A_{k,s}\cdots D_{k,s}$ are obtained from the matching conditions and the relations (5.4.30,5.4.32). These obey the relations[103]

$$D_{k,s} = -B^*_{k,s} \;\;;\;\; C_{k,s} = A^*_{k,s}\,, \tag{5.4.42}$$

and

$$|A_{k,s}|^2 + |B_{k,s}|^2 = 1\,. \tag{5.4.43}$$

During the (RD) era, with $U_s \equiv U_s^>; V_s \equiv V_s^>$ with $U^>, V^>$ given by (5.4.40,5.4.41) the field expansion (5.4.8) in terms of the spinor solutions with out boundary conditions (5.4.35) becomes

$$\psi(\vec{x},\eta) = \frac{1}{\sqrt{V}}\sum_{\vec{k},s}\left[\widetilde{b}_{\vec{k},s}\,\mathcal{U}_s(\vec{k},\eta) + \widetilde{d}^\dagger_{-\vec{k},s}\,\mathcal{V}_s(-\vec{k},\eta)\right]\,e^{i\vec{k}\cdot\vec{x}}\,, \tag{5.4.44}$$

where

$$\widetilde{b}_{\vec{k},s} \;=\; b_{\vec{k},s}A_k + d^\dagger_{-\vec{k},s}D_{k,s} \tag{5.4.45}$$

$$\widetilde{d}^\dagger_{-\vec{k},s} \;=\; d^\dagger_{-\vec{k},s}C_{k,s} + b_{\vec{k},s}B_{k,s}\,. \tag{5.4.46}$$

The relations (5.4.42,5.4.43) imply that the new operators $\widetilde{b},\widetilde{d}$ obey canonical anti-commutation relations. The operators $\widetilde{b}^\dagger$ and $\widetilde{d}^\dagger$ create asymptotic particle and antiparticle states respectively. In particular we find that the number of asymptotic "out" particle and antiparticle states in the Bunch-Davies vacuum state (5.4.22) are the same and given by

$$\langle 0_I|\widetilde{b}^\dagger_{\vec{k},s}\,\widetilde{b}_{\vec{k},s}|0_I\rangle = |D_{k,s}|^2 = \langle 0_I|\widetilde{d}^\dagger_{-\vec{k},s}\,\widetilde{d}_{-\vec{k},s}|0_I\rangle = |B_{k,s}|^2\,. \tag{5.4.47}$$

We identify the number of "out" particles, equal the number of "out" anti-particles as

$$\langle 0_I|\widetilde{b}^\dagger_{\vec{k},s}\,\widetilde{b}_{\vec{k},s}|0_I\rangle = \langle 0_I|\widetilde{d}^\dagger_{-\vec{k},s}\,\widetilde{d}_{-\vec{k},s}|0_I\rangle = |B_{k,s}|^2 \equiv N_k \tag{5.4.48}$$

with $N_k = |B_{k,s}|^2$ being the *distribution function of produced particles and antiparticles*. The relation (5.4.43) implies that

$$|B_{k,s}|^2 \leq 1\,, \tag{5.4.49}$$

for each helicity s, consistent with Pauli exclusion. For $m \ll H_{dS}$ it is found in ref.([103]) that

$$N_k = |B_{k,s}|^2 = \frac{1}{2}\Big[1 - \big(1 - e^{-\frac{k^2}{2mT_H}}\big)^{1/2}\Big]\,, \tag{5.4.50}$$

in terms of the emergent temperature[103]

$$T_H = \frac{H_R}{2\pi} \simeq 10^{-36}\,\mathrm{eV}\,. \tag{5.4.51}$$

$$\mathcal{U}_s(\vec{k},\eta) = e^{-i\int_{\eta_i}^{\eta}\omega_k(\eta')\,d\eta'}\,\widetilde{\mathcal{U}}_s(\vec{k},\eta) \;\;;\;\; \mathcal{V}_s(-\vec{k},\eta) = e^{i\int_{\eta_i}^{\eta}\omega_k(\eta')\,d\eta'}\,\widetilde{\mathcal{V}}_s(-\vec{k},\eta)\,, \tag{5.4.52}$$

where $\widetilde{\mathcal{U}}_s(\vec{k},\eta)$; $\widetilde{\mathcal{V}}_s(-\vec{k},\eta)$ are slowly varying functions of time during this regime, and again η_i is some early time in the adiabatic regime. To leading (zeroth) order in the adiabatic expansion these are given by

$$\widetilde{\mathcal{U}}_s(\vec{k},\eta) = \frac{1}{\Big[2\omega_k(\eta)(\omega_k(\eta)+M(\eta))\Big]^{1/2}} \begin{pmatrix} (\omega_k(\eta)+M(\eta))\,\xi_s \\ k\,s\,\xi_s \end{pmatrix}\,, \tag{5.4.53}$$

$$\widetilde{\mathcal{V}}_s(-\vec{k},\eta) = \frac{1}{\Big[2\omega_k(\eta)(\omega_k(\eta)+M(\eta))\Big]^{1/2}} \begin{pmatrix} -k\,s\,\xi_s \\ (\omega_k(\eta)+M(\eta))\,\xi_s \end{pmatrix}\,. \tag{5.4.54}$$

5.4.1 Energy density, pressure and entropy:

The energy momentum tensor for Dirac fields is given by [297, 156, 57, 258]

$$T^{\mu\nu} = \frac{i}{2}\Big(\overline{\Psi}\gamma^{\mu}\overset{\leftrightarrow}{\mathcal{D}^{\nu}}\Psi\Big) + \mu \leftrightarrow \nu \tag{5.4.55}$$

In terms of conformal time and the conformally rescaled fields (5.4.4) the energy density ρ and pressure P as operators are given by

$$\widehat{\rho}(\vec{x},\eta) = T^{0}_{0}(\vec{x},\eta) = \frac{i}{2a^4(\eta)}\,\Big(\psi^{\dagger}(\vec{x},\eta)\frac{d}{d\eta}\,\psi(\vec{x},\eta) - \frac{d}{d\eta}\,\psi^{\dagger}(\vec{x},\eta)\,\psi(\vec{x},\eta)\Big)\,, \tag{5.4.56}$$

$$\widehat{P}(\vec{x},\eta) = -\frac{1}{3}\sum_{j} T^{j}_{j}(\vec{x},\eta) = \frac{-i}{6a^4(\eta)}\,\Big(\psi^{\dagger}(\vec{x},\eta)\,\vec{\alpha}\cdot\vec{\nabla}\,\psi(\vec{x},\eta) - \vec{\nabla}\psi^{\dagger}(\vec{x},\eta)\cdot\vec{\alpha}\,\psi(\vec{x},\eta)\Big)\,, \tag{5.4.57}$$

The expectation value of the energy momentum tensor in the Bunch-Davies vacuum state is given by

$$\langle 0_I|T^{\mu}_{\nu}|0_I\rangle = \mathrm{diag}\big(\rho(\eta), -P(\eta), -P(\eta), -P(\eta)\big)\,, \tag{5.4.58}$$

only the homogeneous and isotropic component of the energy momentum tensor contributes to the expectation value. Because we want to extract the rapid time dependence during the adiabatic era, we obtain this homogeneous component by averaging the above operators in the comoving volume V, just as in the bosonic case we obtain

$$\frac{1}{V}\int d^3x\, T^{0}_{0}(\vec{x},\eta) = \widehat{\overline{\rho}}(\eta) \quad ; \quad -\frac{1}{3\,V}\int d^3x\,\sum_{j} T^{j}_{j}(\vec{x},\eta) = \widehat{\overline{P}}(\eta)\,. \tag{5.4.59}$$

During the (RD) era and near matter radiation equality when the adiabatic approximation becomes very reliable, we obtain these operators by expanding the fermionic field in the "out" basis as in eqn. (5.4.44), and writing the spinors as in eqn. (5.4.53,5.4.54) separating the fast phases from the slowly varying spinors $\widetilde{U}, \widetilde{V}$. We find

$$\widehat{\rho}(\eta) = \overline{\rho}_{vac}(\eta) + \widehat{\overline{\rho}}_{int}(\eta) + \widehat{\overline{\rho}}_{pp}(\eta) \tag{5.4.60}$$

$$\widehat{P}(\eta) = \overline{P}_{vac}(\eta) + \widehat{\overline{P}}_{int}(\eta) + \widehat{\overline{P}}_{pp}(\eta)\,, \tag{5.4.61}$$

$\overline{\rho}_{vac}; \overline{P}_{vac}$[1] are the zero point ("out" vacuum) contributions to the energy density and pressure. The terms $\widehat{\overline{\rho}}_{int}; \widehat{\overline{P}}_{int}$ feature the fast oscillations associated with the interference between particle and antiparticles similar to the complex bosonic case studied above. As discussed in the previous section, these oscillations average out on comoving time scales equal to or shorter than $\simeq 1/m \ll 1/H(t)$ leaving only the slowly varying contributions $\overline{\rho}_{vac}, \overline{\rho}_{p\bar{p}}$; $\overline{P}_{vac}, \overline{P}_{p\bar{p}}$. Following the same strategy as in the bosonic case, we introduce the zeroth-order adiabatic Hamiltonian,

$$H_0(\eta) = \sum_{\vec{k};s} \left[\widetilde{b}^{\dagger}_{\vec{k},s} \widetilde{b}_{\vec{k},s} + \widetilde{d}^{\dagger}_{\vec{k},s} \widetilde{d}_{\vec{k},s} \right] \omega_k(\eta) \quad ; \quad \left[H_0(\eta), H_0(\eta') \right] = 0 \ \ \forall \eta, \eta' \,, \tag{5.4.62}$$

and the time evolution operator

$$U_0(\eta, \eta_i) = e^{-i \int_{\eta_i}^{\eta} H_0(\eta') \, d\eta'} \,, \tag{5.4.63}$$

from which it follows that

$$U_0^{-1}(\eta, \eta_i) \, \widetilde{b}_{\vec{k},s} \, U_0(\eta, \eta_i) = \widetilde{b}_{\vec{k},s} \, e^{-i \int_{\eta_i}^{\eta} \omega_k(\eta') d\eta'} \quad ; \quad U_0^{-1}(\eta, \eta_i) \, \widetilde{d}_{\vec{k},s} \, U_0(\eta, \eta_i) = \widetilde{d}_{\vec{k},s} \, e^{-i \int_{\eta_i}^{\eta} \omega_k(\eta') d\eta'} \,. \tag{5.4.64}$$

It is clear that the fermionic case is very similar to that of the complex scalar case studied in the previous section with the important difference in the statistics. Following the steps described for the scalar case, we define the Schroedinger picture fermion operator during the adiabatic regime in the (RD) era

$$\psi(\vec{x}, \eta) = U_0(\eta, \eta_i) \, \psi_S(\vec{x}, \eta) \, U_0^{-1}(\eta, \eta_i) \,, \tag{5.4.65}$$

with

$$\psi_S(\vec{x}, \eta) = \frac{1}{\sqrt{V}} \sum_{\vec{k},s} \left[\widetilde{b}_{\vec{k},s} \, \widetilde{\mathcal{U}}_s(\vec{k}, \eta) + \widetilde{d}^{\dagger}_{-\vec{k},s} \, \widetilde{\mathcal{V}}_s(-\vec{k}, \eta) \right] e^{i \vec{k} \cdot \vec{x}} \,, \tag{5.4.66}$$

this field evolves slowly in time in the adiabatic regime. A similar definition of Schroedinger picture operators is carried out for the energy momentum tensor just as in the complex scalar case. The density matrix evolved in time in the Schroedinger picture is given by equation

[1] For explicit expressions, one can refer to our work [305].

(5.3.54).The fermionic "in" Bunch-Davies vacuum state $|0_I\rangle$ is now given in terms of the out states by

$$|0_I\rangle = \Pi_{\vec{k},s}\left\{\left[\cos(\theta_k)\right]\ \sum_{n_{\vec{k},s}=0}^{1}\left(-e^{2i\varphi_-(k)}\ \tan(\theta_k)\right)^{n_{\vec{k},s}}\left|n_{\vec{k},s};\overline{n}_{-\vec{k},s}\right\rangle\right\}, \tag{5.4.67}$$

the fermionic "out" particle-antiparticle pair states are given by

$$\left|n_{\vec{k},s};\overline{n}_{-\vec{k},s}\right\rangle = \frac{\left(\widetilde{b}^{\dagger}_{\vec{k},s}\right)^{n_{\vec{k},s}}}{\sqrt{n_{\vec{k},s}!}}\ \frac{\left(\widetilde{d}^{\dagger}_{-\vec{k},s}\right)^{n_{\vec{k},s}}}{\sqrt{n_{\vec{k},s}!}}\,|0_O\rangle \quad ; \quad n_{\vec{k},s}=0,1\,. \tag{5.4.68}$$

where the "out" vacuum state $|0_O\rangle$ is such that

$$\widetilde{b}_{\vec{k},s}\,|0_O\rangle = 0 \quad ; \quad \widetilde{d}_{\vec{k},s}\,|0_O\rangle = 0\ \forall\vec{k}\,, \tag{5.4.69}$$

and from eqn. (5.4.48)

$$|B_{k,s}|^2 = \sin^2(\theta_k) = N_k\,. \tag{5.4.70}$$

The Schroedinger picture density matrix $\rho_S(\eta) = U_0(\eta,\eta_i)\,|0_I\rangle\,\langle 0_I|\,U_0^{-1}(\eta,\eta_i)$ is now given by

$$\rho_S(\eta) = \Pi_{\vec{k},s}\Pi_{\vec{p},s'}\sum_{n_{\vec{k},s}=0}^{1}\sum_{m_{\vec{p},s'}=0}^{1}\mathcal{C}^{*}_{m_{\vec{p},s'}}(p)\ \mathcal{C}_{n_{\vec{k},s}}(k)\ \left|n_{\vec{k},s};\overline{n}_{-\vec{k},s}\right\rangle\langle m_{\vec{p},s'};\overline{m}_{-\vec{p},s'}|\ \mathcal{A}\,, \tag{5.4.71}$$

where

$$\mathcal{A} = e^{2i\int_{\eta_i}^{\eta}\left[m_{\vec{p},s'}\,\omega_p(\eta')-n_{\vec{k},s}\,\omega_k(\eta')\right]d\eta'}, \tag{5.4.72}$$

and in the fermion case

$$\mathcal{C}_{n_{\vec{k},s}}(k) = \cos(\theta_k)\left(-e^{2i\varphi_-(k)}\ \tan(\theta_k)\right)^{n_{\vec{k},s}} \quad ; \quad n_{\vec{k},s}=0,1\,. \tag{5.4.73}$$

Just as in the scalar case, the rapid oscillatory phases in the terms that are off-diagonal in pair number $m \neq n$, momenta and helicity average out on time scales $\simeq 1/m \ll 1/H(t)$ leading to the decoherence of the density matrix in this basis. Proceeding as in the scalar case we average these terms over time scales intermediate between $1/m$ and the Hubble time scale $1/H(t)$. This averaging, a coarse graining on the short time scale, is a direct consequence of the separation of time scales during the adiabatic regime, with $H(t)/m \ll 1$ and yields a density matrix that is diagonal in the basis of particle-antiparticle pairs (5.4.68).

The loss of coherence in the averaging of correlations implies a loss of information (from these correlations). The calculation of the entropy associated with this loss of information follows the same route as in the scalar case with few modifications consequence of the different statistics. Upon averaging the rapidly varying phases, the density matrix becomes diagonal in the basis of particle antiparticle pairs, and is given by

$$\rho_S^{(d)} = \Pi_{\vec{k},s}\big[\cos^2(\theta_k)\big] \sum_{n_{\vec{k},s}=0}^{1} \Big(\tan^2(\theta_k)\Big)^{n_{\vec{k},s}} \Big|n_{\vec{k},s};\overline{n}_{-\vec{k},s}\Big\rangle \Big\langle n_{\vec{k},s};\overline{n}_{-\vec{k},s}\Big| \,. \tag{5.4.74}$$

We can compare this density matrix with the reduced one obtained by tracing over the antiparticle states,

$$\rho_S^{(r)}(\eta) = \mathrm{Tr}_{\overline{p}}\,\rho_S(\eta) = \Pi_{\vec{k},s}\big[\cos^2(\theta_k)\big] \sum_{n_{\vec{k},s}=0}^{1} \Big(\tan^2(\theta_k)\Big)^{n_{\vec{k},s}} \Big|n_{\vec{k},s}\Big\rangle \Big\langle n_{\vec{k},s}\Big| \,, \tag{5.4.75}$$

exhibiting the equivalence of the diagonal matrix elements, namely the probabilities. The density matrices $\rho_S^{(d)};\rho_S^{(r)}$ feature the *same eigenvalues*, hence the same entropy. Again, this is the statement that the entropy arising from the loss of information in the time averaging or coarse graining, is identical to the entanglement entropy obtained from the reduced density matrix.

The diagonal density matrix (5.4.74) can be written in a familiar quantum statistical mechanics form by introducing a fiducial Hamiltonian

$$\widehat{\mathcal{H}} = \sum_{\vec{k},s} \mathcal{E}_k\, \widehat{\mathcal{N}}_{\vec{k},s} \,, \tag{5.4.76}$$

with

$$\mathcal{E}_k = -\ln[\tan^2(\theta_k)] \quad ; \quad \widehat{\mathcal{N}}_{\vec{k},s} = \sum_{n_{\vec{k},s}=0}^{1} n_{\vec{k},s} \Big|n_{\vec{k},s};\overline{n}_{-\vec{k},s}\Big\rangle \Big\langle n_{\vec{k},s};\overline{n}_{-\vec{k},s}\Big| \,, \tag{5.4.77}$$

and the partition function is given by

$$\mathcal{Z} = \Pi_{\vec{k},s}[\cos^2(\theta_k)]^{-1} = \Pi_{\vec{k},s}[1+\tan^2(\theta_k)] \,, \tag{5.4.78}$$

so that

$$\rho_S^{(d)} = \frac{e^{-\widehat{\mathcal{H}}}}{\mathcal{Z}} \quad ; \quad \mathcal{Z} = \mathrm{Tr}\, e^{-\widehat{\mathcal{H}}} \equiv e^{-\mathbb{F}} \,, \tag{5.4.79}$$

with $\mathbb{F}$ the fiducial free energy. We note that in the fermionic case $\widehat{\mathcal{N}}^2_{\vec{k},s} = \widehat{\mathcal{N}}_{\vec{k},s}$ therefore for fixed $\vec{k}, s$ its eigenvalues are $0, 1$ and from the relations (5.4.48, 5.4.70) it follows that

$$\tan^2(\theta_k) = \frac{N_k}{1 - N_k}\,. \tag{5.4.80}$$

The entropy is now obtained from (5.3.81) but now with

$$U = \mathrm{Tr}\,\rho^{(d)}\,\mathcal{H} = \sum_{\vec{k},s} \frac{\mathcal{E}_k}{e^{\mathcal{E}_k} + 1} = \sum_{\vec{k},s} N_k\,\ln\left[\frac{1 - N_k}{N_k}\right]. \tag{5.4.81}$$

The entropy is now given by

$$S^{(d)} = -2\sum_{\vec{k}} \Big\{ (1 - N_k)\,\ln(1 - N_k) + N_k\,\ln N_k \Big\}\,. \tag{5.4.82}$$

This is a remarkable result, the entanglement entropy is proportional to the quantum kinetic entropy for fermions in terms of the distribution function[83]. The factor 2 accounts for two helicity eigenstates, since the distribution function is the same for both helicities. We highlight that although the number of particles and of antiparticles are the same, the entropy does *not* feature a factor 4 (particle, anti-particle with two helicities) but a factor 2. The reason behind this is the same as in the complex scalar case: particle and antiparticles are produced in *correlated pairs* not independently. This important aspect is also at the heart of the equivalence between the entropy arising from dephasing and decoherence and the entanglement entropy: tracing over one member of the particle-anti-particle pairs in (5.4.71) (either particle or anti-particle) reduces the full density matrix (5.4.71) to (for example tracing over anti-particles)

$$\rho^{(r)}(\eta) = \Pi_{\vec{k},s}\big[\cos^2(\theta_k)\big] \sum_{n_{\vec{k},s}=0}^{1} \Big(\tan^2(\theta_k)\Big)^{n_{\vec{k},s}} \Big|n_{\vec{k},s}\Big\rangle \Big\langle n_{\vec{k},s}\Big|\,, \tag{5.4.83}$$

yielding an entanglement entropy equivalent to (5.4.82). We also find

$$\begin{aligned} &\mathrm{Tr}\,\widetilde{b}^\dagger_{\vec{k},s}\,\widetilde{b}_{\vec{k},s}\,\rho^{(d)}_S = \mathrm{Tr}\,\widetilde{d}^\dagger_{\vec{k},s}\,\widetilde{d}_{\vec{k},s}\,\rho^{(d)}_S = |B_{k,s}|^2 = N_k \\ &\mathrm{Tr}\,\widetilde{b}^\dagger_{\vec{k},s}\,\widetilde{d}^\dagger_{-\vec{k},s}\,\rho^{(d)}_S = \mathrm{Tr}\,\widetilde{d}_{-\vec{k},s}\,\widetilde{b}_{\vec{k},s}\,\rho^{(d)}_S = 0\,. \end{aligned} \tag{5.4.84}$$

Therefore, the energy density and pressure near matter radiation equality when the adiabatic approximation is very reliable and the density matrix has undergone complete decoherence via dephasing, are given by

$$\overline{\rho}(\eta) = \mathrm{Tr}\widehat{\overline{\rho}}(\eta)\,\rho_S^{(d)} \quad ; \quad \overline{P}(\eta) = \mathrm{Tr}\widehat{\overline{P}}(\eta)\,\rho_S^{(d)}\,, \tag{5.4.85}$$

these are obtained to leading (zeroth) order in the adiabatic approximation by using the spinors (5.4.53,5.4.54). As a consequence of decoherence yielding the identities (5.4.84), the particle-antiparticle interference terms vanish. Because the spinors (5.4.53,5.4.54) are eigenstates of the instantaneous conformal Hamiltonian (**??**) with eigenvalues $\pm\omega_k(\eta)$, we find to leading order in the adiabatic expansion[2]

$$\overline{\rho}(\eta) = \underbrace{-\frac{1}{\pi^2 a^4(\eta)}\int_0^\infty k^2 dk\,\omega_k(\eta)}_{\overline{\rho}_0(\eta)} + \underbrace{\frac{2}{\pi^2 a^4(\eta)}\int_0^\infty k^2 dk\,N_k\,\omega_k(\eta)}_{\overline{\rho}_{p\overline{p}}(\eta)}\,, \tag{5.4.86}$$

$$\overline{P}(\eta) = \underbrace{-\frac{1}{3\pi^2 a^4(\eta)}\int_0^\infty k^2 dk\,\frac{k^2}{\omega_k(\eta)}}_{\overline{P}_0(\eta)} + \underbrace{\frac{2}{3\pi^2 a^4(\eta)}\int_0^\infty k^2 dk\,N_k\,\frac{k^2}{\omega_k(\eta)}}_{\overline{P}_{p\overline{p}}(\eta)}\,, \tag{5.4.87}$$

where $\overline{\rho}_0(\eta), \overline{P}_0(\eta)$ are the zero point energy density and pressure and $\overline{\rho}_{p\overline{p}}(\eta), \overline{P}_{p\overline{p}}(\eta)$ are the contributions from gravitational particle production. The zero point and particle production contributions independently obey covariant conservation. As explained in ref.[103] the zero point contribution is absorbed into a renormalization[156, 179, 57, 199, 258], therefore the kinetic-fluid description of gravitationally produced fermionic dark matter near matter radiation equality can now be summarized as

$$\mathcal{N}_{p\overline{p}} = \frac{2}{\pi^2}\int_0^\infty k^2\,N_k\,dk\,, \tag{5.4.88}$$

$$\overline{\rho}_{p\overline{p}}(\eta) = \frac{2}{\pi^2 a^4(\eta)}\int_0^\infty k^2\,N_k\,\omega_k(\eta)\,dk\,, \tag{5.4.89}$$

$$\overline{P}_{p\overline{p}}(\eta) = \frac{2}{3\pi^2 a^4(\eta)}\int_0^\infty k^2\,N_k\,\frac{k^2}{\omega_k(\eta)}\,dk\,, \tag{5.4.90}$$

[2]For higher order contributions see ref.[103].

$$\mathcal{S}_{p\bar{p}} = -\frac{2}{2\pi^2}\int_0^\infty k^2 \Big\{(1-N_k)\,\ln(1-N_k) + N_k\,\ln N_k\Big\} dk\,, \tag{5.4.91}$$

where $\mathcal{N}_{p\bar{p}}$ is the total comoving number density of particles plus antiparticles produced, $\mathcal{S}_{p\bar{p}}$ is the time independent comoving entropy density, and the distribution function N_k is given by eqn. (5.4.50). The kinetic fluid forms of the energy density (5.4.89) and pressure (5.4.90) are exactly the same as obtained in ref.[103] by averaging over the fast phases in the particle-antiparticle interference terms. Therefore, just as in the bosonic case this averaging in the energy momentum tensor and the emergence of the kinetic fluid form in the adiabatic regime is a direct manifestation of decoherence by dephasing in the density matrix, hence also directly related to the emergence of entropy in this case.

With the distribution function (5.4.50), we find

$$\mathcal{N}_{p\bar{p}} = \frac{2}{\pi^2}\Big(2mT_H\Big)^{3/2} \times 0.126\,, \tag{5.4.92}$$

and

$$\mathcal{S}_{p\bar{p}} = \frac{1}{\pi^2}\Big(2mT_H\Big)^{3/2} \times 0.451\,, \tag{5.4.93}$$

with a specific entropy

$$\frac{\mathcal{S}_{p\bar{p}}}{\mathcal{N}_{p\bar{p}}} \simeq 1.8\,. \tag{5.4.94}$$

We note that a specific entropy $\mathcal{O}(1)$ is typical of a thermal species. However, with $m \simeq 10^8\,\text{GeV}$ for a heavy fermion with the correct dark matter abundance[103], the ratio of its comoving entropy to that of the (CMB) today given by (5.3.103) which also features a specific entropy $\mathcal{O}(1)$, is

$$\frac{\mathcal{S}_{p\bar{p}}}{\mathcal{S}_{cmb}} \simeq 10^{-15}\,, \tag{5.4.95}$$

therefore even for a heavy fermionic dark matter species that is gravitationally produced, its entropy is negligible compared to that of the (CMB) today.

5.5 Discussion

Real scalars, Majorana fermions: We have studied complex scalars and Dirac fermions for which particles are different from antiparticles. However, the results apply just as well to real scalars and Majorana fermions, in which cases particles are the same as antiparticles and the correlated pair states are now of the form $\left|n_{\vec{k}}, n_{-\vec{k}}\right\rangle$. The entanglement entropy is exactly the same as for complex scalars or Dirac fermions respectively, since for each value of $\vec{k}$ (and helicity s for fermions), tracing over one member of the pair (say that with $-\vec{k}$) yields exactly the same probabilities, regardless of whether it is a particle or an antiparticle. This is also explicit in the entanglement entropies obtained above since there is no factor 2 for particle and antiparticle, because of the correlated nature of the pair state, independently of whether the members of the pairs are particle and antiparticle or particle-particle with opposite momenta.

The origin of entropy: the "out" basis is a pointer basis. In the language of quantum information, the "out" basis of particles is the "measured" basis and constitutes a *pointer basis*[231]. This is indeed a privileged basis, since the energy momentum tensor in this out particle basis describes the abundance, equation of state and entropy of *particles* (and antiparticles). These are the observable macroscopic variables that describe the properties of dark matter. It is precisely in this basis that the rapid dephasing and coarse graining as a consequence of time averaging over the short time scales leads to decoherence and information loss, with the concomitant emergence of a non-vanishing entropy.

One could take expectation values of the energy momentum tensor (or any other observable related to dark matter) in the "in" vacuum state $|0_I\rangle$ or the density matrix $|0_I\rangle\langle 0_I|$ as is the case in refs.[226, 103]. This expectation value features the rapidly oscillating interference terms between "out" particles and antiparticles, which were averaged out on the short time scales in these references. This averaging in the expectation values in the "in" state $|0_I\rangle$ are a manifestation of the loss of correlations by dephasing, yet do not make explicit the *entropic* content of this decoherence process.

These are precisely the coherences and correlations that are averaged out in the density matrix in the Schroedinger picture in the out basis. Hence, particle "observables" or mea-

surements in the out particle basis in general will undergo this process of decoherence via dephasing even when the matrix elements are obtained in the "in" basis. The coarse graining of the density matrix in the Schroedinger picture in the out basis exhibits directly this decoherence mechanism by dephasing and the emergence of entropy. It also makes explicit that the decoherence time scale is $\simeq 1/m$. Therefore, the origin of entropy is deeply associated with this natural selection of basis of "out particles" to describe the density matrix and the statistical properties of dark matter.

More general arguments for entropy: Although we focused on the entropy in gravitational particle production, the main concepts elaborated here are more general. For example they apply also to the case when particles are produced from inflaton oscillations at the end of inflation[312], or by parametric resonance during reheating[30, 34]. In these cases, a homogeneous scalar field (generically the inflaton) couples non-linearly to the matter bosonic or fermionic fields. If the expectation value of this scalar field depends on time, acting as a time dependent mass term, such coupling leads to production of particle or particle-antiparticle pairs entangled in momentum (and any other conserved quantum number). The "in" basis is generically a superposition of the out particle basis states, therefore the interference effects will also be manifest in a similar manner as studied here, although the occupation number of "out" states will be different for different mechanisms. Because dark matter particles are defined as asymptotic out states in the adiabatic era, a separation of time scales as in the adiabatic Schroedinger picture in which the density matrix evolves in time will feature a structure very similar to that unveiled in the study above, but with different probabilities determined by the different processes. Nevertheless dephasing and decoherence will play a similar role leading to an entropy of the very same form as obtained above but with different N_k.

Entanglement entropy vs. entropy (isocurvature) perturbations: The entanglement entropy discussed above should not be identified with linear entropy or isocurvature *perturbations*. The latter are generically associated with multiple fields with non-vanishing expectation values during inflation[208, 120, 60]. Entropy perturbations in the case when scalar fields do *not* acquire expectation values[131], or for fermionic fields (which cannot acquire expectation values) [132] were analyzed within the context of zero point contribu-

tions to the energy momentum tensor in refs.[131, 132]. However, in refs.[226, 103] it was argued that the renormalization fully subtracting the zero point contribution as is implicitly or explicitly done in the literature, prevents a consistent interpretation of entropy perturbations from the zero point contribution of the energy momentum tensor as advocated in refs.[131, 132]. In our study here the scalar field does *not acquire* an expectation value and we implemented the same renormalization scheme subtracting completely the zero point contribution to the energy momentum tensor as in refs. [226, 103] both for scalar and fermion fields. Therefore the analysis and conclusions of refs.[131, 132] do not apply to our study.

Curvature perturbations and inhomogeneous gravitational potentials will modify the entropies (5.3.96,5.4.82) by modifying the distribution functions $N_k \to N_k + \delta N_k(\vec{x}, t)$ thereby inducing a perturbation in the entanglement entropy. Such perturbation is completely determined by the change in the distribution function which obeys a linearized collisionless Boltzmann equation in presence of the metric perturbations. This equation along with a proper assessment of initial conditions must be studied in detail for a definite understanding of entropy perturbations, a task that is well beyond the scope and objective of our study.

5.6 Conclusions and further questions:

While the evidence for dark matter is overwhelming, direct detection of a particle physics candidate with interactions with (SM) degrees of freedom, necessary for detection, has proven elusive. Therefore dark matter particles featuring only gravitational interaction are logically a suitable alternative. Such candidates are produced gravitationally via cosmological expansion, a phenomenon that received substantial attention in the last few years. In this chapter we studied the emergence of entropy in gravitational production of dark matter particles, focusing on the cases of a complex scalar and a Dirac fermion under a minimal set of assumptions as in refs.[226, 103]. We considered a rapid transition from inflation to radiation domination and focused on comoving super-Hubble wavelengths at the end of inflation, with dark matter fields being in their Bunch-Davies vacua during inflation. The "out" states are correlated particle-antiparticle pairs and the distribution function of gravitationally produced

particles is obtained exactly both for ultra-light scalars and heavier fermions.

Well after the transition and before matter radiation equality there ensues a period of adiabatic evolution when the scale factor $a_{eq} \gg a(t) \gg 10^{-17}/\sqrt{m(eV)}$ characterized by the adiabatic ratio $H(t)/m \ll 1$ with $H(t)$ the Hubble expansion rate and m the particle's mass. During this regime there is a wide separation of time scales with $1/H(t)$ a long time scale of cosmological evolution and $1/m$ a short time scale associated with particle dynamics. As shown in refs.[226, 103], during this regime the energy momentum tensor written in the "out" particle basis (dark matter particles) feature rapidly varying particle-antiparticle interference terms. Averaging these contributions on intermediate time scales renders the energy momentum tensor of the usual kinetic fluid form. We show that these rapidly varying interference terms are manifest in the density matrix in the adiabatic Schroedinger picture in the out particle basis as off diagonal density matrix elements that feature rapid dephasing on short decoherence time scales $\simeq 1/m$. Decoherence by dephasing effectively reduces the density matrix to a diagonal form in the out basis with a non-vanishing von Neumann entropy. In turn, the von Neumann entropy is exactly the same as the *entanglement entropy* obtained by tracing over one member of the correlated particle-antiparticle pair.

Remarkably, we find that the comoving von-Neumann-entanglement entropy density is *almost* of the kinetic fluid form in terms of the distribution function N_k

$$\mathcal{S}_{p\bar{p}} = \pm \frac{1}{2\pi^2} \int_0^\infty k^2 \Big\{ (1 \pm N_k)\, \ln(1 \pm N_k) \mp N_k\, \ln N_k \Big\} dk\,, \tag{5.6.1}$$

where $(+)$ is for *real or complex* bosons and $(-)$ is for each spin/helicity of *Dirac or Majorana* fermions. If the "out" states were described by *independent* particles and/or antiparticles, complex bosons and Dirac fermions would have twice the number of degrees of freedom of real bosons and Majorana fermions and the entropy would feature an extra factor 2 when particles are different from antiparticles. The fact that the entanglement entropies are the same regardless of whether particles are different from antiparticles is a consequence of the pair correlations of the "out" state, explaining the qualifier "*almost*". These particle-antiparticle or particle-particle pairs are entangled in momentum (and helicity in the case of fermions) and the entanglement entropy, obtained by tracing over one member of the pair is the *same* in both cases regardless of whether particles are the same or different from antiparticles.

An important conclusion of our study is that the von Neumann-entanglement- entropy and the kinetic fluid form of the energy momentum are all a consequence of decoherence of the density matrix in the out basis.

We argue that the origin of entropy is deeply related to the natural physical basis of "out" particles that determine the statistical properties of dark matter, such as energy density, pressure and entropy. Furthermore, we also argue that our results are more general and apply also to several other production mechanisms such as parametric amplification and production from inflaton oscillations at the end of inflation.

For an ultra-light bosonic dark matter candidate minimally coupled to gravity we find that while the occupation number is very large in the infrared region, the specific entropy, or entropy per particle, is negligibly small, indicating that this dark matter candidate is produced in a *condensed state*, albeit with vanishing expectation value. For fermionic dark matter the distribution function is nearly thermal[103] and the specific entropy is $\mathcal{O}(1)$ consistent with a thermal species.

Further questions:

a) Observational consequences?: While the energy density and pressure (or equation of state) both have clear observational consequences and directly yield information on clustering properties such as the free streaming length or cut-off in the matter power spectrum[226], we have not yet identified an observational consequence directly associated with entropy. As discussed above, for both cases, ultra light or heavier fermionic gravitationally produced dark matter, their comoving entropy is many orders of magnitude smaller than that for the (CMB) today.

The similarity with the fluid kinetic form suggests that perhaps the entropy *may* play a role in the dynamics of galaxy formation. Pioneering work in refs.[273, 335] studied the non-equilibrium process of violent relaxation in collisionless galactic dynamics in terms of an H-function that is similar to the statistical entropy of a classical dilute gas. It is argued in these references that such H-function increases during this process of relaxation towards an equilibrium state. It is an intriguing possibility that the entanglement entropy that we find *could* play a similar role in understanding the evolution of clustering during the matter dominated era.

Another important question is the role of metric perturbations on the entropy, as mentioned above this would entail a study of the linearized boltzmann equation and further understanding on initial conditions.

b) Interactions:

Although we did not consider the possibility of dark matter self-interactions or interactions with (SM) degrees of freedom, the study of how the entanglement entropy evolves in time as a consequence of such interactions would be of fundamental interest and a worthy endeavor. In principle the evolution of the entropy could be obtained by setting up a quantum kinetic Boltzmann equation for the distribution function N_k. However, a new framework must be developed to implement this program, because typically the Boltzmann equation is obtained by calculating transition amplitudes in S-matrix theory, however the mode functions even during the adiabatic regime are *not* the same as in Minkowski space time. Furthermore, the usual approach takes the infinite time limit to obtain the transition probabilities, which in principle is not warranted in presence of cosmological expansion,

instead a framework similar to that implemented in refs.[227, 106] must be adapted to a quantum kinetic approach.

The first law of thermodyamics when combined with covariant conservation of the energy entails that the total *thermodynamic* entropy is constant, namely the cosmological expansion is adiabatic in the thermodynamic sense in agreement with the Universe being a closed system. However, the entanglement entropy is *not* a thermodynamic entropy, therefore if interactions are included, it is by no means clear that that the entanglement entropy remains constant. Ref.[235] advocated a possible statistical framework to include interactions akin to the Bogoliubov-Born-Green-Kirkwood- Yvon (BBGKY) hierarchy of equations that yields the usual Boltzmann equation. While this suggestion is compelling, the applicability of such framework to study the time evolution of the entanglement entropy merits further study beyond the scope of this chapter.

6.0 Interaction rates in cosmology: heavy particle production and scattering

6.1 Introduction

Processes such as scattering and decay play a fundamental role in early Universe cosmology, from post-inflationary reheating[251, 270] to Big Bang Nucleosynthesis (BBN)[251, 83, 160, 149, 180, 329, 313, 274], and possibly in a successful description of the origin of matter-antimatter asymmetry[336, 250, 116, 115] . The main approach to studying such phenomena relies on the S-matrix formulation of quantum field theory in Minkowski space time. Within this formulation a scattering cross section is obtained from the transition probability per unit time from an initial multiparticle state prepared in the infinite past, to another multiparticle state detected in the infinite future normalized to a unit incoming flux. The cross sections and transition rates obtained in this framework are some of the main ingredients in the kinetic Boltzmann equation that describe the production, evolution and freeze-out of different particle species[251, 83, 160]. In the S-matrix formulation of transition rates, taking the infinite time limit yields exact energy conservation, and consequently reaction thresholds. This approach, when applied to early universe cosmology is at best an approximation, cosmological expansion introduces a distinct time evolution and the different stages, inflation, radiation, matter domination are characterized by different expansion time scales and dynamics. Obviously taking the infinite time limit glosses over the different stages of cosmological expansion and is in general unwarranted. We note that recently, reference[139] has revisited the S-matrix formulation in Minkowski space time analyzing processes in a finite time interval and discussing in detail the subtleties of approaching the asymptotic infinite time limit. Quantum field theory in curved space-time reveals a wealth of unexpected novel phenomena, such as particle production from cosmological expansion [294, 184, 355, 90, 117, 89, 189, 288, 297, 296] along with processes that are forbidden in Minkowski space time as a consequence of energy/momentum conservation. Pioneering investigations of interacting quantum fields in expanding cosmologies generalized the S-matrix formulation for in-out states in Minkowski space-times for model expansion

histories. Self-interacting quantized fields were studied with a focus on renormalization aspects and contributions from pair production to the energy momentum tensor [90, 117]. The decay of a massive particle into two massless particles conformally coupled to gravity was studied in Ref. [52] within a modified formulation of the S-matrix for simple cosmological space times.

Particle decay in de Sitter space-time was studied in Refs. [104, 112], revealing surprising phenomena, such as a quantum of a massive field decaying into two (or more) quanta of the *same* field. These phenomena are a direct consequence of the lack of a global time-like Killing vector, and the concomitant absence of energy conservation. Single particle decay in an post inflationary cosmology has been studied in refs.[236, 227, 103] and more recently reheating during a post-inflation period has been studied implementing a Boltzmann equation that inputs cosmological decay rates[260]. The results on particle decay of refs.[227, 103] revealed noteworthy consequences of the cosmological expansion and lack of energy conservation. An important result for very weakly coupled long lived particles is that the Minkowski space-time decay rate underestimates the lifetime of the particle, with potentially important consequences for weakly coupled dark matter.

Motivation and objectives: Particle interactions are ubiquitous in cosmology during all the epochs with fundamental and phenomenological implications in the description of particle physics processes during the expansion history. While there have been previous studies of single particle decay in inflationary and post inflationary cosmology[52, 236, 227, 103], to the best of our knowledge, there has not yet been a systematic study of *cross sections* and interaction rates including consistently the dynamics of cosmological expansion. Hence, motivated by their importance to describe particle physics processes in the early universe, our objectives in this chapter are the following: **i:)** to address the fundamental question on the validity of the S-matrix formulation as applied to cosmology, **ii:)** to provide an *ab initio* study of interaction rates and cross sections in a spatially flat radiation dominated (RD) cosmology from a full quantum field theoretical analysis in curved space time, providing a consistent formulation that explicitly includes the cosmological expansion. **iii:)** To identify under which circumstances the S-matrix formulation is (approximately) reliable, and when it is not, to establish its limitations. **iv:)** To identify potentially new phenomena that is

not captured by the S-matrix formulation and that may lead to novel phenomenological consequences.

In this chapter we begin this program by studying the case of scalar fields with a contact interaction as a first step towards a deeper understanding of fermionic and gauge degrees of freedom of the standard model or beyond and perhaps of possible dark matter candidates. The lessons learned in this study will provide a stepping stone to approaching more general interactions: if they confirm the validity of an S-matrix approximation to cross sections in cosmology, then our study provides a first principles analysis that lends credibility to this framework, and establishes its limitations. If, on the other hand, our study reveals new phenomena that is not captured by the S-matrix formulation, it may lead to novel phenomenological consequences and will further motivate the study of other interactions relevant to cosmological processes.

Brief summary of results: After discussing field quantization in a (RD) cosmology, and recognizing the daunting conceptual and technical challenges of obtaining transition matrix elements with the exact field modes even at tree level, we introduce an adiabatic expansion that relies on the ratio $H/E \ll 1$ where H is the expansion rate and E the energy of a particle measured by a locally inertial observer. This expansion is valid for all wavelengths well inside the particle horizon at any given time and its reliability improves upon cosmological expansion. At heart it hinges on a wide separation between cosmological and microscopic time scales. In this chapter we consider two bosonic degrees of freedom with a local contact interaction to leading order in this adiabatic expansion. We obtain the interaction rate and cross section during the finite time interval determined by the particle horizon. We show that the leading adiabatic order yields the dominant contribution. As a consequence of the cosmological expansion and a finite particle horizon we find several general noteworthy features of the cross section: **i):** violation of local Lorentz invariance: the cross section for a finite particle horizon features a dependence on the local energy and momenta that explicitly breaks the invariance under local Lorentz transformations. **ii):** the cross section for heavy particle production features two different phenomena a) a freeze-out, whereby the physical momentum falls below the production threshold and the expansion shuts-off the production, b) a time regime during which there is subthreshold production of

a heavier species: the finite particle horizon introduces an energy uncertainty which leads to the relaxation of the threshold condition and opens a window of width $\propto H$ for production of heavier particles for local energy and momenta that are smaller than the threshold value in Minkowski space-time. This is a manifestation of the *antizeno* effect [249, 105, 182]. In other words the energy uncertainty as a consequence of the finite particle horizon allows processes that would be otherwise forbidden by strict energy conservation. A possible implication of this phenomenon may be relevant to dark matter: if heavy dark matter particles are produced via pair annihilation of a much lighter species, sub-threshold production leads to an enhancement of their abundance.

6.2 The model:

In the standard cosmological model, most particle physics processes occur during the radiation dominated (RD) era, therefore we focus on the post-inflationary (RD) universe, described by a spatially flat Friedmann-Robertson-Walker (FRW) cosmology with the metric in comoving coordinates given by

$$g_{\mu\nu} = \mathrm{diag}(1, -a^2, -a^2, -a^2)\,, \tag{6.2.1}$$

where a is the scale factor. It is convenient to pass to conformal time η with $d\eta = dt/a(t)$, in terms of which the metric becomes ($a(t) \equiv a(\eta)$)

$$g_{\mu\nu} = a^2(\eta)\,\eta_{\mu\nu}\,. \tag{6.2.2}$$

where $\eta_{\mu\nu}$ is the Minkowski space-time metric.

During the (RD) stage, the Hubble expansion rate $H(\eta)$ is given by

$$H(\eta) = \frac{1}{a^2(\eta)}\frac{da(\eta)}{d\eta} = 1.66\sqrt{g_{eff}}\,\frac{T_0^2}{M_{Pl}\,a^2(\eta)}\,, \tag{6.2.3}$$

where g_{eff} is the effective number of ultrarelativistic degrees of freedom, which varies in time as different particles become non-relativistic, and T_0 is the temperature of the cosmic microwave background today. We take $g_{eff} = 2$ corresponding to radiation today, which

yields a lower bound on the Hubble scale, in order to estimate order of magnitudes. The scale factor during (RD) is

$$a(\eta) = H_R\,\eta \;\;;\;\; H_R = H_0\,\sqrt{\Omega_R} = 10^{-44}\,\mathrm{GeV} \Rightarrow H(\eta) = \frac{H_R}{a^2(\eta)}\,, \tag{6.2.4}$$

($H(\eta) \equiv H(t)$) where quantities with a subscript 0 refer to the values today, and Ω_R is the ratio of energy density in radiation today to the critical density. The numerical value for H_R follows from taking $g_{eff} = 2$. During this stage the relation between conformal and comoving time is given by

$$\eta = \Big(\frac{2\,t}{H_R}\Big)^{\frac{1}{2}} \Rightarrow a(t) = \Big[2\,t H_R\Big]^{\frac{1}{2}} \;\;;\;\; H(t) = \frac{1}{2\,t}\,. \tag{6.2.5}$$

If particles interact directly with the thermal bath that constitutes the environment during the (RD) era, high temperature and density induce thermal corrections to masses and interaction vertices. In this chapter we do not consider these effects, focusing solely on the conceptual aspects of obtaining interaction rates and cross sections directly in real time accounting for the cosmological expansion. Therefore, the results obtained are general and independent of the thermal aspects of populations, and apply directly, for example to two dark matter particle species that interact weakly with each other via a local contact interaction but not with the standard model degrees of freedom. Including finite temperature and density corrections to these quantities in the case of direct interaction and thermalization with the environmental plasma remains a longer term goal outside the scope of this chapter.

We consider a complex (Ψ) and a real (Φ) scalar field with a local quartic interaction with action given by

$$A = \int d^4x\sqrt{|g|}\Big\{g^{\mu\nu}\,\partial_\mu\Psi^\dagger\partial_\nu\Psi - M^2\Psi^\dagger\Psi + \frac{1}{2}g^{\mu\nu}\,\partial_\mu\Phi\partial_\nu\Phi - \frac{1}{2}m^2\Phi^2 - \lambda\,\Psi^\dagger\,\Psi\,\Phi^2\Big\} \tag{6.2.6}$$

noting that the Ricci scalar vanishes identically in a spatially flat (RD)- (FRW) cosmology. In comoving spatial coordinates and conformal time and upon conformally rescaling the fields as

$$\Psi(\vec{x},t) = \frac{\phi(\vec{x},\eta)}{a(\eta)} \;\;;\;\; \Phi(\vec{x},t) = \frac{\chi(\vec{x},\eta)}{a(\eta)} \;\;;\;\; a(\eta) = a(t(\eta))\,, \tag{6.2.7}$$

the action (6.2.6) becomes

$$A = \int d^3x\, d\eta \Big\{ \tfrac{1}{2} \left(\frac{d\chi}{d\eta}\right)^2 - \tfrac{1}{2} \left(\nabla\chi\right)^2 - \tfrac{1}{2}\chi^2\, m^2\, a^2(\eta) \tag{6.2.8}$$

$$+ \left(\frac{d\phi^\dagger}{d\eta}\right)\left(\frac{d\phi}{d\eta}\right) - \left(\nabla\phi^\dagger\right)\left(\nabla\phi\right) - |\phi|^2\, M^2\, a^2(\eta) - \lambda\, \phi^\dagger(\vec{x},\eta)\, \phi(\vec{x},\eta)\, \chi^2(\vec{x},\eta) \Big\}. \tag{6.2.9}$$

Although this simple model cannot capture all of the important aspects of standard model physics and/or dark matter candidates, it allows us to study ubiquitous phenomena such as scattering and particle production, illuminating the interplay between the dynamics of expansion and threshold kinematics. Furthermore, its analysis leads us to draw general lessons on the technical and conceptual aspects that will pave the way towards understanding interactions more relevant to particle physics models.

6.2.1 Quantization and adiabatic expansion:

We begin with the quantization of free fields [294, 184, 355, 89, 189, 297, 288, 90, 117] as a prelude to the interacting theory. The Heisenberg equations of motion for the conformally rescaled fields ϕ, χ in conformal time are

$$\frac{d^2}{d\eta^2}\,\phi(\vec{x},\eta) - \nabla^2\phi(\vec{x},\eta) + M^2\, a^2(\eta)\, \phi(\vec{x},\eta) \;=\; 0\,, \tag{6.2.10}$$

$$\frac{d^2}{d\eta^2}\,\chi(\vec{x},\eta) - \nabla^2\chi(\vec{x},\eta) + m^2\, a^2(\eta)\, \chi(\vec{x},\eta) \;=\; 0\,. \tag{6.2.11}$$

It is convenient to quantize the fields in a comoving volume V, namely,

$$\phi(\vec{x},\eta) = \frac{1}{\sqrt{V}} \sum_{\vec{k}} \left[a_{\vec{k}}\, g_k(\eta)\, e^{i\vec{k}\cdot\vec{x}} + b^\dagger_{\vec{k}}\, g^*_k(\eta)\, e^{-i\vec{k}\cdot\vec{x}} \right]. \tag{6.2.12}$$

$$\chi(\vec{x},\eta) = \frac{1}{\sqrt{V}} \sum_{\vec{k}} \left[c_{\vec{k}}\, f_k(\eta)\, e^{i\vec{k}\cdot\vec{x}} + c^\dagger_{\vec{k}}\, f^*_k(\eta)\, e^{-i\vec{k}\cdot\vec{x}} \right], \tag{6.2.13}$$

where the mode functions $g_k(\eta); f_k(\eta)$ are solutions of the following equations

$$\left[\frac{d^2}{d\eta^2} + \Omega^2_k(\eta)\right] g_k(\eta) \;=\; 0 \;\;;\;\; \Omega^2_k(\eta) = k^2 + M^2\, a^2(\eta) \tag{6.2.14}$$

$$\left[\frac{d^2}{d\eta^2} + \omega^2_k(\eta)\right] f_k(\eta) \;=\; 0 \;\;;\;\; \omega^2_k(\eta) = k^2 + m^2 a^2(\eta)\,, \tag{6.2.15}$$

and satisfy the Wronskian condition

$$g_k^{'}(\eta)g_k^*(\eta) - g_k^{*'}(\eta)g_k(\eta) = -i \tag{6.2.16}$$

$$f_k^{'}(\eta)f_k^*(\eta) - f_k^{*'}(\eta)f_k(\eta) = -i\,, \tag{6.2.17}$$

so that the annihilation and creation operators are *time independent* and obey the canonical commutation relations $[a_{\vec{k}}, a^\dagger_{\vec{k}'}] = \delta_{\vec{k},\vec{k}'}$; $[c_{\vec{k}}, c^\dagger_{\vec{k}'}] = \delta_{\vec{k},\vec{k}'}$ etc., and the vacuum state $|0\rangle$ is defined as

$$a_{\vec{k}}\,|0\rangle = 0\ ;\ b_{\vec{k}}\,|0\rangle = 0\ ;\ c_{\vec{k}}\,|0\rangle = 0\,. \tag{6.2.18}$$

Since the mode equations for $f_k(\eta), g_k(\eta)$ obey similar equations of motion, we focus on $f_k(\eta)$ from which we can obtain $g_k(\eta)$ by the replacement $m \to M$. Let us introduce the dimensionless variables

$$x = \sqrt{2m\,H_R}\;\eta \quad ; \quad \alpha = -\frac{k^2}{2m\,H_R}\,, \tag{6.2.19}$$

in terms of which the equation (6.2.15) is identified with Weber's equation[209, 15, 293, 70, 276]

$$\frac{d^2}{dx^2}\,f(x) + \Big[\frac{x^2}{4} - \alpha\Big]f(x) = 0\,. \tag{6.2.20}$$

The general solutions are linear combinations of Weber's parabolic cylinder functions $W[\alpha;\pm x]$ [209, 15, 293, 70, 276]. We seek solutions that can be identified with particle states obeying the condition

$$f_k(\eta) \to \frac{e^{-i\int_{\eta^*}^{\eta}\,\omega_k(\eta')\,d\eta'}}{\sqrt{2\,\omega_k(\eta)}}\,, \tag{6.2.21}$$

for wavevectors well inside the particle horizon (Hubble radius) which is discussed below in more detail, along with the Wronskian condition (6.2.17). The lower limit η^* corresponds to a conformal time at which the condition of adiabaticity $\omega_k'(\eta)/\omega_k^2(\eta) \ll 1$, described in detail below (see eqns. (6.2.26,6.2.32)) is fulfilled. These were found in ref.[226], and are given by

$$f_k(\eta) = \frac{1}{(8mH_R)^{1/4}}\Big[\frac{1}{\sqrt{\kappa}}\,W[\alpha;x] - i\sqrt{\mathcal{D}}\,W[\alpha;-x]\Big] \quad ; \quad \mathcal{D} = \sqrt{1+e^{-2\pi|\alpha|}} - e^{-\pi|\alpha|}\,. \tag{6.2.22}$$

It is shown in ref.[226] that the asymptotic behavior of $f_k(\eta)$ is indeed given by (6.2.21) for wavelengths much smaller than the particle horizon as well as in the long time limit. The mode functions $g_k(\eta)$ are obtained from these by the replacement $m \to M$.

A perturbative approach to obtaining a cross section begins by defining the interaction picture wherein fields feature the free field time evolution (6.2.12,6.2.13) with the mode functions obeying the free field equations of motion (6.2.14,6.2.15). The transition matrix elements between initial and final states are obtained in a perturbative expansion in terms of time ordered integrals of products of the interaction Hamiltonian in the interaction picture. Even to lowest order in such perturbative expansion, the transition matrix elements would feature time and momentum integrals of products of the mode functions f_k, g_k given by eqn. (6.2.22) and similarly for g_k. Obviously this is very different from the situation in Minkowski space-time where the mode functions are simple plane wave solutions both in space and time, and integrals over the space-time coordinates lead to energy momentum conservation at each vertex. In a spatially flat (FRW) cosmology there are three space-like Killing vectors associated with spatial translational invariance, therefore the spatial part of the mode functions are the usual plane waves, as manifest in the expansions (6.2.12,6.2.13). Hence, the spatial integrals yield spatial momentum conservation, however, the time integrals involve products of parabolic Weber functions, obviously presenting a formidable technical obstacle. Above and beyond these technical difficulties, it is clear that unlike Minkowski space-time, there is no energy conservation, this is consequence of the lack of a time-like Killing vector in an expanding cosmology. Most particle physics processes in the early Universe are deemed to involve energetic particles, which motivates us to invoke an adiabatic approximation for the mode functions based on the well studied Wentzel-Kramers-Brillouin (WKB) approximation to the solution of the equations for the mode functions[89, 189, 288, 297, 90, 117].

Since both mode functions satisfy the same differential equations, albeit with a different mass term, we will carry out the WKB analysis for $f_k(\eta)$. Writing the solution of the mode equations in the WKB form[89, 189, 288, 297, 90, 117, 150, 348]

$$f_k(\eta) = \frac{e^{-i\int_{\eta_i}^{\eta} W_k(\eta')\,d\eta'}}{\sqrt{2\,W_k(\eta)}}\,, \tag{6.2.23}$$

and inserting this ansatz into (6.2.15) it follows that $W_k(\eta)$ must be a solution of the equation[89]

$$W_k^2(\eta) = \omega_k^2(\eta) - \frac{1}{2}\left[\frac{W_k''(\eta)}{W_k(\eta)} - \frac{3}{2}\left(\frac{W_k'(\eta)}{W_k(\eta)}\right)^2\right]. \tag{6.2.24}$$

This equation can be solved in an *adiabatic expansion*

$$W_k^2(\eta) = \omega_k^2(\eta)\left[1 - \frac{1}{2}\frac{\omega_k^{''}(\eta)}{\omega_k^3(\eta)} + \frac{3}{4}\left(\frac{\omega_k^{'}(\eta)}{\omega_k^2(\eta)}\right)^2 + \cdots\right] \;\; ; \;\; \omega_k(\eta) = \sqrt{k^2 + m^2 a^2(\eta)}\,. \quad (6.2.25)$$

We refer to terms that feature n-derivatives of $\omega_k(\eta)$ as of n-th adiabatic order. The nature and reliability of the adiabatic expansion is revealed by considering the term of first adiabatic order for generic mass m:

$$\frac{\omega_k^{'}(\eta)}{\omega_k^2(\eta)} = \frac{m^2\, a(\eta) a^{'}(\eta)}{\left[k^2 + m^2\, a^2(\eta)\right]^{3/2}}\,, \quad (6.2.26)$$

this is most easily recognized in *comoving* time t, introducing the *local* energy $E_k(t)$ and Lorentz factor $\gamma_k(t)$ measured by a comoving observer in terms of the *physical* momentum $k_p(t) = k/a(t)$

$$E_k(t) = \sqrt{k_p^2(t) + m^2} = \frac{\omega_k(\eta)}{a(\eta)} \quad (6.2.27)$$

$$\gamma_k(t) = \frac{E_k(t)}{m}\,, \quad (6.2.28)$$

and the Hubble expansion rate $H(t) = \frac{\dot{a}(t)}{a(t)} = a^{'}/a^2$. In terms of these variables, the first order adiabatic ratio (6.2.26) becomes

$$\frac{\omega_k^{'}(\eta)}{\omega_k^2(\eta)} = \frac{H(t)}{\gamma_k^2(t)\, E_k(t)}\,. \quad (6.2.29)$$

In similar fashion the higher order terms in the adiabatic expansion for a (RD) cosmology (vanishing Ricci scalar) can be obtained,

$$\begin{aligned}\frac{\omega_k^{''}(\eta)}{\omega_k^3(\eta)} &= \frac{1}{\gamma_k^2(t)}\frac{H^2(t)}{E_k^2(t)}\left[1 - \frac{1}{\gamma_k^2(t)}\right] \\ \frac{\omega_k^{'''}(\eta)}{\omega_k^4(\eta)} &= -\frac{3}{\gamma_k^3(t)}\frac{H^3}{E_k^3}\left[1 - \frac{1}{\gamma_k^2(t)}\right]. \end{aligned} \quad (6.2.30)$$

Consequently, (6.2.25) takes the form:

$$W_k^2(t) = a^2(t) E_k^2(t)\left[1 - \frac{1}{2\gamma_k^2(t)}\frac{H^2(t)}{E_k^2(t)}\left[1 - \frac{5}{2\gamma_k^2(t)}\right] + \cdots\right]. \quad (6.2.31)$$

Since the Ricci scalar ($R \propto a''(\eta)/a^3(\eta)$) vanishes in a (RD) cosmology, it follows that for $m = 0$ ($\gamma_k = \infty$) the mode functions are the same as in Minkowski space-time and the

WKB approximation becomes exact, furthermore, for $k = 0$ ($\gamma_k = 1$) only ω_k'/ω_k^2 remains since higher order derivatives of the frequency ($\omega_{k=0}(\eta) = m\, a(\eta)$) vanish.

These two limits and the expansion terms featured above lead us to identify the ratio

$$\frac{H(t)}{\gamma_k(t)\, E_k(t)} \ll 1\,, \tag{6.2.32}$$

as the small, dimensionless *adiabatic* expansion parameter. We will instead adopt a more stringent condition for the adiabatic approximation, namely

$$\frac{H(t)}{E_k(t)} \ll 1 \Rightarrow E_k(t)\, t \gg 1\,, \tag{6.2.33}$$

where we used the relation (6.2.5) in the second inequality.

The physical interpretation of the ratio $H(t)/E_k(t)$ is clear: typical particle physics degrees of freedom feature either physical de Broglie or Compton wavelengths that are much smaller than the (physical) particle horizon $\propto 1/H(t)$ at any given time during (RD). In a standard (RD) cosmology the particle horizon always grows faster than a physical wavelength, therefore the reliability of the adiabatic expansion improves with the cosmological expansion. The condition (6.2.33) is also equivalent to a "long time limit" in the sense that there are many oscillations of the microscopic degrees of freedom during a Hubble time scale $\simeq 1/H(t)$.

As an example, let us consider processes occurring early in the (RD) stage, for example at the Grand Unification (GUT) scale $\simeq 10^{15}\,\mathrm{GeV}$, assuming that particles feature *physical* momenta at this scale $k_{ph}(\eta) = k/a(\eta) \simeq 10^{15}\,\mathrm{GeV}$ with k being the *comoving* momentum and a mass $\simeq 100\,\mathrm{GeV}$, hence a local Lorentz factor $\gamma_k \simeq 10^{13}$. If the environmental temperature of the plasma is $T \simeq T_{\mathrm{GUT}} \simeq 10^{15}\,\mathrm{GeV}$ and taking as an example the standard model result $g_{eff} \simeq 100$, it follows that $H \simeq 10^{12}\,\mathrm{GeV}$ and approximating $T_{\mathrm{GUT}} \simeq T_{\mathrm{CMB}}/a(\eta_i)$ implying that the scale factor at the GUT scale $a(\eta_i) \simeq 10^{-28}$ and a *comoving* wavevector $k \simeq 10^{-13}\,\mathrm{GeV}$. This situation yields a ratio $H/E \simeq 10^{-3}$, which becomes smaller with the cosmological expansion and the adiabatic ratio is even much smaller on account of the Lorentz factor.

Although the value chosen for the scale factor $a \simeq 10^{-28}$ is probably near the end of inflation, the main point is that even for these values the adiabatic ratio H/E is small

enough that the adiabatic approximation is reliable. As the cosmological expansion proceeds this ratio becomes even smaller, making the adiabatic approximation even more reliable. In conclusion, the assumption of the validity of the adiabatic approximation for wavelengths smaller than the Hubble radius is reliable all throughout the (RD). Hence, our analysis, based on this approximation, is valid during this era of cosmological expansion.

Underlying this analysis of energy scales, the adiabatic approximation entails a wide separation of *time scales*: the expansion time scale $1/H$ is much longer than the microscopic time scales of oscillations associated with particle states $\simeq 1/E$ as implied by the inequality(6.2.33). It is this separation of time scales that warrants the adiabatic approximation and will undergird our analysis below.

This analysis clarifies that the adiabatic approximation breaks down for non-relativistic particles $\gamma_k \simeq 1$ with masses $m \leq H$. This situation corresponds to $k_{ph} \ll m \ll H$, hence the breakdown of the adiabaticity condition is associated with wavelengths that are larger than the particle horizon at a given time. However, since in a (RD) cosmology the particle horizon grows $\propto a^2(\eta)$ whereas physical wavelengths grow $\propto a(\eta)$ and the Compton wavelengths remain constant, eventually a superhorizon mode enters the particle horizon and the adiabatic approximation eventually becomes reliable. This analysis delineates the regime of applicability of the adiabatic approximation and its implementation must always be accompanied with an analysis of the relevant scales.

In this chapter we focus our study on obtaining the cross section to leading orders in the coupling and the adiabatic expansion, the latter implies the *zeroth-adiabatic* order for mode functions, namely

$$f_k(\eta) = \frac{e^{-i\int_{\eta_i}^{\eta}\omega_k(\eta')\,d\eta'}}{\sqrt{2\,\omega_k(\eta)}} \quad ; \quad g_k(\eta) = \frac{e^{-i\int_{\eta_i}^{\eta}\Omega_k(\eta')\,d\eta'}}{\sqrt{2\,\Omega_k(\eta)}}\,. \tag{6.2.34}$$

It is shown explicitly in ref.[226] that the exact mode functions given by eqn. (6.2.22) coincide with zeroth adiabatic order $f_k(\eta)$ given by eqn. (6.2.34) to leading order in the adiabatic expansion $\omega'(\eta)/\omega^2(\eta) \ll 1$ considered in this study.

We will show explicitly that higher order adiabatic corrections provide small contributions to the processes considered here which are further suppressed by the coupling. The phase of

the mode function has an immediate interpretation in terms of comoving time and the local comoving energy (6.2.27), namely

$$e^{-i\int_{\eta_i}^{\eta}\omega_k(\eta')\,d\eta'} = e^{-i\int_{t_i}^{t}E_k(t')\,dt'}\,. \tag{6.2.35}$$

where we used the relations $\omega_k = a(\eta)E_k \;\;;\;\; a(\eta)d\eta = dt$. A similar analysis holds for the phases involving $\Omega_k(\eta)$. This is a natural and straightforward generalization of the phase of *positive frequency particle states in Minkowski space-time* which is precisely the rational for the boundary conditions (6.2.21) on the mode functions[226].

Since as shown in ref.[226] to leading order in the adiabatic expansion the mode functions $f_k(\eta), g_k(\eta)$ in (6.2.12,6.2.13) are given by (6.2.34), the expansion of the ϕ, χ fields (6.2.12,6.2.13) to leading adiabatic order become

$$\phi(\vec{x},\eta) = \sum_{\vec{k}} \frac{1}{\sqrt{2\,V\,\Omega_k(\eta)}}\left[a_{\vec{k}}\,e^{-i\int_{\eta_i}^{\eta}\Omega_k(\eta')\,d\eta'}\,e^{i\vec{k}\cdot\vec{x}} + b^{\dagger}_{\vec{k}}\,e^{i\int_{\eta_i}^{\eta}\Omega_k(\eta')\,d\eta'}\,e^{-i\vec{k}\cdot\vec{x}}\right], \tag{6.2.36}$$

$$\chi(\vec{x},\eta) = \sum_{\vec{k}} \frac{1}{\sqrt{2\,V\,\omega_k(\eta)}}\left[c_{\vec{k}}\,e^{-i\int_{\eta_i}^{\eta}\omega_k(\eta')\,d\eta'}\,e^{i\vec{k}\cdot\vec{x}} + c^{\dagger}_{\vec{k}}\,e^{i\int_{\eta_i}^{\eta}\omega_k(\eta')\,d\eta'}\,e^{-i\vec{k}\cdot\vec{x}}\right], \tag{6.2.37}$$

with the vacuum state $|0\rangle$ obeying the condition (6.2.18).

We will refer to the Fock states created out of the vacuum for the fields $\phi^{\dagger}$; ϕ as $\varphi^{\pm}$ particle-antiparticle respectively and χ particles for the χ fields, where the particle interpretation is warranted by the form of the zeroth-order adiabatic solutions (6.2.34). The Minkowski space-time limit is obtained by setting $a(\eta) = 1$ and $\eta \to t$, so that the frequencies become time independent, and absorbing the dependence on the initial time t_i into a (phase) redefinition of the creation and annihilation operators.

In order to establish a clear identification of the zeroth order adiabatic modes with particles we analyze the free-field Hamiltonian, which in terms of the conformally rescaled field operators and focusing on the χ field is given by

$$H_{\chi}(\eta) = \frac{1}{2}\int d^3x\,\{\pi^2 + (\nabla\chi)^2 + m^2a^2(\eta)\chi^2\} \;\;;\;\; \pi \equiv \chi'\,. \tag{6.2.38}$$

Using the canonical commutation relations, and the Wronskian conditions (6.2.17) it is straightforward to find that the Heisenberg equations of motion obtained with this Hamiltonian are precisely eqn. (6.2.14) for the mode functions f_k, hence for the quantum field χ. Using the expansion (6.2.13) for the χ field and integrating in d^3x we find

$$H_\chi(\eta) = \frac{1}{2}\sum_{\vec{k}}\left\{c^\dagger_{\vec{k}}c_{\vec{k}}\left[|f_k'|^2 + \omega_k^2(\eta)\,|f_k|^2\right] + \left(c_{\vec{k}}c_{-\vec{k}}\left[(f_k')^2 + \omega_k^2(\eta)(f_k)^2\right] + h.c.\right)\right\}. \quad (6.2.39)$$

Writing $f_k(\eta)$ in the WKB form (6.2.23) and keeping the zeroth adiabatic order, we find

$$H_\chi(\eta) = \sum_{\vec{k}} c^\dagger_{\vec{k}}c_{\vec{k}}\,\omega_k(\eta)\,. \quad (6.2.40)$$

A similar analysis for the ϕ field to zeroth order in the adiabatic expansion yields

$$H_\phi(\eta) = \sum_{k}\left(a^\dagger_{\vec{k}}a_{\vec{k}} + b^\dagger_{\vec{k}}b_{\vec{k}}\right)\Omega_k(\eta)\,. \quad (6.2.41)$$

It is straightforward to confirm that the terms $c_{\vec{k}}c_{-\vec{k}}$ in (6.2.39) (and similar for the ϕ field) are of second and higher adiabatic order[227].

6.2.2 Amplitudes and rates:

Since we will study transition rates in a finite time interval it is important to address their proper definition. In S-matrix theory a rate is simply defined by taking the transition probability from $t = -\infty$ to $t = +\infty$ and dividing by the total time interval. In this infinite time limit the total transition probability grows linearly in time, therefore dividing by the total time elapsed yields a time independent transition *rate*. However, during a finite time interval the transition probability features a more subtle time dependence and a consistent definition of the transition rate must be carefully reassessed. Reference[227] introduced a formulation of the time evolution of states in cosmology which leads to an identification of transition probabilities and rates. Such a formulation was also implemented in ref.[105] to study the dynamics of decay directly in real time in Minkowski space-time. For consistency of presentation we summarize the main aspects of this formulation here in order to clarify

the definition of transition rates which are the main focus of this study. We refer the reader to these references for more details. In the interaction picture states evolve as

$$|\Psi(\eta)\rangle_I = U_I(\eta,\eta_0)\,|\Psi(\eta_0)\rangle_I\,, \tag{6.2.42}$$

where the time evolution operator in the interaction picture obeys

$$i\frac{d}{d\eta}U_I(\eta,\eta_0) = H_I(\eta)U_I(\eta,\eta_0) \;\;;\;\; U_I(\eta_0,\eta_0) = 1\,. \tag{6.2.43}$$

whose perturbative solution yields

$$U_I(\eta;\eta_i) = 1 - i\int_{\eta_i}^{\eta} H_I(\eta')\,d\eta' + \cdots \tag{6.2.44}$$

where

$$H_I(\eta) = \lambda\int d^3x\phi^\dagger(\vec{x},\eta)\phi(\vec{x},\eta)\chi^2(\vec{x},\eta)\,, \tag{6.2.45}$$

is the interaction Hamiltonian in the interaction picture. Expanding $|\Psi(\eta)\rangle_I$ in the adiabatic Fock states eigenstates of H_χ, H_ϕ generically labeled as $|n\rangle$, as $|\Psi(\eta)\rangle_I = \sum_n C_n(\eta)\,|n\rangle$ the expansion coefficients (amplitudes) obey

$$i\frac{d}{d\eta}C_n(\eta) = \sum_m C_m(\eta)\,\langle n|\,H_I(\eta)\,|m\rangle\;. \tag{6.2.46}$$

In principle this is an infinite hierarchy of integro-differential equations for the coefficients $C_n(\eta)$; progress can be made, however, by considering states connected by the interaction Hamiltonian to a given order in the interaction. Consider that initially the state is $|A\rangle$ so that $C_A(\eta_i) = 1\,; C_\kappa(\eta_i) = 0$ for $|\kappa\rangle \neq |A\rangle$, and consider a first order transition process $|A\rangle \to |\kappa\rangle$ to intermediate multiparticle states $|\kappa\rangle$ with transition matrix elements $\langle\kappa|H_I(\eta)|A\rangle$. Obviously the state $|\kappa\rangle$ will be connected to other multiparticle states $|\kappa'\rangle$ different from $|A\rangle$ via $H_I(\eta)$. Hence for example up to second order in the interaction, the state $|A\rangle \to |\kappa\rangle \to |\kappa'\rangle$. Restricting the hierarchy to *first order transitions* from the initial state $|A\rangle \leftrightarrow |\kappa\rangle$ results in a coupled set of equations

$$i\frac{d}{d\eta}C_A(\eta) \;=\; \sum_\kappa C_\kappa(\eta)\,\langle A|\,H_I(\eta)\,|\kappa\rangle \;\;;\;\; C_A(\eta_i) = 1\,, \tag{6.2.47}$$

$$i\frac{d}{d\eta}C_\kappa(\eta) \;=\; C_A(\eta)\,\langle\kappa|\,H_I(\eta)\,|A\rangle \;\;;\;\; C_\kappa(\eta_i) = 0\,. \tag{6.2.48}$$

The hermiticity of H_I leads to the result

$$\frac{d}{d\eta}\left\{|C_A(\eta)|^2+\sum_\kappa |C_\kappa(\eta)|^2\right\}=0\Rightarrow |C_A(\eta)|^2+\sum_\kappa |C_\kappa(\eta)|^2=1\,, \tag{6.2.49}$$

this is the statement of unitarity and we have used the initial conditions on the amplitude. For the cases under consideration, for example that of pair annihilation $\varphi^+\varphi^-\to\chi\chi$ studied below, the initial state $|A\rangle$ is the two particle state $|A\rangle=\left|1^+_{\vec{k}_1};1^-_{\vec{k}_2}\right\rangle$ namely with a particle-antiparticle pair of momenta $\vec{k}_1;\vec{k}_2$ respectively and the states $|\kappa\rangle$ being a final state of two χ particles, namely $|\kappa\rangle=|1_{\vec{p}_3};1_{\vec{p}_4}\rangle$.

Following ref.[227] we solve the system of equations (6.2.47,6.2.48) to leading order in the interaction consistently with our tree level calculation of the transition amplitude, yielding

$$\frac{d}{d\eta}C_A(\eta)=-\int_{\eta_i}^{\eta}d\eta'\,\Sigma_A(\eta,\eta')\;\;C_A(\eta)\;\;;\;\;C_A(\eta_i)=1\,, \tag{6.2.50}$$

$$C_\kappa(\eta)=-i\int_{\eta_i}^{\eta}\langle\kappa|\,H_I(\eta')\,|A\rangle\;C_A(\eta')\,d\eta'\,, \tag{6.2.51}$$

where the self-energy

$$\Sigma_A(\eta;\eta')=\sum_\kappa\langle A|\,H_I(\eta)\,|\kappa\rangle\,\langle\kappa|\,H_I(\eta')\,|A\rangle\;. \tag{6.2.52}$$

The solution of eqn. (6.2.50) yields the probability of remaining in the initial state $|A\rangle$ as

$$\mathcal{P}_A(\eta)=|C_A(\eta)|^2=e^{-\int_{\eta_i}^{\eta}\Gamma_A(\eta')d\eta'}\;\;;\;\;\Gamma_A(\eta)=2\int_{\eta_i}^{\eta}d\eta_1\,\mathrm{Re}\left[\Sigma_A(\eta,\eta_1)\right], \tag{6.2.53}$$

and the transition rate

$$\frac{1}{\mathcal{P}_A(\eta)}\frac{d}{d\eta}\mathcal{P}_A(\eta)=-\Gamma_A(\eta)\,. \tag{6.2.54}$$

To leading order in the interaction, using the unitarity condition (6.2.49) we find that the total probability of final states is given by

$$\mathcal{P}_{tot}(\eta)=\sum_\kappa|C_\kappa(\eta)|^2=\int_{\eta_i}^{\eta}\Gamma_A(\eta')\,d\eta'=2\int_{\eta_i}^{\eta}d\eta_2\int_{\eta_i}^{\eta_2}d\eta_1\mathrm{Re}\Sigma_A[\eta_2;\eta_1]\,, \tag{6.2.55}$$

hence

$$\frac{d}{d\eta}\mathcal{P}_{tot}(\eta)=\Gamma_A(\eta)\,. \tag{6.2.56}$$

This is a manifestation of the optical theorem in real time which licenses us to *define* the comoving transition *rate* as

$$\Gamma_{i\to f}(\eta) = \frac{d}{d\eta}\mathcal{P}_{tot}(\eta) = \Gamma_A(\eta) = 2\int_{\eta_i}^{\eta} d\eta_1 \mathrm{Re}\Sigma_A[\eta;\eta_1]\,. \tag{6.2.57}$$

In Minkowski space-time in the long time limit $t\to\infty$ the rate Γ_A becomes independent of time and at long time $\mathcal{P}_A = e^{-\Gamma_A t}$ while the total probability to final states $\mathcal{P}_{tot} = \Gamma_A\, t$. Therefore, in this case defining the rate as $\mathcal{P}_{tot}/t$ yields the same result as $d\mathcal{P}_{tot}/dt$. In cosmology where the background is time dependent and momenta are redshifted by the expansion, or during a finite time interval during which the linear growth in time of the final total probability is not yet established, the two different definitions obviously yield different results. This indicates the subtleties associated with definitions of transition rates in a finite time interval.

The total number of "events" is given by $\mathcal{P}_{tot}(\eta)$ namely the (conformal) time integral of the transition rate, which is manifestly positive. Therefore, motivated by the above analysis based on unitarity and the optical theorem we *define* the transition *rate* as in eqn. (6.2.57). Some subtleties associated with this definition, and an analysis of an alternative definition closer to that in Minkowski space- time and its caveats will be discussed in section (6.5).

6.2.3 Pair annihilation: $\varphi^+\varphi^-\to\chi\chi$

For this process

$$|i\rangle = \left|1^+_{\vec{k}_1};1^-_{\vec{k}_2}\right\rangle \quad;\quad |f\rangle = |1_{\vec{p}_3};1_{\vec{p}_4}\rangle\,, \tag{6.2.58}$$

these are eigenstates of the zeroth order adiabatic Hamiltonians (6.2.40,6.2.41), and the transition matrix element $\langle f|H_I(\eta)|i\rangle$ is given by

$$\langle f|H_I(\eta)|i\rangle = \frac{-i\,\lambda}{2\,V}\,\delta_{\vec{k}_1+\vec{k}_2-\vec{p}_3-\vec{p}_4}\;\frac{e^{-i\int_{\eta_i}^{\eta}\left(\Omega_{k_1}(\eta')+\Omega_{k_2}(\eta')-\omega_{p_3}(\eta')-\omega_{p_4}(\eta')\right)d\eta'}}{\Big[\Omega_{k_1}(\eta_1)\Omega_{k_2}(\eta_1)\omega_{p_3}(\eta_1)\omega_{p_4}(\eta_1)\Big]^{1/2}}\,, \tag{6.2.59}$$

therefore, accounting for a symmetry factor 1/2! for indistinguishable final states, the self energy (6.2.52) is given by

$$\Sigma[\eta_2;\eta_1] = \frac{\lambda^2}{8V}\int\frac{d^3p_3}{(2\pi)^3}\,\frac{e^{i\int_{\eta_1}^{\eta_2}\left(\Omega_{k_1}(\eta')+\Omega_{k_2}(\eta')-\omega_{p_3}(\eta')-\omega_{p_4}(\eta')\right)\,d\eta'}}{\Big[\mathcal{W}(\eta_1)\,\mathcal{W}(\eta_2)\Big]^{1/2}}\,, \tag{6.2.60}$$

with

$$\mathcal{W}(\eta_1) = \Omega_{k_1}(\eta_1)\Omega_{k_2}(\eta_1)\omega_{p_3}(\eta_1)\omega_{p_4}(\eta_1)\,, \tag{6.2.61}$$

and $p_4 = |\vec{p}_3 - \vec{k}_1 - \vec{k}_2|$. Therefore the transition rate (6.2.57) is given by

$$\Gamma_{i\to f}(\eta) = 2\int_{\eta_i}^{\eta} d\eta_1 \mathrm{Re}\Sigma[\eta;\eta_1]\,. \tag{6.2.62}$$

It is illuminating to relate the above results to the usual formulation of transition rates from an initial state $|i\rangle$ at the initial time η_i to a final state $|f\rangle$ at time η. The transition amplitude is given by

$$\mathcal{A}_{i\to f}(\eta) = \langle f|\, U_I(\eta,\eta_i)\,|i\rangle \tag{6.2.63}$$

and the transition probability by

$$\mathcal{P}_{i\to f}(\eta) = |\,\langle f|\, U_I(\eta,\eta_i)\,|i\rangle\,|^2\,. \tag{6.2.64}$$

To leading order in the coupling we find

$$\begin{aligned}
\mathcal{A}_{i\to f}(\eta) &= \frac{-i\,\lambda}{2\,V^2}\int d^3x\; e^{i\left(\vec{k}_1+\vec{k}_2-\vec{p}_3-\vec{p}_4\right)\cdot\vec{x}}\int_{\eta_i}^{\eta}\frac{e^{-i\int_{\eta_i}^{\eta_1}\left(\Omega_{k_1}(\eta')+\Omega_{k_2}(\eta')-\omega_{p_3}(\eta')-\omega_{p_4}(\eta')\right)\,d\eta'}}{\Big[\Omega_{k_1}(\eta_1)\Omega_{k_2}(\eta_1)\omega_{p_3}(\eta_1)\omega_{p_4}(\eta_1)\Big]^{1/2}}\,d\eta_1 \\
&= \frac{-i\,\lambda}{2\,V}\,\delta_{\vec{k}_1+\vec{k}_2-\vec{p}_3-\vec{p}_4}\int_{\eta_i}^{\eta}\frac{e^{-i\int_{\eta_i}^{\eta_1}\left(\Omega_{k_1}(\eta')+\Omega_{k_2}(\eta')-\omega_{p_3}(\eta')-\omega_{p_4}(\eta')\right)\,d\eta'}}{\Big[\Omega_{k_1}(\eta_1)\Omega_{k_2}(\eta_1)\omega_{p_3}(\eta_1)\omega_{p_4}(\eta_1)\Big]^{1/2}}\,d\eta_1\,.
\end{aligned} \tag{6.2.65}$$

The total transition probability to the final states is given by

$$\mathcal{P}_{i\to f}(\eta) = \frac{1}{2!}\sum_{\vec{p}_3}\sum_{\vec{p}_4}|\mathcal{A}_{i\to f}(\eta)|^2\,, \tag{6.2.66}$$

which can be written compactly as

$$\mathcal{P}_{i\to f}(\eta) = \int_{\eta_i}^{\eta} d\eta_2\int_{\eta_i}^{\eta} d\eta_1\Sigma[\eta_2;\eta_1]\,, \tag{6.2.67}$$

where $\Sigma[\eta_2;\eta_1]$ is given by (6.2.60). Introducing $\Theta(\eta_2-\eta_1)+\Theta(\eta_1-\eta_2)=1$, in (6.2.67), where Θ is the Heaviside step function, relabelling $\eta_1\leftrightarrow\eta_2$ in the term with $\Theta(\eta_1-\eta_2)$ and using that $\Sigma[\eta_1;\eta_2]=\Sigma^*[\eta_2;\eta_1]$ we find

$$\mathcal{P}_{i\to f}(\eta) = 2\int_{\eta_i}^{\eta} d\eta_2\int_{\eta_i}^{\eta_2} d\eta_1\mathrm{Re}\Sigma[\eta_2;\eta_1]\,, \tag{6.2.68}$$

which coincides with $\mathcal{P}_{tot}$ given by eqn. (6.2.55). Thus defining the comoving transition *rate* as

$$\Gamma_{i\to f}(\eta) = \frac{d}{d\eta}\mathcal{P}_{i\to f}(\eta) \tag{6.2.69}$$

one finds the result (6.2.57) obtained from unitarity and the optical theorem. Consistently with the definition (6.2.57) of the transition rate we define the comoving cross section as the transition rate per unit comoving flux for one incoming particle, namely,

$$\sigma(\eta) = \frac{\Gamma_{i\to f}(\eta)}{\left(\frac{v_{rel}(\eta)}{V}\right)}\,, \tag{6.2.70}$$

with $v_{rel}(\eta)$ being the comoving relative velocity, for collinear pair annihilation it is given by

$$v_{rel}(\eta) = \frac{|\vec{k}_1|}{\Omega_{k_1}(\eta)} + \frac{|\vec{k}_2|}{\Omega_{k_2}(\eta)}\,. \tag{6.2.71}$$

We note that

$$\frac{|\vec{k}|}{\Omega_k(\eta)} = \frac{|\vec{k}_{ph}(\eta)|}{E^{\phi}_k(\eta)}\,. \tag{6.2.72}$$

where

$$\vec{k}_{ph}(\eta) = \frac{\vec{k}}{a(\eta)} \quad ; \quad E^{\phi}_k(\eta) = \sqrt{k^2_{ph}(\eta) + M^2} = \frac{\Omega_k(\eta)}{a(\eta)}\,, \tag{6.2.73}$$

are the physical momenta and energy measured by a locally inertial observer. The time dependence of the relative velocity is a simple consequence of the cosmological redshift.

In section (6.5) we discuss subtleties and caveats emerging from the treatment during a finite time interval as is necessary within the cosmological setting.

6.3 Massless χarticles:

The integral over η_1 yielding $\Gamma_{i\to f}$ cannot be done analytically, even a numerical attempt is a daunting challenge because of the large range of $a(\eta)$ and momenta that must be explored numerically. Instead, our strategy is to leverage the adiabatic approximation and the wide separation of time scales that it entails. We first study the case of *massless* χ- particles in the final state, the lessons of which will prove useful in the more general case of massive particles. For massless χ particles we find

$$2\,\Sigma[\eta;\eta_1] = \frac{\lambda^2}{4V}\,\frac{e^{i\int_{\eta_1}^{\eta}\left(\Omega_{k_1}(\eta')+\Omega_{k_2}(\eta')\right)d\eta'}}{\Big[\Omega_{k_1}(\eta)\Omega_{k_2}(\eta)\Omega_{k_1}(\eta_1)\Omega_{k_2}(\eta_1)\Big]^{1/2}}\;\; I[\eta;\eta_1]\,, \tag{6.3.1}$$

where we introduced the time kernel

$$I[\eta;\eta_1] = \int \frac{d^3p}{(2\pi)^3}\,\frac{e^{-i\left(p+\left|\vec{K}-\vec{p}\right|\right)\,(\eta-\eta_1)}}{p\left|\vec{K}-\vec{p}\right|}\;\;;\;\;\vec{K}=\vec{k}_1+\vec{k}_2\,. \tag{6.3.2}$$

The momentum integral can be done by introducing a convergence factor $\eta-\eta_1\to\eta-\eta_1-i\epsilon$ with $\epsilon\to 0^+$, yielding

$$I[\eta;\eta_1] = -\frac{i}{4\pi^2}\,\frac{e^{-i|\vec{K}|(\eta-\eta_1-i\epsilon)}}{\eta-\eta_1-i\epsilon} = \frac{e^{-i|\vec{K}|(\eta-\eta_1-i\epsilon)}}{4\pi^2}\left\{-i\mathcal{P}\Big(\frac{1}{\eta-\eta_1}\Big)+\pi\,\delta(\eta-\eta_1)\right\}, \tag{6.3.3}$$

where $\mathcal{P}$ stands for the principal part. The "short distance" singularity as $\eta\to\eta_1$ is the same as in Minkowski space-time and stems from the large momentum behavior of the integral in p, namely linear in p. This linear divergence is manifest as the $\simeq 1/(\eta-\eta_1)$ as $\eta\to\eta_1$. Such "short-distance" singularity remains even when the particles in the final state are massive

Introducing this result into equations (6.2.62,6.2.70) and gathering terms we obtain

$$\sigma(\eta) = \frac{\lambda^2}{16\,\pi\Omega_{k_1}(\eta)\Omega_{k_2}(\eta)v_{rel}(\eta)}\,\frac{1}{2}\left[1+\frac{2}{\pi}\int_{\eta_i}^{\eta}\mathcal{R}_{12}[\eta;\eta_1]\,\frac{\sin[J(\eta;\eta_1)]}{\eta-\eta_1}\,d\eta_1\right], \tag{6.3.4}$$

where

$$\mathcal{R}_{12}[\eta;\eta_1] = \left[\frac{\Omega_{k_1}(\eta)\Omega_{k_2}(\eta)}{\Omega_{k_1}(\eta_1)\Omega_{k_2}(\eta_1)}\right]^{1/2}, \tag{6.3.5}$$

and

$$J(\eta;\eta_1) = \int_{\eta_1}^{\eta}\Big(\Omega_{k_1}(\eta')+\Omega_{k_2}(\eta')-\left|\vec{K}\right|\Big)\,d\eta'\,. \tag{6.3.6}$$

The flux factor can be written in an illuminating manner, namely

$$\Omega_{k_1}(\eta)\Omega_{k_2}(\eta)v_{rel}(\eta) = a^2(\eta)\left[\left(\mathcal{P}_1(\eta)\cdot\mathcal{P}_2(\eta)\right)^2 - M^4\right]^{1/2}, \tag{6.3.7}$$

and

$$\mathcal{P}_1(\eta)\cdot\mathcal{P}_2(\eta) = \eta_{ab}\,\mathcal{P}_1^a(\eta)\mathcal{P}_2^b(\eta) \tag{6.3.8}$$

in terms of the Minkowski metric $\eta_{ab} = \text{diag}(1,-1,-1,-1)$ and the four vectors in the local inertial frame

$$\mathcal{P}^a(\eta) = \left(E_k^\phi(\eta), \vec{k}_{ph}(\eta)\right), \tag{6.3.9}$$

where $\vec{k}_{ph}(\eta), E_k(\eta)$ are given by eqn. (6.2.73) for the respective particles. Therefore, up to the prefactor $a^2(\eta)$ the flux factor is the same as in Minkowski space-time but in terms of the local energies and momenta featuring the cosmological redshift, yielding

$$\sigma(\eta) = \frac{\lambda^2}{16\,\pi\,a^2(\eta)\left[\left(\mathcal{P}_1(\eta)\cdot\mathcal{P}_2(\eta)\right)^2 - M^4\right]^{1/2}}\,\frac{1}{2}\left[1 + \frac{2}{\pi}\int_{\eta_i}^{\eta}\mathcal{R}_{12}[\eta;\eta_1]\,\frac{\sin[J(\eta;\eta_1)]}{\eta-\eta_1}\,d\eta_1\right]. \tag{6.3.10}$$

The remaining time integral in (6.3.10) cannot be done in closed form, nor is it useful to attempt a numerical study because of the large range of scales involved both in time and momenta. Instead, we implement the adiabatic approximation to extract its behavior and to be able to generalize to other processes. Using that during (RD) $a(\eta) = H_R\,\eta$, we write:

$$\Omega_k^2(\eta_1) = k^2 + M^2a^2(\eta_1) = k^2 + M^2a^2(\eta) + M^2a^2(\eta)\left[\left(\frac{\eta-\eta_1}{\eta}\right)^2 - 2\left(\frac{\eta-\eta_1}{\eta}\right)\right], \tag{6.3.11}$$

we now introduce

$$\Omega_T(\eta) = \Omega_{k_1}(\eta) + \Omega_{k_2}(\eta), \tag{6.3.12}$$

as the total comoving energy scale of the process, and define:

$$\tau = \Omega_T(\eta)(\eta-\eta_1) \;\;;\;\; z(\eta) = \Omega_T(\eta)\,\eta, \tag{6.3.13}$$

In terms of these variables we obtain the relation

$$\Omega_k(\eta_1) = \Omega_k(\eta)\,f_k(\tau) \;\;;\;\; f_k(\tau) = \left[1 - \frac{2\,\tau}{\gamma_k^2(\eta)\,z(\eta)}\left[1 - \frac{\tau}{2\,z(\eta)}\right]\right]^{1/2}, \tag{6.3.14}$$

where

$$\gamma_k(\eta) = \frac{\Omega_k(\eta)}{M\, a(\eta)} = \frac{E_k(\eta)}{M}\,, \tag{6.3.15}$$

is the local Lorentz factor. We note that

$$z(\eta) = \frac{E_{tot}(\eta)}{H(\eta)}\,, \tag{6.3.16}$$

therefore, the adiabaticity condition (6.2.33) implies that

$$z(\eta) \gg 1\,. \tag{6.3.17}$$

The integral defining $J(\eta, \eta_1)$, eqn. (6.3.6), can be done explicitly by implementing the following steps: introducing

$$\Omega_T(\eta)\,\left(\eta - \eta'\right) \equiv x\,, \tag{6.3.18}$$

it follows that

$$\Omega_k(\eta') = \Omega_k(\eta)\, f_k(x) \tag{6.3.19}$$

where $f_k(x)$ is given by eqn. (6.3.14) with τ replaced by x. The integral (6.3.6) is now carried out in terms of the variable x with the result

$$J(\eta, \eta_1) = J_0(\tau; \eta) + J_1(\tau; \eta)\,, \tag{6.3.20}$$

where

$$J_0(\tau;\eta) = \tau\left[1 - \frac{|\vec{K}|}{\Omega_T(\eta)}\right] \quad ; \quad J_1(\tau;\eta) = \frac{\Omega_{k_1}(\eta)}{\Omega_T(\eta)}\,\Delta_{k_1}(\tau) + \frac{\Omega_{k_2}(\eta)}{\Omega_T(\eta)}\,\Delta_{k_2}(\tau)\,, \tag{6.3.21}$$

where for each frequency $(1, 2)$

$$\Delta(\tau) = \frac{\gamma z}{2}\left\{\left(\frac{1}{\gamma} - 2\,\frac{\tau}{\gamma\, z}\right) - \left(\frac{1}{\gamma} - \frac{\tau}{\gamma\, z}\right) f_k(\tau) - \frac{\gamma^2 - 1}{\gamma^2}\,\ln\left[\frac{\left(\frac{1}{\gamma} - \frac{\tau}{\gamma\, z}\right) + f_k(\tau)}{\frac{1}{\gamma} + 1}\right]\right\} \simeq -\frac{\tau^2}{2\,\gamma^2\, z} + \cdots \tag{6.3.22}$$

with $f_k(\tau)$ given by eqn. (6.3.14) and we have suppressed the arguments $k; \eta$ in $\gamma; z$. For $\tau/\gamma z \ll 1$ it follows that

$$\Delta(\tau) \simeq -\frac{\tau^2}{2\,\gamma^2\, z} + \cdots \tag{6.3.23}$$

The important aspect is that $J_0(\tau;\eta)$ is zeroth order adiabatic, whereas $J_1(\tau;\eta)$ is of first and higher adiabatic order, because $1/z = H(\eta)/E_{tot}(\eta) \ll 1$. The integral term in eqn. (6.3.10) can now be written as

$$\frac{2}{\pi}\int_{\eta_i}^{\eta} \mathcal{R}_{12}[\eta;\eta_1]\,\frac{\sin[J(\eta;\eta_1)]}{\eta-\eta_1}\,d\eta_1 = \mathcal{S}_0(\eta)+\mathcal{S}_1(\eta) \tag{6.3.24}$$

where

$$\mathcal{S}_0(\eta) = \frac{2}{\pi}\int_0^{\overline{z}(\eta)} \left[\frac{1}{f_{k_1}(\tau)\,f_{k_2}(\tau)}\right]^{1/2} \frac{\sin[J_0(\tau;\eta)]\cos[J_1(\tau;\eta)]}{\tau}\,d\tau\,, \tag{6.3.25}$$

$$\mathcal{S}_1(\eta) = \frac{2}{\pi}\int_0^{\overline{z}(\eta)} \left[\frac{1}{f_{k_1}(\tau)\,f_{k_2}(\tau)}\right]^{1/2} \frac{\sin[J_1(\tau;\eta)]\cos[J_0(\tau;\eta)]}{\tau}\,d\tau\,, \tag{6.3.26}$$

and we introduced

$$\overline{z}(\eta) = z(\eta)\left(1-\frac{\eta_i}{\eta}\right) \;\;;\;\; \frac{\eta_i}{\eta} \ll 1\,. \tag{6.3.27}$$

Since in the integrals $0 \le \tau \le z$, for local Lorentz factors $\gamma \gg 1$ it is clear from eqn. (6.3.23) that $J_1 \ll 1$ in the whole integration domain, therefore the contribution from $\mathcal{S}_0$ dominates and $\mathcal{S}_1$ can be safely neglected, furthermore in eqn. (6.3.25) we can replace the term $\cos[J_1] \simeq 1$. The case of non-relativistic particles with $\gamma \simeq 1$ but consistently with the adiabatic expansion $z \gg 1$ requires further analysis since near the upper limit $\tau \simeq z$ and, in principle, the higher order adiabatic corrections may yield contributions comparable to the zeroth order adiabatic.

The contributions (6.3.25,6.3.26) feature drastically different behavior: the integrand of $\mathcal{S}_0$ peaks at $\tau \simeq 0$ with an amplitude that is of $\mathcal{O}(1)$ and falls off very fast, whereas $\mathcal{S}_1$ vanishes $\propto \tau/\gamma\, z$ at small τ, is always of higher adiabatic order as it features powers of $1/z$, and oscillates rapidly, averaging out on long time scales. Furthermore, since the integrand of $\mathcal{S}_0$ is localized within the region $0 \le \tau \le \pi$, it follows that in this region of integration $\cos[J_1(\tau;\eta)] \simeq 1$ and $f_k(\tau) \simeq 1$ for $z \gg 1$. For $\tau \simeq z$ the integrands are of $\mathcal{O}(1/z) \ll 1$, therefore the integrand of $\mathcal{S}_0$ can be replaced by $\sin[J_0(\tau;\eta)]$ and the contribution from $\mathcal{S}_1$ can be safely neglected for $z \gg 1$. This analysis is verified numerically, figures (27) and (28) show the integrands of $\mathcal{S}_0$ and $\mathcal{S}_1$ respectively for $\vec{k}_1 = -\vec{k}_2$ (center of mass) and $z = 100, \gamma = 2$ with similar features for the full range of parameters with $z \gg 1$.

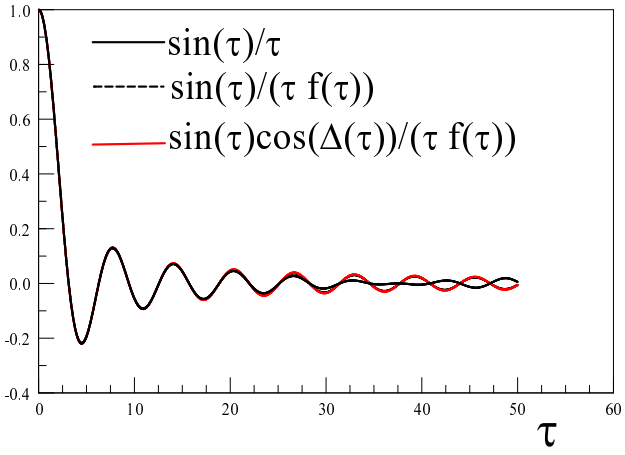

Figure 27: Integrand of $\mathcal{S}_0$ for $z = 100$, $\gamma = 2$. The difference between the expressions is visible only at large τ. Figure taken from [306].

The total integrals for $\mathcal{S}_0(\eta)$ and $\mathcal{S}_1(\eta)$ vs. $z(\eta) = \Omega_T(\eta)\eta$ are shown in figures (29) and (30) for pair annihilation in the center of mass for $\gamma = 2$.

Asymptotically for $z(\eta) = \Omega_T(\eta)\eta \gg 1$ the contributions $\mathcal{S}_0(\eta) \to 1$ and $\mathcal{S}_1(\eta) \to 0$. Since for large $z(\eta) = \Omega_T(\eta)\eta$ the terms $f_k(\eta) \to 1$; $\cos(\Delta(\eta)) \to 1$ and the integrand of $\mathcal{S}_0(\eta)$ is dominated by the region $\tau \simeq 0$, for $\Omega_T(\eta)\eta \gg 1$ the contribution $\mathcal{S}_0(\eta)$ can be well approximated by setting $f_k = 1$; $\cos(\Delta) = 1$, in which case, for pair annihilation in the center of mass, we can replace

$$\mathcal{S}_0(\eta) = \frac{2}{\pi} Si[\Omega_T(\eta)\eta] \tag{6.3.28}$$

where $Si[x]$ is the sine-integral function. Figure (31) displays $\mathcal{S}_0(\eta) - \frac{2}{\pi} Si[\Omega_T(\eta)\eta]$ vs $\Omega_T(\eta)\eta$ for $\gamma = 2$ and annihilation in the center of mass showing that this difference becomes negligibly small for $\Omega_T(\eta)\eta \gg 1$.

A main conclusion of this analysis, confirmed by the numerical study, is that the con-

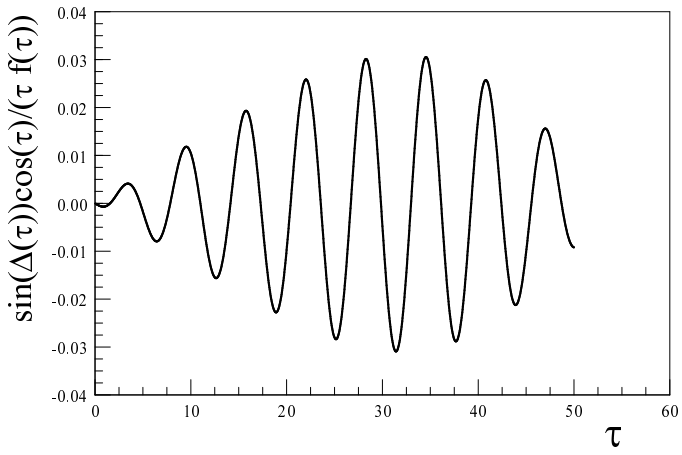

Figure 28: Integrand of $\mathcal{S}_1(\tau)$ vs τ for $z = 100; \gamma = 2$. Figure taken from [306].

tribution from the two-body phase space integral yields a *time kernel* proportional to $1/\tau$. It is the rapid fall off of this kernel that ensures that the contributions of the adiabatic corrections $\propto \tau/z$ are *suppressed* by $\mathcal{O}(1/z)$ as compared to the zeroth order terms. At the time scale $\tau \simeq z$ when the terms of higher adiabatic order begin to be of the same order as the leading terms, the time kernel has been suppressed by $\simeq 1/z$ thereby suppressing their contributions. This is an important corollary of the simpler, massless case, it is the rapid fall-off of the time kernel that ensures the reliability of the adiabatic expansion in the time integrals, a result that is not obvious *a priori*.

As we will see below, this result holds generally for any mass of the outgoing particles with a time kernel that falls off *faster* than $1/\tau$ for massive particles in the out state, thereby improving the reliability of the adiabatic expansion in the time integrals for the cross section.

This analysis also shows that in the limit $z(\eta) = \Omega_T(\eta)\,\eta \gg 1$ the contribution from $\mathcal{S}_1(\eta)$ can be safely neglected. Similar results and conclusions are obtained for $\vec{k}_1 + \vec{k}_2 \neq 0$

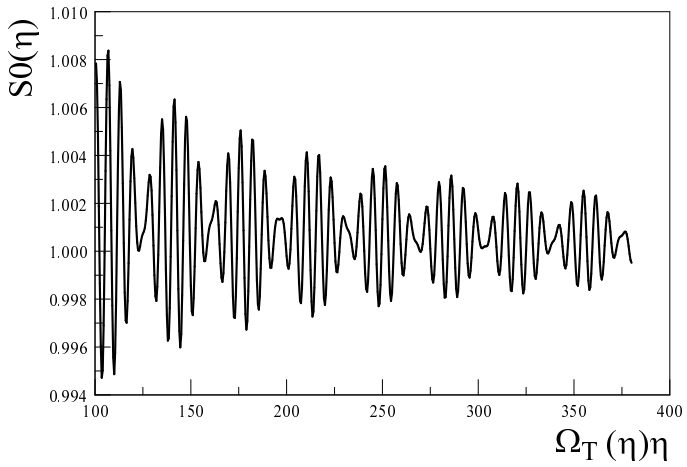

Figure 29: $\mathcal{S}_0(\eta)$ vs $\Omega_T(\eta)\eta$ for $\gamma = 2$ and annihilation in the center of mass. For $\Omega_T(\eta)\eta \gg 1$ asymptotes to 1. Figure taken from [306].

in which case, taking $\eta_i \to 0$

$$\mathcal{S}_0(\eta) = \frac{2}{\pi}\, Si[(\Omega_T(\eta) - K)\eta] \quad ; \quad K = |\vec{k}_1 + \vec{k}_2|\,. \tag{6.3.29}$$

Gathering all these results, we find the final form of the pair annihilation cross section valid for $\Omega_T(\eta)\eta = E_T(t)/H(t) \gg 1$, where $\Omega_T(\eta)$ is defined in eqn. (6.3.12) and $E_T(t) = \Omega_T(\eta)/a(\eta)$,

$$\sigma(\eta) = \frac{\lambda^2}{16\,\pi\, a^2(\eta)\left[\big(\mathcal{P}_1(\eta)\cdot\mathcal{P}_2(\eta)\big)^2 - M^4\right]^{1/2}}\,\frac{1}{2}\Big[1 + \frac{2}{\pi} Si\big[\big(\Omega_T(\eta) - K\big)\eta\big]\Big]\,. \tag{6.3.30}$$

Up to the scale factor dependence in the denominator, this result is remarkably similar to the cross section during a finite time interval in Minkowski space-time.

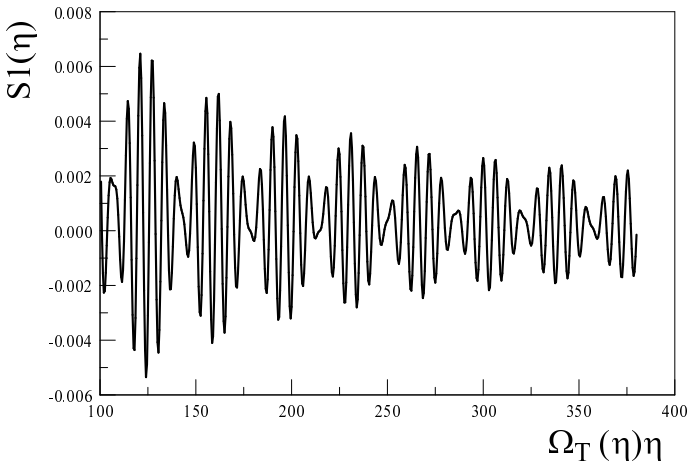

Figure 30: $\mathcal{S}_1(\eta)$ vs $\Omega_T(\eta)\eta$ for $\gamma = 2$ and annihilation in the center of mass. For $\Omega_T(\eta)\eta \gg 1$ asymptotes to 0. Compare the vertical scale to that in Figure (29). Figure taken from [306].

The $1/a^2(\eta)$ dependence of the cross section has a simple interpretation: we have obtained a *comoving* cross section, by obtaining the comoving transition rate and dividing by the comoving flux. Since the cross section has dimensions of area, upon cosmological expansion all physical lengths scale with $a(\eta)$ therefore, a *physical* cross section should be identified with

$$\sigma_{ph}(\eta) = a^2(\eta)\sigma(\eta)\,, \tag{6.3.31}$$

which in terms of the physical (local) four momenta and comoving time agrees with the cross section in Minkowski space-time during a finite time interval

The bracket in (6.3.30) has an important interpretation that paves the way towards understanding the general case of massive particles in the final state. This interpretation begins with writing the time kernel $I[\eta;\eta_1]$ in eqn. (6.3.2) in terms of a spectral representation,

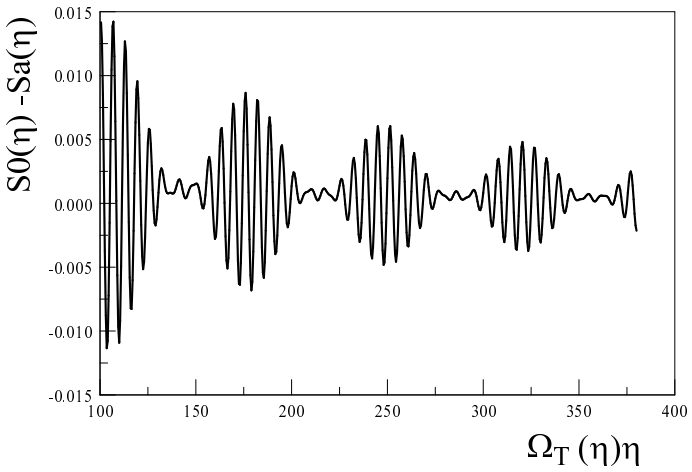

Figure 31: $\mathcal{S}_0(\eta) - S_a(\eta)$ with $S_a(\eta) = \frac{2}{\pi} Si[\Omega_T(\eta)\eta]$ vs $\Omega_T(\eta)\eta$ for $\gamma = 2$ and annihilation in the center of mass. Figure taken from [306].

namely

$$I[\eta;\eta_1] = \int_{-\infty}^{\infty} \rho(K_0, K)\, e^{-iK_0(\eta-\eta_1)}\, dK_0\,, \tag{6.3.32}$$

with

$$\rho(K_0, K) = \int \frac{d^3p}{(2\pi)^3} \frac{\delta\big(K_0 - p - \big|\vec{K} - \vec{p}\big|\big)}{p\,\big|\vec{K} - \vec{p}\big|} = \frac{1}{4\pi^2}\,\Theta(K_0^2 - K^2)\,\Theta(K_0)\,. \tag{6.3.33}$$

The spectral density $\rho(K_0, K)$ is identified as the Lorentz invariant phase space for two massless particles in Minkowski space-time.

The result (6.3.3) and analysis above showed that the time kernel is dominated by the region $0 \leq \tau \simeq \pi$ and its rapid fall-off $\propto 1/\tau$ suppresses the integration region for $\tau \simeq z(\eta) \gg 1$. Therefore the integral $J(\tau;\eta)$ (eqn. (6.3.6)) can be safely replaced by the zeroth-adiabatic order result $J_0(\tau;\eta)$ in eqn. (6.3.21), effectively replacing

$$e^{i\int_{\eta_1}^{\eta}\left(\Omega_{k_1}(\eta')+\Omega_{k_2}(\eta')\right)d\eta'} \;\to\; e^{i\left[\Omega_{k_1}(\eta)+\Omega_{k_2}(\eta)\right](\eta-\eta_1)}\,, \tag{6.3.34}$$

hence neglecting the higher adiabatic order contribution $J_1(\tau;\eta)$, and the factor $\mathcal{R}_{12}[\eta;\eta_1]$ in eqn. (6.3.4) can be set to $\mathcal{R}_{12}[\eta;\eta_1]=1$ to leading adiabatic order. Therefore, to leading (zeroth) adiabatic order, and now taking $\eta_i\to 0$, we find the comoving transition rate $\Gamma_{i\to f}$ given by eqn. (6.2.62) as

$$\Gamma_{i\to f}(\eta)=\frac{\lambda^2}{4V}\,\frac{1}{\Omega_{k_1}(\eta)\Omega_{k_2}(\eta)}\int_{-\infty}^{\infty}\rho(K_0,K)\,\frac{\sin\Big[\Big(K_0-\Omega_T(\eta)\Big)\eta\Big]}{\Big(K_0-\Omega_T(\eta)\Big)}\,dK_0\,. \tag{6.3.35}$$

Although the transition rate features oscillations, under the same approximations keeping the leading (zeroth) adiabatic order, we find the integral over a short time interval during which the time dependent frequencies do not change much

$$\int_0^{\eta}\Gamma_{i\to f}(\eta')\,d\eta'=\frac{\lambda^2}{2V}\,\frac{1}{\Omega_{k_1}(\eta)\Omega_{k_2}(\eta)}\int_{-\infty}^{\infty}\rho(K_0,K)\left[\frac{\sin\Big[\Big(K_0-\Omega_T(\eta)\Big)\eta/2)\Big]}{\Big(K_0-\Omega_T(\eta)\Big)}\right]^2 dK_0\,. \tag{6.3.36}$$

This result is manifestly positive as anticipated by the relation (6.2.55), and is reminiscent of Fermi's Golden rule: formally, the limit $\eta\to\infty$ inside the bracket in the integral in (6.3.36) yields $\pi\,\eta\,\delta(K_0-\Omega_T(\eta))$, leading to the usual result as in Minkowski space-time.However, taking the infinite time limit is clearly inconsistent with the time dependence of the (conformal) energies and the redshift of physical momenta.

Using the result (6.3.33) for the spectral density, changing variables to $(K_0-\Omega_T(\eta))(\eta-\eta_i)\equiv X$ and taking $\eta_i\to 0$, the integral in (6.3.35) becomes

$$\begin{aligned}\int_{-\infty}^{\infty}\rho(K_0,K)\,\frac{\sin\Big[\Big(K_0-\Omega_T(\eta)\Big)\,\eta\Big]}{\Big(K_0-\Omega_T(\eta)\Big)}\,dK_0 &= \frac{1}{4\pi^2}\int_{-(\Omega_T(\eta)-K)\eta}^{\infty}\frac{\sin\big[X\big]}{X}\,dX\\ &= \frac{1}{8\pi}\left[1+\frac{2}{\pi}\,Si\Big[\Big(\Omega_T(\eta)-K\Big)\eta\Big]\right]\end{aligned} \tag{6.3.37}$$

yielding exactly the cross section (6.3.30). This analysis will prove useful to study the general case with massive particles in the initial and final states in the next section.

In the limit $\big(\Omega_T(\eta)-K\big)\eta\to\infty$ the cross section (6.3.30) becomes

$$\sigma(\eta)=\frac{\lambda^2}{16\,\pi\,a^2(\eta)\left[\big(\mathcal{P}_1(\eta)\cdot\mathcal{P}_2(\eta)\big)^2-M^4\right]^{1/2}}\,, \tag{6.3.38}$$

which is *invariant under local Lorentz transformations* at a fixed conformal time, namely

$$\mathcal{P}^a(\eta) \to \Lambda^a_b \mathcal{P}^b(\eta) \tag{6.3.39}$$

where Λ^a_b are the Lorentz transformation matrices at a fixed (conformal) time η. However, for finite η, the Si function and consequently the cross section (6.3.30) is not invariant under the local Lorentz transformation. A similar behavior is found for the cross section during finite time in Minkowski space-time during a finite time interval the cross section is *not* Lorentz invariant (as expected) but Lorentz invariance is restored in the infinite time limit. Since η is the particle horizon (for $\eta_i \to 0$), it follows that the finiteness of the particle horizon entails a violation of local Lorentz invariance. This important aspect is general as discussed in the next section.

Ultrarelativistic limit: In the ultrarelativistic limit $\Omega_{k_{1,2}} \simeq k_{1,2}$

$$\sigma(\eta) = \frac{\lambda^2}{32\,\pi\,k_1\,k_2}\,\frac{1}{2}\left[1 + \frac{2}{\pi} Si\big[\big(k_1 + k_2 - K\big)\eta\big]\right], \tag{6.3.40}$$

which is the same as for Minkowski space-time with the replacement $\eta \to t$. This behavior is expected since in the ultrarelativistic limit in conformal time in a (RD) cosmology the mode functions are exactly the same as in Minkowski space-time since the frequencies do not depend on time. This is a manifestation of the equivalence principle.

Non-relativistic limit: in this limit $\Omega_k \simeq M\,a(\eta)$ and we find

$$\sigma(\eta) = \frac{\lambda^2}{16\,\pi\,M\,a(\eta)(k_1 + k_2)}\,\frac{1}{2}\left[1 + \frac{2}{\pi} Si\big[\big(2\,M\,a(\eta) - K\big)\eta\big]\right]. \tag{6.3.41}$$

Taking the asymptotic limit so that $Si\big[\big(2\,M\,a(\eta) - K\big)\eta\big] \to \pi/2$ it follows that the physical cross section $a^2(\eta)\,\sigma(\eta)$ features the same form as in Minkowski space-time but in terms of the physical, redshifted momenta.

6.4 General case: massive particles.

For the general case with massive particles in the final state, the time kernel introduced in eqns. (6.3.1,6.3.2) now becomes

$$I[\eta;\eta_1] = \int \frac{d^3p}{(2\pi)^3} \frac{e^{-i\int_{\eta_1}^{\eta}\left(\omega_p^{(3)}(\eta')+\omega_q^{(4)}(\eta')\right)d\eta'}}{\left[\omega_p^{(3)}(\eta)\,\omega_q^{(4)}(\eta)\right]^{1/2}\left[\omega_p^{(3)}(\eta_1)\,\omega_q^{(4)}(\eta_1)\right]^{1/2}} \;\; ; \;\; \vec{q} = \vec{p} - \vec{K}\,, \tag{6.4.1}$$

with

$$\omega_k^{(i)}(\eta) = \sqrt{k^2 + m_i^2\,a^2(\eta)} \;\; ; \;\; i = 3,4 \tag{6.4.2}$$

allowing the final state to be that of two particles of different masses as a general case.

Unlike the case of massless particles in the final state, we cannot perform the momentum integral in eqn. (6.4.1), neither the time integral in eqn. (6.2.62) in closed form.

The study of the massless case in the previous section showed that the time kernel is localized at $\tau = \Omega_T(\eta - \eta_1) \lesssim 1$ and its rapid fall off $\propto 1/\tau$ for large τ suppresses the higher order adiabatic corrections $\propto \tau/z$. The behavior $1/\tau$ as $\tau \to 0$ is a consequence of the large momentum dominance of the integral in the time kernel. This is manifest in the spectral representation, eqn. (6.3.32) where the spectral density $\rho(K_0, K) \to$ constant as $K_0 \to \infty$. The short time behavior is the same for massive or massless final states. Following the same steps leading up to eqn. (6.3.14) for the frequencies of the incoming states, and in terms of $x = \Omega_T(\eta)(\eta - \eta')$ (see eqn. (6.3.18)) and $z = \Omega_T(\eta)\eta$ we find

$$\omega_k^{(i)}(\eta') = \omega_k^{(i)}(\eta)\, f_k^{(i)}(x) \;\; ; \;\; i = 3,4 \tag{6.4.3}$$

where

$$f_k^{(i)}(x) = \left[1 - g_k^{(i)}\left[\frac{x}{z}\right]\right]^{1/2} \;\; ; \;\; g_k^{(i)}[w] = \frac{2\,w}{(\gamma_k^{(i)}(\eta))^2}\left(1 - \frac{w}{2}\right) \;\; ; \;\; 0 \le w < 1\,, \tag{6.4.4}$$

and $\gamma_k^{(i)}(\eta) = \omega_k^{(i)}(\eta)/m^{(i)}\,a(\eta)$ for each species. The function $g_k^{(i)}[x/z]$ encodes the corrections to the leading adiabatic order as is explicit in the $1/z$ factor. It attains its maximum for $\gamma_k^{(i)} = 1$, which yields the largest deviation from the adiabatic zeroth order, and in this case,

$$f_k^{(i)}(x) = 1 - x\,, \tag{6.4.5}$$

yielding an *upper bound* on the corrections to the leading adiabatic order. We now replace this upper bound into (6.4.1) obtaining

$$I^{(ub)}[\eta,\eta_1] = \frac{1}{(1-\frac{\tau}{z})}\int \frac{d^3p}{(2\pi)^3}\frac{e^{-i(\omega_p^{(3)}(\eta)+\omega_q^{(4)}(\eta))T}}{\omega_p^{(3)}(\eta)\;\omega_q^{(4)}(\eta)} \quad ; \quad \vec{q}=\vec{p}-\vec{K}\,, \tag{6.4.6}$$

where we defined

$$T = (\eta-\eta_1)\Big[1-\frac{\tau}{2z}\Big]\,. \tag{6.4.7}$$

The superscript (ub) in (6.4.6) refers to the fact that this time kernel gives an upper bound to the corrections beyond the leading adiabatic order. Under this upper-bound approximation we can now cast the momentum integral as a spectral representation just as in the case of Minkowski space-time, namely

$$\int \frac{d^3p}{(2\pi)^3}\frac{e^{-i(\omega_p^{(3)}(\eta)+\omega_q^{(4)}(\eta))T}}{\omega_p^{(3)}(\eta)\;\omega_q^{(4)}(\eta)} = \int_{-\infty}^{\infty}\rho(K_0,K)e^{-iK_0\,T}\,dK_0\,, \tag{6.4.8}$$

with

$$\rho(K_0,K) = \int \frac{d^3p}{(2\pi)^3}\frac{\delta\Big(K_0-\omega_p^{(3)}(\eta)-\omega_p^{(4)}(\eta)\Big)}{\omega_p^{(3)}(\eta)\;\omega_q^{(4)}(\eta)}\,, \tag{6.4.9}$$

being exactly the spectral density in Minkowski space-time but depending parametrically on η and given by,

$$\rho(K_0,K) = \frac{1}{4\pi^2}\left[1-\frac{(m_3-m_4)^2\,a^2(\eta)}{K_0^2-K^2}\right]^{1/2}\left[1-\frac{(m_3+m_4)^2\,a^2(\eta)}{K_0^2-K^2}\right]^{1/2}\Theta\big(K_0-K_T(\eta)\big)\,, \tag{6.4.10}$$

where the threshold $K_T(\eta)$ is

$$K_T(\eta) = \sqrt{K^2+(m_3+m_4)^2\,a^2(\eta)} \quad ; \quad \vec{K}=\vec{k_1}+\vec{k_2}\,. \tag{6.4.11}$$

We can now use the results to extract the short and long time behavior of the upper bound time kernel given by eqn. (6.4.6).

i:) Short time regime. This region corresponds to $K_T\,T \ll 1$, in this case $\eta_1 \simeq \eta$, therefore $\tau/z \ll 1$. The short time behavior is the same for massless or massive particles in the final state and yields

$$I^{(ub)} \simeq -\frac{i}{4\pi^2}\,\frac{e^{-i\,K_T\,(\eta-\eta_1)}}{(\eta-\eta_1)-i\epsilon} + \text{finite}\,. \tag{6.4.12}$$

where *finite* stands for a finite constant as $\eta \to \eta_1$, the short time behavior (6.4.12) is similar to the result (6.3.3). In this short time region, the corrections $\propto \tau/z$ to the leading adiabatic order can be neglected, as analyzed in detail in the previous section for massless particles in the final state.

ii:) Long time regime: $K_T\, T \gg 1$**.** We find that if the spectral density vanishes at threshold as $\rho(K_0, K) \propto (K_0 - K_T)^\alpha$ as $K_0 \to K_T$, the long time behavior of the time kernel (7.3.13) is $\propto 1/K_T^\alpha T^{\alpha+1}$. For both massless particles in the final state $\alpha = 0$ yielding the behavior $1/T$, for one massless and one massive particle in the final state $\alpha = 1$ and the long time behavior is $\propto 1/T^2$ and for both massive particles $\alpha = 1/2$ yielding the long time behavior $1/T^{3/2}$. In order to analyze the contribution from the corrections to the zeroth adiabatic order terms, it is convenient to analyze the short and long time behavior in terms of the variables $z = \Omega_T(\eta)\eta$ and $\tau = \Omega_T(\eta)(\eta - \eta_1)$ introduced in the previous section. In these variables the time integrals restrict τ to the interval $0 \leq \tau \leq \overline{z}$ with $\overline{z}$ given by eqn. (6.3.27) and $\eta_i/\eta \ll 1$, as in the massless case of the previous section. The short time region corresponds to $\tau \ll z$ during which the corrections to the zeroth order adiabatic $\propto \tau/z$ are negligible, as discussed in the massless case. For the case of massive particles in the final state, the long time behavior of the upper bound approximation to the time kernel $I^{(ub)}$ (6.4.6) yields for $\alpha = 1/2, 1$

$$I^{(ub)}[\tau, z] \propto \frac{1}{\tau^\alpha \left(1 - \frac{\tau}{2z}\right)^{1+\alpha}} \left[\frac{1}{\tau} + \frac{1}{z - \tau}\right]. \tag{6.4.13}$$

Near the end point of the time integrals $\tau \simeq \overline{z}$ the second term in the bracket in (6.4.13) dominates. From the definition of $\overline{z}$, eqn. (6.3.27) it follows that

$$z - \overline{z} = z\,\frac{\eta_i}{\eta} = \Omega_T(\eta)\eta_i = \frac{\Omega_T(\eta)}{\Omega_T(\eta_i)}\, z_i\,, \tag{6.4.14}$$

where

$$z_i = \Omega_T(\eta_i)\eta_i \gg 1\,, \tag{6.4.15}$$

because for consistency the adiabatic approximation must hold at the initial time. Furthermore, since $\Omega_T(\eta)/\Omega_T(\eta_i) \geq 1$ it follows that near the upper limit of integration

$$I^{(ub)}[\tau \simeq \overline{z}, z] \lesssim \frac{1}{z_i\, z^\alpha} \ll 1\,. \tag{6.4.16}$$

Hence, the integration region where the corrections to the zeroth adiabatic order become important, namely $\tau \simeq \overline{z}$ is strongly suppressed by the rapid fall-off of the time kernel by a factor $1/(z_i z^\alpha) \ll 1$. Furthermore, since $I^{(ub)}$ is an upper bound, the contribution of this region of integration is even smaller than the bound from eqn. (6.4.16). This analysis is valid for any masses of final state particles and confirms that the time kernel strongly suppresses the region of integration $\tau \simeq z$ in which the higher order adiabatic corrections could compete with the zeroth order. This result is in agreement with the case of massless final states studied in the previous section, and shows that the case of massive particles in the final state is even more suppressed than the massless one. This analysis demonstrates that we can safely neglect the higher order adiabatic corrections encoded in the contributions $\propto \tau/z, \tau^2/z^2 \cdots$, keeping solely the zeroth order contributions. This is tantamount to replacing $f_k^{(i)}(x) \to 1$ in all frequencies associated with the final states (see eqns. (6.4.3,6.4.4)), as well as $f_k(\tau) \to 1$ in all frequencies of the initial states (see eqn. (6.3.14)). These replacements yield the time kernel (6.4.1)

$$I[\eta;\eta_1] = \int \frac{d^3p}{(2\pi)^3} \frac{e^{-i\left(\omega_p^{(3)}(\eta)+\omega_q^{(4)}(\eta)\right)(\eta-\eta_1)}}{\omega_p^{(3)}(\eta)\,\omega_q^{(4)}(\eta)} = \int_{-\infty}^{\infty} \rho(K_0,K) e^{-iK_0(\eta-\eta_1)}\, dK_0\,, \tag{6.4.17}$$

where the spectral density $\rho(K_0,k)$ is given by (6.4.10). Incorporating these replacements in eqn. (6.3.1) yields

$$2\,\Sigma[\eta;\eta_1] = \frac{\lambda^2}{4V} \frac{e^{i\Omega_T(\eta)(\eta-\eta_1)}}{\Omega_{k_1}(\eta)\Omega_{k_2}(\eta)} \;\; I[\eta;\eta_1]\,, \tag{6.4.18}$$

with $\Omega_T(\eta) = \Omega_{k_1}(\eta) + \Omega_{k_2}(\eta)$. We now obtain the transition rate $\Gamma_{i\to f}$, eqn. (6.2.62) by carrying out the *time integral* in η_1, and from eqn. (6.2.70) the cross section to leading order in the adiabatic approximation for particles in the initial state with arbitrary masses $M_{1,2}$ is given by

$$\sigma(\eta) = \frac{\lambda^2}{4\,a^2(\eta)\left[\left(\mathcal{P}_1(\eta)\cdot\mathcal{P}_2(\eta)\right)^2 - M_1^2\,M_2^2\right]^{1/2}} \int_{-\infty}^{\infty} \rho(K_0;K)\, \frac{\sin\Big[\big(K_0-\Omega_T(\eta)\big)(\eta-\eta_i)\Big]}{\big(K_0-\Omega_T(\eta)\big)}\, dK_0\,, \tag{6.4.19}$$

where we have used the relation to the flux given by (6.3.7). For massive particles with masses m_3, m_4 in the final state the spectral density is given by eqns. (6.4.10,6.4.11).

This is our main result for the general case of massive particles both in the initial and final state with masses $M_{1,2}$ and $m_{3,4}$ respectively. It is now straightforward to confirm that for the case of massless particles in the final state, the spectral density is given by (6.3.33) and using the result given by eqn. (6.3.37) the (pair annihilation) cross section is given precisely by eqn. (6.3.30).

6.4.1 Pair annihilation: $\overline{\phi}\phi \to \chi\chi$

In this case the initial state particles are of equal mass $M_1 = M_2 = M$ and final state particles are also of equal mass $m_3 = m_4 = m \neq 0$. We take $\eta_i \to 0$ and changing variables to $K_0 = \Omega_T(\eta) + X/\eta$ we find

$$\sigma(\eta) = \frac{\lambda^2}{16\,\pi^2\,a^2(\eta)\left[\left(\mathcal{P}_1(\eta)\cdot\mathcal{P}_2(\eta)\right)^2 - M^4\right]^{1/2}} \int_{-\overline{X}(\eta)}^{\infty} \widetilde{\rho}(X;\eta)\,\frac{\sin\left[X\right]}{X}\,dX\,, \tag{6.4.20}$$

where

$$\overline{X}(\eta) = \frac{E_T(\eta) - K_{Tp}(\eta)}{H(\eta)}\;\;;\;\; E_T(\eta) = \frac{\Omega_T(\eta)}{a(\eta)}\;\;;\;\; K_{Tp}(\eta) = \left[K^2_{ph}(\eta) + 4\,m^2\right]^{1/2}\;\;;\;\; K_{ph}(\eta) = \frac{K}{a(\eta)}\,, \tag{6.4.21}$$

with $H(\eta) = a'(\eta)/a^2(\eta) = 1/(a(\eta)\eta)$ the Hubble expansion rate in (RD), and

$$\widetilde{\rho}(X;\eta) = \left[1 - \frac{4m^2}{\mathcal{S}(\eta) + X^2H^2(\eta) + 2XE_T(\eta)H(\eta)}\right]^{\frac{1}{2}}, \tag{6.4.22}$$

where

$$\mathcal{S}(\eta) = \Big(\mathcal{P}_1(\eta) + \mathcal{P}_2(\eta)\Big)^2 = E^2_T(\eta) - K^2_{ph}(\eta)\,, \tag{6.4.23}$$

is the local Mandelstam variable depending adiabatically on time through the local four momenta (6.3.9) with the Minkowski scalar product (6.3.8), therefore $\mathcal{S}(\eta)$ is invariant under the local Lorentz transformations (6.3.39). However, for $H(\eta) \neq 0$ the cross section (6.4.20) is not invariant under local Lorentz transformations: both the spectral density which depends explicitly on E_T and the lower limit $\overline{X}$ which depends both on E_T and K_{Tp} violate explicitly the invariance under local Lorentz transformations. We note that the physical cross section $\sigma_{ph}(\eta) = a^2(\eta)\,\sigma(\eta)$ with $\sigma(\eta)$ given by (6.4.20) is strikingly similar to the cross section in Minkowski space-time but during a finite time interval.

The infinite time limit corresponds to $\eta \to \infty$, namely $H(\eta) \to 0$. In this limit the X integral in eqn. (6.4.20) yields

$$\int_{-\overline{X}(\eta)}^{\infty} \widetilde{\rho}(X;\eta)\, \frac{\sin\left[X\right]}{X}\, dX \quad \underset{\eta\to\infty}{\longrightarrow} \quad \pi \left[1 - \frac{4m^2}{\mathcal{S}(\eta)}\right]^{\frac{1}{2}} \Theta\Big(\mathcal{S}(\eta) - 4m^2\Big)\,. \tag{6.4.24}$$

In this "infinite time limit" the cross section becomes

$$\sigma(\eta) \quad \underset{\eta\to\infty}{\longrightarrow} \quad \frac{\lambda^2 \left[1 - \frac{4m^2}{\mathcal{S}(\eta)}\right]^{\frac{1}{2}}}{16\,\pi\, a^2(\eta) \left[\Big(\mathcal{P}_1(\eta)\cdot\mathcal{P}_2(\eta)\Big)^2 - M^4\right]^{1/2}} \Theta\Big(\mathcal{S}(\eta) - 4m^2\Big)\,, \tag{6.4.25}$$

where the $\Theta\Big(\mathcal{S}(\eta) - 4m^2\Big)$ function reflects the kinematic threshold depending adiabatically on time through the red-shifted momenta. Up to the explicit dependence on the scale factor in the denominator, at a fixed η this is the annihilation cross section in Minkowski space-time, the infinite time limit leads to local Lorentz invariance. The threshold Θ function in (6.4.25) has the following origin: first we note that $\overline{X}(\eta)$ given by eqn. (6.4.21) can also be written as $\overline{X}(\eta) = (\mathcal{S}(\eta) - 4m^2)/[(E_T(\eta) + K_{Tp}(\eta))H(\eta)]$ where the denominator is always positive. Therefore, for $\mathcal{S} > 4m^2$ as $H(\eta) \to 0$ it follows that $\overline{X}(\eta) \to \infty$ and the X integral in eqn. (6.4.20) yields a non-vanishing result, whereas for $\mathcal{S} < 4m^2$ and $H \to 0$ the lower limit $\overline{X}(\eta) \to -\infty$ and this integral vanishes in the "long time limit". Hence, the emergence of the sharp kinematic threshold is a consequence of taking the infinite time limit. However, the particle horizon $\eta - \eta_i$ is finite, consequently the cross section must be considered during a finite time interval, thereby allowing several novel processes.

6.4.1.1 Freeze-out of the cross section:

Consider the specific case of pair annihilation in the center of mass (CoM), namely with $K = 0$ and with $M \ll m$, and in a time regime during which the incoming particles feature a physical momentum $k_{ph}(\eta) > \sqrt{m^2 - M^2}$ corresponding to the (CoM) total local energy above the (physical) production threshold $2m$. As time evolves the scale factor grows and the physical wavevector is redshifted *below* the threshold value for production of the heavier species, when this happens the total local energy falls below threshold and the integral in (6.4.20) begins to diminish, vanishing fast because $H(\eta)$ is becoming smaller with

cosmological expansion. We refer to this phenomenon as a *freeze-out* of the production cross section.

We emphasize that this freeze-out is different from the usual freeze-out of species as a consequence of the dilution of the particle density in a Boltzmann equation. Instead the freeze-out of the cross section is solely a consequence of considering the cross section during a *finite time* including explicitly the time dependence of the kinematic threshold, local energy in terms of the redshifted momentum, and the Hubble radius. This phenomenon can be understood in the simpler case of $K = 0$, (CoM) from the integral in (6.4.20) which in this case can be written solely in terms of the ratios $K_T/E_T = 2m/E_T$ and E_T/H,

$$Int(K_T/E_T) = \int_{-\overline{X}(\eta)}^{\infty} \widetilde{\rho}(K_T/E_T; X\, H/E_T)\, \frac{\sin\left[X\right]}{X}\, dX\,. \tag{6.4.26}$$

Figure (32) displays $Int(K_T/E_T)$ vs. K_T/E_T for $E_T/H = 20; K = 0$, for $K_T/E_T \ll 1$ the integral approaches $\pi\, \widetilde{\rho}(K_T/E_T; 0)$ and vanishes for $K_T/E_T \gg 1$, confirming the above analysis.

Although Figure (32) shows this phenomenon for a fixed ratio E_T/H, this ratio actually grows during cosmological expansion, the main conclusion is confirmed by this numerical example. As H diminishes under cosmological expansion the contribution from $K_T/E_T > 1$ diminishes, and in the strict limit $H \to 0$ the step function determining the kinematic threshold in eqn. (6.4.24) emerges.

It is clear that taking the infinite time limit ($H = 0$) too early will not capture this dynamics: if k_{ph} is larger than the threshold value, the cross section grows rather than remaining constant as the step function in (6.4.24) would suggest, as the redshifted k_{ph} falls below threshold it begins to diminish, vanishing rapidly but smoothly as $H \to 0$ rather than the abrupt vanishing suggested by the step function in (6.4.24).

6.4.1.2 Anti-Zeno effect: production below threshold.

The analysis above and the results displayed in Figure(32) also suggest another phenomenon consequence of the finite time, the possibility of pair production when the total (local) energy is below threshold, which is evident in Figure(32) in the tail for $K_T/E_T > 1$.

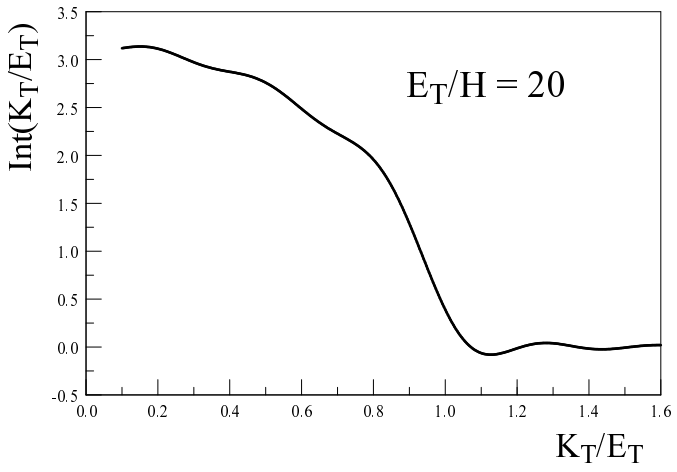

Figure 32: The function $Int(K_T/E_T)$ vs K_T/E_T for $K_T = 2m$; $E_T/H = 20$. Figure taken from [306].

To understand the origin of this phenomenon it is convenient to re-write the integral in (6.4.19) in terms of the local energy and the Hubble rate, setting $\eta_i \to 0$,

$$\int_{-\infty}^{\infty} \rho(K_0; K)\, \frac{\sin\Big[\big(K_0 - \Omega_T(\eta)\big)\eta\Big]}{\big(K_0 - \Omega_T(\eta)\big)}\, dK_0 = \int_{-\infty}^{\infty} \rho\big[K_{0p}(\eta); K_p(\eta)\big]\, \mathrm{sinc}[K_{0p}; E_T; H]\, dK_{0p}(\eta)\,, \tag{6.4.27}$$

where

$$\mathrm{sinc}[K_{0p}; E_T; H] = \frac{\sin\Big[\big(K_{0p}(\eta) - E_T(\eta)\big)/H(\eta)\Big]}{\big(K_{0p}(\eta) - E_T(\eta)\big)}\,, \tag{6.4.28}$$

and for two equal masses in the final state $m_3 = m_4 = m$

$$\rho\big[K_{0p}(\eta); K_p(\eta)\big] = \left[1 - \frac{4m^2}{K_{0p}^2(\eta) - K_p^2(\eta)}\right]^{1/2} \Theta\big(K_{0p}(\eta) - K_{Tp}(\eta)\big)\,, \tag{6.4.29}$$

with

$$K_{0p}(\eta) = \frac{K_0}{a(\eta)} \quad ; \quad K_p(\eta) = \frac{K_p}{a(\eta)} \quad ; \quad K_{Tp}(\eta) = \frac{K_T(\eta)}{a(\eta)}\,. \tag{6.4.30}$$

The *sinc* function (6.4.28) is strongly peaked at $K_0 = E$ with height $1/H$ and width $\simeq 2\pi H$.

If E_T is below threshold, but within a distance $\simeq \pi H$ from threshold, the "wings" of this function still overlap with the spectral density yielding a non-vanishing overlap integral. This is a manifestation of the phenomenon of threshold relaxation found within a different context in ref.[227] and of the *antizeno* effect which refers to the enhanced production as a consequence of uncertainty[249]. Such an effect has been studied in quantum field theory in ref.[105]. Figure(33) shows both functions for $K = 0$ in the case when E_T is below the production threshold. The width of the oscillatory function is $\simeq 2\pi H$, the figure clearly shows that the "wings" of the *sinc* (6.4.28) function have a non-vanishing overlap with the spectral density.

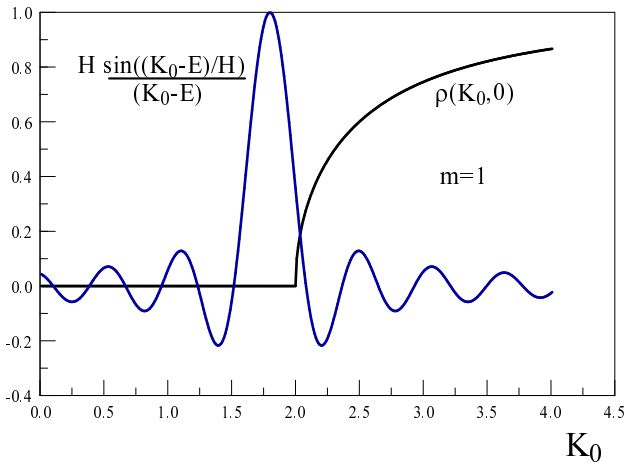

Figure 33: $\rho(K_0, 0)$ and $H\ \sin[(K_0 - E)/H]/(K_0 - E)$ vs K_0 in units of m ($m = 1, K_T = 2, K = 0$) for $E_T \equiv E = 1.8$, $E/H = 20$. Figure taken from [306].

The overlap between the *sinc* function (6.4.28) and $\rho(K_0, K)$ is a consequence of *uncertainty*, the Hubble scale H introduces a (physical) energy uncertainty associated with the time scale $1/H$. It is this energy uncertainty, a consequence of the finite time scale $1/H$,

which is reflected in the broadening of the *sinc* function that allows the overlap with the spectral density even when it is peaked below threshold thus allowing the production of more energetic states. This is the origin of the non-vanishing result for the integral (6.4.26) for $K_T/E > 1$ displayed in Figure (32). This phenomenon has been recognized as the *antizeno* effect in the quantum optics literature[249] and has been observed in trapped cold sodium atoms[182] where the time uncertainty is introduced through the measurement process. In this case it is the inverse of *the particle horizon* (η in comoving or $a(\eta)\eta = 1/H = 2\,t$ in physical coordinates), namely the age of the Universe, which introduces the uncertainty. Under cosmological expansion the particle horizon increases, therefore the uncertainty diminishes, the *sinc* function becomes narrower and the overlap with the spectral density becomes smaller and eventually vanishes, therefore closing the uncertainty window for sub-threshold production.

The condition for the resulting integral to have a non-vanishing contribution and for significant below-threshold production is

$$K_T - E_T \simeq \pi\, H \Rightarrow 4m^2 - \mathcal{S} = 2\pi\, E_T\, H\,, \tag{6.4.31}$$

where we have considered $m_3 = m_4 = m$ in the final state and we kept the leading order in the adiabatic expansion for $E_T \gg H$. In Minkowski space-time the threshold condition is $\mathcal{S}_M = 4m^2$ therefore writing $\mathcal{S} = \mathcal{S}_M - \delta\mathcal{S}$ the finite particle horizon relaxes the threshold condition for production with

$$\delta\mathcal{S} = 2\,\pi E_T H\,. \tag{6.4.32}$$

It is noteworthy that the right hand side of the condition (6.4.32) breaks local Lorentz invariance.

Since the integral in (6.4.20) vanishes for $K_T - E_T \gg H$ and reaches the asymptotic infinite time limit for $E_T - K_T \gg H$ only a small window of width $\simeq H$ in energy and momentum yields sub-threshold production. Writing the condition (6.4.31) as

$$K_T = E_T\Big(1 + \pi\frac{H}{E_T}\Big)\,, \tag{6.4.33}$$

the long time limit $E_T/H \gg 1$ ($\Omega_T(\eta)\eta \gg 1$) invoked in the derivation of the cross section (6.4.20), implies that $K_T \simeq E_T \gg H$ yielding the general condition for subthreshold production

$$2m^2 - M^2 - k_{ph1}k_{ph2} - E_1E_2 \simeq \pi H\, E_T\,. \tag{6.4.34}$$

As a simple example, consider annihilation of the incoming particles in their (CoM) with threshold $K_T = 2m$, subthreshold production of daughter particles would occur with

$$k_{ph} = \Big[m^2 - M^2 - \pi\, m\, H\Big]^{1/2}\,, \tag{6.4.35}$$

for example with $m = 10^5\,\mathrm{GeV}, M = 10^2\,\mathrm{GeV}, H \simeq 10^2\,\mathrm{GeV}$ production of the heavier particle still occurs with a value of k_{ph} which is $\simeq 10^2\,\mathrm{GeV}$ below the corresponding threshold value in Minkowski space-time. This value of the Hubble rate during (RD) corresponds to an ambient temperature $T \simeq 10^{10}\,\mathrm{GeV}$ and $H/E_T \simeq 10^{-3}$. Consider a more general example with $m \gg M, H$ and $k_{ph1} \gg k_{ph2} \gg M$, writing $k_{ph2} = \alpha\, k_{ph1}$ with $\alpha \ll 1$, the inequality (6.4.34) is fulfilled for

$$k_{ph1} \simeq k_M - \frac{\pi H}{4\alpha} \quad ; \quad k_M = \Big[\frac{2m^2 - M^2}{2\alpha}\Big]^{1/2}\,, \tag{6.4.36}$$

therefore for $\alpha \ll 1$ below threshold production occurs for values of k_{ph1} which are smaller than that in Minkowski space-time (k_M) by $\pi H/4\alpha \gg H$. For the masses chosen above, and taking as an example $\alpha \simeq 10^{-2}$, sub-threshold production consistent with $H/E \ll 1$ occurs for $H \lesssim 10^3\,\mathrm{GeV} \Rightarrow a(\eta) \lesssim 10^{-24}$, again corresponding to an ambient temperature $T \lesssim 10^{10}\,\mathrm{GeV}$. An important consequence of this phenomenon is that if heavy dark matter is produced via pair annihilation of a much lighter species, sub-threshold production implies an enhancement of the dark matter abundance.

As cosmological expansion proceeds, H diminishes and the window for sub-threshold production closes. The important aspect of this analysis is that the finite value of H, namely a finite particle horizon $\propto 1/H$ provides an uncertainty allowing processes that would be forbidden by strict energy conservation.

In this case with only the "wings" of the *sinc* function overlapping with the spectral density, it is possible (but not certain) that the transition rate becomes *negative* during a brief transient period. Whether the transition rate becomes negative during a transient

depends on momenta and the behavior of the spectral density near threshold. This important aspect is discussed in more detail in section (6.5). However, as in the previous section, we can integrate the transition rate within a finite and short time interval during which the conformal energies do not vary much, to leading (zeroth) order in the adiabatic expansion we obtain

$$\int_0^\eta \Gamma_{i\to f}(\eta')\,d\eta' = \frac{\lambda^2}{2V}\,\frac{1}{\Omega_{k_1}(\eta)\Omega_{k_2}(\eta)}\int_{-\infty}^{\infty}\rho\big[K_{0p}(\eta);K_p(\eta)\big]\,\Big[\mathrm{sinc}[K_{0p};E_T;H/2]\Big]^2\,dK_{0p}(\eta)\,. \tag{6.4.37}$$

This result is manifestly positive in agreement with (6.2.55), and again similar to Fermi's Golden rule, however, now taking (formally) the limit $H\to\infty$ the bracket inside the integral in (6.4.37) yields $\pi\,H(\eta)\,\delta(K_{0p}-E_T(\eta))$ which would lead to a vanishing result since the spectral density vanishes for $K_{0p}=E_T(\eta)$ but multiplies $H\to\infty$. The total integral yields a finite and positive result, which however does *not* grow secularly with conformal time.

6.4.2 Scattering:

The results obtained above apply directly to the scattering process $\varphi\,\chi\to\varphi\,\chi$ with minor modifications, a combinatoric and symmetry factor for the final state resulting in $\lambda^2\to\lambda^2/2$, different masses in the initial state m,M and in the flux factor, and a different spectral density reflecting the two different masses of the particles in the initial and final states. Following the same steps leading up to (6.4.20) we now find

$$\sigma(\eta) = \frac{\lambda^2}{16\,\pi^2\,a^2(\eta)\,\Big[\big(\mathcal{P}_1(\eta)\cdot\mathcal{P}_2(\eta)\big)^2-M^4\Big]^{1/2}}\int_{-\overline{X}(\eta)}^{\infty}\widetilde{\rho}_+(X;\eta)\,\widetilde{\rho}_-(X;\eta)\,\frac{\sin\big[X\big]}{X}\,dX\,, \tag{6.4.38}$$

where

$$\widetilde{\rho}_\pm(X;\eta)=\left[1-\frac{(M\pm m)^2}{\mathcal{S}(\eta)+X^2H^2(\eta)+2XE_T(\eta)H(\eta)}\right]^{\frac{1}{2}}\;\;;\;\;E_T(\eta)=(\Omega_{k_1}(\eta)+\omega_{k_2}(\eta))/a((\eta))\,, \tag{6.4.39}$$

and in this case

$$\overline{X}(\eta)=\frac{E_T(\eta)-K_{Tp}(\eta)}{H(\eta)}\;\;;\;\;K_{Tp}(\eta)=\Big[K_{ph}^2(\eta)+(M+m)^2\Big]^{1/2}\,. \tag{6.4.40}$$

It is straightforward to confirm that, for collinear scattering

$$K_{Tp}(\eta) = \Big[E_T^2(\eta) - 2(k_{ph1}k_{ph2} + E_1E_2 - mM)\Big]^{1/2} \leq E_T\,. \tag{6.4.41}$$

We note that for $H \neq 0$ the cross section is *not* invariant under the local Lorentz transformation, again as a consequence of the finite particle horizon, or equivalently finite time.

In the long time limit $H \to 0$ we find

$$\sigma_{ph}(\eta \to \infty) = \frac{\lambda^2\,\widetilde{\rho}_+(0;\eta)\,\widetilde{\rho}_-(0;\eta)}{32\,\pi\left[\big(\mathcal{P}_1(\eta)\cdot\mathcal{P}_2(\eta)\big)^2 - M^4\right]^{1/2}}\,. \tag{6.4.42}$$

This is the result in Minkowski space-time, manifestly invariant under local Lorentz transformations but with the kinematic variables depending adiabatically on time. We emphasize that this is an approximation that formally corresponds to taking the scale factor $a(\eta) \to \infty$, therefore leading to an infinite redshift of the physical momenta that enter in the flux prefactor.

6.5 Discussion

Subtleties of the transition rate: In a finite time interval, the transition rate and cross section feature oscillations as a consequence of time-energy uncertainty. It is possible that within some range of (local) energy and momenta the transition rate may be negative in some circumstances. This is more explicit in the case of sub-threshold production analyzed in section (6.4.1). For this situation since the transition rate at large time vanishes, transient phenomena consistent with time-energy uncertainty yields the oscillatory behavior that probes the subthreshold region during a time interval and may lead to negative values. Whereas the total number of events (6.2.55) is manifestly positive, the event *rate* may become negative during these transients. This subtle behavior can be traced to the definition of the transition rate (6.2.57), which may indeed become negative during a finite time interval in some circumstances. This is not a feature of the cosmological setting as it is also the case in Minkowski space-time which coincides in the infinite time limit with the usual definition

as the total transition probability, (which grows linearly in time at long time), divided by the total time elapsed. There are at least two arguments in favor of the definition (6.2.57): **a:)** the total number of detected events is generally obtained as

$$N = \sigma\, L \quad ; \quad L = \int \mathcal{L}(t) dt\,, \tag{6.5.1}$$

where L is the integrated luminosity and the luminosity $\mathcal{L}(t)$ has units of $cm^{-2}\, s^{-1}$. Obviously such definition of the number of events at a detector assumes a time independent cross section, and from this definition $\sigma = N/L$ is manifestly positive. Allowing the cross section to depend on time, the total number of events should, consequently, be defined as

$$N = \int \mathcal{L}(t)\, \sigma(t) dt \Rightarrow \frac{dN}{dt} = \sigma(t)\mathcal{L}(t)\,. \tag{6.5.2}$$

This definition is consistent with eqn. (6.2.57). **b:)** consider a process $1 + 2 \to 3 + 4$, the gain term in the Boltzmann equation for the distribution function of particle 3 is

$$\frac{df_3(t)}{dt} = \int d[1] \int d[2] f_1(t)\, f_2(t) (\sigma(t) v_{12}) \tag{6.5.3}$$

with v_{12} the relative velocity. Therefore the definition of $\sigma(t)$ in terms of the transition rate given eqn. (6.2.57) is consistent with the usual Boltzmann equation.

Although it remains to be shown that the transition rate in the appropriate Boltzmann equation in cosmology is determined by $\sigma\, v_{12}$ (however this is the usual formulation), the main point of eqn. (6.5.3) is that it explicitly implies that the *rate* of change of the population is defined as its *time derivative* namely df/dt, consistently with our definition for the transition rate (6.2.55).

One may propose an alternative definition of the transition rate which is manifestly positive as the time average (now in conformal time) (taking $\eta_i \to 0$)

$$\overline{\Gamma(\eta)} \equiv \frac{1}{\eta} \int_0^\eta \Gamma(\eta')\, d\eta'\,, \tag{6.5.4}$$

where the integral is given by (6.4.37), and define a time-averaged cross section by dividing by an instantaneous unit flux at time η in a long time limit. In cosmology such a definition would not be consistent: the integral in (6.5.4) depends on the expansion history, and multiplying by the flux at a late time when the physical momenta and relative velocity

had undergone a large redshift would not describe the cosmological evolution consistently. Therefore, we conclude that despite the subtleties and the counterintuitive possibility of a negative transition *rate* mainly in the case of subthreshold phenomena, the definition of the rate (6.2.57) is consistent with unitarity, the optical theorem, a manifestly positive *total* number of events, the usual relation between the total number of events at a detector in terms of the integrated luminosity, and the Boltzmann equation. The time integral of the transition rate (6.2.57) yields the total transition probability that is manifestly positive. The cross section *per se* is an ingredient whose time integral in combination with flux factors or distribution functions yields the total number of events which is positive (eqn. (6.2.55)). Furthermore, the phenomena discussed above such as local Lorentz violation and sub-threshold production yielding contributions to events that would be forbidden by strict energy conservation will remain features of the time integrated quantities.

General lessons and possible cosmological consequences:

- **Threshold relaxation and energy uncertainty:** Although our study above has focused on a model local interaction, there are many general lessons that we can draw from it. To begin with, the lack of strict energy conservation quantified by the uncertainty H in local physical energy variable is a direct result of the finite particle horizon or, equivalently, finite time. Comparison with the analysis in Minkowski space-time but during a finite time interval highlights that this feature is indeed quite generic. The S-matrix approach is always formulated with in-states prepared in the infinite past and out states measured in the infinite future, clearly warranted in typical experimental situations. However, is unwarranted during the early stages of cosmological history with a finite particle horizon. A direct consequence of the (local physical) energy uncertainty $\simeq H$ is that kinematic thresholds that reflect strict energy momentum conservation are relaxed within a window of order H thereby allowing processes that would be otherwise forbidden by strict energy conservation. This is the case for sub-threshold production studied above. This is a fundamental and generic feature of processes in cosmology and are independent of the particular interaction between the various fields.

  As an example of potential cosmological importance of this phenomenon, let us consider

that post-inflation reheating occurs at a high energy/temperature scale, for example intermediate between the GUT and the Standard Model scales, $T \simeq 10^9\,\mathrm{GeV}$. This temperature corresponds to a scale factor $a(t) \simeq 10^{-20}$ and a Hubble expansion rate $H \simeq$ GeV, which determines the energy uncertainty that characterizes threshold relaxation. This uncertainty window would allow scattering or production processes that would be forbidden by strict energy conservation to produce degrees of freedom near the scale of this uncertainty. Reheating at a higher energy/temperature scale would widen this uncertainty window.

Consequences of energy uncertainty within a finite time interval have been recently discussed also within different contexts[172, 50].

- **Violations of local Lorentz invariance:** We recognized a violation of Lorentz invariance as a consequence of the finite time analysis, both with cosmological expansion as well as Minkowski space-time during a finite time interval. In Minkowski space-time such violation of Lorentz invariance is expected, a finite time interval is not a Lorentz invariant concept. Within the context of an expanding cosmology, a finite time analysis of interaction rates and cross sections is a necessity: an infinite time limit as implied in the S-matrix formulation, ignores both formally and conceptually the different stages in the expansion history, the cosmological redshift of physical wavevectors and the finiteness of the particle horizon. It is this necessity to consider processes directly in real and finite time that leads unequivocally to violation of local Lorentz invariance. At heart, a finite time analysis is simply a recognition of a finite particle horizon $\propto 1/H$ in physical coordinates, which introduces an energy uncertainty $\propto H$. The cross section for pair annihilation during a finite time interval in Minkowski space-time, which also displays a similar violation of Lorentz invariance. However, in a "terrestrial" experiment the energy and time scales justify taking the infinite time limit: with typical time scales of $10^{-4}\,\mathrm{secs}$ (a beam travelling few km until detection) the typical energy uncertainty is $\simeq 10^{-10}\,\mathrm{eV}$ and typical detector momentum resolutions $\simeq \mathrm{KeV} - \mathrm{MeV}$ the finite time corrections are experimentally completely negligible, justifying the infinite time limit with the concomitant Lorentz invariant cross section.

  Possible sources of Lorentz violations have been advocated within the context of quantum

gravity and Planck scale physics[267, 237, 138, 253] with possible consequences for CP and CPT violation. Our study here shows that Lorentz violations emerge naturally as a consequence of considering fundamental processes in an expanding cosmology directly in real time and accounting for the finite particle horizon. The example of pair annihilation displays the consequences of the finite time in the form of the freeze-out and antizeno effects that lead to small but non-vanishing sub-threshold production of heavy particles as analyzed in the previous section. The freeze-out of a production cross section as a consequence of the redshift of wavevectors below the threshold, is, similarly, an inescapable consequence of the cosmological expansion, hence it is a generic feature associated with the finite time evolution. These phenomena are directly correlated with the violation of local Lorentz invariance. To be sure, within the adiabatic approximation these effects are small and the window for their impact closes with the cosmological expansion. However, during the time that this window remains open, the Lorentz violating processes *may* be of importance for CP violation and perhaps baryogenesis. The possible impact of these Lorentz violating aspects deserve further scrutiny.

- **Impact on quantum kinetics:** An important cosmological application of the transition rate (6.2.57) and cross section, is to input these into a quantum kinetic Boltzmann equation for the distribution function of particles. A kinetic equation for the distribution function of a φ particle $\mathcal{F}_\varphi(\vec{k},\eta)$ for example, is of the form $d\,\mathcal{F}_\varphi(\vec{k}_1,\eta)/d\eta$ = gain − loss where the "loss" term inputs the transition rate (6.2.57) and the gain term inputs the rate for the reverse process $\chi\chi \to \overline{\varphi}\varphi$. An important feature of quantum kinetic equations is detailed balance which leads to local thermodynamic equilibrium as a fixed point of the kinetic equation. However, detailed balance depends crucially on energy-momentum conservation both in the gain and loss terms[251, 83, 160]. The results of the previous section indicate that there *may* be possible important modifications arising from the energy uncertainty $\propto H$ and lack of energy conservation. These could lead to modifications of detailed balance and consequently introduce novel non-equilibrium effects, which along with the violation of local Lorentz invariance could, potentially, be important for baryogenesis and leptogenesis, even when such effects are small, of $\mathcal{O}(H)$ as compared to temperature or energy scales. These intriguing possibilities deserve further

and deeper study.

- **Resonant cross sections smoothed by a finite particle horizon:** The energy uncertainty introduced by H brings an interesting possibility for the case of resonant cross sections, where the resonance is a consequence of a massive particle exchange as an intermediate state. In S-matrix theory in a resonant reaction the intermediate state goes on-shell and the enhancement of the cross section is a consequence of this intermediate state propagating over long time scales, a pole in the cross section is actually smoothed out by the lifetime of the intermediate state that has gone "on-shell". The (Breit-Wigner) width of the cross section is a manifestation of the lifetime of the intermediate state. We conjecture that a similar case of an intermediate stage "going on its mass shell" in an expanding cosmology only propagates during the particle horizon. Therefore for a very long-lived intermediate state during the regime when the particle horizon is smaller than the lifetime, we expect a resonant cross section will feature a width $\propto H$ rather than the natural width of the decaying state. As H diminishes, the width of the intermediate state will replace H in the broadening of the cross section. This possibility would have potentially interesting consequences in dark sectors that are connected to the Standard Model via mediators, when such mediators could lead to resonant cross sections. We are currently studying this scenario.
- **No corrections to Big Bang Nucleosynthesis:** Although our study has focused on a quartic contact interaction among bosonic fields and does not apply directly to the case of (BBN), one of the general lessons drawn from this study is the dependence on the various energy and time scales. The effects of finite time such as local Lorentz violation and threshold relaxation in production cross sections are phenomena associated with the ratio $(K_T - E)/H$. (BBN) occurs during the (RD) era at a time scale $t \simeq$ few minutes and temperatures $T \simeq$ few MeV corresponding to $H \simeq 10^{-24}\,\text{GeV}$ with nucleon energies $\simeq$ GeV and binding energies $\simeq$ few MeV therefore the relevant ratio is $E/H \simeq 10^{27}$ which leads to the energy conserving limit of the cross section. Therefore, without a doubt the interesting phenomena associated with finite time do not modify the standard results of (BBN).
- **When is the S-matrix approximately reliable?, and when is it not?** The study

of the previous sections along with the main results invites the above questions. The adiabatic approximation described in this study and the comparison with the results of a finite time analysis in Minkowski space-time, all suggest that, as expected, for a Hubble rate $H(t)$ much smaller than the typical local energies, the uncertainty $\propto 1/H$ can be safely neglected. Taking the infinite time limit in the transition amplitudes, *but* allowing the redshift of momenta in the local energies of the external particles and in reaction thresholds, which lead to the freeze-out of the cross sections, yields a reasonably reliable approximation. Such is the case for (BBN). However, there are at least two scenarios wherein the S-matrix approach will ultimately be unreliable: very early during (RD) when H is large, comparable with the mass scales of particles, or whenever the adiabatic approximation breaks down. The first instance would be relevant for a description of thermalization during reheating if it occurs at a high energy scale. The second scenario applies in the case of super-Hubble wavelengths for particles with masses smaller than the Hubble rate. Under these circumstances, quantization with the full mode functions such as the parabolic Weber functions in the (RD) case is required, and even the program described in this study which relies on the validity of the adiabatic approximation would need a reassessment.

On wave packets:

As discussed in elementary textbooks, a (more) correct description of scattering and or production should invoke a treatment of initial states in terms of wave packets localized in space-time. While formally correct, practically all calculations describe initial states as Fock eigenstates of momentum, namely plane waves, disregarding the fact that these are not localized. Invoking wave packets, while addressing the issue of locality of the initial state presents several conceptual and technical challenges even in Minkowski space-time: wave packets spread through dispersion since each wave vector evolves differently in time, this, by itself prevents a formal infinite time limit. The localization in space and in momentum components must be assumed to be such that the incoming "beams" are localized in space-time but yet be nearly monochromatic so the momenta of the initial and final states which are the labels of the S-matrix elements, are fairly well defined. Last, but by no means least, wave

packets do not transform as irreducible representations of the Lorentz group, thereby breaking Lorentz invariance. These are well known shortcomings of a wave packet description. A thorough analysis of many of these issues within the context of the asymptotic formulation of the S-matrix has been discussed recently in ref.[139]. In a cosmological space-time these conceptual and technical subtleties of the wave packet formulation are compounded by two important aspects: i) each Fock momentum state in the wave packet components evolves with a non-local phase in time, ii) the cosmological redshift of the momenta. The width in momentum (or localization length in space) also determines an uncertainty. All these aspects introduce yet several more layers of technical complications which ultimately need to be addressed. These notwithstanding, the general lessons and novel phenomena described above are overarching and robust and qualitatively not affected by a wave packet treatment.

6.6 Conclusions and further questions

Motivated by the importance of transition rates and cross sections in a wide range of processes in the early Universe, this chapter is devoted to obtaining these fundamental ingredients from first principles in a spatially flat, radiation dominated cosmology. The main objectives are to re-assess the usual S-matrix approach, which takes the infinite time limit, as applied to the cosmological setting, to highlight its shortcomings and provide a systematic framework that includes consistently the cosmological expansion, the finite particle horizon and to explore their consequences. We begin this program by focusing on bosonic fields interacting via a quartic local contact interaction, a simpler setting which, however, allows us to study various important processes such as production of a heavier species and scattering, and yields important and more general lessons. Field quantization in the cosmological curved space-time explicitly shows the conceptual and daunting technical obstacles to implementing the usual approach to transition rates and cross sections. To overcome these obstacles we introduce a physically motivated adiabatic approximation that relies on a separation of time scales encoded in a small ratio $H(t)/E(t)$ with $H(t)$ the Hubble expansion rate and $E(t)$ a typical particle energy measured by a local observer. The smallness of this ratio corresponds

to typical wavelengths (either de Broglie or Compton) much smaller than the particle horizon at a given time and also to a wide separation between the (shorter) microscopic time scale of oscillations $\propto 1/E$ and the (longer) time scale of expansion $\propto 1/H$. We show that the leading (zeroth) adiabatic order dominates the transition rates and obtain the cross section for various processes during a finite time interval consistently with a finite particle horizon. We compare these cross sections to those in Minkowski space-time within a finite time interval. We find several novel effects associated with the finite particle horizon in the case of production of a heavier species from the annihilation of a lighter species: **i)** Freeze-in of the production cross section: the cosmological redshift of physical momenta eventually diminishes it below the production threshold, keeping a finite time in the cross section reveals that it vanishes fast but continuously when this happens and production shuts off. **ii)** A finite particle horizon ($1/H$ in physical coordinates) determines an uncertainty in the (local) energy of order H allowing processes that would be forbidden by strict energy conservation. In particular this uncertainty allows *sub-threshold* production of heavier particles within a window of width $\simeq H$ in (local) energy, during a small interval of time. If a heavy dark matter particle is produced via the pair annihilation of a much lighter species, sub-threshold production may lead to a larger dark matter abundance after the cross section freezes-out.

We also find the important result that allowing for the finite particle horizon leads to a *violation of local Lorentz invariance*, this is a general result for all processes and is a direct consequence of explicitly keeping the cosmological time evolution in the transition rates.

An important corollary of our study is the limitation of the adiabatic approximation: processes that involve wavelengths that are larger than the particle horizon and masses $m \ll H$ at a given time must be studied non-perturbatively with the full mode functions, for bosonic particles these are linear combinations of Weber's parabolic cylinder functions given by (6.2.22).

We comment on possible implications of these results, for example their impact on CP and CPT violation, quantum kinetics, baryogenesis and/or leptogenesis as well as possible new phenomena associated with resonant cross sections. The adiabatic approximation advocated in this chapter should pave the way towards a deeper understanding of interactions of the Standard Model in the regime of validity of such approximation.

Caveats with the definition of a transition rate during finite time intervals have been identified and discussed. We explored alternative definitions, which, however are inconsistent with the time dependence of energy and cosmological redshift of physical momenta. These aspects should motivate a further exploration of the concept of transition rates including transient phenomena in early Universe cosmology.

Furthermore, we have discussed under what circumstances a modified S-matrix approach is approximately reliable, and when it is not, and in the latter case we have identified the proper quantization procedure.

In summary, this study has revealed hitherto unexplored consequences of considering these fundamental processes in the early Universe with proper account of the finite particle horizon i.e, finite time, in their description. The results open new avenues of inquiry that will be the subject of forthcoming studies.

7.0 Infrared dressing in real time: emergence of anomalous dimensions

7.1 Introduction

The infrared behavior of interacting quantum field theories featuring massless fields has been of longstanding interest within the context of scattering amplitudes and the S-matrix in gauge theories[91, 264, 133, 245, 243, 353, 343, 255]. Infrared singularities associated with the emission and/or absorption of soft massless quanta by charged fields has continued to be studied within the context of gauge theories in high energy physics[261, 142, 191, 229], quantum coherence and infrared phenomena[122, 205, 334], as well as precision calculation of physical observables motivated by collider experiments[222, 223, 187], but also of infrared aspects of gravity[330, 241].

Our main interest in the subject is motivated by the possibility that soft bremsstrahlung could yield an important mechanism for production of ultralight dark matter particles in an expanding cosmology. Motivated by this possibility, in this chapter we explore the consequences of infrared divergences associated with emission and absorption of soft massless quanta directly in real time in *non-gauge theories* thereby bypassing the subtle aspects associated with gauge invariance, but addressing the main physics of the infrared behavior and the dynamics of dressing in real time. As for example in QED the infrared singularities associated with charged single particle states are a consequence of the single particle mass shell coinciding with the multiparticle threshold.

The focus of this chapter is restricted to the study of infrared divergences associated with the dressing of charged single particle states arising from absorption and emission of massless neutral quanta in non-gauge theories, not on the more overarching infrared aspects of the S-matrix in gauge theories explored in refs.[91]-[187].

Our main objective is to study the dynamics of dressing in real time, namely the time evolution of an initial state and the nature of the asymptotic many-particle state that emerges from the dressing of the charged single particle state by soft massless quanta of the neutral field in the asymptotic long time limit.

While we are ultimately interested in the cosmological applications, for which an S-matrix approach that relies on the infinite time limit is not the most useful framework to study time dependent phenomena, initiating this study of real time dressing dynamics in Minkowski space time may prove relevant for further understanding of infrared phenomena in gauge theories and gravity. Recently[139] a re-evaluation of the Lehmann, Symanzik and Zimmermann reduction formula for asymptotic states beginning with a finite time analysis and proceeding to the infinite time limit has exhibited the subleties of this limit.

Brief summary of main results:

In this chapter we introduce a dynamical resummation method(DRM)[105], based on a generalization of the dynamical renormalization group[124, 204, 102] to study the time evolution of initial states and the physics of soft dressing directly in real time. In this chapter we focus on various non-gauge theories that feature infrared singularities akin to those found in QED, hence it is possible that the results found in this study may prove a useful guide in gauge theories, and perhaps, in gravity[330, 241]. Our main results are the following:

Models with infrared divergences: We consider both a super renormalizable model and a renormalizable model of a charged field coupled to a massless field which while featuring very different ultraviolet behavior exhibit the same infrared threshold singularities. We establish a parallel between the infrared singularities of these models and those associated with a theory at a critical point[35, 204]. We do so by mapping the behavior of the single particle propagator near threshold to that of a critical Euclidean field theory at a fixed point. We then implement a renormalization group (RG) resummation of the infrared behavior that leads to scaling with anomalous dimension. Performing a Fourier transform in time of the (RG) resummed propagator reveals that the survival probability of a single particle state decays in time asymptotically as a power law with an anomalous dimension $\propto t^{-\Delta}$. A dynamical resummation method (DRM) is introduced that provides a resummation of self-energy corrections directly in real time[105]. This method is manifestly unitary and directly related to the dynamical renormalization group[124, 204, 102] but extends it in significant ways: not only it reproduces the power law decay in time with anomalous dimension Δ which is shown to be determined by the derivative of the spectral density at threshold, but

also yields a physical description of the dynamics of dressing of the charged particle by a soft cloud of massless quanta.

Universality: We find that the infrared divergence is a consequence of a linearly vanishing spectral density at threshold with a finite slope Δ. Implementing the (DRM) leads to the survival probability of the single particle state decaying at asymptotically long time as $\propto t^{-\Delta}$, reproducing the result from the (RG) improved propagator. The anomalous dimension Δ is completely determined by the slope of the spectral density at threshold. Therefore we interpret this behavior as a manifestation of universality, in the sense that models that feature very different ultraviolet behavior but similar infrared threshold behavior with spectral densities vanishing linearly at threshold, yield similar asymptotic dynamics. Obviously different models yield different values of the anomalous dimension Δ, however, whatever the value of Δ all of these models feature an asymptotic survival probability $\propto t^{-\Delta}$ with scaling behavior. This is similar to universality in critical phenomena where scaling behavior near a critical point is described in terms of critical exponents which are insensitive to the ultraviolet behavior of the theory.

Massless axion-like particles: Motivated by their possible relevance in cosmology, we studied the case of effective field theories of a massless axion-like pseudoscalar particle coupled to fermionic degrees of freedom. We considered both pseudoscalar and pseudovector couplings. In both cases we find that the emission and absorption of the massless quanta results in spectral densities that vanish faster than linear at threshold, thus preventing infrared divergences. These theories do not feature decay with anomalous dimensions ($\Delta = 0$). We provide a criterion for the determination of infrared divergences in general non-gauge effective field theories valid up to one loop level.

The entangled dressing cloud and its entropy: The (DRM) describes unitary time evolution and yields the asymptotic multiparticle state that results from the evolution of the initial single particle state. We show explicitly how unitarity is manifest in the asymptotic long time limit when the initial state has completely decayed (with a power law). This asymptotic pure state is an entangled state between the charged particle and the soft cloud with amplitudes that exhibit the infrared enhancement and the anomalous dimension. If a detector only measures the charge of the asymptotic state, but is insensitive

to the massless quanta, tracing the asymptotic state over the unobserved degrees of freedom yields a mixed state. The probabilities display the infrared enhancement, which is, however, compensated by contributions vanishing with the anomalous dimension. The entanglement entropy is obtained directly in real time, its time evolution is completely determined by the (DRM) equations, it describes the information flow from an initial single particle state to the asymptotic entangled multiparticle state and is infrared finite as a consequence of the anomalous dimension.

7.2 Super renormalizable, and renormalizable models:

We study the dynamics of infrared dressing in two models that feature different ultraviolet behavior but share similar infrared behavior near the multiparticle threshold, and effective field theory models of a charged fermion field coupled to a massless axion-like particle.

7.2.1 Super renormalizable case:

Let us consider the case of a massive complex, charged scalar field ϕ coupled to a massless real scalar field χ.

$$\mathcal{L} = \partial^\mu \phi^\dagger \partial_\mu \phi - M^2 \phi^\dagger \phi + \frac{1}{2}\,\partial^\mu \chi \partial_\mu \chi - \lambda\,\phi^\dagger \phi\,\chi \tag{7.2.1}$$

Including the one-loop self energy, the Dyson-resummed ϕ propagator is

$$G_\phi(P) = \frac{1}{P^2 - M^2 - \Sigma(P^2)} \tag{7.2.2}$$

where

$$\Sigma(P^2) = -\frac{\widetilde{\lambda}^2}{(4\pi)^2}\,L + \frac{\widetilde{\lambda}^2}{(4\pi)^2}\,I(P^2/M^2) \tag{7.2.3}$$

where in dimensional regularization in dimension $D = 4 - \varepsilon$

$$\widetilde{\lambda} = \lambda\,\mu^{-\varepsilon/2} \;\;;\;\; L = \frac{2}{\varepsilon} - \gamma_E + \ln(4\pi) - \ln\Big[\frac{M^2}{\mu^2}\Big] \tag{7.2.4}$$

and

$$I(\alpha) = \int_0^1 \ln\Big[x - \alpha\,x\,(1-x) - i\tilde{\epsilon}\Big]\,dx \;\;;\;\; \tilde{\epsilon} \to 0^+ \,. \tag{7.2.5}$$

Subtracting the self-energy at $P^2 = M_p^2$, the renormalized mass, at which the inverse propagator vanishes, namely

$$\Sigma(P^2) = \Sigma(M_p^2) + \overline{\Sigma}(P^2)\,, \tag{7.2.6}$$

where

$$M_p^2 = M^2 + \Sigma(P^2 = M_p^2) \tag{7.2.7}$$

it follows that

$$G(P^2) = \frac{1}{P^2 - M_p^2 - \overline{\Sigma}(P^2)}\,, \tag{7.2.8}$$

with

$$\overline{\Sigma}(P^2) = \frac{\lambda_R^2}{(4\pi)^2}\,\frac{P^2 - M_p^2}{P^2}\,\ln\Big[\frac{M_p^2 - P^2 - i\tilde{\epsilon}}{M_p^2}\Big]\,. \tag{7.2.9}$$

To leading order we have replaced bare by renormalized quantities in $\overline{\Sigma}$. Although the inverse propagator vanishes at $P^2 = M_p^2$, $d\overline{\Sigma}/dP^2$ features an infrared singularity at $P^2 = M_p^2$ which is the beginning of the multiparticle cut and the threshold for emission of soft quanta, since

$$\mathrm{Im}\overline{\Sigma}(P^2) = -\pi\,\frac{\lambda_p^2}{(4\pi)^2}\,\frac{P^2 - M_p^2}{P^2}\,\Theta(P^2 - M_p^2)\,. \tag{7.2.10}$$

Near $P^2 = M_p^2$ the propagator becomes

$$G(P^2) = \frac{1}{(P^2 - M_p^2)\Big[1 - g^2\,\ln\Big(\frac{M_p^2 - P^2}{M_p^2}\Big)\Big]}\quad ;\quad g = \frac{\lambda_R}{4\pi\,M_p}\,, \tag{7.2.11}$$

where in the argument of the logarithm $P^2 \to P^2 + i\tilde{\epsilon}$. This behavior for $P^2 \simeq M_p^2$ is reminiscent of critical phenomena[35] which suggests the implementation of a renormalization group resummation, The result is the renormalization group improved propagator

$$G^{RG}(P^2) = \frac{1}{(P^2 - M_p^2)\Big[\frac{M_p^2 - P^2}{M_p^2}\Big]^{-g^2}}\,. \tag{7.2.12}$$

The forward time evolution is obtained from the inverse Fourier transform in frequency:

$$\widetilde{G}(t) = \int \frac{dp_0}{2\pi} e^{-ip_0 t}\,G^{RG}(P^2)\,, \tag{7.2.13}$$

and the long time limit is determined by the behavior of $G^{RG}(P^2)$ for $P^2 \simeq M_p^2$. Writing $P^2 = (p_0 - E_p)(p_0 + E_p)$ with $E_p^2 = \vec{p}^2 + M_p^2$, and changing variables to $(p_0 - E_p) = x/t$ the integral becomes (with $x \to x + i\tilde{\epsilon}$)

$$\widetilde{G}(t) = e^{-iE_p t} \int \frac{dx}{2\pi} \frac{e^{-ix}}{x} \frac{i}{2E_p + \frac{x}{t}} \frac{1}{\Big[-\frac{x}{M_p\, t} \Big(\frac{2E_p + x/t}{M_p} \Big) \Big]^{-g^2}} \,, \tag{7.2.14}$$

which in the long time limit becomes

$$\widetilde{G}(t) \propto \frac{e^{-iE_p t}}{2E_p} \Big[\frac{M_p}{2E_p} \Big]^{-2g^2} \Big[E_p\, t \Big]^{-g^2} \,. \tag{7.2.15}$$

Therefore a renormalization group improvement of the branch cut singularity beginning at $P^2 = M_p^2$ yields long time power law decay with anomalous dimension $g^2 = (\lambda_R/4\pi M_p)^2$. This asymptotic scaling behavior is a consequence of the infrared singularity at threshold of the propagator. The propagator (7.2.14) describes the asymptotic time evolution of the amplitude, therefore, the survival probability of the initial state is

$$|\widetilde{G}(t)|^2 \propto \Big[E_p\, t \Big]^{-2\, g^2} \,. \tag{7.2.16}$$

For a typical decaying state this survival probability would be of the form $e^{-\Gamma t}$ with Γ being the total decay width.

7.2.2 Renormalizable case:

As an example of a renormalizable case we consider a Dirac fermion Yukawa coupled to a massless real scalar field Φ, namely

$$\mathcal{L} = \frac{1}{2}\,\partial_\mu\Phi\partial^\mu\Phi + \overline{\Psi}\Big(i\not{\partial} - M\Big)\Psi - Y\,\overline{\Psi}\Phi\Psi\,. \tag{7.2.17}$$

The fermion propagator is given by

$$S(P) = \frac{i}{\not{P} - M - \Sigma(\not{P})}\,. \tag{7.2.18}$$

The one loop self energy is given by

$$\Sigma(\not{P}) = -\frac{\widetilde{Y}^2}{(4\pi)^2}\left\{\Big(\frac{\not{P}}{2} + M\Big)L - \int_0^1 \big[\not{P}(1-x) + M\big]\ln\big[x - \alpha x(1-x) - i\tilde{\epsilon}\big]\,dx\right\}, \tag{7.2.19}$$

where in dimensional regularization with $D = 4 - \varepsilon$

$$\widetilde{Y}^2 = Y^2\,\mu^{-\varepsilon} \;\;;\;\; L = \Big\{\frac{2}{\varepsilon} - \gamma_E + \ln(4\pi) - \ln\big[\frac{M^2}{\mu^2}\big]\Big\} \;\;;\;\; \alpha = \frac{P^2}{M^2}\,. \tag{7.2.20}$$

First, we renormalize the mass by requesting that the inverse propagator vanishes at $\not{P} = M_p$ from which it follows that

$$M_p = M + \Sigma(\not{P} = M_p)\,, \tag{7.2.21}$$

secondly, we introduce the off-shell wave function renormalization constant Z and renormalized coupling y_R as

$$Z^{-1} = 1 - \frac{\widetilde{Y}^2\,L}{2\,(4\pi)^2} \;\;;\;\; y_R^2 = \frac{Z\,\widetilde{Y}^2}{(4\pi)^2} \tag{7.2.22}$$

yielding

$$S(\not{P}) = \frac{i\,Z}{\not{P} - M_p - \widetilde{\Sigma}(\not{P})}\,, \tag{7.2.23}$$

where to leading order in the Yukawa coupling,

$$\widetilde{\Sigma}(\not{P}) = y_R^2\Big[\not{P}\left(\frac{\alpha^2-1}{2\alpha^2}\right) + M_p\left(\frac{\alpha-1}{\alpha}\right)\Big]\,\ln\Big[1-\alpha\Big] \;\;;\;\; \alpha \equiv \frac{P^2}{M_p^2} + i\tilde{\epsilon}\,. \tag{7.2.24}$$

Near the mass shell $\not{P} \simeq M_p$ we find the behavior

$$S(\not{P}) = \frac{i\,Z\,\Big(\not{P} + M_p\Big)}{\Big(P^2 - M_p^2\Big)\,\Big[1 - 4\,y_R^2\,\ln\Big[\frac{M_p^2 - P^2}{M_p^2}\Big]\Big]}\,. \tag{7.2.25}$$

Up to the overall (ultraviolet divergent) constant Z this propagator features the same type of infrared singularity as in the super renormalizable case and we invoke a similar renormalization group resummation leading to the renormalization group improved propagator

$$S^{RG}(P) = \frac{i\,Z\left(\not{P} + M_p\right)}{\left(P^2 - M_p^2\right)\left[\frac{M_p^2 - P^2}{M_p^2}\right]^{-4y_R^2}} \quad ; \quad P^2 \to P^2 + i\tilde{\epsilon}\ . \tag{7.2.26}$$

We note that the behavior near $P^2 \simeq M_P^2$ is very similar to the super renormalizable case, given by eqn. (7.2.12).

As in the super renormalizable case, the forward time evolution is obtained by the inverse Fourier transform, the long time limit is determined by the threshold region $P^2 \simeq M_P^2$. Projecting onto a positive energy spinor (for forward time evolution) and proceeding as in the previous case, with $p_0 - E_p = x/t$, we find in the long time limit

$$\widetilde{S}(t) \propto Z\, e^{-iE_p t}\left[\frac{M_R}{2E_p}\right]^{1-8y_R^2}\Big[E_p\, t\Big]^{-4y_R^2}\ , \tag{7.2.27}$$

Again the scaling behavior at long time is a manifestation of the infrared singularity at threshold.

We note that in the form of the propagators (7.2.11,7.2.25) the discontinuity of the propagator across the two particle cut vanishes linearly in $p_0 - E_p$, this feature will prove to be important in the emergence of power law decay in time as explicitly shown by the dynamical resummation method of next section.

7.2.3 Massless axion-like particles:

We consider massless axion-like particles as pseudoscalar real massless fields, and two different couplings to a fermion field: **a:)** pseudoscalar Yukawa coupling $ig\phi\,\overline{\Psi}\gamma^5\Psi$, **b:)** pseudovector coupling $g\partial_\mu\phi\,\overline{\Psi}\gamma^\mu\gamma^5\Psi$.

a:) This is also a renormalizable case. The propagator is given by eqn. (7.2.19), and in this case, it is straightforward to conclude that the self-energy $\Sigma(\not{P})$ is obtained from that of the scalar case (7.2.17) by simply replacing $M \to -M$. Following the same renormalization

procedure as in the scalar case, after mass and (off-shell) wave function renormalization the propagator in this, pseudoscalar case (ps), reads

$$S_{ps}(\not P) = \frac{i\, Z_{ps}}{\not P - M_p - \widetilde{\Sigma}_{ps}(\not P)}\,, \tag{7.2.28}$$

with

$$\widetilde{\Sigma}_{ps}(\not P) = g_R^2\Big[\not P\left(\frac{\alpha^2-1}{2\alpha^2}\right) - M_p\left(\frac{\alpha-1}{\alpha}\right)\Big]\,\ln\Big[1-\alpha\Big] \;\;;\;\; \alpha \equiv \frac{P^2}{M_p^2} + i\widetilde{\epsilon} \;\;;\;\; g_R^2 = Z_{ps}\,\frac{g^2}{(4\pi)^2}\,. \tag{7.2.29}$$

In this case, we now find that near the mass shell at $\not P \simeq M_p$ the propagator is

$$S_{ps}(\not P) = \frac{i\, Z_{ps}\left(\not P + M_p\right)}{\left(P^2 - M_p^2\right)\left[1 - g_R^2\,\frac{(P^2-M_p^2)}{M_p^2}\,\ln\left[\frac{M_p^2-P^2-i\widetilde{\epsilon}}{M_p^2}\right]\right]}\,. \tag{7.2.30}$$

The logarithm associated with the two-particle cut yields a contribution to the self-energy of the form

$$\Sigma_{cut}(P^2) \propto \frac{(P^2-M_p^2)^2}{M_p^2}\,\ln\Big[\frac{M_p^2-P^2-i\widetilde{\epsilon}}{M_p^2}\Big]\,, \tag{7.2.31}$$

yielding

$$\mathrm{Im}\Sigma_{cut}(P^2) \propto \frac{(P^2-M_p^2)^2}{M_p^2}\Theta(P^2-M_p^2)\,, \tag{7.2.32}$$

therefore the pseudoscalar axion coupling does not lead to infrared divergences.

b:) This is a non-renormalizable coupling, with g featuring mass dimension (-1) in 4-space-time dimensions. The one loop self energy is given by $(D = 4-\varepsilon)$

$$\Sigma(\not P) = -ig^2\int\frac{d^Dk}{(2\pi)^D}\frac{\not k\gamma^5(\not P+\not k+M)\not k\gamma^5}{k^2((k+P)^2-M^2)} \tag{7.2.33}$$

$$= -ig^2\int\frac{d^Dk}{(2\pi)^D}\frac{k^2\not k - Mk^2 + 2\not k k\cdot P - k^2\not P}{k^2((k+P)^2-M^2)}. \tag{7.2.34}$$

which can be written as

$$\Sigma(\not P) = \not P\,\Sigma_V(P^2) + M\,\Sigma_S(P^2)\,. \tag{7.2.35}$$

with

$$\Sigma_V(P^2) = g^2 \frac{(P^2+M^2)A_0 - (P^2-M^2)^2 B_0(P^2)}{32\pi^2 P^2} \tag{7.2.36}$$

$$\Sigma_S(P^2) = g^2 \frac{A_0}{16\pi^2} \tag{7.2.37}$$

and

$$A_0 = M^2\big[1+L\big] \quad ; \quad B_0(P^2) = 2 + L + \frac{M^2-P^2}{p^2}\ln\Big[\frac{M^2-P^2-i\epsilon}{M^2}\Big], \tag{7.2.38}$$

where L is given by eqn. (7.2.20). Although the divergence proportional to $\not{P}$ cannot be renormalized, it is clear however, that near the mass-shell $P^2 \simeq M_p^2$ the logarithm describing the two particle cut yields a term of the form

$$\Sigma_{cut}(\not{P} \simeq M_p) \propto (P^2-M_p^2)^3 \ln\Big[\frac{M_p^2-P^2-i\epsilon}{M_p^2}\Big], \tag{7.2.39}$$

yielding

$$\mathrm{Im}\Sigma_{cut}(\not{P} \simeq M_p) \propto (P^2-M_p^2)^3\Theta(P^2-M_p^2), \tag{7.2.40}$$

therefore, also in this case there is no infrared divergence at the position of the mass-shell. Perhaps in this case this is an expected consequence of the derivative coupling, which brings two extra powers of momenta in the loop that relieves the infrared divergence.

We conclude that in both cases, either in the pseudoscalar or pseudovector axion coupling, there is no infrared divergence associated with the beginning of the multiparticle cut, at least up to one-loop order studied here.

7.3 Dynamical resummation method (DRM):

We now introduce a method that implements a dynamical resummation directly in time[105] that is intimately related to the dynamical renormalization group[124, 204, 102]. We first describe the resummation method in generality, relate it to the dynamical renormalization group, and apply the results to the cases studied in the previous section.

Consider a system whose Hamiltonian $H = H_0 + H_I$ with H_I a perturbation. The time evolution of states in the interaction picture of H_0 is given by

$$i\frac{d}{dt}|\Psi_I(t)\rangle = H_I(t)\,|\Psi_I(t)\rangle\,, \tag{7.3.1}$$

where the interaction Hamiltonian in the interaction picture is

$$H_I(t) = e^{iH_0\,t} H_I e^{-iH_0\,t} \tag{7.3.2}$$

This has the formal solution

$$|\Psi_I(t)\rangle = U(t,t_0)|\Psi_I(t_0)\rangle \tag{7.3.3}$$

where the time evolution operator in the interaction picture $U(t,t_0)$ obeys

$$i\frac{d}{dt}U(t,t_0) = H_I(t)U(t,t_0)\,. \tag{7.3.4}$$

Now we can expand

$$|\Psi_I(t)\rangle = \sum_n C_n(t)|n\rangle\,, \tag{7.3.5}$$

where $|n\rangle$ are eigenstates of the unperturbed Hamiltonian, $H_0\,|n\rangle = E_n\,|n\rangle$, and form a complete set of orthonormal states. In the quantum field theory case these are many-particle Fock states. From eq.(7.3.1) one finds the *exact* equation of motion for the coefficients $C_n(t)$, namely

$$\dot{C}_n(t) = -i\sum_m C_m(t)\langle n|H_I(t)|m\rangle\,. \tag{7.3.6}$$

Although this equation is exact, it generates an infinite hierarchy of simultaneous equations when the Hilbert space of states spanned by $\{|n\rangle\}$ is infinite dimensional. However,

this hierarchy can be truncated by considering the transition between states connected by the interaction Hamiltonian at a given order in H_I. Thus consider the situation depicted in figure 34 where one state, $|A\rangle$, couples to a set of states $\{|\kappa\rangle\}$, which couple back to $|A\rangle$ via H_I.

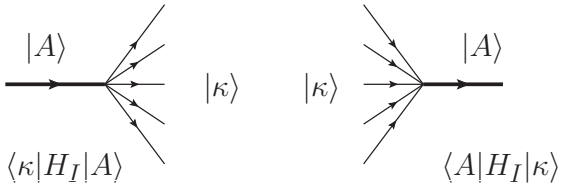

Figure 34: Transitions $|A\rangle \leftrightarrow |\kappa\rangle$ in first order in H_I. Figure taken from [307].

Under these circumstances, we have

$$\dot{C}_A(t) = -i \sum_\kappa \langle A|H_I(t)|\kappa\rangle \, C_\kappa(t) \tag{7.3.7}$$

$$\dot{C}_\kappa(t) = -i \, C_A(t) \langle\kappa|H_I(t)|A\rangle \tag{7.3.8}$$

where the sum over κ is over all the intermediate states coupled to $|A\rangle$ via H_I.

Consider the initial value problem in which at time $t_0 = 0$ the state of the system $|\Psi(t=0)\rangle = |A\rangle$ i.e.

$$C_A(0) = 1, \; C_\kappa(0) = 0. \tag{7.3.9}$$

We can solve eq.(7.3.8) and then use the solution in eq.(7.3.7) to find

$$C_\kappa(t) = -i \int_0^t \langle\kappa|H_I(t')|A\rangle \, C_A(t') \, dt' \tag{7.3.10}$$

$$\dot{C}_A(t) = -\int_0^t \Sigma(t,t') \, C_A(t') \, dt' \tag{7.3.11}$$

where

$$\Sigma(t,t') = \sum_\kappa \langle A|H_I(t)|\kappa\rangle\langle\kappa|H_I(t')|A\rangle = \sum_\kappa e^{i(E_A - E_\kappa)(t-t')} \, |\, \langle A|\, H_I(0)\, |\kappa\rangle \,|^2 \tag{7.3.12}$$

where we used (7.3.2). It is convenient to write $\Sigma(t,t')$ in a spectral representation, namely

$$\Sigma(t,t') = \int_{-\infty}^{\infty} \rho(p_0) \, e^{-i(p_0 - E_A)(t-t')} \, dp_0 \, , \tag{7.3.13}$$

where we have introduced the spectral density

$$\rho(p_0) = \sum_\kappa \, |\, \langle A|\, H_I(0)\, |\kappa\rangle\, |^2\, \delta(p_0 - E_\kappa)\,. \tag{7.3.14}$$

The integro-differential equation with *memory* (7.3.11) yields a non-perturbative solution for the time evolution of the amplitudes and probabilities. Inserting the solution for $C_A(t)$ into eq.(7.3.10) one obtains the time evolution of amplitudes $C_\kappa(t)$ from which we can compute the time dependent probability to populate the state $|\kappa\rangle$, namely $|C_\kappa(t)|^2$.

The hermiticity of the interaction Hamiltonian H_I, and the equations (7.3.7,7.3.8) yield

$$\frac{d}{dt}\Big[|C_A(t)|^2 + \sum_\kappa |C_\kappa(t)|^2\Big] = 0 \tag{7.3.15}$$

which together with the initial conditions in eqs.(7.3.9) yields the unitarity relation

$$|C_A(t)|^2 + \sum_\kappa |C_\kappa(t)|^2 = 1\,, \tag{7.3.16}$$

which is the statement that the time evolution operator $U(t,0)$ is unitary, namely

$$\begin{aligned} \langle \Psi_I(t)|\Psi_I(t)\rangle &= |C_A(t)|^2 + \sum_\kappa |C_\kappa(t)|^2 \\ &= \langle \Psi(0) U^\dagger(t,0) U(t,0)\Psi(0)\rangle = \langle \Psi(0)|\Psi(0)\rangle = |C_A(0)|^2 = 1\,. \end{aligned} \tag{7.3.17}$$

In general it is quite difficult to solve eq.(7.3.11) exactly, so that an approximation scheme must be invoked.

The time evolution of $C_A(t)$ determined by eq.(7.3.11) is *slow* in the sense that the time scale is determined by a weak coupling kernel Σ which is second order in the coupling. This allows us to use an approximation in terms of a consistent expansion in time derivatives of C_A. Define

$$W_0(t,t') = \int_0^{t'} \Sigma(t,t'')dt'' \tag{7.3.18}$$

so that

$$\Sigma(t,t') = \frac{d}{dt'} W_0(t,t'), \quad W_0(t,0) = 0. \tag{7.3.19}$$

Integrating by parts in eq.(7.3.11) we obtain

$$\int_0^t \Sigma(t,t')\, C_A(t')\, dt' = W_0(t,t)\, C_A(t) - \int_0^t W_0(t,t')\, \frac{d}{dt'} C_A(t')\, dt'. \tag{7.3.20}$$

The second term on the right hand side is formally of *fourth order* in H_I suggesting how a systematic approximation scheme can be developed. Setting

$$W_1(t,t') = \int_0^{t'} W_0(t,t'')dt'', \Rightarrow \frac{d}{dt'}W_1(t,t') = W_0(t,t'); \quad W_1(t,0) = 0 \tag{7.3.21}$$

and integrating by parts again, we find

$$\int_0^t W_0(t,t')\,\frac{d}{dt'}C_A(t')\,dt' = W_1(t,t)\,\dot{C}_A(t) + \cdots \tag{7.3.22}$$

leading to

$$\int_0^t \Sigma(t,t')\,C_A(t')\,dt' = W_0(t,t)\,C_A(t) - W_1(t,t)\,\dot{C}_A(t) + \cdots \tag{7.3.23}$$

This process can be implemented systematically resulting in higher order differential equations. Since $W_1 \simeq H_I^2\,;\,\dot{C}_A \simeq H_I^2$ the second term in (7.3.23) is $\simeq H_I^4$. We consistently neglect this term because to this order the states $|\kappa\rangle$ may also have non-vanishing matrix elements with states $|\kappa'\rangle$ other than $|A\rangle$ and the hierarchy would have to include these other states, therefore yielding contributions of $\mathcal{O}(H_I^4)$. Hence up to leading order $\simeq H_I^2$ the equation eq.(7.3.11) becomes

$$\dot{C}_A(t) = -W_0(t,t)C_A(t) \tag{7.3.24}$$

where

$$W_0(t,t) = \int_{-\infty}^{\infty} \rho(p_0)\left[\frac{1-e^{-i(p_0-E_A)t}}{i(p_0-E_A)}\right] dp_0\,, \tag{7.3.25}$$

yielding

$$C_A(t) = e^{-it\,\delta E(t)}\,e^{-\frac{\gamma(t)}{2}}\,, \tag{7.3.26}$$

where we used that $C_A(0) = 1$, with

$$\delta E(t) = \int_{-\infty}^{\infty} \frac{\rho(p_0)}{(E_A-p_0)}\left[1 - \frac{\sin\Big((E_A-p_0)t\Big)}{(E_A-p_0))t}\right] dp_0\,, \tag{7.3.27}$$

and

$$\gamma(t) = 2\int_{-\infty}^{\infty} \rho(p_0)\frac{\Big[1-\cos\Big((E_A-p_0)t\Big)\Big]}{\big(E_A-p_0\big)^2}\,dp_0\,. \tag{7.3.28}$$

The survival probatility of the initial state is given by

$$|\langle A|\Psi(t)\rangle|^2 = |C_A(t)|^2 = e^{-\gamma(t)}\,. \tag{7.3.29}$$

In the long time limit

$$\delta E(t) \underset{t\longrightarrow\infty}{\longrightarrow} \delta E_\infty = \int_{-\infty}^{\infty} \mathcal{P}\,\frac{\rho(p_0)}{(E_A - p_0)}\,dp_0\,, \tag{7.3.30}$$

where $\mathcal{P}$ stands for the principal part, yielding a renormalization of the bare frequency of the state A, namely $E_A + \delta E_\infty = E_{AR}$, whereas the long time limit of $\gamma(t)$ yields the decay law of the initial state.

The spectral density is only non-vanishing for $p_0 \geq E_T$ where E_T is the beginning of the multiparticle threshold. The long time limit of (7.3.28) is dominated by the region of the spectral density $p_0 \simeq E_A$, therefore it depends on whether $E_A < E_T$ or $E_A \geq E_T$.

i) $E_A < E_T$**:** in this case the oscillatory function averages out in the long time limit since the region $p_0 \simeq E_A$ is not within the region of support of the spectral density, therefore

$$\gamma(t) \underset{t\longrightarrow\infty}{\longrightarrow} z_A = 2\int_{E_T}^{\infty} \frac{\rho(p_0)}{(E_A - p_0)^2}\,dp_0\,, \tag{7.3.31}$$

yielding

$$|C_A(t)|^2 \underset{t\longrightarrow\infty}{\longrightarrow} \mathcal{Z}_A = e^{-z_A}\,, \tag{7.3.32}$$

where $\mathcal{Z}_A$ is the wave function renormalization. Since $\rho(p_0) \geq 0$ (see eqn. (7.3.14)) $z_A > 0$ and $\mathcal{Z}_A < 1$ consistently with the unitarity condition (7.3.16). This case describes a stable particle, with its mass shell described by an isolated pole below the multiparticle threshold.

ii) $E_A > E_T$**:** in this case, $\rho(E_A) \neq 0$, and the long time limit is dominated by the neighborhood of E_A, subtracting $\rho(E_A)$ from the spectral density, we find in the long time limit

$$\gamma(t) \underset{t\longrightarrow\infty}{\longrightarrow} \Gamma_A\, t + z_A + \mathcal{O}(1/t) + \cdots\,, \tag{7.3.33}$$

where

$$\Gamma_A = 2\pi\rho(E_A) \;\;;\;\; z_A = 2\int_{-\infty}^{\infty} \mathcal{P}\,\frac{\rho(p_0)}{(E_A - p_0)^2}\,dp_0\,, \tag{7.3.34}$$

yielding

$$|C_A(t)|^2 \underset{t\longrightarrow\infty}{\longrightarrow} \mathcal{Z}_A\, e^{-\Gamma_A t} \;\;;\;\; \mathcal{Z}_A = e^{-z_A}\,. \tag{7.3.35}$$

Therefore this case describes an unstable, decaying state, namely a resonance.

iii) $E_A = E_T$**:** in this case the multiparticle threshold coincides with the position of the mass and the spectral density vanishes at $p_0 = E_A$. The long time dynamics is now determined by how the spectral density vanishes at threshold. In the case that the spectral density vanishes *linearly* at threshold, the p_0 integral in $\gamma(t)$ (eqn. (7.3.28)) features a logarithmic divergence at long time. This is the case for the super-renormalizable and renormalizable cases (eqns. (7.2.11,7.2.25) respectively) studied in the previous section, where the discontinuity of the propagator across the two-particle cut vanishes linearly at threshold in the variably $p_0 - E_P$, namely

$$\rho(p_0) \underset{p_0 \longrightarrow E_A}{\longrightarrow} \Delta(p_0 - E_A) \;\; ; \;\; \Delta = \Big[d\rho(p_0)/dp_0 \Big]_{p_0 = E_A} . \tag{7.3.36}$$

To understand this case more clearly, and to extract the infrared divergence, it proves convenient to change variables to $(p_0 - E_A) = s\, E_A$ with $\rho(p_0) \equiv \overline{\rho}(s)$ and $\tau = E_A\, t$, yielding

$$\begin{aligned} \gamma(t) &= \frac{2}{E_A} \int_0^\infty \overline{\rho}(s)\, \frac{1 - \cos(s\tau)}{s^2}\, ds \\ &= \frac{2}{E_A} \int_0^1 \overline{\rho}(s)\, \frac{1 - \cos(s\tau)}{s^2}\, ds + \frac{2}{E_A} \int_1^\infty \overline{\rho}(s)\, \frac{1 - \cos(s\tau)}{s^2}\, ds \, . \end{aligned} \tag{7.3.37}$$

The first integral features an infrared divergence, whereas the second is infrared finite and the cosine term averages out in the long time limit. With the threshold behavior (7.3.36), let us write for the first integral

$$\overline{\rho}(s) = \Delta\, E_A\, s + \widetilde{\rho}(s) \;\; ; \;\; \widetilde{\rho}(s) \underset{s \longrightarrow 0}{\longrightarrow} \propto s^n \;\; ; \;\; n \geq 2 \, , \tag{7.3.38}$$

leading to

$$\gamma(t) = 2\, \Delta \int_0^1 \frac{1 - \cos(s\tau)}{s}\, ds + \mathcal{F}(\tau) \underset{t \longrightarrow \infty}{\longrightarrow} 2\Delta\, \ln \big[E_A\, t \big] + z_A \, , \tag{7.3.39}$$

where the remaining function $\mathcal{F}(\tau) \underset{\tau \longrightarrow \infty}{\longrightarrow} \mathcal{F}_\infty$ a time-independent asymptotic long time limit. This case leads to the relaxation of the amplitude with an *anomalous dimension*, namely

$$|C_A(t)|^2 \underset{t \longrightarrow \infty}{\longrightarrow} \Big[E_A t \Big]^{-2\Delta}\, \mathcal{Z}_A \;\; ; \;\; \mathcal{Z}_A = e^{-z_A} \, , \tag{7.3.40}$$

in agreement with the results (7.2.15,7.2.27) obtained by the inverse Fourier transform of a *renormalization group improved* propagator. Therefore this dynamical resummation method

provides a real time implementation of the renormalization group. The wave function renormalization constant $\mathcal{Z}_A$ is infrared finite, however it is ultraviolet divergent in a renormalizable (or non-renormalizable) theory.

If $\Delta = 0$ and the spectral density vanishes faster than linear near threshold it follows from the above result that $\gamma(t) \to z_A$ in the long time limit.

7.3.1 Equivalence with the dynamical renormalization group

In the interaction picture, the time evolution of a state is given by

$$|\psi(t)\rangle = U(t,t_0)\,|\psi(t_0)\rangle\,, \tag{7.3.41}$$

where

$$U(t,t_0) = 1 - i\int_{t_0}^{t} H_I(t')\,dt' - \int_{t_0}^{t}\int_{t_0}^{t'} H_I(t')\,H_I(t'')\,dt'\,dt'' + \mathcal{O}(H_I^3) \quad , \quad U(t_0,t_0) = 1\,. \tag{7.3.42}$$

If at $t_0 = 0$ the initial state is $|\psi(t_0)\rangle = C_A(0)\,|A\rangle$ the survival amplitude at time t is given by

$$C_A(t) = C_A(0)\langle A|U(t,0)\,|A\rangle = C_A(0)\Bigg[1 - i\,t\,\langle A|H_I(0)|A\rangle - \int_0^t\int_0^{t'}\sum_\kappa |\langle A|H_I(0)|\kappa\rangle|^2\, e^{i(E_A-E_\kappa)(t'-t'')}\,dt'\,dt'' + \mathcal{O}(H_I^3)\Bigg]\,, \tag{7.3.43}$$

where we have introduced $\sum_\kappa |\kappa\rangle\,\langle\kappa| = 1$ in the second order term, and introduced the initial amplitude $C_A(0)$ to clarify the nature of the dynamical renormalization group. We will be mainly concerned with the examples discussed in the previous sections, for which $\langle A|\,H_I(0)\,|A\rangle = 0$. In terms of the spectral density (7.3.14) we find

$$C_A(t) = C_A(0)\Big\{1 + \mathcal{S}_A^{(2)}(t) + \mathcal{O}(H_I^3)\Big\}\,, \tag{7.3.44}$$

where

$$\mathcal{S}_A^{(2)}(t) = -i\,t\,\delta E(t) - \frac{1}{2}\,\gamma(t)\,, \tag{7.3.45}$$

where the superscript in $\mathcal{S}$ refers to the order in perturbation theory and $\delta E(t); \gamma(t)$ are given by eqns. (7.3.27,7.3.28) respectively. From the results (7.3.30,7.3.33,7.3.39) it follows that

$\mathcal{S}_A^{(2)}(t)$ features *secular growth in time*, namely it grows in time invalidating the reliability of the perturbative expansion at long time. The dynamical renormalization group[124, 204, 102] provides a resummation framework that improves the convergence at long time. It begins by evolving in time up to a time τ long enough to establish the secular growth, but short enough so that perturbation theory is still reliable and absorbing the time evolution into a renormalization of the amplitude. This program is implemented as follows, writing

$$C_A(0) = C_A(\tau)\, R_A(\tau) \quad , \quad R_A(\tau) = 1 + r_A^{(2)}(\tau) + \mathcal{O}(H_I^3)\,, \tag{7.3.46}$$

where $r_A^{(2)}(\tau) \simeq \mathcal{O}(H_I^2)$, etc. Up to second order in the interaction we obtain

$$C_A(t) = C_A(\tau)\Big[1 + \big(r_A^{(2)}(\tau) + \mathcal{S}_A^{(2)}(t)\big) + \cdots\Big]\,, \tag{7.3.47}$$

the counterterm $r_A^{(2)}(\tau)$ is chosen to cancel $\mathcal{S}_A^{(2)}(t)$ at the renormalization time scale $t = \tau$, namely

$$r_A^{(2)}(\tau) = -\mathcal{S}_A^{(2)}(\tau)\,. \tag{7.3.48}$$

The time dependent amplitude $C_A(t)$ *does not* depend on the arbitrary renormalization scale τ, hence

$$\frac{d}{d\tau} C_A(t) = 0\,, \tag{7.3.49}$$

this is the dynamical renormalization group equation. Consistently keeping up to terms of $\mathcal{O}(H_I^2)$ this equation leads to

$$\frac{\dot{C}_A(\tau)}{C_A(\tau)} = -\dot{r}_A^{(2)}(\tau) + \mathcal{O}(H_I^4) + \cdots \tag{7.3.50}$$

where the dots stand for $d/d\tau$. Using the renormalization condition (7.3.48) the solution is given by

$$C_A(\tau) = C_A(\tau_0)\; e^{\left(\mathcal{S}_A^{(2)}(\tau) - \mathcal{S}_A^{(2)}(\tau_0)\right)}\,, \tag{7.3.51}$$

now we can choose $\tau = t$; $\tau_0 = 0$ and $C_A(0) = 1$ with the result

$$C_A(t) = e^{-it\,\delta E(t)}\, e^{-\frac{\gamma(t)}{2}}\,, \tag{7.3.52}$$

which is precisely the result given by eqn. (7.3.26). This solution provides a resummation of the perturbative series up to second order in the coupling. In the case in which the mass

shell is embedded in the particle continuum, the long time behavior of the amplitude is $C_A(t) = \mathcal{Z}_A\, e^{-i\Delta E_\infty t}\, e^{-\Gamma t/2}$ yielding the usual exponential decay law in agreement with eqn. (7.3.35). Therefore, the dynamical resummation method described in the previous section is equivalent to the dynamical renormalization group resummation of secular terms. However, a bonus of the dynamical resummation method is that it also yields the coefficients $C_\kappa(t)$ given by eqn. (7.3.8), and a direct connection with unitarity (see eqn. (7.3.16)).

Armed with these general results, we now address the cases studied in the previous section.

7.3.2 Super-renormalizable case:

The interaction Hamiltonian in the interaction picture for the model described by eqn. (7.2.1) is

$$H_I(t) = \lambda \int d^3x\, \phi^\dagger(\vec{x},t)\, \phi(\vec{x},t)\, \chi(\vec{x},t)\,, \tag{7.3.53}$$

where the time evolution is that of free fields. In this case the state $|A\rangle = \left|1^\phi_{\vec{p}}\right\rangle$ i.e. a single particle state of the field ϕ and the states $|\kappa\rangle = \left|1^\phi_{\vec{k}}\,;\, 1^\chi_{\vec{q}}\right\rangle$, a two particle intermediate state. We quantize the fields in a volume V with a discrete momentum representation, eventually V is taken to infinity. The matrix element

$$\left\langle 1^\phi_{\vec{p}}\right| H_I(0) \left|1^\phi_{\vec{k}}\,;\, 1^\chi_{\vec{q}}\right\rangle = \frac{\lambda\, V\, \delta_{\vec{p},\vec{k}+\vec{q}}}{\left[2VE_p 2VE_k 2V\omega_q\right]^{1/2}}\,, \tag{7.3.54}$$

where $E_p = \sqrt{p^2+M^2}, \omega_q = |\vec{q}|$ are the energies of the ϕ,χ particle respectively, and the total energy of this intermediate state is $E_\kappa = E_k + \omega_q$. With $\sum_\kappa = \sum_{\vec{p}}\sum_{\vec{q}}$ the spectral density (7.3.14) is given by

$$\rho(p_0;p) = \frac{\lambda^2}{8E_p}\int \frac{d^3k}{(2\pi)^3}\,\frac{\delta(p_0 - E_k - |\vec{p}-\vec{k}|)}{E_k\,|\vec{p}-\vec{k}|}\,. \tag{7.3.55}$$

For $p_0 = E_p$ this is identified with the Lorentz invariant phase space for two body decay, which must vanish by kinematics because a massive particle cannot emit or absorb a massless particle on shell. Therefore the spectral density must vanish as $p_0 \longrightarrow E_p$.

We find

$$\rho(p_0;p) = \frac{\lambda^2}{32\,\pi^2\,E_p}\,(p_0 - E_p)\left(\frac{p_0+E_p}{p_0^2-p^2}\right)\Theta(p_0-E_p)\,, \tag{7.3.56}$$

vanishing linearly as $\Delta\,(p_0 - E_p)$ at threshold with $\Delta = (\lambda/4\pi M)^2$. Introducing the variables $s = (p_0 - E_p)/E_p$; $T = E_p\,t$; $R = M/E_p$ we find that the function $\gamma(t)$ in eqn. (7.3.28) can be written as

$$\gamma(t) = I_1(T) + I_2(T)\,, \tag{7.3.57}$$

with

$$I_1(T) = \Delta\,R^2\int_0^1 \left[\frac{2+s}{R^2+2s+s^2}\right]\left[\frac{1-\cos(s\,T)}{s}\right]ds \tag{7.3.58}$$

$$I_2(T) = \Delta\,R^2\int_1^\infty \left[\frac{2+s}{R^2+2s+s^2}\right]\left[\frac{1-\cos(s\,T)}{s}\right]ds\,. \tag{7.3.59}$$

The integral $I_1(T)$ features an infrared divergence at $s=0$, which can be isolated by subtracting the first bracket inside the integral in (7.3.58) at $s=0$, yielding

$$I_1(T) = 2\Delta\int_0^1\left[\frac{1-\cos(s\,T)}{s}\right]ds + \Delta\int_0^1\left[\frac{R^2-4-2s}{R^2+2s+s^2}\right](1-\cos(s\,T))\,ds\,. \tag{7.3.60}$$

In the long time limit the $\cos(sT)$ terms in I_2 and the second term in (7.3.60) average out, yielding

$$\gamma(t) \underset{t\longrightarrow\infty}{\longrightarrow} 2\,\Delta\,\ln\big[E_p t\big] + z_\phi\,, \tag{7.3.61}$$

where

$$z_\phi = \Delta\left\{2\gamma_E + \int_0^1\left[\frac{R^2-4-2s}{R^2+2s+s^2}\right]ds + R^2\int_1^\infty\left[\frac{2+s}{R^2+2s+s^2}\right]\frac{ds}{s}\right\}, \tag{7.3.62}$$

with γ_E the Euler-Mascheroni constant. Therefore the long time behavior of the survival probability is given by

$$|C_\phi(t)|^2 = \Big[E_p\,t\Big]^{-2\Delta}\,\mathcal{Z}_\phi \quad ; \quad \mathcal{Z}_\phi = e^{-z_\phi}\,, \tag{7.3.63}$$

displaying the power law decay of the probability with anomalous dimension $2\,\Delta$ in complete agreement with the result from the renormalization group improved propagator eqn. (7.2.16). We note that the wave function renormalization $\mathcal{Z}_\phi$ is infrared finite and also ultraviolet finite as befits a super renormalizable theory.

7.3.3 Renormalizable case:

For the renormalizable case described by the Lagrangian density (7.2.17) the interaction Hamiltonian in the interaction picture of free fields is

$$H_I(t) = Y \int d^3x \overline{\Psi}(\vec{x},t)\Phi(\vec{x},t)\Psi(\vec{x},t)\,, \tag{7.3.64}$$

with the state $|A\rangle = \left|1^{\psi}_{\vec{p},\alpha}\right\rangle$ and the intermediate states $|\kappa\rangle = \left|1^{\psi}_{\vec{k},\beta};1^{\phi}_{\vec{q}}\right\rangle$. The matrix elements are given by

$$\left\langle 1^{\psi}_{\vec{k},\beta};1^{\phi}_{\vec{q}}\right| H_I(0) \left|1^{\psi}_{\vec{p},\alpha}\right\rangle \;=\; V\,Y\delta_{\vec{p},\vec{k}+\vec{q}}\;\frac{\overline{\mathcal{U}}_{\vec{k},\beta,a}\mathcal{U}_{\vec{p},\alpha,a}}{\left[2VE_p 2VE_k 2V|\vec{q}|\right]^{1/2}} \tag{7.3.65}$$

$$\left\langle 1^{\psi}_{\vec{p},\alpha}\right| H_I(0) \left|1^{\psi}_{\vec{k},\beta};1^{\phi}_{\vec{q}}\right\rangle \;=\; V\,Y\delta_{\vec{p},\vec{k}+\vec{q}}\;\frac{\overline{\mathcal{U}}_{\vec{p},\alpha,b}\mathcal{U}_{\vec{k},\beta,b}}{\left[2VE_p 2VE_k 2V|\vec{q}|\right]^{1/2}}\,. \tag{7.3.66}$$

With $\sum_\kappa = \sum_{\vec{k}}\sum_{\vec{q}}\sum_\beta$ and averaging over the initial polarizations α, the spectral density (7.3.14) becomes

$$\rho(p_0;p) = \frac{Y^2}{4E_p}\int \frac{d^3k}{(2\pi)^3}\,\frac{\delta(p_0 - E_k - |\vec{p}-\vec{k}|)}{E_k\,|\vec{p}-\vec{k}|}\left[k\cdot p + M^2\right], \tag{7.3.67}$$

which is found to be

$$\rho(p_0;p) = \frac{Y^2}{32\pi^2 E_p}\,(p_0 - E_p)\left[\frac{p_0+E_p}{p_0^2-p^2}\right]\left\{p_0\left[\frac{E_p-p_0}{p_0^2-p^2}\right](p_0^2-p^2+M^2)+p_0^2-p^2+3M^2\right\}\Theta(p_0-E_p)\,. \tag{7.3.68}$$

We note that for $p_0 \simeq E_P$, $\rho(p_0,p) \simeq \Delta(p_0 - E_p) + \cdots$ where $\Delta = Y^2/(4\pi^2)$ and the dots stand for terms that vanish as $(p_0 - E_p)^n$, $n \geq 2$ near threshold. To separate the infrared contribution, we change variables to $p_0 - E_p = sE_p$; $\rho(p_0) \equiv \overline{\rho}(s)$ and $T = E_p\,t$ and write

$$\overline{\rho}(s) = \Delta\,E_p\,s + \widetilde{\rho}(s) \;\;;\;\; \Delta = \frac{Y^2}{4\pi^2}\,, \tag{7.3.69}$$

with $\widetilde{\rho}(s) \underset{s\longrightarrow 0}{\longrightarrow} \propto s^n$; $n \geq 2$, yielding

$$\gamma(t) = J_1(T) + J_2(T) \tag{7.3.70}$$

with

$$J_1(T) = 2\,\Delta \int_0^1 \frac{1-\cos(sT)}{s}\,ds = 2\,\Delta\Big\{\,\ln[E_p t] + \gamma_E - Ci[E_p t]\Big\}\,, \tag{7.3.71}$$

$$J_2(T) = 2\int_0^1 \widetilde{\rho}(s)\,\frac{1-\cos(sT)}{s^2}\,ds + 2\int_1^\infty \overline{\rho}(s)\,\frac{1-\cos(sT)}{s^2}\,ds\,. \tag{7.3.72}$$

In $J_2(T)$ the cosine term averages out in the long time limit and this conribution approaches a time independent asymptotic value, which however is ultraviolet divergent because $\overline{\rho}(s) \simeq s$ as $s \to \infty$. Therefore in the long time limit we find

$$\gamma(t) \;\underset{t\longrightarrow\infty}{\longrightarrow}\; 2\Delta\,\ln\big[E_p\,t\big] + \widetilde{z}_\psi\,, \tag{7.3.73}$$

yielding the survival probability

$$|C_\psi(t)|^2 = \mathcal{Z}_\psi\,\big[E_p\,t\big]^{-2\,\Delta} \tag{7.3.74}$$

which agrees with the power law decay of the amplitude with anomalous dimension in eqn. (7.2.27). In this case the wave function renormalization $\mathcal{Z}_\psi$ is infrared finite but ultraviolet divergent since this is a renormalizable theory.

7.3.4 Axion couplings:

In the case of the pseudoscalar coupling $ig\bar{\Psi}\gamma^5\phi\Psi$ the matrix elements are given by

$$\Big\langle 1^\psi_{\vec{k},\beta}; 1^\phi_{\vec{q}}\Big|\,H_I(0)\,\Big|1^\psi_{\vec{p},\alpha}\Big\rangle \;=\; ig\,V\,\delta_{\vec{p},\vec{k}+\vec{q}}\;\frac{\overline{\mathcal{U}}_{\vec{k},\beta,a}\,\gamma^5\,\mathcal{U}_{\vec{p},\alpha,a}}{\Big[2VE_p 2VE_k 2V|\vec{q}|\Big]^{1/2}} \tag{7.3.75}$$

$$\Big\langle 1^\psi_{\vec{p},\alpha}\Big|\,H_I(0)\,\Big|1^\psi_{\vec{k},\beta}; 1^\phi_{\vec{q}}\Big\rangle \;=\; ig\,V\,\delta_{\vec{p},\vec{k}+\vec{q}}\;\frac{\overline{\mathcal{U}}_{\vec{p},\alpha,b}\,\gamma^5\,\mathcal{U}_{\vec{k},\beta,b}}{\Big[2VE_p 2VE_k 2V|\vec{q}|\Big]^{1/2}}\,. \tag{7.3.76}$$

With $\sum_\kappa = \sum_{\vec{k}}\sum_{\vec{q}}\sum_\beta$ and averaging over the initial polarizations α, the spectral density (7.3.14) now becomes

$$\rho(p_0;p) = \frac{g^2}{4E_p}\int\frac{d^3k}{(2\pi)^3}\,\frac{\delta(p_0 - E_k - |\vec{p}-\vec{k}|)}{E_k\,|\vec{p}-\vec{k}|}\,\big[k\cdot p - M^2\big]\,. \tag{7.3.77}$$

Following the same steps as in the scalar Yukawa coupling case we find

$$\rho(p_0;p) = \frac{g^2}{32\pi^2 E_p}\,(p_0 - E_p)^2\,\Big[\frac{p_0+E_p}{p_0^2-p^2}\Big]\Big\{p_0 + E_p - p_0\Big[\frac{p_0^2-p^2+M^2}{p_0^2-p^2}\Big]\Big\}\Theta(p_0-E_p)\,. \tag{7.3.78}$$

In this case the $(p_0 - E_p)^2$ completely cancels the denominator in $\gamma(t)$ eqn. (7.3.28) therefore there are no infrared singularities and the asymptotic long time limit $\gamma(t) \to z_\psi$ which, however, is ultraviolet divergent. The behavior $\propto (p_0 - E_P)^2$ near threshold is, as expected, in complete agreement with the result (7.2.32) of the self energy.

For the pseudovector coupling $g\partial_\mu\phi\bar{\Psi}\gamma^\mu\gamma^5\Psi$ we now find

$$\rho(p_0;p) = \frac{g^2}{4E_p}\int \frac{d^3k}{(2\pi)^3}\,\frac{\delta(p_0 - E_k - |\vec{p}-\vec{k}|)}{E_k\,|\vec{p}-\vec{k}|}\left[(k\cdot q)\,(p\cdot q)\right] \;\;;\;\; q^\mu = (|\vec{p}-\vec{k}|;\vec{p}-\vec{k})\,, \tag{7.3.79}$$

with the result

$$\rho(p_0,p) = \frac{g^2}{32\pi^2}\,(p_0 - E_p)^3\left[\frac{(p_0+E_p)^2}{p_0^2-p^2}\right]\left[1+\frac{M^2}{p_0^2-p^2}\right]\Theta(p_0-E_p)\,. \tag{7.3.80}$$

The behavior $\simeq (p_0 - E_p)^3$ near threshold is consistent with the results (7.2.39,7.2.40), and implies that in this case there is no infrared singularity, and furthermore $\gamma(t) \xrightarrow[t\to\infty]{} z_\psi$ with z_ψ being ultraviolet divergent. Therefore, we conclude that either pseudoscalar or pseudovector axion couplings do not yield infrared divergences.

Criterion for infrared divergences: The study of the previous sections allows us to provide a general criterion to determine which type of (non-gauge) interactions even from effective field theories yield infrared divergences at one loop level and which ones do not. The typical form of the spectral density at one loop level can be written as

$$\rho(p_0) \propto \int \frac{d^3k}{(2\pi)^3}\,\frac{\delta(p_0 - E_k - \omega_q)}{E_k\,\omega_q}\,\mathcal{F}[(k\cdot p);(k\cdot q);(q\cdot p)]\,, \tag{7.3.81}$$

where $\mathcal{F}$ is a Lorentz invariant function of the scalar products of the on-shell four vectors $p^\mu = (E_p,\vec{p})$; $k^\mu = (E_k,\vec{k})$; $q^\mu = (\omega_q;\vec{p}-\vec{k})$; $\omega_q = |\vec{p}-\vec{k}|$. The most general form of $\mathcal{F}[(k\cdot p);(k\cdot q);(q\cdot p)]$ is a combination of polynomials, namely

$$\mathcal{F}[(k\cdot p);(k\cdot q);(q\cdot p)] = \sum_{m.n,l} a_{mnl}\,(k\cdot p)^m\,(k\cdot q)^m\,(q\cdot p)^l \;\;;\;\; (m,n,l) = 0,1,2\cdots\,, \tag{7.3.82}$$

with a_{mnl} coefficients that depend on the particular effective field theory interaction. As it will become clear below, it suffices to consider only monomials in these products.

The angular integration in (7.3.81) is performed yielding

$$\rho(p_0) \propto \frac{1}{4\pi^2\,p}\int_{E_-}^{E_+} \mathcal{F}[(k\cdot p);(k\cdot q);(q\cdot p)]\big|_{\omega_q = p_0 - E_k}\,dE_k\,, \tag{7.3.83}$$

where

$$E_\pm = \frac{(p_0 \pm p)^2 + M^2}{2(p_0 \pm p)} \Rightarrow E_+ - E_- = (p_0 - E_p)\,\frac{p\,(p_0 + E_p)}{p_0^2 - p^2}\,. \tag{7.3.84}$$

The vanishing of the integral as $p_0 \to E_p$ reflects the vanishing of the phase space for on-shell emission of the massless quanta. As discussed above, the infrared divergence arises from the contribution to the spectral density that vanishes linearly at threshold. Since $E_+ - E_-$ vanishes linearly as $p_0 \to E_p$, only terms in $\mathcal{F}[(k\cdot p);(k\cdot q);(q\cdot p)]$ that remain finite in this limit yield infrared divergences. Therefore it is now a matter of analyzing the behavior of the various scalar products to reveal which contributions do yield infrared divergences. We find (using the delta function constraint in (7.3.83))

$$p\cdot k = \frac{1}{2}(p_0 - E_p)\big[p_0 + E_p - 2E_k\big] + M^2 \xrightarrow[p_0\to E_p]{} M^2 \quad \Rightarrow \quad \text{IR div} \tag{7.3.85}$$

$$p\cdot q = \frac{1}{2}(p_0 - E_p)\big[-p_0 + E_p + 2E_k\big] \xrightarrow[p_0\to E_p]{} \propto (p_0 - E_p) \quad \Rightarrow \quad \text{NO IR} \tag{7.3.86}$$

$$k\cdot q = \frac{1}{2}(p_0 - E_p)\big[p_0 + E_p\big] \xrightarrow[p_0\to E_p]{} \propto (p_0 - E_p) \quad \Rightarrow \quad \text{NO IR div}\,. \tag{7.3.87}$$

This analysis explains why the scalar Yukawa coupling with $\mathcal{F} = p\cdot k + M^2$ yields an infrared divergence whereas the pseudoscalar axion Yukawa coupling with $\mathcal{F} = p\cdot k - M^2$ does not. It also reveals that effective field theories with derivative couplings that necessarily yield $\mathcal{F} \propto p\cdot q$; $k\cdot q$ do not yield infrared divergences at one loop order. It is important to highlight that these arguments are only valid at one loop level in *non-gauge* theories, we were not able to extend them generically beyond this order in perturbation theory.

7.4 Unitarity and dressing cloud

In the cases in which the infrared divergences at threshold lead to the decay of the single particle amplitude with a power law with anomalous dimension, at long time this amplitude vanishes. Unitarity must be fulfilled by "populating" the intermediate states with amplitudes $C_\kappa(\infty)$ such that $\sum_\kappa |C_\kappa(\infty)|^2 = 1$. The fulfillment of unitarity when the amplitude of the initial state vanishes altogether, and the coefficients $|C_\kappa|^2$ being formally of $\mathcal{O}(\Delta)$ implies that the sum over the intermediate states must be proportional to $1/\Delta$. This integral must

be singular in the limit $\Delta \to 0$ bringing about a non-perturbative cancellation of the Δ from the coefficients. We now study how this result from unitarity emerges in the long time limit.

From eqn. (7.3.10) we find

$$C_\kappa(t) = -i \, \langle \kappa | \, H_I(0) \, | A \rangle \int_0^t e^{i\Omega t'} \, C_A(t') \, dt' \quad ; \quad \Omega = E_\kappa - E_A \, , \tag{7.4.1}$$

and

$$|C_\kappa(t)|^2 = | \, \langle A | \, H_I(0) \, | \kappa \rangle \, |^2 \int_0^t \int_0^t e^{i\Omega t_1} \, C_A(t_1) \, e^{-i\Omega t_2} \, C_A^*(t_2) \, dt_1 \, dt_2 \, . \tag{7.4.2}$$

Inside the integrals we replace the amplitudes $C_A(t)$ by eqn. (7.3.26). Since at early time the amplitude departs from $C_A(0) = 1$ by a perturbatively small amount, we will replace them by the long time limit (7.3.39)

$$C_A(t) = e^{-i\delta E_\infty \, t} \, e^{-\frac{\gamma(t)}{2}} \quad ; \quad \gamma(t) = 2\Delta \ln \big[E_A t\big] + z_A \, , \tag{7.4.3}$$

(see eqn. (7.3.40)) and absorb δE_∞ into a renormalization of E_A (mass renormalization). The integrand in the double time integral in (7.4.2) is now given by (E_A in Ω now stands for the renormalized energy)

$$J(t_1, t_2) = e^{i \, \Omega(t_1 - t_2)} \, e^{-\frac{1}{2}(\gamma(t_1) + \gamma(t_2))} \, , \tag{7.4.4}$$

writing the double time integral in (7.4.2) as

$$\int_0^t \int_0^t J(t_1, t_2) \, \Big(\Theta(t_1 - t_2) + \Theta(t_2 - t_1) \Big) \, dt_1 \, dt_2 = 2 \int_0^t dt_1 e^{-\frac{\gamma(t_1)}{2}} \int_0^{t_1} \cos[\Omega(t_1 - t_2)] \, e^{-\frac{\gamma(t_2)}{2}} \, dt_2 \, , \tag{7.4.5}$$

where in the term with $\Theta(t_2 - t_1)$ on the left hand side of (7.4.5) we relabelled $t_1 \leftrightarrow t_2$ and used that $J(t_2, t_1) = J^*(t_1, t_2)$ with $\gamma(t)$ being real. Now writing

$$\cos[\Omega(t_1 - t_2)] = \frac{d}{dt_2} G[t_1; t_2] \quad ; \quad G[t_1; t_2] = \int_0^{t_2} \cos[\Omega(t_1 - t')] \, dt' \quad ; \quad G[t_1; 0] = 0 \, , \tag{7.4.6}$$

in the t_2 integral in (7.4.5), integrating by parts using (7.4.6) and neglecting the term proportional to the time derivative of $\gamma(t_2)$ because it is of $\mathcal{O}(H_I^2)$, hence consistently neglecting terms of $\mathcal{O}(H_I^4)$ in (7.4.2) we find that the double integral in (7.4.2) becomes

$$\int_0^t \int_0^t e^{-i\Omega t_1} \, C_A(t_1) \, e^{i\Omega t_2} \, C_A^*(t_2) \, dt_1 \, dt_2 = \frac{2 \, \mathcal{Z}_A}{\Omega} \int_0^t \sin \big[\Omega \, t_1\big] \, \big[E_A t_1\big]^{-2\Delta} \, dt_1 \, . \tag{7.4.7}$$

In the limit $t \to \infty$ in (7.4.7) we can rescale $\Omega t_1 \equiv u$ and using a representation of the gamma function we find

$$|C_\kappa(\infty)|^2 = 2\,\mathcal{Z}_A \left[\frac{|\langle A|\, H_I(0)\,|\kappa\rangle\,|^2}{(E_\kappa - E_A)^2}\right]\left[\frac{E_\kappa - E_A}{E_A}\right]^{2\Delta}\Gamma[1-2\Delta]\,\sin\left[\frac{\pi}{2}(1-2\Delta)\right]. \tag{7.4.8}$$

In terms of the spectral density (7.3.14) and introducing $\overline{Z}_A = \mathcal{Z}_A\,\Gamma[1-2\Delta]\,\sin\left[\frac{\pi}{2}(1-2\Delta)\right]$ we obtain

$$\sum_\kappa |C_\kappa(\infty)|^2 = 2\,\overline{Z}_A \int_{-\infty}^{\infty} \frac{\rho(p_0)}{(p_0 - E_A)^2}\left[\frac{p_0 - E_A}{E_A}\right]^{2\Delta} dp_0\,, \tag{7.4.9}$$

This is the general result for the cases with infrared divergences at threshold. We now apply this result to the super renormalizable case as an example, of which the renormalizable case is a simple extension. In this case (see section (7.3.2)) the state $|A\rangle = \left|1^\phi_{\vec{p}}\right\rangle$ and the states $|\kappa\rangle = \left|1^\phi_{\vec{k}}\,;\,1^\chi_{\vec{q}}\right\rangle$ with energy $E_\kappa = E_k + \omega_q$; $\vec{q} = \vec{p} - \vec{k}$ and $\rho(p_0)$ is given by eqn. (7.3.56) and $\Delta = (\lambda/4\pi M)^2$. In terms of $s = (p_0 - E_p)/E_p$; $R = M/E_p$ we find

$$\sum_\kappa |C_\kappa(\infty)|^2 = \Delta\,R^2\,\overline{Z}_\phi \int_0^\infty \left[\frac{2+s}{R^2+2s+s^2}\right] s^{2\Delta-1}\,ds\,, \tag{7.4.10}$$

notice that naively setting $\Delta = 0$ in $s^{2\Delta-1}$ in the integrand in (7.4.10) leads to an infrared divergence. It is precisely this anomalous dimension that renders the integral finite and $\propto 1/\Delta$ thereby cancelling the Δ in the prefactor. This is seen as follows: writing $\int_0^\infty \cdots ds = \int_0^1 \cdots ds + \int_1^\infty \cdots ds$ and in the first integral replace

$$\left[\frac{2+s}{R^2+2s+s^2}\right] = \frac{2}{R^2} + \frac{s}{R^2}\left[\frac{R^2-4-2s}{R^2+2s+s^2}\right], \tag{7.4.11}$$

the first term on the right hand side of (7.4.11) when input in the first integral ($\int_0^1 \cdots ds$) yields $1/(R^2\Delta)$, finally yielding

$$\sum_\kappa |C_\kappa(\infty)|^2 = \overline{Z}_\phi\left[1 + \Delta\,\mathcal{I}[R;\Delta]\right], \tag{7.4.12}$$

where

$$\mathcal{I}[R;\Delta] = \int_0^1 \left[\frac{R^2-4-2s}{R^2+2s+s^2}\right] s^{2\Delta}\,ds + R^2\int_1^\infty \left[\frac{2+s}{R^2+2s+s^2}\right] s^{2\Delta-1} ds\,. \tag{7.4.13}$$

With $\Gamma[1-2\Delta]\,\sin\left[\frac{\pi}{2}(1-2\Delta)\right] = 1 + 2\Delta\,\gamma_E + \mathcal{O}(\Delta^2)$ and from eqn. (7.3.62,7.3.63) $\mathcal{Z}_\phi = 1 - 2\Delta\gamma_E - \Delta\,\mathcal{I}[R;0] + \mathcal{O}(\Delta^2)$ it follows that $\overline{Z}_\phi = 1 - \Delta\,\mathcal{I}[R;0] + \mathcal{O}(\Delta^2)$. Since $\mathcal{I}[R;\Delta]$ is infrared finite, to lowest order we can replace $\mathcal{I}[R;\Delta] \simeq \mathcal{I}[R;0] + \mathcal{O}(\Delta)$ inside the bracket in eqn. (7.4.12), hence, neglecting consistently terms of $\mathcal{O}(\Delta^2) \simeq H_I^4$ and higher, we find

$$\sum_\kappa |C_\kappa(\infty)|^2 = 1 + \mathcal{O}(\Delta^2 \simeq H_I^4)\,. \tag{7.4.14}$$

therefore unitarity is fulfilled consistently up order $\mathcal{O}(H_I^4)$ that we have considered. It now becomes clear that the non-perturbative dynamical renormalization group resummation yielding the anomalous dimension is precisely the mechanism by which unitarity is fulfilled. The extension to the renormalizable case with scalar Yukawa coupling is straightforward with a similar result up to order $\mathcal{O}(H_I^4)$ that we considered.

No infrared divergences: In the cases where there are no infrared divergences, such as that of axion like particle couplings, the asymptotic long time dynamics follows from eqn. (7.4.3) with $\Delta = 0$, namely

$$C_A(t) = \mathcal{Z}_A^{1/2}\, e^{-i\delta E_\infty\, t} \quad ; \quad \mathcal{Z}_A = e^{-z_A}\,, \tag{7.4.15}$$

with (see eqns. (7.3.31,7.3.32))

$$z_A = 2\int_{-\infty}^{\infty} \frac{\rho(p_0)}{(E_A - p_0)^2}\, dp_0\,. \tag{7.4.16}$$

Inserting these expressions into eqn. (7.4.2), absorbing the phase ΔE_∞ into a renormalization of the single particle frequencies and carrying out the time integrals, we now find

$$|C_\kappa(t)|^2 = \mathcal{Z}_A\,|\,\langle A|\,H_I(0)\,|\kappa\rangle\,|^2 \left[\frac{1-\cos[(E_\kappa - E_A)t]}{(E_\kappa - E_A)^2}\right], \tag{7.4.17}$$

yielding

$$\sum_\kappa |C_\kappa(t)|^2 = 2\,\mathcal{Z}_A \int \rho(p_0)\left[\frac{1-\cos[(p_0 - E_A)t]}{(p_0 - E_A)^2}\right] dp_0\,. \tag{7.4.18}$$

Since in the cases in which there are no infrared divergences, as $p_0 \to E_A$

$$\rho(p_0) \simeq (p_0 - E_A)^n \quad ; \quad n \geq 2\,, \tag{7.4.19}$$

the oscillatory contribution in (7.4.18) averages out in the long time limit yielding the asymptotic behavior as $t \to \infty$

$$\sum_{\kappa} |C_\kappa(\infty)|^2 = 2\,\mathcal{Z}_A \int \frac{\rho(p_0)}{(p_0 - E_A)^2}\, dp_0\,. \tag{7.4.20}$$

The unitarity relation (7.3.16) at asymptotically long time becomes,

$$\mathcal{Z}_A \left[1 + 2 \int \frac{\rho(p_0)}{(p_0 - E_A)^2}\, dp_0 \right] = 1\,. \tag{7.4.21}$$

with

$$\mathcal{Z}_A = e^{-z_A} \simeq 1 - z_A + \cdots = 1 - 2 \int \frac{\rho(p_0)}{(p_0 - E_A)^2}\, dp_0 \; + \mathcal{O}(H_I^4)\,, \tag{7.4.22}$$

it is clear that the unitarity relation (7.4.21) is fulfilled up to $\mathcal{O}(H_I^4)$ which is consistent with the order that we have considered.

7.4.1 The entangled dressing cloud:

Focusing on the super renormalizable case, with an obvious extension to the renormalizable case, the states $|A\rangle = \left|1^\phi_{\vec{p}}\right\rangle$ and $|\kappa\rangle = \left|1^\phi_{\vec{k}}; 1^\chi_{\vec{q}}\right\rangle$ with $E_\kappa = E_k + q$. Denoting the coefficients $C_A(t) \equiv C_p(t)$; $C_\kappa(t) \equiv C_{\vec{k},\vec{q}}(t)$, the time evolved state (in the interaction picture) is

$$|\Psi(t)\rangle = C_p(t) \left|1^\phi_{\vec{p}}\right\rangle + \sum_{\vec{q},\vec{k}} C_{\vec{k},\vec{q}}(t) \left|1^\phi_{\vec{k}}; 1^\chi_{\vec{q}}\right\rangle\,, \tag{7.4.23}$$

where

$$C_p(t) = e^{-i\delta E_\infty\, t} \Big[E_p\, t\Big]^{-\Delta}\, \mathcal{Z}_\phi^{1/2}\,, \tag{7.4.24}$$

and the coefficients $C_{\vec{k},\vec{q}}(t)$ obtained from eqn.(7.3.10). The asymptotic state after the probability to remain in the initial state has vanished is given by (in the interaction picture)

$$|\Psi(\infty)\rangle = \sum_{\vec{k},\vec{q}} C_{\vec{k};\vec{q}}(\infty) \left|1^\phi_{\vec{k}}; 1^\chi_{\vec{p}-\vec{k}}\right\rangle\,, \tag{7.4.25}$$

with (see eqn. (7.4.8), and $\vec{q} = \vec{p} - \vec{k}$)

$$|C_{\vec{k};\vec{q}}(\infty)|^2 = 2\,\mathcal{Z}_\phi \left[\frac{|\left\langle 1^\phi_{\vec{p}}\right| H_I(0) \left|1^\phi_{\vec{k}}; 1^\chi_{\vec{q}}\right\rangle|^2}{(E_k + q - E_p)^2}\right] \Big[\frac{E_k + q - E_p}{E_p}\Big]^{2\Delta}\, \Gamma[1 - 2\Delta]\, \sin\big[\frac{\pi}{2}(1 - 2\Delta)\big], \tag{7.4.26}$$

where the corresponding matrix elements are given by eqn. (7.3.54), and from eqn. (7.4.14)

$$\sum_{\vec{k},\vec{q}} |C_{\vec{k};\vec{q}}(\infty)|^2 = 1 + \mathcal{O}(H_I^4)\,. \tag{7.4.27}$$

It is important to compare the time evolved state (7.4.23) with previous studies. In ref.[223] the state dressed by soft massless quanta was obtained up to first order in time-ordered perturbation theory (see eqn. (5) in ref.[223]), whereas the state $|\Psi(t)\rangle$ (7.4.23) describes a non-perturbative resummation of the perturbative series, as is evident in the anomalous dimension.

Furthermore, the dressed states considered in references[133, 243, 255, 205, 334] are built from a coherent state of photons, which are very different from the state $|\Psi(t)\rangle$ which in the long time limit is a superposition of single charged and a single massless particle states, and the probabilities include wave function renormalization constants.

This is an entangled state of the charged particle ϕ and the cloud of massless quanta χ. At asymptotically long time, the probability of finding a $\phi_{\vec{k}}, \chi_{\vec{q}}$ pair is $|C_{\vec{k},\vec{q}}(\infty)|^2$ and by unitarity $\sum_{\vec{q},\vec{k}} |C_{\vec{k},\vec{q}}(\infty)|^2 = 1$ as explicitly shown in eqn. (7.4.14). The density matrix

$$\wp = |\Psi(\infty)\rangle \langle\Psi(\infty)| \tag{7.4.28}$$

describes a pure state with $\mathrm{Tr}\wp = 1$.

However, consider that this asymptotic state is measured by a detector that is only sensitive to the charge of the ϕ field, but insensitive to the charge neutral massless quanta of the χ field. Such measurement amounts to tracing the density matrix over the unobserved χ field yielding the mixed state described by the reduced density matrix

$$\mathrm{Tr}_\chi \wp = \sum_{\vec{k}} |C_{\vec{p};\vec{k}}(\infty)|^2 \left|1^\phi_{\vec{k}}\right\rangle \left\langle 1^\phi_{\vec{k}}\right| \,, \tag{7.4.29}$$

from which we interpret $|C_{\vec{p},\vec{k}}(\infty)|^2$ as the distribution function of the charged fields in the asymptotic state.

Although this discussion has focused on the asymptotic state, it can be extended to include the full time evolution of the state $|\Psi(t)\rangle$. Tracing over the unobserved χ states the reduced density matrix at any given time is

$$\mathrm{Tr}_\chi \wp(t) = |C_p(t)|^2 \left|1^\phi_{\vec{p}}\right\rangle \left\langle 1^\phi_{\vec{p}}\right| + \sum_{\vec{k}} |C_{\vec{p};\vec{k}}(t)|^2 \left|1^\phi_{\vec{k}}\right\rangle \left\langle 1^\phi_{\vec{k}}\right| . \tag{7.4.30}$$

This mixed state features a von Neumann entropy

$$S_\phi(t) = -|C_p(t)|^2 \ln\left(|C_p(t)|^2\right) - \sum_{\vec{k}} |C_{\vec{p};\vec{k}}(t)|^2 \ln\left(|C_{\vec{p};\vec{k}}(t)|^2\right), \tag{7.4.31}$$

since $C_p(0) = 1$; $C_{\vec{p};\vec{k}}(0) = 0$, it follows that $S_\phi(0) = 0$. The time evolution of the entropy is completely determined by the (DRM) equations (7.3.10,7.3.11) and in the cases with infrared divergences $C_p(\infty) = 0$; $C_{\vec{p};\vec{k}}(\infty) \neq 0$, asymptotically at long time

$$S_\phi(\infty) = -\sum_{\vec{k}} |C_{\vec{p};\vec{k}}(\infty)|^2 \ln\left(|C_{\vec{p};\vec{k}}(\infty)|^2\right) > 0\,, \tag{7.4.32}$$

with the probabilities $|C_{\vec{p};\vec{k}}(\infty)|^2$ obeying the unitarity condition (7.4.27). Unitary time evolution entails a flow of information from the initial single particle state to the asymptotic entangled two particle state with a concomitant growth of the entanglement entropy whose time evolution is completely determined by the (DRM) equations (7.3.10,7.3.11).

The entanglement entropy resulting from the correlations between hard charged particles and soft photons in QED was studied in ref.[334] within the context of the coherent dressed states proposed in ref.[255]. As mentioned above these states are very different from the dressed state obtained from the unitary time evolution of the initial single particle state by the (DRM), thus preventing a meaningful comparison.

The entanglement entropy (7.4.32) is infrared finite, although the coefficients $|C_{\vec{p};\vec{k}}(\infty)|^2$ feature the infrared enhancement near threshold $E_k+q \to E_p$ exhibited by their denominators in (7.4.26), it is compensated by the power law with anomalous dimension in the numerator. An integral within a small region in which the denominator vanishes is rendered finite by the anomalous dimension. Indeed, as discussed in the previous section, it is the numerator with the anomalous dimension in the coefficients (7.4.8) that ultimately leads to an infrared finite integral of $|C_{\vec{p};\vec{k}}(\infty)|^2$ and the fulfillment of unitarity, eqn. (7.4.14).

The calculation of the entanglement entropy either (7.4.31) or its asymptotic form (7.4.32) is complicated by the logarithms and does not seem a priori to yield a useful quantity since it depends non only on the anomalous dimension but also on the couplings, the volume[1] and the ultraviolet aspects of the theory through the wave function renormalization constant $\mathcal{Z}$. While the growth of entropy and information flow from the initial state to the asymptotic multiparticle state as a consequence of unitary time evolution and its dependence on the anomalous dimension are interesting conceptually, it remains to be understood if it provides any observational consequence.

7.5 Discussion:

Scaling behavior and renormalization group invariance: In the cases in which there is an infrared divergence at threshold the survival probability at long time is given by

$$|C_A(t)|^2 = \mathcal{Z}_A \Big[E_A t\Big]^{-2\Delta} . \tag{7.5.1}$$

This scaling behavior can be written in a manifestly renormalization group invariant form as

$$|C_A(t)|^2 = \mathcal{Z}_A[\mu] \Big[\mu t\Big]^{-2\Delta} \;\; ; \;\; \mathcal{Z}_A[\mu] = \mathcal{Z}_A \Big[\frac{E_A}{\mu}\Big]^{-2\Delta} , \tag{7.5.2}$$

so that $|C_A(t)|$ is independent of the renormalization scale μ, namely

$$\frac{\partial |C_A(t)|^2}{\partial \ln[\mu]} = 0 \Rightarrow \frac{\partial \ln \mathcal{Z}_A[\mu]}{\partial \ln[\mu]} = 2\Delta \;\; ; \;\; \mathcal{Z}_A[E_A] = \mathcal{Z}_A \, . \tag{7.5.3}$$

The renormalization group invariance of the above result can also be made explicit by noting that we can also write the integral in the first term in $I_1(T)$ (7.3.60) as $\int_0^{s_0} + \int_{s_0}^1$ with $s_0 = \mu/E_p$, and μ an arbitrary renormalization scale. Obviously the result is independent of the scale μ and the long time limit (7.3.61) would become

$$\gamma(t) \;\; \underset{t\longrightarrow\infty}{\longrightarrow} \;\; 2\,\Delta \, \ln\Big[\mu t\Big] + z_\phi[\mu] \, . \tag{7.5.4}$$

[1] A similar volume dependence has been discussed in ref.[334].

Since $\gamma(t)$ is independent of the arbitrary scale μ it obeys the renormalization group equation

$$\mu \frac{d\,\gamma(t)}{d\mu} = 0\,, \tag{7.5.5}$$

the solution (7.3.63) corresponds to $\mu = E_p$.

Exponential vs. power law decay: Instead of the model described by the Lagrangian density (7.2.1) with two fields, let us consider, for example the case of three fields ϕ_1, ϕ_2, χ with χ a massless field and both ϕ_1, ϕ_2 are charged and massive with $M_1 > M_2$ and a cubic interaction among all fields, $\mathcal{L} = \lambda\, \phi_1^\dagger\, \phi_2\, \chi + \text{h.c.}$. In this case the heavier field ϕ_1 can decay into the ϕ_2, χ, hence the ϕ_1 single particle pole is now embedded in the two-particle continuum with threshold at $M_2 < M_1$. The survival probability for a single ϕ_1 particle state of momentum $\vec{p}$ decays in time in the long time limit as $e^{-\Gamma_p\, t}$ with $\Gamma_p = 2\pi\, \rho(p_0 = E_p^{(1)})$. As $M_2 \to M_1$ from below, the decay rate $\Gamma_p \to 0$ as now the threshold coincides with the position of the mass shell of ϕ_1 and the spectral density vanishes at threshold by kinematics. This is the case in which infrared singularities emerge when the spectral density vanishes linearly at threshold. In this case the asymptotic long time limit is determined by the subleading secular terms that do not grow linearly in time, but as described above, only logarithmically, and as M_2 becomes larger than M_1 the single particle ϕ_1 pole moves below the multiparticle threshold, it is now an isolated pole below the continuum describing a stable particle.

Infrared dressing and the S-matrix: In this chapter we focused on studying the dynamics of dressing by soft quanta directly in real time in model quantum field theories that feature infrared divergences akin to those in gauge theories. This is undoubtedly only a first step, and of much more limited scope than addressing infrared aspects in S-matrix elements between asymptotic states in gauge theories. While a direct extrapolation of our results to the understanding or resolution of these divergences in S-matrix elements must await a deeper study, we can comment on some *possible* implications. To begin with, the S-matrix considers the time evolution of states prepared in the infinite past towards the infinite future, hence it is an infinite time limit of the finite time analysis presented here. As we have shown, the amplitude of the single particle state vanishes as a power law with anomalous dimension in this limit, this is in agreement with the vanishing of the on-shell

wave function renormalization as a consequence of infrared divergences, namely the vanishing of the amplitude of the single particle "pole". Therefore, even when an initial single particle state is "prepared" in the infinite past, it dresses itself with soft quanta becoming the asymptotic entangled state given for example by (7.4.25) with the coefficients obeying the unitarity condition (7.4.27) a result of unitary time evolution as expressed by the sum rule (7.3.17). It is then this entangled, multiparticle state that should be considered as the "in" state and also describes the asymptotic "out" states in the S-matrix calculation of a cross section or transition rate. Therefore, an assessment of the infrared finiteness of S-matrix elements between asymptotic states entails a calculation of the scattering processes not in terms of single particles, but in terms of the entangled multiparticle states of the form (7.4.25). An analysis along these lines was originally presented in refs.[133, 243] but with dressed states as coherent states, which are very different from the states (7.4.25) as discussed above. Scattering of "Kulish-Faddeev"[255] dressed states has been considered in ref.[330], again, such states are strikingly different from the multiparticle state (7.4.25) which has been obtained directly from the real time evolution and whose amplitude satisfies the sum rule (7.4.27), a direct consequence of unitary time evolution. A challenging open question is how to incorporate the non-perturbative resummation that evolves the single particle state into the dressed entangled state (7.4.25) consistently with Feynman calculus ubiquitous in S-matrix calculations.

Therefore, the infrared finiteness of the S-matrix based on the dressed states whose spectral properties feature the anomalous dimensions associated with the non-perturbative resummation of infrared emission and absorption, remains an open question which undoubtedly merits further and deeper study well beyond the limited scope of this chapter.

Loop corrections to the mass of the light field: In this chapter we focused on the infrared aspects associated with the emission and absorption of a massless scalar particle which are akin to those in gauge theories. One of our motivations is to learn how to describe these processes in real time with a view towards a cosmological setting as a potential mechanism of production of ultra light dark matter. In a non-gauge theory the masslessness of the scalar field must be protected by some symmetry, for example the scalar field in our examples could be a Goldstone boson associated with a spontaneously broken symmetry

beyond the standard model or an axion-like *scalar* pseudo-Goldstone boson. In absence of protecting symmetries radiative corrections may induce a non-vanishing (and perhaps large) mass and such symmetry should be responsible for the near masslessness of such an ultra light dark matter candidate. While our results describe the dynamics of dressing and is of fundamental character, their applicability must be carefully considered in particular cases by assessing whether radiative corrections (higher order loop corrections) induce a large mass invalidating the results based on the masslessness of the scalar particle.

7.6 Conclusions and further questions:

In this chapter we studied the infrared aspects of the dressing dynamics of charged states by the emission and absorption of massless neutral quanta directly in time, specifically in non-gauge theories. While motivated by possible cosmological implications for production of ultra-light axion-like particles, and focused on the time evolution of initial single particle states, our study provides a complementary exploration of infrared phenomena ubiquitous in the S-matrix formulation of gauge theories, and possibly of infrared phenomena in gravity. We have considered super renormalizable and renormalizable theories that while featuring very different ultraviolet behavior, nonetheless share similar infrared behavior. Infrared singularities in these theories arise as a consequence of the charged particle mass shell merging with the beginning of a multiparticle branch cut in the charged particle self-energy and are, therefore, akin to infrared divergences in gauge theories. We map this infrared divergence into similar divergences of an Euclidean critical theory and implement a renormalization group resummation of the propagator yielding scaling behavior near threshold. This translates into a survival probability of the charged single particle state that decays as a power law in time with an anomalous dimension, namely $t^{-\Delta}$. We introduced a dynamical resummation method that extends the dynamical renormalization group and obtain the time dependent amplitudes of the single charged particle state, and the excited multiparticle states. This method is manifestly unitary and yields the survival probability directly in time. It clearly reveals that infrared dynamics arises when the spectral density vanishes linearly at threshold and

yields the power law decay of the survival probability $t^{-\Delta}$ explicitly relating the anomalous dimension Δ to the slope of the spectral density at threshold. This behavior points to a certain universality in the sense that theories with very different ultraviolet behavior but with similar behavior of the spectral density near threshold feature similar power law decay with anomalous dimensions.

The dynamical resummation method yields the unitary time evolution of the single charged particle state and explicitly shows that the dressed state is an entangled state of the charged field and massless quanta.

Tracing over the massless neutral quanta yields a reduced density matrix from which we extract the entanglement entropy at all time. Unitary time evolution entails an information flow from the initial single particle state with vanishing entropy to the asymptotic dressed state with an infrared finite entropy as a consequence of the anomalous dimension.

We find that effective field theories of massless axion-like particles coupled to charged fermions do not feature infrared divergences and provide a criterion generally valid for non-gauge theories up to one loop to determine if and when infrared divergences arise.

These results lead to several questions that merit further study: **i)** how to extend the (DRM) to gauge theories consistently with gauge invariance, **ii)** how to combine the (DRM) that describes the time evolution of initial states with the S-matrix, which describes transition amplitudes from in-states prepared in the infinite past, to out states in the infinite future. **iii)** aspects of coherence of dressed states have been addressed recently in refs.[122, 205, 334], the (DRM) yields the dressed state as a function of time, it is very different from that in these references. While the entanglement entropy is infrared finite, it depends not only on the anomalous dimension Δ but also on the ultraviolet behavior of the theory with no a priori direct relationship to observables.

Perhaps the results of our study could lead to further understanding of infrared effects in gauge theories and gravity and may provide a useful framework to study similar phenomena directly in time in cosmology.

Bibliography

[1] Dijet resonance searches with the ATLAS detector at 14 TeV LHC. Technical report, CERN, Geneva, Mar 2015. All figures including auxiliary figures are available at https://atlas.web.cern.ch/Atlas/GROUPS/PHYSICS/PUBNOTES/ATL-PHYS-PUB-2015-004.

[2] Morad Aaboud et al. A search for pair-produced resonances in four-jet final states at $\sqrt{s} = 13$ TeV with the ATLAS detector. *Eur. Phys. J. C*, 78(3):250, 2018.

[3] Georges Aad et al. Search for pair production of a new heavy quark that decays into a W boson and a light quark in pp collisions at $\sqrt{s} = 8$ TeV with the ATLAS detector. *Phys. Rev. D*, 92(11):112007, 2015.

[4] Georges Aad et al. Search for new resonances in mass distributions of jet pairs using 139 fb^{-1} of pp collisions at $\sqrt{s} = 13$ TeV with the ATLAS detector. *JHEP*, 03:145, 2020.

[5] Georges Aad et al. Search for squarks and gluinos in final states with jets and missing transverse momentum using 139 fb^{-1} of $\sqrt{s}$ =13 TeV pp collision data with the ATLAS detector. *JHEP*, 02:143, 2021.

[6] R. Aaij et al. Search for long-lived scalar particles in $B^+ \to K^+\chi(\mu^+\mu^-)$ decays. *Phys. Rev. D*, 95(7):071101, 2017.

[7] Roel Aaij et al. Search for hidden-sector bosons in $B^0 \to K^{*0}\mu^+\mu^-$ decays. *Phys. Rev. Lett.*, 115(16):161802, 2015.

[8] A. Abada et al. FCC-ee: The Lepton Collider: Future Circular Collider Conceptual Design Report Volume 2. *Eur. Phys. J. ST*, 228(2):261–623, 2019.

[9] L. F. Abbott and P. Sikivie. A Cosmological Bound on the Invisible Axion. *Phys. Lett. B*, 120:133–136, 1983.

[10] A. H. Abdelhameed et al. Description of CRESST-III Data. 5 2019.

[11] K. Abe et al. Search for heavy neutrinos with the T2K near detector ND280. *Phys. Rev. D*, 100(5):052006, 2019.

[12] C. Abel et al. Measurement of the permanent electric dipole moment of the neutron. *Phys. Rev. Lett.*, 124(8):081803, 2020.

[13] B. Abi et al. Measurement of the Positive Muon Anomalous Magnetic Moment to 0.46 ppm. *Phys. Rev. Lett.*, 126(14):141801, 2021.

[14] Medina Ablikim et al. Amplitude Analysis of the Decays $\eta' \to \pi^+\pi^-\pi^0$ and $\eta' \to \pi^0\pi^0\pi^0$. *Phys. Rev. Lett.*, 118(1):012001, 2017.

[15] M. Abramowitz and I. A. Stegun. *Handbook of Mathematical Functions*. Dover, NY, 1964.

[16] P. Abreu et al. Search for neutral heavy leptons produced in Z decays. *Z. Phys. C*, 74:57–71, 1997. [Erratum: Z.Phys.C 75, 580 (1997)].

[17] N. Aghanim et al. Planck 2018 results. VI. Cosmological parameters. *Astron. Astrophys.*, 641:A6, 2020.

[18] A. Aguilar-Arevalo et al. Results on low-mass weakly interacting massive particles from a 11 kg-day target exposure of DAMIC at SNOLAB. *Phys. Rev. Lett.*, 125:241803, 2020.

[19] A. A. Aguilar-Arevalo et al. Dark Matter Search in a Proton Beam Dump with MiniBooNE. *Phys. Rev. Lett.*, 118(22):221803, 2017.

[20] A. A. Aguilar-Arevalo et al. Dark Matter Search in Nucleon, Pion, and Electron Channels from a Proton Beam Dump with MiniBooNE. 2018.

[21] C. Ahdida et al. Sensitivity of the SHiP experiment to Heavy Neutral Leptons. *JHEP*, 04:077, 2019.

[22] C. A. Aidala et al. The SeaQuest Spectrometer at Fermilab. *Nucl. Instrum. Meth. A*, 930:49–63, 2019.

[23] Giulio Aielli et al. Expression of interest for the CODEX-b detector. *Eur. Phys. J. C*, 80(12):1177, 2020.

[24] Evgeny K. Akhmedov, V. A. Rubakov, and A. Yu. Smirnov. Baryogenesis via neutrino oscillations. *Phys. Rev. Lett.*, 81:1359–1362, 1998.

[25] Y. Akrami et al. Planck 2018 results. X. Constraints on inflation. *Astron. Astrophys.*, 641:A10, 2020.

[26] Yashar Akrami, Frederico Arroja, M Ashdown, J Aumont, Carlo Baccigalupi, M Ballardini, Anthony J Banday, RB Barreiro, Nicola Bartolo, S Basak, et al. Planck 2018 results-x. constraints on inflation. *Astronomy & Astrophysics*, 641:A10, 2020.

[27] Sergey Alekhin et al. A facility to Search for Hidden Particles at the CERN SPS: the SHiP physics case. *Rept. Prog. Phys.*, 79(12):124201, 2016.

[28] R. Alemany et al. Summary Report of Physics Beyond Colliders at CERN. 2 2019.

[29] Jim Alexander et al. Dark Sectors 2016 Workshop: Community Report. 8 2016.

[30] Rouzbeh Allahverdi, Robert Brandenberger, Francis-Yan Cyr-Racine, and Anupam Mazumdar. Reheating in inflationary cosmology: theory and applications. *Annual Review of Nuclear and Particle Science*, 60:27–51, 2010.

[31] Adam Alloul, Neil D. Christensen, Céline Degrande, Claude Duhr, and Benjamin Fuks. FeynRules 2.0 - A complete toolbox for tree-level phenomenology. *Comput. Phys. Commun.*, 185:2250–2300, 2014.

[32] Wolfgang Altmannshofer, Stefania Gori, Dean J. Robinson, and Douglas Tuckler. The Flavor-locked Flavorful Two Higgs Doublet Model. *JHEP*, 03:129, 2018.

[33] J. Alwall, R. Frederix, S. Frixione, V. Hirschi, F. Maltoni, O. Mattelaer, H. S. Shao, T. Stelzer, P. Torrielli, and M. Zaro. The automated computation of tree-level and next-to-leading order differential cross sections, and their matching to parton shower simulations. *JHEP*, 07:079, 2014.

[34] Mustafa A Amin, Mark P Hertzberg, David I Kaiser, and Johanna Karouby. Nonperturbative dynamics of reheating after inflation: a review. *International Journal of Modern Physics D*, 24(01):1530003, 2015.

[35] D. J. Amit. *Field theory, the renormalization group and critical phenomena.* McGraw-Hill, N.Y, 1978.

[36] Haipeng An, Xiangdong Ji, and Fanrong Xu. P-odd and CP-odd Four-Quark Contributions to Neutron EDM. *JHEP*, 02:043, 2010.

[37] A. Anastasi et al. Precision measurement of the $\eta \to \pi^+\pi^-\pi^0$ Dalitz plot distribution with the KLOE detector. *JHEP*, 05:019, 2016.

[38] P. Anderson and L. Parker. Phys. *Rev. D*, 36:2963, 1987.

[39] D. Antypas et al. New Horizons: Scalar and Vector Ultralight Dark Matter. 3 2022.

[40] L Aphecetche et al. PHENIX calorimeter. *Nucl. Instrum. Meth. A*, 499:521–536, 2003.

[41] E. Aprile et al. Light Dark Matter Search with Ionization Signals in XENON1T. *Phys. Rev. Lett.*, 123(25):251801, 2019.

[42] Paul Archer-Smith and Yue Zhang. Higgs Portal From The Atmosphere To Hyper-K. *Phys. Lett. B*, 817:136309, 2021.

[43] Paola Arias, Davide Cadamuro, Mark Goodsell, Joerg Jaeckel, Javier Redondo, and Andreas Ringwald. WISPy Cold Dark Matter. *JCAP*, 06:013, 2012.

[44] Nima Arkani-Hamed, Raffaele Tito D'Agnolo, and Hyung Do Kim. Weak scale as a trigger. *Phys. Rev. D*, 104(9):095014, 2021.

[45] Q. Arnaud et al. First results from the NEWS-G direct dark matter search experiment at the LSM. *Astropart. Phys.*, 97:54–62, 2018.

[46] A. V. Artamonov et al. Study of the decay $K^+ \to \pi^+\nu\bar{\nu}$ in the momentum region $140 < P_\pi < 199$ MeV/c. *Phys. Rev. D*, 79:092004, 2009.

[47] A. V. Artamonov et al. Search for heavy neutrinos in $K^+ \to \mu^+\nu_H$ decays. *Phys. Rev. D*, 91(5):052001, 2015. [Erratum: Phys.Rev.D 91, 059903 (2015)].

[48] A.V. Artamonov et al. New measurement of the $K^+ \to \pi^+\nu\bar{\nu}$ branching ratio. *Phys. Rev. Lett.*, 101:191802, 2008.

[49] Asimina Arvanitaki, Savas Dimopoulos, and Ken Van Tilburg. Resonant absorption of bosonic dark matter in molecules. *Phys. Rev. X*, 8(4):041001, 2018.

[50] A. Arza. *arXiv:*, 2009:03870.

[51] Takehiko Asaka and Mikhail Shaposhnikov. The νMSM, dark matter and baryon asymmetry of the universe. *Phys. Lett. B*, 620:17–26, 2005.

[52] J. Audretsch and P. Spangehl. Phys. *Rev.*, 33, 1985.

[53] C. A. Baker, D. D. Doyle, P. Geltenbort, K. Green, M. G. D. van der Grinten, P. G. Harris, P. Iaydjiev, S. N. Ivanov, D. J. R. May, J. M. Pendlebury, J. D. Richardson, D. Shiers, and K. F. Smith. Improved experimental limit on the electric dipole moment of the neutron. *Physical Review Letters*, 97(13), sep 2006.

[54] J. L. Ball, I. Fuentes-Schuller, and F. P. Schuller. Phys. *Lett. A*, 359:550, 2006.

[55] Peter Ballett, Tommaso Boschi, and Silvia Pascoli. Heavy Neutral Leptons from low-scale seesaws at the DUNE Near Detector. *JHEP*, 03:111, 2020. [JHEP20,111(2020)].

[56] Peter Ballett, Silvia Pascoli, and Mark Ross-Lonergan. MeV-scale sterile neutrino decays at the Fermilab Short-Baseline Neutrino program. *JHEP*, 04:102, 2017.

[57] J. Fernando Barbero, A. Ferreiro, J. Navarro-Salas, and E. J. S. Villase nor. Phys. *Rev. D*, 98:025016, 2018.

[58] S. M. Barnett and P. M. Radmore. *Methods in Theoretical Quantum Optics*. Oxford Science Publications-Clarendon Press, Oxford, 1977.

[59] Matthias Bartelmann. Gravitational Lensing. *Class. Quant. Grav.*, 27:233001, 2010.

[60] N. Bartolo, S. Matarrese, and A. Riotto. Phys. *Rev. D*, 64(12350):4, 2001.

[61] Brian Batell, Joshua Berger, and Ahmed Ismail. Probing the Higgs Portal at the Fermilab Short-Baseline Neutrino Experiments. *Phys. Rev. D*, 100(11):115039, 2019.

[62] Brian Batell, Jared A. Evans, Stefania Gori, and Mudit Rai. Dark Scalars and Heavy Neutral Leptons at DarkQuest. *JHEP*, 05:049, 2021.

[63] Brian Batell, Ayres Freitas, Ahmed Ismail, and David Mckeen. Flavor-specific scalar mediators. *Phys. Rev. D*, 98(5):055026, 2018.

[64] Brian Batell, Ayres Freitas, Ahmed Ismail, and David Mckeen. Probing Light Dark Matter with a Hadrophilic Scalar Mediator. *Phys. Rev. D*, 100(9):095020, 2019.

[65] Brian Batell, Ayres Freitas, Ahmed Ismail, David McKeen, and Mudit Rai. Renormalizable models of flavor-specific scalars. *Phys. Rev. D*, 104(11):115032, 2021.

[66] Brian Batell and Akshay Ghalsasi. Thermal misalignment of scalar dark matter. *arXiv preprint arXiv:2109.04476*, 2021.

[67] Brian Batell, Akshay Ghalsasi, and Mudit Rai. Dynamics of dark matter misalignment through the higgs portal. *arXiv preprint arXiv:2211.09132*, 2022.

[68] Brian Batell, Maxim Pospelov, and Adam Ritz. Exploring portals to a hidden sector through fixed targets. *Physical Review D*, 80(9):095024, 2009.

[69] Brian Batell, Maxim Pospelov, and Adam Ritz. Multi-lepton Signatures of a Hidden Sector in Rare B Decays. *Phys. Rev. D*, 83:054005, 2011.

[70] H. Bateman. *Higher Transcendental Functions, vol. II.* McGraw-Hill, N.Y, 1953.

[71] Marco Battaglieri et al. US Cosmic Visions: New Ideas in Dark Matter 2017: Community Report. In *U.S. Cosmic Visions: New Ideas in Dark Matter*, 7 2017.

[72] J. Beacham et al. Physics Beyond Colliders at CERN: Beyond the Standard Model Working Group Report. *J. Phys. G*, 47(1):010501, 2020.

[73] Benedetta Belfatto, Revaz Beradze, and Zurab Berezhiani. The CKM unitarity problem: A trace of new physics at the TeV scale? *Eur. Phys. J. C*, 80(2):149, 2020.

[74] Benedetta Belfatto and Zurab Berezhiani. Are the CKM anomalies induced by vector-like quarks? Limits from flavor changing and Standard Model precision tests. 3 2021.

[75] Alexander Belyaev, Neil D. Christensen, and Alexander Pukhov. CalcHEP 3.4 for collider physics within and beyond the Standard Model. *Comput. Phys. Commun.*, 184:1729–1769, 2013.

[76] G. W. Bennett et al. Final Report of the Muon E821 Anomalous Magnetic Moment Measurement at BNL. *Phys. Rev. D*, 73:072003, 2006.

[77] F. Bergsma et al. Search for Axion Like Particle Production in 400-GeV Proton - Copper Interactions. *Phys. Lett.*, 157B:458–462, 1985.

[78] F. Bergsma et al. A Search for Decays of Heavy Neutrinos in the Mass Range 0.5-GeV to 2.8-GeV. *Phys. Lett. B*, 166:473–478, 1986.

[79] Asher Berlin, Nikita Blinov, Stefania Gori, Philip Schuster, and Natalia Toro. Cosmology and Accelerator Tests of Strongly Interacting Dark Matter. *Phys. Rev. D*, 97(5):055033, 2018.

[80] Asher Berlin, Stefania Gori, Philip Schuster, and Natalia Toro. Dark Sectors at the Fermilab SeaQuest Experiment. *Phys. Rev. D*, 98(3):035011, 2018.

[81] J. Bernabeu, A. Santamaria, J. Vidal, A. Mendez, and J. W. F. Valle. Lepton Flavor Nonconservation at High-Energies in a Superstring Inspired Standard Model. *Phys. Lett. B*, 187:303–308, 1987.

[82] G Bernardi, G Carugno, J Chauveau, F Dicarlo, M Dris, J Dumarchez, M Ferro-Luzzi, J-M Levy, D Lukas, J-M Perreau, et al. Further limits on heavy neutrino couplings. *Physics Letters B*, 203(3):332–334, 1988.

[83] J. Bernstein. *Kinetic theory in the expanding Universe*. Cambridge Monographs on Mathematical Physics, Cambridge University Press, NY, 1988.

[84] Jeffrey M. Berryman, Andre de Gouvea, Patrick J Fox, Boris Jules Kayser, Kevin James Kelly, and Jennifer Lynne Raaf. Searches for Decays of New Particles in the DUNE Multi-Purpose Near Detector. *JHEP*, 02:174, 2020.

[85] G. Bertone, D. Hooper, and J. Silk. *Physics Reports*, 405:279, 2005.

[86] F. Bezrukov and D. Gorbunov. Light inflaton Hunter's Guide. *JHEP*, 05:010, 2010.

[87] F. Bezrukov, D. Gorbunov, and I. Timiryasov. Uncertainties of hadronic scalar decay calculations. 12 2018.

[88] N. D. Birrell. Proc. *R. Soc. Lond., B*, 361:513, 1978.

[89] N. D. Birrell and P. C. W. Davies. *Quantum fields in curved space time*. Cambridge Monographs on Mathematical Physics, Cambridge University Press, Cambridge, 1982.

[90] N. D. Birrell and L. H. Ford. *, title = Annals of Physics, volume = 122, year = 1979, unidentified = 1,.*

[91] F. Bloch and A. Nordsieck. Phys. *Rev.*, 52:54, 1937.

[92] A. Blondel et al. Standard model theory for the FCC-ee Tera-Z stage. In *Mini Workshop on Precision EW and QCD Calculations for the FCC Studies : Methods and Techniques*, volume 3/2019 of *CERN Yellow Reports: Monographs*, Geneva, 9 2018. CERN.

[93] Dietrich Bödeker and Jan Nienaber. Scalar field damping at high temperatures. *Phys. Rev. D*, 106(5):056016, 2022.

[94] Iryna Boiarska, Kyrylo Bondarenko, Alexey Boyarsky, Volodymyr Gorkavenko, Maksym Ovchynnikov, and Anastasia Sokolenko. Phenomenology of GeV-scale scalar portal. *JHEP*, 11:162, 2019.

[95] M. Bona et al. Model-independent constraints on $\Delta F = 2$ operators and the scale of new physics. *JHEP*, 03:049, 2008.

[96] Kyrylo Bondarenko, Alexey Boyarsky, Torsten Bringmann, Marco Hufnagel, Kai Schmidt-Hoberg, and Anastasia Sokolenko. Direct detection and complementary constraints for sub-GeV dark matter. *JHEP*, 03:118, 2020.

[97] Kyrylo Bondarenko, Alexey Boyarsky, Dmitry Gorbunov, and Oleg Ruchayskiy. Phenomenology of GeV-scale Heavy Neutral Leptons. *JHEP*, 11:032, 2018.

[98] Kyrylo Bondarenko, Alexey Boyarsky, Maksym Ovchynnikov, and Oleg Ruchayskiy. Sensitivity of the intensity frontier experiments for neutrino and scalar portals: analytic estimates. *JHEP*, 08:061, 2019.

[99] Marco Bonvini, Stefano Forte, and Giovanni Ridolfi. Soft gluon resummation of Drell-Yan rapidity distributions: Theory and phenomenology. *Nucl. Phys. B*, 847:93–159, 2011.

[100] L. Bouchet, E. Jourdain, J. P. Roques, A. Strong, R. Diehl, F. Lebrun, and R. Terrier. INTEGRAL SPI All-Sky View in Soft Gamma Rays: Study of Point Source and Galactic Diffuse Emissions. *Astrophys. J.*, 679:1315, 2008.

[101] D. Boyanovsky. Phys. *Rev. D*, 98:023515, 2018.

[102] D Boyanovsky and HJ De Vega. Dynamical renormalization group approach to relaxation in quantum field theory. *Annals of Physics*, 307(2):335–371, 2003.

[103] D. Boyanovsky and N. Herring. Phys. *Rev. D*, 100:023531, 2019.

[104] D. Boyanovsky, R. Holman, and S. Prem Kumar. Inflaton decay in De Sitter spacetime. *Phys. Rev. D*, 56:1958–1972, 1997.

[105] Daniel Boyanovsky. Quantum decay in renormalizable field theories: Quasiparticle formation, zeno and anti-zeno effects. *Annals of Physics (New York)*.

[106] Daniel Boyanovsky and Nathan Herring. Phys. *Rev. D*, 100:023531, 2019.

[107] Alexey Boyarsky, Maksym Ovchynnikov, Oleg Ruchayskiy, and Vsevolod Syvolap. Improved big bang nucleosynthesis constraints on heavy neutral leptons. *Phys. Rev. D*, 104(2):023517, 2021.

[108] Suddhasattwa Brahma, Omar Alaryani, and Robert Brandenberger. Entanglement entropy of cosmological perturbations. *Physical Review D*, 102(4):043529, 2020.

[109] G. C. Branco, J. T. Penedo, Pedro M. F. Pereira, M. N. Rebelo, and J. I. Silva-Marcos. Addressing the CKM Unitarity Problem with a Vector-like Up Quark. 3 2021.

[110] R. Brandenberger, V. Mukhanov, and T. Prokopec. Phys. *Rev.Lett.*, 69:3606, 1992.

[111] R. Brandenberger and V. Mukhanov T. Prokopec. Phys. *Rev. D*, 48:2443, 1993.

[112] J. Bros, H. Epstein, and U. Moschella. Jcap **0802**. *00*, 11, 2010.

[113] Dawid Brzeminski, Zackaria Chacko, Abhish Dev, and Anson Hook. Time-varying fine structure constant from naturally ultralight dark matter. *Phys. Rev. D*, 104(7):075019, 2021.

[114] Mathieu Buchkremer, Giacomo Cacciapaglia, Aldo Deandrea, and Luca Panizzi. Model Independent Framework for Searches of Top Partners. *Nucl. Phys. B*, 876:376–417, 2013.

[115] W. Buchmuller, P. Di Bari, and M. Plumacher. Annals of physics315. 305, 2005.

[116] W. Buchmuller, R. D. Peccei, and T. Yanagida. Ann. *Rev. Nucl. Part*, 55, 2005.

[117] TS Bunch, P Panangaden, and L Parker. On renormalisation of $\lambda\phi 4$ field theory in curved space-time. i. *Journal of Physics A: Mathematical and General*, 13(3):901, 1980.

[118] Annarita Buonaura. SHiP: a new facility with a dedicated detector for studying ν_τ properties and nucleon structure functions. *PoS*, DIS2016:260, 2016.

[119] C. P. Burgess, Maxim Pospelov, and Tonnis ter Veldhuis. The Minimal model of nonbaryonic dark matter: A Singlet scalar. *Nucl. Phys. B*, 619:709–728, 2001.

[120] C. T. Byrnes and D. Wands. Phys. *Rev. D*, 74:043529, 2006.

[121] Davide Cadamuro and Javier Redondo. Cosmological bounds on pseudo Nambu-Goldstone bosons. *JCAP*, 02:032, 2012.

[122] D. Carney, L. Chaurette, D. Neuenfeld, and D. W. Semenoff. Phys. *Rev. Lett.*, 119:18, 2018.

[123] M. A. Castagnino, L. Chimento, D. D. Harari, and J. Math C. Nunez. Phys. **25**. 360, 1984.

[124] L.-Y. Chen, N. Goldenfeld, and Y. Oono. Phys. *Rev. Lett.*, 73:1311, 1996.

[125] Ki-Young Choi, Takeo Inami, Kenji Kadota, Inwoo Park, and Osamu Seto. Searching for Axino-Like Particle at Fixed Target Experiments. *Phys. Dark Univ.*, 27:100460, 2020.

[126] Eung Jin Chun. Bosonic dark matter in a coherent state driven by thermal fermions. *Phys. Lett. B*, 825:136880, 2022.

[127] D. J. H. Chung, P. Crotty, E. W. Kolb, and A. Riotto. Phys. *Rev. D*, 64:043503, 2001.

[128] D. J. H. Chung, L. L. Everett, H. Yoo, and P. Zhou. Phys. *Lett. B*, 712:147, 2012.

[129] D. J. H. Chung, E. W. Kolb, and Jhep A. J. Long. 189:2019, 1901.

[130] D. J. H. Chung, E. W. Kolb, and A. Riotto. Phys. *Rev. D*, 59:023501, 1999.

[131] D. J. H. Chung, E. W. Kolb, A. Riotto, and L. Senatore. Phys. *Rev. D*, 72:023511, 2005.

[132] D. J. H. Chung, H. Yoo, and P. Zhou. Phys. *Rev. D*, 91:043516, 2015.

[133] V. Chung. Phys. *Rev.*, 140, 1965.

[134] Douglas Clowe, Marusa Bradac, Anthony H. Gonzalez, Maxim Markevitch, Scott W. Randall, Christine Jones, and Dennis Zaritsky. A direct empirical proof of the existence of dark matter. *Astrophys. J. Lett.*, 648:L109–L113, 2006.

[135] Sidney R. Coleman and Erick J. Weinberg. Radiative Corrections as the Origin of Spontaneous Symmetry Breaking. *Phys. Rev. D*, 7:1888–1910, 1973.

[136] CMS collaboration et al. Search for chargino-neutralino production in final states with a higgs boson and a w boson. Technical report, Tech. Rep. CMS-PAS-SUS-20-003, CERN, Geneva, Switzerland, 2021.

[137] E. Aprile (Xenon Collaboration). Phys. *Rev. Lett.*, 121(11130):2, 2018.

[138] Don Colladay and V Alan Kostelecký. Cpt violation and the standard model. *Physical Review D*, 55(11):6760, 1997.

[139] John Collins. A new approach to the LSZ reduction formula. 4 2019.

[140] Pilar Coloma, Enrique Fernández-Martínez, Manuel González-López, Josu Hernández-García, and Zarko Pavlovic. GeV-scale neutrinos: interactions with mesons and DUNE sensitivity. *Eur. Phys. J. C*, 81(1):78, 2021.

[141] Pilar Coloma, Pilar Hernández, Víctor Muñoz, and Ian M. Shoemaker. New constraints on Heavy Neutral Leptons from Super-Kamiokande data. *Eur. Phys. J. C*, 80(3):235, 2020.

[142] H. F. Contopanagos and M. B. Einhorn. Phys. *Rev. D*, 45:1291, 1992.

[143] Eduardo Cortina Gil et al. Measurement of the very rare $K^+ \to \pi^+ \nu\bar{\nu}$ decay. *JHEP*, 06:093, 2021.

[144] Eduardo Cortina Gil et al. Search for π^0 decays to invisible particles. *JHEP*, 02:201, 2021.

[145] Xiangyi Cui et al. Dark Matter Results From 54-Ton-Day Exposure of PandaX-II Experiment. *Phys. Rev. Lett.*, 119(18):181302, 2017.

[146] David Curtin et al. Exotic decays of the 125 GeV Higgs boson. *Phys. Rev. D*, 90(7):075004, 2014.

[147] David Curtin et al. Long-Lived Particles at the Energy Frontier: The MATHUSLA Physics Case. *Rept. Prog. Phys.*, 82(11):116201, 2019.

[148] David Curtin, Patrick Meade, and Harikrishnan Ramani. Thermal Resummation and Phase Transitions. *Eur. Phys. J. C*, 78(9):787, 2018.

[149] Richard H. Cyburt, Brian D. Fields, Keith A. Olive, and Tsung-Han Yeh. Rev. *Mod. Phys.*, 88:015004, 2016.

[150] R. Dabrowski and G. V. Dunne. Phys. *Rev.*, D90, 2016.

[151] G. D'Ambrosio, G. F. Giudice, G. Isidori, and A. Strumia. Minimal flavor violation: An Effective field theory approach. *Nucl. Phys. B*, 645:155–187, 2002.

[152] Luc Darmé, Sebastian A. R. Ellis, and Tevong You. Light Dark Sectors through the Fermion Portal. *JHEP*, 07:053, 2020.

[153] J. de Favereau, C. Delaere, P. Demin, A. Giammanco, V. Lemaître, A. Mertens, and M. Selvaggi. DELPHES 3, A modular framework for fast simulation of a generic collider experiment. *JHEP*, 02:057, 2014.

[154] P. F. de Salas, D. V. Forero, S. Gariazzo, P. Martínez-Miravé, O. Mena, C. A. Ternes, M. Tórtola, and J. W. F. Valle. 2020 global reassessment of the neutrino oscillation picture. *Journal of High Energy Physics*, 2021(2), feb 2021.

[155] Celine Degrande, Claude Duhr, Benjamin Fuks, David Grellscheid, Olivier Mattelaer, and Thomas Reiter. UFO - The Universal FeynRules Output. *Comput. Phys. Commun.*, 183:1201–1214, 2012.

[156] Adrian del Rio, Jose Navarro-Salas, and Francisco Torrenti. Renormalized stress-energy tensor for spin-1/2 fields in expanding universes. *Physical Review D*, 90(8):084017, 2014.

[157] H Dijkstra, T Ruf, SHiP Collaboration, et al. Heavy flavour cascade production in a beam dump. *CERN-SHiP-NOTE-2015-009*, 2015.

[158] Michael Dine and Willy Fischler. The Not So Harmless Axion. *Phys. Lett. B*, 120:137–141, 1983.

[159] Babette Döbrich, Joerg Jaeckel, and Tommaso Spadaro. Light in the beam dump - ALP production from decay photons in proton beam-dumps. *JHEP*, 05:213, 2019. [Erratum: JHEP 10, 046 (2020)].

[160] S. Dodelson. *Modern Cosmology*. Academic Press, Boston, 2003.

[161] L. Dolan and R. Jackiw. Symmetry Behavior at Finite Temperature. *Phys. Rev. D*, 9:3320–3341, 1974.

[162] Mingyi Dong et al. CEPC Conceptual Design Report: Volume 2 - Physics \& Detector. 11 2018.

[163] John F. Donoghue, J. Gasser, and H. Leutwyler. The Decay of a Light Higgs Boson. *Nucl. Phys. B*, 343:341–368, 1990.

[164] Marco Drewes, Jan Hajer, Juraj Klaric, and Gaia Lanfranchi. NA62 sensitivity to heavy neutral leptons in the low scale seesaw model. *JHEP*, 07:105, 2018.

[165] Hassan Easa, Thomas Gregoire, and Daniel Stolarski. New Limits on Coloured Three Jet Resonances. *JHEP*, 09:131, 2020.

[166] Daniel Egana-Ugrinovic, Samuel Homiller, and Patrick Meade. Aligned and Spontaneous Flavor Violation. *Phys. Rev. Lett.*, 123(3):031802, 2019.

[167] Daniel Egana-Ugrinovic, Samuel Homiller, and Patrick Meade. Light Scalars and the Koto Anomaly. *Phys. Rev. Lett.*, 124(19):191801, 2020.

[168] Daniel Egana-Ugrinovic, Samuel Homiller, and Patrick Roddy Meade. Higgs bosons with large couplings to light quarks. *Phys. Rev. D*, 100(11):115041, 2019.

[169] Y. Ema, R. Jinno, K. Mukaida, and K. Nakayama. Phys. *Rev. D*, 94:063517, 2016.

[170] Y. Ema, K. Nakayama, and Jhep Y. Tang. 135:2018, 1809.

[171] F. Englert and R. Brout. Broken symmetry and the mass of gauge vector mesons. *Phys. Rev. Lett.*, 13:321–323, Aug 1964.

[172] Recai Erdem and Kemal Gültekin. A mechanism for formation of bose-einstein condensation in cosmology. *Journal of Cosmology and Astroparticle Physics*, 2019(10):061, 2019.

[173] J. R. Espinosa, M. Quiros, and F. Zwirner. On the nature of the electroweak phase transition. *Phys. Lett. B*, 314:206–216, 1993.

[174] Rouven Essig, Roni Harnik, Jared Kaplan, and Natalia Toro. Discovering New Light States at Neutrino Experiments. *Phys. Rev. D*, 82:113008, 2010.

[175] Rouven Essig, Eric Kuflik, Samuel D. McDermott, Tomer Volansky, and Kathryn M. Zurek. Constraining Light Dark Matter with Diffuse X-Ray and Gamma-Ray Observations. *JHEP*, 11:193, 2013.

[176] Jared A. Evans. Detecting Hidden Particles with MATHUSLA. *Phys. Rev. D*, 97(5):055046, 2018.

[177] Jonathan Feng, Iftah Galon, Felix Kling, and Sebastian Trojanowski. FASER: ForwArd Search ExpeRiment at the LHC. 2017.

[178] Jonathan L. Feng, Iftah Galon, Felix Kling, and Sebastian Trojanowski. Dark Higgs bosons at the ForwArd Search ExpeRiment. *Phys. Rev. D*, 97(5):055034, 2018.

[179] A. Ferreiro. *A. del Rio, J.* Navarro-Salas, S. Pla, F. Torrenti.

[180] Brian D. Fields. The primordial lithium problem. *Annual Review of Nuclear and Particle Science*, 61(1):47–68, 2011.

[181] Anastasiia Filimonova, Ruth Schäfer, and Susanne Westhoff. Probing dark sectors with long-lived particles at BELLE II. *Phys. Rev. D*, 101(9):095006, 2020.

[182] M. C. Fischer, B. Gutiérrez-Medina, and M. G. Raizen. Phys. *Rev. Lett*, 87:040402, 2001.

[183] Thomas Flacke, Claudia Frugiuele, Elina Fuchs, Rick S. Gupta, and Gilad Perez. Phenomenology of relaxion-Higgs mixing. *JHEP*, 06:050, 2017.

[184] L. H. Ford. Phys. *Rev. D*, 35:2955, 1987.

[185] Saeid Foroughi-Abari and Adam Ritz. LSND Constraints on the Higgs Portal. *Phys. Rev. D*, 102(3):035015, 2020.

[186] Anthony Fradette, Maxim Pospelov, Josef Pradler, and Adam Ritz. Cosmological beam dump: constraints on dark scalars mixed with the Higgs boson. *Phys. Rev. D*, 99(7):075004, 2019.

[187] C. Frye, H. Hannesdottir, N. Paul, M. D. Schwartz, and K. Yan. Phys. *Rev. D*, 99:056015, 2019.

[188] I. Fuentes, R. B. Mann, E. Martin-Martinez, and S. Moradi. Phys. *Rev. D*, 82:045030, 2010.

[189] S. A. Fulling. *Aspects of quantum field theory in curved space-time*. Cambridge University Press, Cambridge, 1989.

[190] S. A. Fulling, L. Parker, and B. L. Hu. Phys. *Rev. D*, 10:3905, 1974.

[191] Hideo Furugori, Shin'ichi Nojiri, et al. Dressed asymptotic states and qed infrared physics. *Physical Review D*, 104(12):125004, 2021.

[192] Liping Gan, Bastian Kubis, Emilie Passemar, and Sean Tulin. Precision tests of fundamental physics with η and η' mesons. 7 2020.

[193] S. Gardner, R. J. Holt, and A. S. Tadepalli. New Prospects in Fixed Target Searches for Dark Forces with the SeaQuest Experiment at Fermilab. *Phys. Rev. D*, 93(11):115015, 2016.

[194] M. Gasperini and M. Giovannini. Phys. *Lett. B*, 301:334, 1993.

[195] M Gasperini and M Giovannini. Quantum squeezing and cosmological entropy production. *Classical and Quantum Gravity*, 10(9):L133–L136, sep 1993.

[196] M. Gasperini and M. Giovannini. in "string gravity and physics at the planck energy scale" (world scientific. *Singapor*, 1995.

[197] Corrado Gatto, Brenda Fabela Enriquez, and Maria Isabel Pedraza Morales. The REDTOP project: Rare Eta Decays with a TPC for Optical Photons. *PoS*, ICHEP2016:812, 2016.

[198] Murray Gell-Mann, Pierre Ramond, and Richard Slansky. Complex Spinors and Unified Theories. *Conf. Proc. C*, 790927:315–321, 1979.

[199] S. Ghosh. Phys. *Rev. D*, 91:12407, 2016.

[200] S. L. Glashow. The Future of Elementary Particle Physics. *NATO Sci. Ser. B*, 61:687, 1980.

[201] S. L. Glashow, J. Iliopoulos, and L. Maiani. Weak interactions with lepton-hadron symmetry. *Phys. Rev. D*, 2:1285–1292, Oct 1970.

[202] Sheldon L. Glashow. Partial-symmetries of weak interactions. *Nuclear Physics*, 22(4):579–588, 1961.

[203] Vladimir V. Gligorov, Simon Knapen, Michele Papucci, and Dean J. Robinson. Searching for Long-lived Particles: A Compact Detector for Exotics at LHCb. *Phys. Rev. D*, 97(1):015023, 2018.

[204] N. Goldenfeld. *Lectures on phase transitions and the renormalization group*. CRC Press, Taylor & Francis, Florida, 2018.

[205] C. Gomez, R. Letschka, and S. Zell. Eur. *Phys. Jour. C*, 78:610, 2018.

[206] Dmitry Gorbunov, Igor Krasnov, Yury Kudenko, and Sergey Suvorov. Heavy Neutral Leptons from kaon decays in the SHiP experiment. *Phys. Lett. B*, 810:135817, 2020.

[207] Dmitry Gorbunov and Mikhail Shaposhnikov. How to find neutral leptons of the νMSM? *JHEP*, 10:015, 2007. [Erratum: JHEP 11, 101 (2013)].

[208] C. Gordon, D. Wands, B. A. Bassett, and R. Maartens. Phys. *Rev. D*, 63:023506, 2000.

[209] I. S. Gradshteyn and I. M. Ryzhik. *Table of Integrals, Series and Products*. Academic Press, New York, 1980.

[210] Peter W. Graham, David E. Kaplan, Jeremy Mardon, Surjeet Rajendran, and William A. Terrano. Dark Matter Direct Detection with Accelerometers. *Phys. Rev. D*, 93(7):075029, 2016.

[211] Peter W. Graham, David E. Kaplan, and Surjeet Rajendran. Cosmological Relaxation of the Electroweak Scale. *Phys. Rev. Lett.*, 115(22):221801, 2015.

[212] Peter W. Graham and Adam Scherlis. Stochastic axion scenario. *Phys. Rev. D*, 98(3):035017, 2018.

[213] B. Graner, Y. Chen, E. G. Lindahl, and B. R. Heckel. Reduced Limit on the Permanent Electric Dipole Moment of Hg199. *Phys. Rev. Lett.*, 116(16):161601, 2016. [Erratum: Phys.Rev.Lett. 119, 119901 (2017)].

[214] A. A. Grib, S. G. Mamayev, V. M. Mostepanenko, and Gen.Rel.and Grav. 7, 535 (1976); a. *A. Griv, B. A. Levitsky, V. M. Mostepanenko, Teor.Mat.Fiz.*, 19:59, 1974.

[215] Benjamin Grinstein, Lawrence J. Hall, and Lisa Randall. Do B meson decays exclude a light Higgs? *Phys. Lett. B*, 211:363–369, 1988.

[216] D. E. Gruber, J. L. Matteson, L. E. Peterson, and G. V. Jung. The spectrum of diffuse cosmic hard x-rays measured with heao-1. *Astrophys. J.*, 520:124, 1999.

[217] John F. Gunion, Howard E. Haber, Gordon L. Kane, and Sally Dawson. *The Higgs Hunter's Guide*, volume 80. 2000.

[218] Rajan Gupta, Boram Yoon, Tanmoy Bhattacharya, Vincenzo Cirigliano, Yong-Chull Jang, and Huey-Wen Lin. Flavor diagonal tensor charges of the nucleon from (2+1+1)-flavor lattice QCD. *Phys. Rev. D*, 98(9):091501, 2018.

[219] G. S. Guralnik, C. R. Hagen, and T. W. B. Kibble. Global conservation laws and massless particles. *Phys. Rev. Lett.*, 13:585–587, Nov 1964.

[220] S. Habib, C. Molina-Paris, and E. Mottola. Phys. *Rev. D*, 61:024010, 1999.

[221] Tao Han, Ian Lewis, and Thomas McElmurry. QCD Corrections to Scalar Diquark Production at Hadron Colliders. *JHEP*, 01:123, 2010.

[222] H. Hannesdottir and M. D. Schwartz. Phys. *Rev. D*, 101(10500):1, 2020.

[223] Holmfridur Hannesdottir and Matthew D Schwartz. A finite s-matrix. *arXiv preprint arXiv:1906.03271*, 2019.

[224] Edward Hardy and Robert Lasenby. Stellar cooling bounds on new light particles: plasma mixing effects. *JHEP*, 02:033, 2017.

[225] S. Hashiba and J. Yokoyama. Phys. *Rev. D*, 99:043008, 2019.

[226] N. Herring, D. Boyanovsky, and A. Zentner. Phys. *Rev. D*, 101:083516, 2020.

[227] N. Herring, B. Pardo, D. Boyanovsky, and A. R. Zentner. Phys. *Rev. D*, 98:083503, 2018.

[228] Peter W. Higgs. Broken symmetries and the masses of gauge bosons. *Phys. Rev. Lett.*, 13:508–509, Oct 1964.

[229] H. Hirai and S. Sugishita. Jhep 02. 25, 2021.

[230] Martin Hirsch and Zeren Simon Wang. Heavy neutral leptons at ANUBIS. *Phys. Rev. D*, 101(5):055034, 2020.

[231] Yonit Hochberg, Yue Zhao, and Kathryn M. Zurek. Phys. *Rev. Lett.*, 1301:2016, 2018.

[232] John Horgan. *The End of Science: Facing the Limits of Knowledge in the Twilight of the Scientific Age*. New York: Abacus, 1996.

[233] J. K. Hoskins, R. D. Newman, R. Spero, and J. Schultz. Experimental tests of the gravitational inverse-square law for mass separations from 2 to 105 cm. *Phys. Rev. D*, 32:3084–3095, Dec 1985.

[234] B. L. Hu. Phys. *Lett. A*, 71:169, 1978.

[235] B. L. Hu and Henry E. Kandrup. Phys. *Rev. D*, 35:1776, 1987.

[236] I. Vilja J. Lankinen. Phys. *Rev. D*, 5004:2018, 2018.

[237] T. Jacobson, S. Liberati, and D. Mattingly. *, title = Annals of Physics, volume = 321, year = 2006, unidentified = 150,.*

[238] Aliaksei Kachanovich, Ulrich Nierste, and Ivan Nišandžić. Higgs portal to dark matter and $B \to K^{(*)}$ decays. *Eur. Phys. J. C*, 80(7):669, 2020.

[239] K. Kajantie, M. Laine, K. Rummukainen, and Mikhail E. Shaposhnikov. Is there a hot electroweak phase transition at $m_H \gtrsim m_W$? *Phys. Rev. Lett.*, 77:2887–2890, 1996.

[240] Jernej F. Kamenik and Christopher Smith. FCNC portals to the dark sector. *JHEP*, 03:090, 2012.

[241] D. Kapec, M. Perry, A.-M. Raclariu, and A. Strominger. Phys. *Rev. D*, 96:085002, 2017.

[242] Alexandros Karam, Martti Raidal, and Eemeli Tomberg. Gravitational dark matter production in palatini preheating. *Journal of Cosmology and Astroparticle Physics*, 2021(03):064, 2021.

[243] T. W. B. Kibble and J. Math. Phys.9(1968) 315; phys. *Rev.*, 173:1968, 1968.

[244] Kwang Je Kim and Yung-Su Tsai. IMPROVED WEIZSACKER-WILLIAMS METHOD AND ITS APPLICATION TO LEPTON AND W BOSON PAIR PRODUCTION. *Phys. Rev. D*, 8:3109, 1973.

[245] T. Kinoshita. Progress of theoretical physics, 5, 1045 (1950); j. *Math. Phys.*, 3:650, 1962.

[246] Felix Kling and Sebastian Trojanowski. Heavy Neutral Leptons at FASER. *Phys. Rev. D*, 97(9):095016, 2018.

[247] Felix Kling and Sebastian Trojanowski. FORESEE: FORward Experiment SEnsitivity Estimator for the LHC and future hadron colliders. 5 2021.

[248] Simon Knapen and Dean J. Robinson. Disentangling Mass and Mixing Hierarchies. *Phys. Rev. Lett.*, 115(16):161803, 2015.

[249] A. G. Kofman and G. Kurizki. Nature **405**, 546 (2000); z. *Naturforsch.*, A 56:83, 2001.

[250] E. W. Kolb and M. S. Turner Ann. Rev. *Nucl. Part*, 33:645, 1983.

[251] E. W. Kolb and M. S. Turner. *The Early Universe*. Addison-Wesley, 1990.

[252] Edward W. Kolb and Michael S. Turner. *The Early Universe*, volume 69. 1990.

[253] V Alan Kostelecký. Developments in lorentz and cpt violation. In *CPT AND LORENTZ SYMMETRY: Proceedings of the Eighth Meeting on CPT and Lorentz Symmetry*, pages 41–44. World Scientific, 2020.

[254] Gordan Krnjaic. Probing Light Thermal Dark-Matter With a Higgs Portal Mediator. *Phys. Rev. D*, 94(7):073009, 2016.

[255] P. P. Kulish and L. D. Faddeev. Theor. *Math. Phys.*, 4:745, 1970.

[256] V. Kuzmin and I. Tkachev. Phys. *Rev. D*, 59:12300, 1998.

[257] V. A. Kuzmin and I. I. Tkachev. Phys. *Rept.*, 320:199, 1999.

[258] A. Landete, J. Navarro-Salas, and F. Torrenti. Phys. *Rev. D*, 4030:2014, 2013.

[259] J. Lankinen, O. Kerppo, and I. Vilja. Phys. *Rev. D*, 101:063529, 2020.

[260] J. Lankinen, O. Kerppo, and I. Vilja. Phys. *Rev. D*, 101, 2020.

[261] M. Lavelle and D. McMullan. Jhep 0603, 026 (2006); nucl. *Phys.Proc.Suppl.*, 174:51, 2000.

[262] Oliver Leaman. *Key Concepts in Eastern Philosophy.* Routledge, 1999.

[263] Hyun Min Lee. Lectures on physics beyond the Standard Model. *J. Korean Phys. Soc.*, 78(11):985–1017, 2021.

[264] T. D. Lee and M. Nauenberg. Phys. *Rev.*, 133, 1964.

[265] Louis Lello, Daniel Boyanovsky, and Richard Holman. Superhorizon entanglement entropy from particle decay in inflation. *Journal of High Energy Physics*, 2014(4):1–35, 2014.

[266] H. Leutwyler and Mikhail A. Shifman. Light Higgs Particle in Decays of K and η Mesons. *Nucl. Phys. B*, 343:369–397, 1990.

[267] S. Liberati and L. Maccione. Ann. *Rev.of Nuc. and Part*, 59, 2009.

[268] S-Y. Lin, C-H. Chou, and B. L. Hu. Phys. *Rev. D*, 81:084018, 2010.

[269] Tongyan Lin. Dark matter models and direct detection. *PoS*, 333:009, 2019.

[270] Andrei Linde. *Particle physics and inflationary cosmology*, volume 5. CRC press, 1990.

[271] D. Liventsev et al. Search for heavy neutrinos at Belle. *Phys. Rev. D*, 87(7):071102, 2013. [Erratum: Phys.Rev.D 95, 099903 (2017)].

[272] C. Lourenco and H. K. Wohri. Heavy flavour hadro-production from fixed-target to collider energies. *Phys. Rept.*, 433:127–180, 2006.

[273] D. Lynden-Bell. Mnras 136. 101, 1967.

[274] J. Pradler M. Pospelov. Ann. *Rev. Nucl. Part*, 60:539, 2010.

[275] L. N. Machado, H. A. S. Costa, I. G. da Paz, M. Sampaio, and J. B. Araujo. Phys. *Rev. D*, 98(12500):9, 2018.

[276] W. Magnus, F. Oberhettinger, and R. P. Soni. *Formulas and Theorems for the Special Functions of Mathematical Physics*. Springer-Verlag, NY, 1966.

[277] Michal Malinsky, J. C. Romao, and J. W. F. Valle. Novel supersymmetric SO(10) seesaw mechanism. *Phys. Rev. Lett.*, 95:161801, 2005.

[278] E. Martin-Martinez and N. C. Menicucci. Class. *Quantum Grav.*, 29(22400):3, 2012.

[279] John McDonald. Gauge singlet scalars as cold dark matter. *Phys. Rev. D*, 50:3637–3649, 1994.

[280] Peter Minkowski. $\mu \to e\gamma$ at a Rate of One Out of 10^9 Muon Decays? *Phys. Lett. B*, 67:421–428, 1977.

[281] H. B. Moghaddam, R. Brandenberger, and J. Yokoyama Phys. Rev. *D*, 95:063529, 2017.

[282] R. N. Mohapatra. Mechanism for Understanding Small Neutrino Mass in Superstring Theories. *Phys. Rev. Lett.*, 56:561–563, 1986.

[283] R. N. Mohapatra and J. W. F. Valle. Neutrino Mass and Baryon Number Nonconservation in Superstring Models. *Phys. Rev. D*, 34:1642, 1986.

[284] Rabindra N. Mohapatra and Goran Senjanovic. Neutrino Mass and Spontaneous Parity Nonconservation. *Phys. Rev. Lett.*, 44:912, 1980.

[285] Alexander Monin, Alexey Boyarsky, and Oleg Ruchayskiy. Hadronic decays of a light Higgs-like scalar. *Phys. Rev. D*, 99(1):015019, 2019.

[286] Matthew Moulson. KLEVER: An experiment to measure BR($K_L \to \pi^0\nu\bar{\nu}$) at the CERN SPS. *PoS*, ICHEP2018:529, 2019.

[287] V. Mukhanov. *Physical Foundations of Cosmology*. Cambridge University Press, Oxford, 2005.

[288] V. Mukhanov and S. Winitzki. *Introduction to quantum effects in gravity*. Cambridge University Press, Cambridge, 2012.

[289] Viatcheslav Mukhanov and Sergei Winitzki. *Introduction to quantum effects in gravity*. Cambridge University Press, 6 2007.

[290] B. M. K. Nefkens et al. New measurement of the rare decay $\eta \to \pi^0\gamma\gamma$ with the Crystal Ball/TAPS detectors at the Mainz Microtron. *Phys. Rev.*, C90(2):025206, 2014.

[291] Isaac Newton, Daniel Bernoulli, Colin MacLaurin, and Leonhard Euler. *Philosophiae naturalis principia mathematica*, volume 1. excudit G. Brookman; impensis TT et J. Tegg, Londini, 1833.

[292] M. A. Nielsen and I. L. Chuang. *Quantum Computation and Quantum Information*. Cambridge University Press, Cambridge, UK, 2010.

[293] F. W. Olver, D. W. Lozier, R. F. Boisvert, and C. W. Clark. *NIST Handbook of Mathematical Functions*. Cambridge Univ. Press, N.Y, 2010.

[294] L. Parker. Phys. *Rev. Lett*, 21, 1971.

[295] L. Parker and S. A. Fulling. Phys. *Rev. D*, 9:341, 1974.

[296] L. Parker and S. A. Fulling. Phys. *Rev.*, D9, 1974.

[297] L. Parker and D. Toms. *Quantum field theory in curved spacetime: quantized fields and gravity*. Cambridge Monographs in Mathematical Physics, Cambridge, 2009.

[298] Rajesh R. Parwani. Resummation in a hot scalar field theory. *Phys. Rev. D*, 45:4695, 1992. [Erratum: Phys.Rev.D 48, 5965 (1993)].

[299] Federico Piazza and Maxim Pospelov. Sub-eV scalar dark matter through the super-renormalizable Higgs portal. *Phys. Rev. D*, 82:043533, 2010.

[300] John Preskill, Mark B. Wise, and Frank Wilczek. Cosmology of the Invisible Axion. *Phys. Lett. B*, 120:127–132, 1983.

[301] J. Pumplin, D. R. Stump, J. Huston, H. L. Lai, Pavel M. Nadolsky, and W. K. Tung. New generation of parton distributions with uncertainties from global QCD analysis. *JHEP*, 07:012, 2002.

[302] Mariano Quiros. Finite temperature field theory and phase transitions. In *ICTP Summer School in High-Energy Physics and Cosmology*, pages 187–259, 1 1999.

[303] Stuart Raby and Geoffrey B. West. The Branching Ratio for a Light Higgs to Decay Into $\mu^+\mu^-$ Pairs. *Phys. Rev. D*, 38:3488, 1988.

[304] M. Rai and D. Boyanovsky. Phys. *Rev. D*, 102:063532, 2020.

[305] Mudit Rai and Daniel Boyanovsky. Origin of entropy of gravitationally produced dark matter: The entanglement entropy. *Phys. Rev. D*, 102(6):063532, 2020.

[306] Mudit Rai and Daniel Boyanovsky. Interaction rates in cosmology: heavy particle production and scattering. *Class. Quant. Grav.*, 38(19):195014, 2021.

[307] Mudit Rai, Lisong Chen, and Daniel Boyanovsky. Infrared dressing in real time: emergence of anomalous dimensions. *Phys. Rev. D*, 104:085021, 2021.

[308] Brian Albert Robson. *Redefining Standard Model Cosmology*. IntechOpen, Rijeka, Jun 2019.

[309] Valery A. Rubakov and Dmitry S. Gorbunov. *Introduction to the Theory of the Early Universe: Hot big bang theory*. World Scientific, Singapore, 2017.

[310] V. C. Rubin, N. Thonnard, and W. K. Ford, Jr. Rotational properties of 21 SC galaxies with a large range of luminosities and radii, from NGC 4605 /R = 4kpc/ to UGC 2885 /R = 122 kpc/. *Astrophys. J.*, 238:471, 1980.

[311] Abdus Salam. Weak and Electromagnetic Interactions. *Conf. Proc. C*, 680519:367–377, 1968.

[312] J. M. Sanchez-Velazquez, J. A. R. Cembranos, and L. J. Garay. Jhep 06. 84, 2020.

[313] S. Sarkar. Reports on progress in physics. 59:1493, 1998.

[314] J. Schechter and J. W. F. Valle. Neutrino Masses in SU(2) x U(1) Theories. *Phys. Rev. D*, 22:2227, 1980.

[315] Matthew D. Schwartz. *Quantum Field Theory and the Standard Model*. Cambridge University Press, 3 2014.

[316] Douglas Scott. The standard model of cosmology: A skeptic's guide. *Proc. Int. Sch. Phys. Fermi*, 200:133–153, 2020.

[317] Chien-Yeah Seng, Jordy de Vries, Emanuele Mereghetti, Hiren H. Patel, and Michael Ramsey-Musolf. Nucleon electric dipole moments and the isovector parity- and time-reversal-odd pion–nucleon coupling. *Phys. Lett. B*, 736:147–153, 2014.

[318] Vladimir Shiltsev. Fermilab Proton Accelerator Complex Status and Improvement Plans. *Mod. Phys. Lett. A*, 32(16):1730012, 2017.

[319] Vanda Silveira and A. Zee. SCALAR PHANTOMS. *Phys. Lett. B*, 161:136–140, 1985.

[320] A. M. Sirunyan et al. Search for vectorlike light-flavor quark partners in proton-proton collisions at $\sqrt{s}$ =8 TeV. *Phys. Rev. D*, 97:072008, 2018.

[321] Albert M Sirunyan et al. Search for narrow and broad dijet resonances in proton-proton collisions at $\sqrt{s} = 13$ TeV and constraints on dark matter mediators and other new particles. *JHEP*, 08:130, 2018.

[322] Albert M Sirunyan et al. Search for Low-Mass Quark-Antiquark Resonances Produced in Association with a Photon at $\sqrt{s}$ =13 TeV. *Phys. Rev. Lett.*, 123(23):231803, 2019.

[323] Albert M Sirunyan et al. Search for low mass vector resonances decaying into quark-antiquark pairs in proton-proton collisions at $\sqrt{s} = 13$ TeV. *Phys. Rev. D*, 100(11):112007, 2019.

[324] Albert M Sirunyan et al. Search for high mass dijet resonances with a new background prediction method in proton-proton collisions at $\sqrt{s} = 13$ TeV. *JHEP*, 05:033, 2020.

[325] Albert M Sirunyan et al. Searches for physics beyond the standard model with the M_{T2} variable in hadronic final states with and without disappearing tracks in proton-proton collisions at $\sqrt{s} = 13$ TeV. *Eur. Phys. J. C*, 80(1):3, 2020.

[326] Albert M Sirunyan et al. Search for supersymmetry in final states with two oppositely charged same-flavor leptons and missing transverse momentum in proton-proton collisions at $\sqrt{s} = 13$ TeV. *JHEP*, 04:123, 2021.

[327] Torbjörn Sjöstrand, Stefan Ask, Jesper R. Christiansen, Richard Corke, Nishita Desai, Philip Ilten, Stephen Mrenna, Stefan Prestel, Christine O. Rasmussen, and Peter Z. Skands. An introduction to PYTHIA 8.2. *Comput. Phys. Commun.*, 191:159–177, 2015.

[328] Torbjorn Sjostrand, Stephen Mrenna, and Peter Z. Skands. A Brief Introduction to PYTHIA 8.1. *Comput. Phys. Commun.*, 178:852–867, 2008.

[329] Gary Steigman. Primordial nucleosynthesis in the precision cosmology era. *Annual Review of Nuclear and Particle Science*, 57(1):463–491, 2007.

[330] A Strominger. Lectures on the infrared structure of gravity and gauge theory, 1703.05448. *G. Compére and A. Fiorucci, Advanced Lectures on General Relativity*, 1801.

[331] Fuminobu Takahashi, Wen Yin, and Alan H. Guth. QCD axion window and low-scale inflation. *Phys. Rev. D*, 98(1):015042, 2018.

[332] M. Tanabashi et al. Review of Particle Physics. *Phys. Rev. D*, 98(3):030001, 2018.

[333] Tommi Tenkanen. Dark matter from scalar field fluctuations. *Phys. Rev. Lett.*, 123(6):061302, 2019.

[334] T. N. Tomaras and N. Toumbas. Phys. *Rev. D*, 101:065006, 2020.

[335] S Tremaine. M. h enon and d. lynden-bell, mon. not. r. *Astr. Soc*, 219:285, 1986.

[336] M. Trodden. Rev. of mod. *Phys.*, 71:1463, 1999.

[337] Tran N. Truong and R.S. Willey. Branching Ratios for Decays of Light Higgs Bosons. *Phys. Rev. D*, 40:3635, 1989.

[338] Yu-Dai Tsai, Patrick deNiverville, and Ming Xiong Liu. Dark Photon and Muon $g-2$ Inspired Inelastic Dark Matter Models at the High-Energy Intensity Frontier. *Phys. Rev. Lett.*, 126(18):181801, 2021.

[339] A. Vaitaitis et al. Search for neutral heavy leptons in a high-energy neutrino beam. *Phys. Rev. Lett.*, 83:4943–4946, 1999.

[340] R. Van De Water. *talk at U.S. Cosmic Visions: New Ideas in Dark Matter workshop, March 23-25, 2017, College Park, MD, USA*, 2017.

[341] M.B. Voloshin. Once Again About the Role of Gluonic Mechanism in Interaction of Light Higgs Boson with Hadrons. *Sov. J. Nucl. Phys.*, 44:478, 1986.

[342] T A Wagner, S Schlamminger, J H Gundlach, and E G Adelberger. Torsion-balance tests of the weak equivalence principle. *Classical and Quantum Gravity*, 29(18):184002, aug 2012.

[343] S. Weinberg. Phys. *Rev.*, 140, 1965.

[344] S. Weinberg. *Gravitation and Cosmology: principles and applications of the general theory of relativity.* John Wiley, N.Y, 1972.

[345] Steven Weinberg. A model of leptons. *Phys. Rev. Lett.*, 19:1264–1266, Nov 1967.

[346] Steven Weinberg. Gauge and Global Symmetries at High Temperature. *Phys. Rev. D*, 9:3357–3378, 1974.

[347] R. S. Willey and H. L. Yu. Neutral Higgs Boson From Decays of Heavy Flavored Mesons. *Phys. Rev. D*, 26:3086, 1982.

[348] S. Winitzki. Phys. *Rev.*, D72:104011, 2005.

[349] Martin Wolfgang Winkler. Decay and detection of a light scalar boson mixing with the Higgs boson. *Phys. Rev. D*, 99(1):015018, 2019.

[350] Tsutomu Yanagida. Horizontal gauge symmetry and masses of neutrinos. *Conf. Proc. C*, 7902131:95–99, 1979.

[351] Shan-Qing Yang, Bi-Fu Zhan, Qing-Lan Wang, Cheng-Gang Shao, Liang-Cheng Tu, Wen-Hai Tan, and Jun Luo. Test of the gravitational inverse square law at millimeter ranges. *Phys. Rev. Lett.*, 108:081101, Feb 2012.

[352] Yuhao Yang. Introduction to thermal field theory, 2011.

[353] D. R. Yennie, S. C. Frautschi, and H. Suura. , annals phys.13 379 (1961); g. *Grammer, Jr*, 8:4332, 1973.

[354] Junichi Yokoyama and Andrei D. Linde. Is warm inflation possible? *Phys. Rev. D*, 60:083509, 1999.

[355] Y. B. Zeldovich and A. A. Starobinsky. Sov. *Phys. JETP*, 34, 1977.

[356] F. Zwicky. On the Masses of Nebulae and of Clusters of Nebulae. , 86:217, October 1937.

[357] P. A. Zyla et al. Review of Particle Physics. *PTEP*, 2020(8):083C01, 2020.